Trindade Gonçalves, Francisco José (2015) Engineering of demagnetisation fields in exchange biased antidots studied using ferromagnetic resonance and Lorentz microscopy. PhD thesis.

http://theses.gla.ac.uk/6875/

Copyright and moral rights for this thesis are retained by the author

A copy can be downloaded for personal non-commercial research or study, without prior permission or charge

This thesis cannot be reproduced or quoted extensively from without first obtaining permission in writing from the Author

The content must not be changed in any way or sold commercially in any format or medium without the formal permission of the Author

When referring to this work, full bibliographic details including the author, title, awarding institution and date of the thesis must be given

Glasgow Theses Service
http://theses.gla.ac.uk/
theses@gla.ac.uk

Engineering of demagnetisation fields in exchange biased antidots studied using ferromagnetic resonance and Lorentz microscopy

Francisco José Trindade Gonçalves

Thesis presented for the degree of
Doctor of Philosophy

Materials and Condensed Matter Physics Group
School of Physics and Astronomy
University of Glasgow
United Kingdom

November 2015

Abstract

Nanostructured ferromagnetic materials have gained considerable attention recently for use in novel devices in the areas of data storage, microwave signal processing and propagation of electromagnetic waves. Structural modifications allow a control over the internal magnetic properties of the system down to the nanoscale. Lateral confinement gives rise to a distribution of demagnetisation fields in the plane of the thin film which can create interesting effects on static and dynamic magnetic properties.

In the context of this dissertation, nanostructuring is used as a means to engineer the static and dynamic response of magnetic systems. In particular, periodic arrays of holes embedded in continuous films are studied. With patterning one observes the emergence of an anisotropic field dependence as well as the emergence of non-uniform spin precession modes due to the dipole distribution at the film interfaces. These properties were probed primarily using a technique called broadband ferromagnetic resonance, whereby a microwave field drives the local spin dynamics of the magnetic system.

A way to further modify the magnetic properties induced due to the symmetry of the periodic structuring is by introducing an unidirectional field contribution which is characteristic of an exchange biased system. It was found that the magnetic pole distribution in antidots is particularly sensitive to the effects of exchange bias, giving rise to an asymmetric frequency response with respect to the applied field. The asymmetric microwave properties of an exchange biased FeMn/NiFe system with antidot structuring, obtained using electron beam lithography, are investigated. The ferromagnetic resonance (FMR) spectra exhibited several magnetostatic spin wave modes with 8-fold and 4-fold anisotropy components. Brillouin light scattering measurements showed the presence of a magnonic band gap as expected for this type of structure. To interpret these observations, the spin precessional modes obtained experimentally are correlated with localised mode profiles obtained by micromagnetic simulations.

The prospects of using patterned exchange biased systems to engineer microwave properties is greatly increased if one goes beyond the 2-dimensional perspective. In multilayered structures, one can modify the magnetic properties layer-by-layer to

achieve the desired response. This concept is demonstrated here by using a three dimensional structure in which an exchange biased and a free magnetic layer are stacked upon one another and patterned with an antidot configuration. The exchange bias acts as a pinning field for one layer, while the free layer reverses, promoting a zero net moment state. Interlayer dipole interactions are found to result in the partial cancellation of the microwave response. Micromagnetic simulations support the existence of a diminished microwave response which was confirmed by FMR measurements of an equivalent structure. The net moment cancellation, indicative of the antiparallel alignment, was observed on a Lorentz differential phase contrast scanning transmission electron microscope equipped with an FMR probe, which was designed and built for the purpose. This unique tool allows access to complex microwave response while the ground state of a nanostructured film is imaged via Lorentz microscopy. From the magnetostatic viewpoint, our results differ greatly from previous studies in a way that this sample shows distinct magnetic history and the near remanence states exhibit unique magnetic textures: magnetic vortices.

The applicability of the TEM in-situ FMR probe was extended to the mapping of radio frequency electromagnetic (EM) fields using low angle diffraction (LAD) imaging. The electron beam, propagating in a sample free environment, experiences the field distribution generated by the microstrip waveguide, which alters the electron amplitude and phase, as described by the Aharonov-Bohm effect, and results in different intensity profiles at the detector. As the microwave frequencies were varied, the different polarisation states are imaged directly. Microwave simulations allowed the EM field distribution to be calculated, which was used to reproduce the LAD results. A knowledge of the near field distribution in antennas is often a challenging task so this technique opens up new opportunities for planar devices operating in high vacuum conditions.

Declaration

The work presented in this thesis is based on research carried out primarily at the Materials and Condensed Matter Physics Group, School of Physics and Astronomy University of Glasgow, Scotland during the years 2011-15. Part of experimental results were obtained in collaboration within MCMP group as well as other research groups. The collaborations are detailed below.

- Prof. Ko-Wei Lin and Ms. Shan Su from the department of Materials Science and Engineering, National Chung Hsing University, Taiwan, provided the NiO/NiFe antidot template and the TEM cross sectional images of the structure. Prof. J. van Lierop and Dr. R. Desautels from the Department of Physics and Astronomy, University of Manitoba, Canada, provided the magnetometry data (SQUID) relative to the antidot template.

- Prof. Robert Bowman and Dr. Sinead O'Reily from the centre for nanostructured media, Queen's University Belfast, Belfast, provided the NiFe/FeMn thin films.

- Dr. Gonzalo V. Fernandez from the physics department of the University of York carried out the deposition of the IrMn/CoFe thin films and the magnetometry measurements.

- Dr. G. Gubbiotti from the Ghost Laboratory, University of Perugia, Italy, performed the BLS experiments.

- Dr. Sam McFadzean, Dr. Gary Paterson and myself carried out the data acquisition relative to the study of the cross sections discussed in Chapter 4 and 5. Dr. Damien McGrouther, Dr. Ciaran Ferguson and myself carried out the data acquisition relative to the Lorentz DPC studies discussed in Chapter 5.

- The fabrication of the microstrip waveguides was done in close collaboration with Dr. Evgeny Sirotkin former collaborator at the Scottish Microelectronics Centre, University of Edinburgh, Scotland.

Part of the work presented in this thesis has been published in:

Anisotropy engineering using exchange bias on antidot templates, F. J. T. Goncalves, R. D. Desautels, S. Su, T. Drysdale, J. van Lierop, K.-W. Lin, D. S. Schmool, and R. L. Stamps, AIP Advances 5.6 (2015), p. 067101. doi: 10.1063/1.4922055.

No part of this thesis has been submitted for any other degree or qualification and all the analysis is my own work unless referenced to the contrary in the text.

Copyright © 2015.

"The copyright of this thesis rests with the author. No quotations from it should be published without the author's prior written consent and information derived from it should be acknowledged".

Acknowledgements

First, I would like to acknowledge the contribution of my supervisors Prof. Bob Stamps and Prof. David Schmool and thank them for their guidance throughout the whole PhD. The interesting discussions on how to best manage resources time, expectations as well as the discussions we had about physics were and will certainly continue being pivotal in my development as a researcher. I particularly appreciated the fact that I was given the opportunity to work with a wide range of collaborating institutions, to attend relevant scientific conferences, many research meetings and was given the freedom to define the path I found more suitable to achieve my goals.

I want to thank Dr. Gary Paterson for the always useful contribution in the laboratory and for having a very scientific approach to problems. Whenever I was stuck with some experiments, he was always there to give the right advice. Also I would like to acknowledge the contribution of Dr. Timothy Drysdale and Dr. Rhet Magaraggia and thank them for their help in the field of microwave technology and instrumentation.

From the microscopy side, I have benefited greatly from expert TEM users such as Drs. Damien McGrouther, Stephen McVitie, Samuel McFadzean, Donald MacLaren, Ciaran Ferguson, Kerry O'Shea and Maria José Romero. In particular Dr. Damien McGrouther, who actively collaborated throughout the whole research work and shared enthusiasm in the development of the in-situ FMR rods. A special thanks to Dr. Ciaran Ferguson for always having time for interesting discussions about magnetism. At some point we succeeded in having our own research group! Also, an acknowledgement note to Colin How and William Smith who were always there to help with the TEM and the FIB, with who I also enjoyed playing football and squash (Colin, someday I'll beat you at squash).

A thanks note to my collaborators Drs. Sinead O'Reilly, Gonzalo Fernandez and

Prof. Ko-Wei Lin for the thin film deposition, and to the nanofabrication experts: the JWNC staff, Dr. Stephen Thoms, Dr. Pedro Parreira and Dr. Evgeny Sirotkin (from SMC, Edinburgh). Also, a thanks note to Dr. Gianluca Gubbiotti for the very useful discussions about light scattering experiments. My thanks to Drs. May Wheeler and Ales Hrabec for the opportunity to contribute to the already high standard research work they develop.

I would also like to acknowledge the very constructive feedback received from the PhD Viva examiners, Prof. Robert Hicken and Prof. Jonathan Weaver, as well as the cooperation and professionalism of the convener, Dr. Donald MacLaren.

On a personal level, I can say that my whole family and friends were pretty much the driving force and the support over the last four years. In fact, ever since I manifested interest in anything all, my Mum and Dad provided support (and funds) and encouragement. It is always a pleasure to go back home as the welcome is warm. Also, without the enthusiasm and unconditional support of my sister Paula and Filipe I would have not reached this stage. Of course my brothers Sérgio and João and my sister Sofia did greatly in keeping me in the line. I can also say that the birth and development of my niece Ana Beatriz had a major impact on my life. Thanks for being so curious, smart and kind. Maybe one day you will become a scientist!

A few words to my "home town" friends Joana, Maria, Luis and José who I keep contact with and were always there despite my, sometimes, unpredictable attitude. The friends I made during my university studies in Portugal did also have a great impact on my PhD/career: Luis Guerra, Tomás Magalhães and Carlos Campos, who I admire for their brilliance, courage and creativity.

At last but not least, I want to acknowledge the amazing group of friends I made since I moved to Scotland. Them being my friend and flatmate Aaron, my friends Natalia, Ciaran, Pedro, Shabir, Stefanie, Silvia, Marco and Gary Paterson (yes, a repeat). We made each others lives more exciting, full of great evenings together, football, pseudo-politics chat and shared two of the greatest wonders of the research world: the espresso coffee maker and the pub. Because of them I gained great interest in many things I would otherwise find hard to have interest in. Thank you!

Contents

Abstract iii

Declaration v

Acknowledgements vii

1 Thesis overview 1

2 Introduction 10

2.1 Magnetisation dynamics 10

2.1.1 Dynamic susceptibility and resonance equation 11

2.1.2 Smit-Beljers resonance equation 13

2.2 Spin waves 15

2.3 Relaxation mechanisms 17

3 Overview of the techniques 21

3.1 Introduction 21

3.2 VNA-FMR 22

3.2.1 Transmission line and S-Parameters 22

3.2.2 Detection of the precessing magnetisation 27

3.2.3 FMR measurements and data acquisition 29

3.2.4 FMR Analysis 31

3.3 In-situ FMR rod 34

3.3.1 Single-port setup 35

3.3.2 Two-port setup 38

3.3.3 Excitation spectra of spin waves 39

3.4 Lorentz microscopy 43

3.4.1 Fresnel . . . 44
3.4.2 Low angle diffraction . . . 44
3.4.3 Differential phase contrast . . . 48

4 Unbalanced magnetic pole distribution on exchange biased antidot templates 51

4.1 Introduction . . . 51
4.2 Experimental data and discussion . . . 53
4.3 Micromagnetic simulations . . . 56
4.4 Conclusions . . . 58

5 Competing anisotropies in exchange biased 2-D nano-structured systems 60

5.1 Introduction . . . 61
5.2 Film growth and patterning . . . 62
5.3 Mode structure . . . 66
5.3.1 Field dependent magnetodynamics using VNA-FMR and BLS 67
5.3.2 Spin wave dispersion using BLS . . . 71
5.3.3 Angular dependence of FMR and magnetic anisotropies . . . 72
5.4 Partial patterning and mode analysis . . . 78
5.4.1 Partial patterning . . . 78
5.4.2 Origin of the dynamic modes . . . 82
5.5 Asymmetry . . . 85
5.6 Conclusions . . . 87

6 3-D nanostructures: Lorentz DPC and VNA-FMR studies on bi-layered antidots 88

6.1 Introduction . . . 89
6.2 Fabrication, patterning and magnetic properties . . . 91
6.3 Lorentz DPC studies of S2 . . . 94
6.4 Ferromagnetic resonance of antidot bi-layers . . . 103
6.5 Conclusions . . . 108

7 TEM in-situ dynamic experiments: the mapping of electromagnetic fields **110**

7.1 Introduction . . . 111
7.2 Theoretical considerations . . . 112
7.3 Experimental results . . . 115
7.4 Microwave simulations . . . 123
7.5 Discussion . . . 127
7.6 Conclusions . . . 134

8 Conclusions and outlook **135**

A Fabrication of antidots **165**

B Micromagnetic simulations **171**

B.0.1 Spatially uniform excitation . . . 172
B.0.2 Spatially non-uniform excitation . . . 174

C Microwave simulations using CST **176**

D Appendix- Chapter 5 **180**

D.1 Applied field direction in tilt series . . . 180
D.2 Single exchange biased layer . . . 183
D.3 Cancellation region in S2 . . . 185
D.4 Balancing the Vortex profile . . . 187

E Appendix- Chapter 6 **188**

E.1 Processing the experimental data . . . 188
E.2 E/H-field distribution . . . 190

Chapter 1

Thesis overview

Nanomagnetism research is devoted to the understanding and application of magnetic structures with nanometric features in material science and technology. In patterned materials consisting of a periodic lattice of holes (Fig. 1.1), also known as antidot lattices (ADL), the emergent magnetic properties span static and slow magnetisation processes at one extreme, up to fast dynamics, in the GHz to THz frequency range at the other extreme [1]. Due to structuring, the ground state of the magnetisation can be affected near the holes and the response to applied fields modified. Investigations of the static properties of ADL are carried out, mainly to further two important applications: (1) the incorporation of ADL in data storage technology [2] and multi-state magnetic logic, due to the possibility of achieving well controlled switching [3, 4] and (2) to use effects of magnetic domain configurations on the dynamic properties for microwave applications. In recent years, several spin wave based devices were proposed, covering applications in the field of microwave signal manipulation [5–8]. The feasibility of a spin wave logic gate is discussed in [9] by Kostylev et al. where a Mach-Zender type curent controlled interferometer is used to perform logical operations with spin waves propagating in a ferromagnetic film. Spin wave multiplexers controlled via current switching in bifurcated nanostripes was proposed in [10], magnon transistors in [11].

Antidots are seen as viable for use as non-volatile memory elements, due to the stability with which magnetic states are pinned by the effective anisotropy at the hole-to-hole sites [12, 13]. The tailoring of static magnetic properties such as coercivity and anisotropy is achieved by modification of the lattice parameters

[14–17].

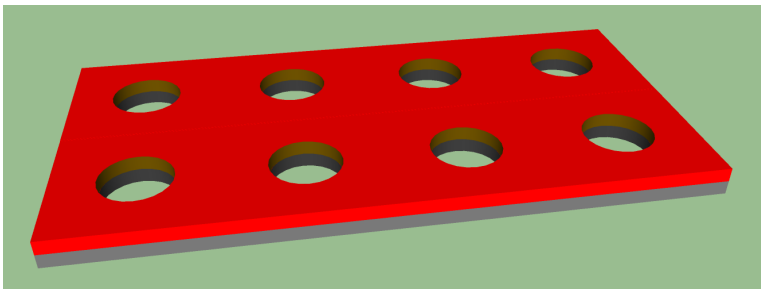

Figure 1.1: Schematic illustration of an ADL, i.e., a periodic lattice of holes.

Further modifications to the spin configuration can be achieved with exchange bias (EB). Exchange bias emerges due to interface coupling between an antiferromagnet (AF) and a ferromagnet (FM), where an exchange anisotropy can be achieved if the heterostructure is allowed to cool from above the Néel temperature (T_N) of the AF [18–20]. This phenomena was first observed and described by W. H. Meiklejohn and Bean [21] in Co/CoO (shell) particles. While the spins in the FM are strongly pinned by an external field, the temperature should be raised to allow a phase transition of the AF, from anti-parallel to disordered state. At this stage, the spins at the interface of the AF couple to those of the FM layer. The AF phase is restored by lowering the temperature below T_N and the pinned interface spins provide the reference for the anti-parallel alignment. In this way, an interface anisotropy can be achieved. Because the AF can only be modified with very strong applied fields (due to high anisotropy), the interface spins remain pinned, even when the FM layer undergoes reversal. This is the reason as to why exchange bias is unidirectional. Experimentally, the effect of exchange bias is seen through a field displacement of the hysteresis and enhanced coercivity can also be obtained, depending on the degree of magnetic disorder of the domain structure at the interface and the AF anisotropy [20, 22]. The effect of exchange bias is illustrated in Fig. 1.2.

Exchange bias has been applied in spin valves [23–25] and is applied in microwave engineering [26–29]. While the effect of EB in isolated nanostructures is reported in the literature [30–34], in particular for AF/FM dots [35–37] and AF/FM stripes [38–40], there are few reports on the effect of EB on ADL structures. Those available mostly focus on the reversal behaviour and on the effect of patterning on the AF domain size, which ultimately defines the strength of the EB field [41–43].

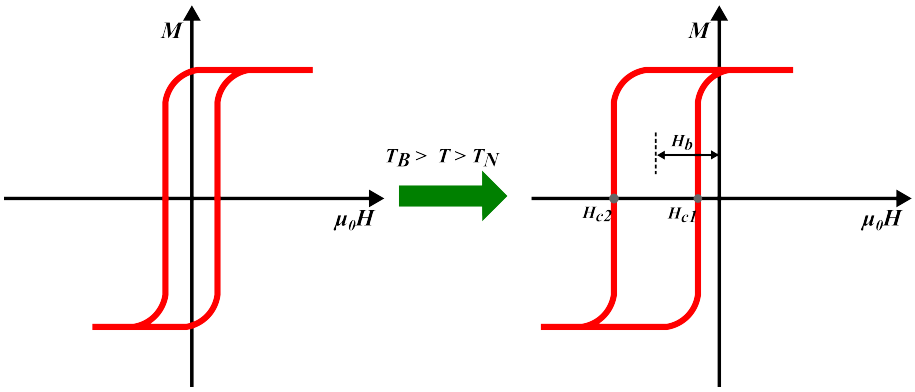

Figure 1.2: Illustration of the lateral displacement of an hysteresis loop, due to exchange bias, which can be determined as $H_b = (H_{c1} - H_{c2})/2$.

In the context of exchange biased ADL, several phenomena are still to be understood, such as the enhancement of the bias field with structuring, the domain reversal in the ADL and how EB can in general provide advantages in such structures. An understanding of the reversal mechanisms in ADL is relevant as the dynamic properties greatly depend on the static spin configuration. For this purpose, high resolution imaging techniques, such as Lorentz microscopy and magnetic force microscopy allow an understanding of some features of the domain reversal, namely the extent to which domains extend and rotate within the lattice [44, 45] while the magnetisation undergoes reversal. This field has room for improvement, following the increase in the resolution of the imaging techniques [46] and the development of in-situ excitation experiments, such as the TEM in-situ technique reported in this thesis.

By modifying the ground state via structuring and exchange bias, the fast dynamic magnetisation processes are also affected [47]. The magnetisation dynamics in ferromagnetic materials are described by the Landau-Lifshitz (LL) torque equation, introduced in 1935 [48], in which precessional and damping terms were considered. Neglecting the damping, the dynamic component of the magnetisation $\vec{M}(r,t)$ is written in the form of $\dfrac{\partial \vec{M}(r,t)}{\partial t} = \gamma\mu_0 \vec{M}(r,t) \times \vec{H}_{eff}(r,t)$, where γ is the gyromagnetic ratio and μ_0 is the vacuum permeability. The effective field can be written as $\vec{H}_{eff}(r,t) = \vec{H}_{ex}(r,t) + \vec{H}_d(r,t) + \vec{H}_0$, where the term $\vec{H}_{ex}(r,t)$ corresponds to the exchange field, the term $\vec{H}_d(r,t)$ corresponds to a general form of the magnetostatic field, which is discussed ahead, and $\vec{H}_0$ can be seen as a static uniform bias field. In the limit of linear excitations, the term $\vec{M}(r,t)$ may be written in the form of the

dynamic component, $\vec{m}(r,t)$, assumed to be orthogonal to the direction of $\vec{M}(r,t)$ and simultaneously $|\vec{M}| \gg |\vec{m}|$. In the solution to the linearised LL equation for an ADL, and following the more general theory of electrons in crystals, introduced by Bloch in 1930 [49, 50], the dynamic magnetisation $\vec{m}(r,t)$ assumes the form of a Bloch wave $\delta\vec{m}_k = \delta\tilde{m}_k e^{ik.r}$, where k is the Bloch wavevector associated with the periodicity of the ADL , and $\delta\tilde{m}_k$ is a spin wave [51, 52] – a magnetic fluctuation intrinsically associated with the excitation of the magnetic configuration away from equilibrium [53, 54].

A particularity of the ADL is that further constraints are imposed on the spin textures and spin dynamics due to the emergence of inhomogeneities in the demagnetisation fields, $\vec{H}_d(r)$, which are a direct consequence of the magnetic pole distribution around the hole interfaces. The calculation of the demagnetisation fields, explicitly for ADL, can be found in Refs. [55–59]. Often, the distribution of the demagnetisation field is accessible via micromagnetic simulations. Figure 1.3 shows the distribution of the static magnetisation $\vec{M}(r)$ (left) and the distribution of the demagnetisation fields, $\vec{H}_d(r)$. The deformation of both $\vec{M}(r)$ and $\vec{H}_d(r)$, in particular near the holes, is rather noticeable.

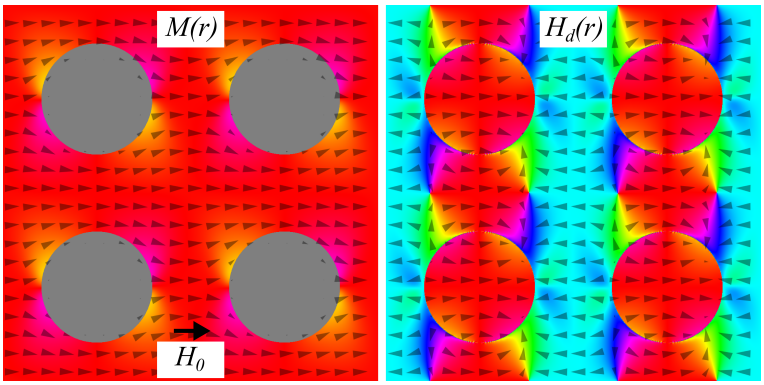

Figure 1.3: Illustration of the distribution of the magnetisation (left) and demagnetisation fields (right).colour code follows the arrow code. Results obtained from micromagnetic simulations. Results obtained from an ADL with 280 nm diameter holes, and a periodicity of 420 nm. the magnetic parameters used are: M_s= 1 T, A_{ex}= 13e^{-12} J/m, α= 0.02 and static field H= 0.04 T.

Spin wave modes may be considered as localised, if the spin precession amplitude is confined to the interfaces between holes, or as extended modes, if the spin precession extends through the ADL. This sort of artificially created spin wave band structure

is referred to as a magnonic crystal [6, 60, 61]. The localisation of magnetostatic spin wave modes will be discussed in the context of chapter 5. The direction of the spin wave propagation is also important, since group velocity (v_g) is also affected by $\vec{H}_d(r)$ and the direction relative to $\vec{M}(r)$. Spin waves which propagate along the direction perpendicular to the static magnetisation ($\vec{M}(r)$, in plane) are considered Damon-Eshbach modes, $\vec{k} \perp \vec{M}$, and backward volume modes if $\vec{k} \| \vec{M}(r)$. In the latter, the frequency of the spin waves decreases with increase in k due to negative v_g ($v_g = \partial\omega/\partial k < 0$)[55, 62].

When it comes to the classification of spin waves, it is convenient to establish three regimes. The infinite wavelength excitation ($k = 0$) regime is often called the ferromagnetic resonance limit. The first experimental evidence for resonant absorption of microwave power, i.e. ferromagnetic resonance, was published by Griffiths in 1946 [63]. Later in 1948, this observation was described in physical terms by Kittel [64], which established the dependence of the resonance frequency as a function of the applied field and the internal properties of the magnetic material. Ferromagnetic resonance will be described in greater detail in chapter 2.

In the limit of finite wavelength excitations, the spin wave energy has contributions from dipole-dipole interactions and exchange interactions. The dipole contribution dominates in the μm range, at long wavelengths, while exchange interactions dominate in the nm range, as illustrated in Fig. 1.4. For the case of short wavelength spin wave excitations, the first results published date back to 1966, when Fleury et al. observed light scattering induced by spin waves in antiferromagnetic (FeF_2) films [65]. A decade later, an array of grooves was patterned in yttrium iron garnet (YIG) resulting in what is accepted as the first experimental study of magnetostatic spin wave propagation in patterned materials [66]. The grooves were etched on the surface of the material so that with modulation in thickness one would obtain a periodically impedance mismatched transmission line for spin waves, enabling selective microwave filtering behaviour. The theoretical work presented in Refs. [67–71] established a theoretical basis for the origin of the dipole and exchange spin waves. Magnonics has motivated renewed interest in the spin wave properties of YIG [72, 73] and also in metallic materials [74, 75]. Metals are important in the sense that charge carriers can also encode information through their spin properties [76–78].

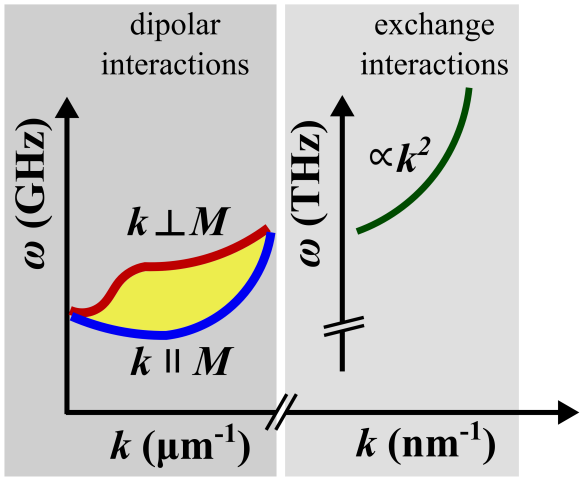

Figure 1.4: Illustration of the spin wave dispersion for both dipolar and exchange interaction regime. Figure adapted from Ref. [79]. Note the k^2 dependence of the frequency as the wave number increases.

As for the materials employed, the most common are YIG, $Ni_{80}Fe_{20}$ [80] and $Co_{40}Fe_{40}B_{20}$ [61], in single layer configuration. Materials are required to have reduced spin wave dissipation (low damping, α) in order to achieve decay lengths well above the micrometer range ($\sim$ 50 μm for $Ni_{80}Fe_{20}$), which would make them more useful for device integration. The study of the fundamental properties can be performed in a material such as $Ni_{80}Fe_{20}$ because is widely accessible, suitable for nano-scale patterning and has a relatively low damping (α= 0.008 [81]). However, YIG (α= 0.0003) [81, 82] and CoFeB (α= 0.0042 [83]) may be better candidates for applications since they have lower damping.

A series of experiments revealed the degree of confinement of spin wave modes with respect to the ADL. In 2004 Yu et al. [84, 85] established the existence of localised standing spin wave modes between adjacent holes and the spatial profile of these modes was directly observed by Pechan et al. [86]. The degree to which spin wave modes are confined or extended to the hole-to-hole spacing is explored in the work by Neusser et al. [60, 87] as well as in several other Refs. [88–91]. It was found that localised and extended modes coexist in the ADL, as shown in most cases by analysing the mode profile distribution obtained by micromagnetic simulations. The configurations used were ADL with square symmetry, where the spacing and hole diameter was varied in the range of 1000-100 nm. The main goals were to understand the nature of the modes, in terms of the anisotropy induced in

the static configuration as well as the effect of the demagnetisation and patterning in the magnetostatic and exchange spin waves. Other lattice symmetries were being studied, such as rectangular shape [86], hexagonal shape [92, 93], rhombic [94] and octagonal [95]. The shape of the holes has also been extensively modified [15, 96–98]. These studies revealed the symmetry of the anisotropic behaviour and demonstrated the possibility of tailoring magnonic band gaps. When the periodicity, d, of the structuring is comparable to the wavelength , λ, of the spin waves ($d \sim \lambda$), which is the case for the ADL systems here discussed, scattering of spin waves can occur, resulting in the emergence of frequency band gaps and mode crossing.

Band structure engineering in two dimensional structured magnetic materials had only been demonstrated in 1996 by Vasseur et al. [56]. The early 2000's marked the beginning of the magnonics 'race' with theoretical predictions that band gaps, would be achievable in single ferromagnetic layers, with modulated structure [99] in the plane of the film. This theoretical work was demonstrated experimentally in 2003 by Gulyaev et al. [100], when it was found that ADL results in forbidden and allowed energy states, regarding the propagation of spin waves. Since then, the development of fabrication and characterisation techniques enabled the study of spin waves in well defined nanostructures and revealed exceptional features and applications. Research on the topic has been particularly focused on studying possibilities of tuning the spin wave dispersion as a function of the structural parameters such as shape and periodicity of the holes [52, 101–103]. A universal dependence of the spin wave dispersion as a function of the ADL parameters has recently been introduced in S. Tacchi et al. [104].

The vast majority of the literature is directed to single layered systems while fewer reports were found approaching multi-layered ADL structures. These are expected to have similar properties (layer-by-layer) but with an additional degree of tuning provided by the inter-layer interaction, either through exchange coupling or dipole-dipole interactions. In particular, two concepts are yet to be fully understood and explored: the effect of exchange bias on the static and dynamic response of an ADL and the effect of inter-layer dipolar interactions in multi-layered structures. Similarly to the dipolar interactions occurring between magnetic poles, in the plane of an ADL, in a multi-layered system, the distribution of the poles can also induce

coupling effects between adjacent layers.

Multi-layered ADL structures may be regarded as stacked layers of EB films (or FM layers spaced by non-magnetic films) or hybrid structures comprised of single ADL films with different magnetic materials filling the holes, also called bi-component magnonic crystals (BMC) [105, 106]. In BMC, the spin wave channels can be rotated over a wider rotation angle, relative to the symmetry of the lattice, when compared to single film ADL [52, 107, 108]. Magnetic ADL systems, comprised of multiple layers are studied in order to understand the effect layering in the spin wave properties [109]. In particular, one aims at understanding the effects the interlayer dipole interactions in the spin wave response of the system [110, 111].

The focus of this thesis is the effect of the demagnetisation fields on the magneto-static and dynamic properties of exchange biased ADL, in single and multi-layer configuration. This thesis is structured as follows.

- In **Chapter 2**, the phenomena of magnetisation dynamics is discussed in detail. Firstly, by describing the torque equation and then by presenting the solution for the dynamic equilibrium, i.e. resonance condition, upon excitation with microwave driving fields via: 1) magnetic susceptibility and 2) Smit-Beljers method using the free energy. Finite wavelength excitations, spin waves, and energy dissipation mechanisms are also discussed in the following sections.

- A description of the experimental techniques employed in the characterisation of the magnetic structures is provided in **Chapter 3**. Special focus is given to the broadband vector network analyser ferromagnetic resonance, VNA-FMR, used in this work. In addition to the standard VNA-FMR method, an FMR probe was designed and developed for transmission electron microscopy (TEM) in-situ microwave experiments. The details of this experimental set-up can be found in Sec. 3.3. Different Lorentz microscopy techniques used in this work, are described in Sec. 3.4.

- The first of a series of antidot structures, produced using the hole template method, is discussed in **Chapter 4**. A comparison is made between a simple antidot film and an exchange biased film, to determine the effect of exchange bias on the magnetic pole distribution at the hole sites. Ferromagnetic resonance

experiments are presented and the discussion is supported by micromagnetic simulations.

- The dynamic properties of an exchange biased antidot lattice structure, fabricated using electron beam lithography, are investigated in **Chapter 5**. Ferromagnetic resonance experiments reveal a complex mode structure, which is highly dependent on the direction of the applied field relative to the structuring. Brillouin light scattering measurements show a magnonic band gap, as expected for this type of structure. Micromagnetic simulations support the discussion on the anisotropy and magnetostatic spin wave properties.

- In **Chapter 6**, a multilayered exchange biased antidot structure, fabricated using focused ion beam, is investigated using Lorentz TEM and VNA-FMR. A new characterisation method was used in this chapter, as some of the results were obtained using Lorentz TEM with in-situ microwave excitation.

- Lastly, **Chapter 7** deviates from the study of ADL in a way that it concerns the characterisation of the measurement technique that enables the TEM in-situ microwave experiments, which can be applied for any type of structure. Here, the concept of deflecting electrons due to the Lorentz force, while in the presence of microwave fields, must be taken into account when considering the TEM with in-situ experiments, since travelling electrons will experience the dynamic fields in the region of the probe. An understanding of the electron interaction with the microwave probe is needed so that direct waveguide-electron interactions can be distinguished from effects due to the presence of the magnetic sample.

Chapter 2

Introduction

The concept of magnetisation dynamics is discussed by first describing the torque equation and then solving it to obtain the dynamic susceptibility, upon excitation with microwave driving fields. It is also demonstrated how the equilibrium condition, i.e., the resonance condition may be determined following the Smit-Beljers formulation using the free energy of the magnetic system. Finite wavelength excitations, spin waves, and energy dissipation mechanisms are also discussed in this chapter.

2.1 Magnetisation dynamics

The classical description of magnetisation dynamics follows the Landau Lifshitz Gilbert (LLG) equation, LLG, which is shown in Eq. 2.1,

$$\frac{\partial \vec{M}(r,t)}{\partial t} = -\gamma\Big[\vec{M}(r,t) \times \vec{H}(r,t)\Big] + \frac{\alpha}{M}\left[\vec{M}(r,t) \times \frac{\partial \vec{M}(r,t)}{\partial t}\right], \qquad (2.1)$$

where γ is the gyromagnetic ratio, $\vec{H}$ an external field, M is the saturation magnetisation and α is a dimensionless parameter representing the LLG dissipation term λ/M. The first term on the right hand side of Eq. 2.1 corresponds to the precessional motion of the magnetisation around the equilibrium direction set by the free energy. The second term corresponds to the damped motion, which tends to restore the magnetisation towards the equilibrium direction. The damped precessional motion of the magnetisation in the presence of a magnetic field is illustrated in Fig. 2.1. The solution to Eq. 2.1 is obtained under the assumptions that the perturbations in both magnetisation and applied field are subject to $\vec{m}(r,t) \ll \vec{M}(r,t)$ and $\vec{h}(r,t) \ll \vec{H}(r,t)$.

Secondly the equation of motion must be solved when the system is at equilibrium. The equilibrium condition can be expressed in the form of $\vec{M}(r) \times \vec{H}(r) = 0$ or equivalently via the energy minimisation condition, $\frac{\partial E}{\partial \theta}$ and $\frac{\partial E}{\partial \phi} = 0$, where E represents the free energy of the system which typically written as a function of the azimuthal (ϕ) and polar (ϕ) components.

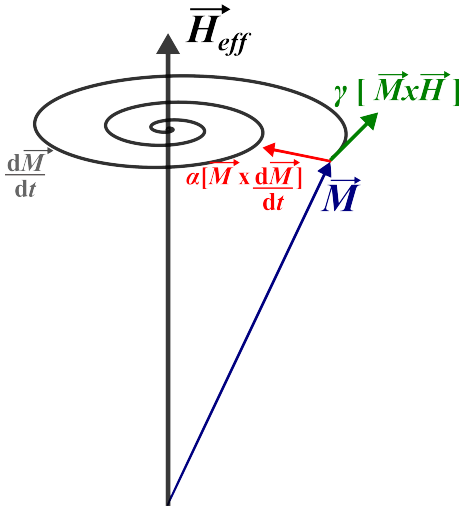

Figure 2.1: Schematic of the magnetisation precession around the direction of an effective field (H_{eff}). Following the LLG equation, the motion is defined by a precessional and a damping term.

In a ferromagnetic material such as $Ni_{80}Fe_{20}$, where $\mu_0 M = 1$ T and anisotropy is neglected due to its polycrystalline nature, the precession occurs in the gigahertz frequency (10^9Hz) range. The dynamic susceptibility is calculated next, to demonstrate the shape of the absorption of a ferromagnetic material, at resonance.

2.1.1 Dynamic susceptibility and resonance equation

Consider an oscillating magnetic field $\vec{h}(r,t)$ in the transverse direction relative to a magnetic field $\vec{H}(r,t)$ ($\vec{h}(r,t) \perp \vec{H}(r,t)$) applied along the x-axis. For a linear response one assumes that the same transverse component of the magnetisation will be driven, without changing the magnitude of $\vec{M}(r,t)$ ($|\vec{m}| \ll |\vec{M}|$) [112]. The components of the applied field and the magnetisation can be expressed as:

$$\vec{H} = \begin{pmatrix} H_x - N_x M \\ h_y - N_y m_y \\ h_z - N_z m_z \end{pmatrix} \qquad \vec{M} = \begin{pmatrix} M_x \\ m_y \\ m_z \end{pmatrix} \tag{2.2}$$

where N_x, N_y and N_z are the demagnetisation factors.

The linearised equation of Eq. 2.1 is as follows

$$i\omega\vec{m} + \gamma\vec{m} \times \vec{H} + \frac{i\alpha\omega}{\vec{M}}\vec{m} \times \vec{M} = -\gamma\vec{M} \times \vec{h} \tag{2.3}$$

Considering the terms of eq. 2.2, the solution to Eq. 2.3 can be expressed as

$$\begin{pmatrix} \omega_H + \omega_M(N_y - N_x) - i\omega\alpha & i\omega \\ -i\omega & \omega_H + \omega_M(N_z - N_x) + i\omega\alpha \end{pmatrix} \begin{pmatrix} m_y \\ m_z \end{pmatrix} = \omega_M \begin{pmatrix} h_y \\ h_z \end{pmatrix}, \tag{2.4}$$

where $\omega_M = \gamma M_s$ and $\omega_H = \gamma H$.

To determine the susceptibility tensor, one modifies Eq. 2.4 in order to satisfy $\vec{m} = \left(\begin{smallmatrix} \chi_{yy} & \chi_{zy} \\ \chi_{yz} & \chi_{zz} \end{smallmatrix}\right)\vec{h}$ [113, 114], resulting in

$$\overline{\overline{\chi}} = \frac{\omega_M}{\omega_{res}^2 - \beta} \begin{pmatrix} \omega_H + \omega_M(N_z - N_x) + i\omega\alpha & -i\omega \\ i\omega & \omega_H + \omega_M(N_y - N_x) + i\omega\alpha \end{pmatrix}, \tag{2.5}$$

where ω_{res}^2 and β are written as

$$\omega_{res}^2 = (\omega_H + \omega_M(N_y - N_x))(\omega_H + \omega_M(N_z - N_x) \tag{2.6a}$$

$$\beta = \omega^2(1 + \alpha^2) + i\omega\alpha(2\omega_H + \omega_M(N_z + N_y - 2N_x)), \tag{2.6b}$$

Assuming that the strongest component of the excitation field is aligned with the y-axis, the dominant susceptibility term is χ_{yy} [1]. The real and imaginary parts of $\chi_{yy} = \chi_{yy}^{'} + i\chi_{yy}^{''}$ can be determined conveniently from Eq. 2.5. Considering $\alpha \ll 1$, one can make the approximation $1+\alpha^2 \approx 1$ and consequently $\chi_{yy}^{'}$ and $\chi_{yy}^{''}$ can be written as

$$\chi_{yy}^{\prime} \approx \frac{\omega_M(\omega_H + \omega_{eff})(\omega_{res}^2 - \omega^2)}{(\omega_{res}^2 - \omega^2)^2 + \alpha^2\omega^2(2\omega_H + \omega_{eff})^2} \tag{2.7a}$$

$$\chi_{yy}^{\prime\prime} \approx \frac{\alpha\omega\omega_M(\omega^2 + (\omega_H + \omega_{eff})^2)}{(\omega_{res} - \omega^2)^2 + \alpha^2\omega^2(2\omega_H + \omega_{eff})^2}. \tag{2.7b}$$

[1] Here, it is assumed that the magnetic specimen is smaller than the width of the signal line. If the sample is larger than signal line, the susceptibility term χ_{yz} may also be considered due to the out-of-plane field components near the edges of the signal line.

The real and imaginary parts of the susceptibility are plotted in Fig. 2.2. At resonance, $\omega = \omega_{res}$, the real part of χ is zero and the imaginary part reaches a maximum. The real and imaginary components represent the in-phase and out-of-phase components of m_y relative to the excitation field (h_y). If only the precessional motion was considered (α= 0) then χ= χ'. The imaginary part is proportional to the damping term α. When $\chi'' \neq 0$, a continuous source of excitation is required to maintain the precession of the magnetisation. This term can be seen as proportional to the energy transferred from the excitation field to the magnetic system and follows the shape of a Lorentzian function with a peak at ω_{res} and frequency linewidth $\Delta\omega_{res}$. The expression for ω_{res} shown in Eq. 2.6b corresponds to the well known Kittel formula for the resonance frequency of an ellipsoid [115]. For the case of a thin film magnetised in plane ($N_x = N_y = 0$, $N_z = 1$) the resonance equation and frequency linewidth are given by

$$\omega_{res}^2 = \omega_H(\omega_H + \omega_M) \tag{2.8a}$$

$$\Delta\omega_{res} = \alpha(2\omega_H + \omega_M) \approx \alpha\mu_0\gamma M(forH \ll M), \tag{2.8b}$$

Equation 2.8 is linearly dependent on the resonance frequency and on the damping coefficient α. The resonance linewidth may also be obtained by finding the peaks of χ'.

2.1.2 Smit-Beljers resonance equation

The resonance frequency can also be determined via the total free energy, U, of the system. This method is more convenient for magnetic systems where the internal field constrains the orientation of the magnetisation to a specific direction. The equilibrium condition can be determined from an energy minimization condition and thus should follow the condition that $\int_V UdV$ reaches a minimum. As the energy is treated as a whole, the term $\vec{H}$ shown in Eq. 2.1 may be considered an effective field term related to the total free energy by $\vec{H}_{eff} = \dfrac{-\partial U}{\partial M}$.

A knowledge of which energy terms act upon the system allows to directly determine the resonance equation by applying the method proposed by Smit and Beljers [112]. To follow this method one has to convert the cartesian projection of the

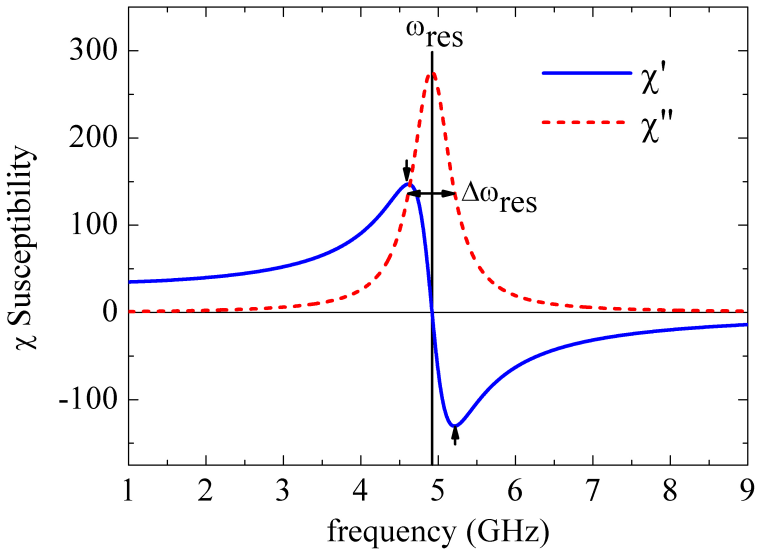

Figure 2.2: Plotted data represents the analytical calculation of the dynamic susceptibility following Eq. 2.7. Parameters used: γ= 28 GHzT^{-1}, $\mu_0 M_s$= 1 T, $\mu_0 H$= 0.03 T, $\alpha = 0.02$.

magnetisation into a spherical coordinate system where $\vec{M}(\theta,\phi) = M\cos\phi\sin\theta\hat{x} + M\sin\phi\sin\theta\hat{y} + M\cos\theta\hat{z}$, where $\hat{x}$,$\hat{y}$,$\hat{z}$ are unit vectors. The only variables are the azimuthal angle, θ, and the polar angle, ϕ. The resonance frequency can be obtained directly from the Smit-Beljers equation as follows

$$\omega = \frac{\gamma}{M\sin\theta_0}\left(U_{\theta\theta}U_{\phi\phi} - U_{\theta\phi}^2\right)^{1/2} \tag{2.9}$$

where $U_{\theta,\theta}$= $\frac{\partial^2 U}{\partial\theta^2}$, $U_{\phi\phi}$ = $\frac{\partial^2 U}{\partial\phi^2}$ and $U_{\theta\phi}$= $\frac{\partial^2 U}{\partial\phi\partial\theta}$. The angles θ_0 and ϕ_0 represent the equilibrium direction which can be obtained by solving the conditions shown in Eq. 2.10.

$$\left(\frac{\partial U}{\partial\theta}\right)_{\theta=\theta_0,\phi=\phi_0} = 0 \qquad \left(\frac{\partial U}{\partial\phi}\right)_{\theta=\theta_0,\phi=\phi_0} = 0 \tag{2.10}$$

As an example, consider the total free energy as

$$U = -\mu_0 MH\left[\cos(\phi-\phi_H)\sin\theta\sin\theta_H + \cos\theta\cos\theta_H\right] - K_1\cos^2\phi\sin^2\theta + \mu_0\frac{M^2}{2}\cos^2\theta, \tag{2.11}$$

where the first term corresponds to the Zeeman energy, the second term is the uniaxial anisotropy energy and the third term corresponds to the out-of-plane shape anisotropy. From Eq. 2.9 and Eq. 2.10, the resonance frequency can be determined

as

$$\omega_{res}^2 = \gamma^2\mu_0^2\left[(H\cos(\phi_0-\phi_H)+H_k\cos^2\phi_0+M)(H\cos(\phi_0-\phi_H)+H_k\cos 2\phi_0)\right] \tag{2.12}$$

where, for the case of magneto-crystalline anisotropy, $H_k = K_1/M$, with K_1 being the uniaxial anisotropy constant. All ferromagnetic films are defined in terms of their effective field, $\vec{H}_{eff}$. As each contribution to the effective field is of vectorial nature, a closer analysis to the angular variation of the magnetic properties will reveal a certain type of symmetry. Figure 2.3 illustrates the dependence of ω_{res} on the direction relative to the easy axis of an uniaxial anisotropy field, assuming the magnetisation at equilibrium ($\phi_0 = \phi_H$). In the $\phi_H = 0°$ condition, the applied field is aligned with the easy direction and therefore at $\mu_0 H = 0$ T one measures a net precession as a result of the anisotropy field. If the $\phi_H = 90°$ direction is considered, when the applied field is equal in amplitude to the anisotropy field ($H = -H_k$) the net moment is reduced due to some disorder in the magnetic configuration and the torque vanishes ($\omega_{res} \to 0$). When $H < |H_k|$, the saturation condition is not satisfied ($M = M_{sat}$) so domain formation and rotation is expected. In this field region the coherent precession is only partially restored due to the fact that the magnetic moment is canted with regards to the magnetic field and also due to gradual rotation of the magnetic domains towards the easy direction.

2.2 Spin waves

In magnetic systems at finite temperature, as well as systems where spins are forcedly misaligned at interfaces, fluctuations between spins should be considered and collective fluctuations of spins are called spin waves. Under the appropriate boundary conditions, spin waves can be described by the propagation direction relative to $\vec{M}$ and $\vec{H}$. Figure 2.4 illustrates the difference between the uniform precession mode where all spins precess with the same phase and the spin wave mode where deviations between consecutive spins allow the emergence of a spin wave, with wavelength λ_S.

Due to the boundary conditions, only certain wavelengths are allowed. Spin waves can be divided according to their characteristic wave number. For $k < 1/10$ μm^{-1} the origin of spin waves is related to dipole fields. These are also called magnetostatic

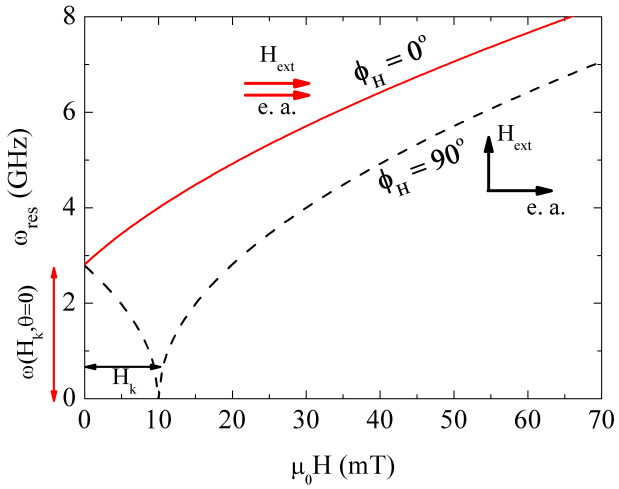

Figure 2.3: Resonance frequency as a function of applied field for the directions parallel and perpendicular to the uniaxial anisotropy direction. The axis parallel to the anisotropy is said to be the easy axis $\phi_H = 0°$, whereas the axis perpendicular to the anisotropy is said to be the had axis, $\phi_H = 90°$.

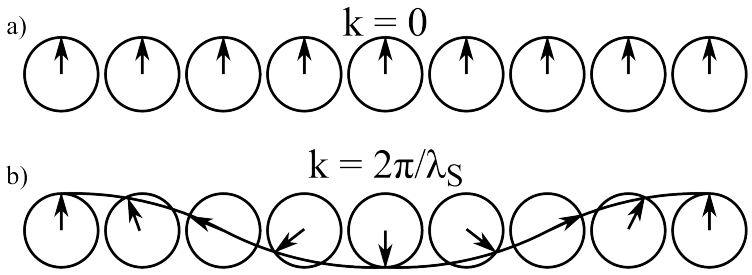

Figure 2.4: Illustrations of a) uniform precession mode ($k = 0$), and b) emergence of spin waves due to canting between consecutive spins. Spin waves have a characteristic finite wavelength, λ_S and can be mediated by dipolar interactions and exchange interactions.

spin wave modes. In the configuration where $\vec{k} \perp \vec{M}$, the modes are called Damon Eshbach modes [68] or magnetostatic surface waves. The limit where $\vec{k} \parallel \vec{M}$, the waves are called backward volume waves. In a configuration where $\vec{H}$ is out-of-plane and $\vec{k}$ lies in the plane of the film, the modes are denominated as forward volume waves.

For $k > 1/100$ nm^{-1}, exchange interactions become dominant, the dispersion relation becomes proportional to k^2 and independent of the propagation direction. These are called exchange spin waves. A more detailed dispersion relation for these types of spin waves can be found in Ref. [71], where all possible propagation directions are discussed thoroughly.

In a case where spin waves propagate along a direction perpendicular to $\vec{M}$ and $\vec{H}$ ($\vec{k} \perp \vec{M}$), the solution to Eq. 2.1 is

$$\omega^2 = (\omega_H + \frac{\omega_M}{2})^2 - (\frac{\omega_M}{2})^2 exp(-2kd). \tag{2.13}$$

The last term accounts for the existence of spin waves of dipolar origin, with wave number, k, and confined between two interfaces separated by d. The spin wave dispersion, $\omega(k)$, in magnonic structures can be calculated following a theoretical model as demonstrated in Refs. [53, 56]. Alternatively one can perform micromagnetic simulations and process the time and space dependent magnetisation components [116].

For the present work, dipole field dominated standing spin wave modes are discussed in chapter 5. These were measured in the frequency range of 1-15 GHz and characteristic wave number of $k \sim$ 1/300 nm^{-1}. The localised resonance modes arise in nanostuctured materials where the amplitude distribution of the excited magnetostatic spin waves is equivalent to the periodicity of defects. Experimentally, the VNA-FMR technique is used to determine the $\omega(H)$ dispersion relation. Brillouin light scattering is used for the measurement of both $\omega(H)$ and spin wave dispersion. $\omega(k)$.

2.3 Relaxation mechanisms

In the LLG equation (Eq. 2.1), the second term represents the damped motion of the magnetisation which is associated with the exchange of energy between the excitation field and the magnetic system. This energy then dissipates through the magnetic system and ultimately to the atomic lattice in processes broadly designated as relaxation. In an ordered magnetic system several relaxation mechanisms take place. The primary distinction between mechanisms lies in whether the energy is dissipated via: a) direct or defect mediated spin-spin relaxation and; b) spin-lattice relaxation mechanism in which the spin system transfers energy in the form of heat (phonons). The diagram shown in Fig. 2.5 illustrates the relaxation mechanisms.

Attention is given only to the relaxation mechanisms occurring in metallic thin films. Following the convention in the literature, relaxation mechanisms can be grouped as intrinsic or extrinsic. Intrinsic mechanisms are dominated by spin-lattice

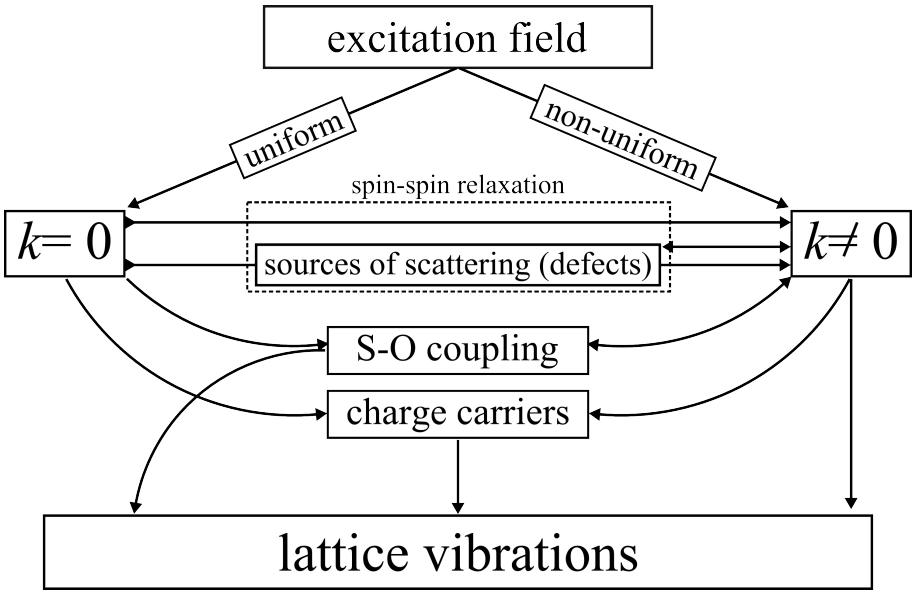

Figure 2.5: Energy dissipation mechanisms. Figure adapted from Ref. [112]. Spin-spin interactions, spin-orbit (S-O) coupling and defects may promote the energy dissipation through excitation of spin waves, but ultimately, the dissipation mechanisms end with energy transfer from the spin system to the atomic lattice.

relaxation mediated by incoherent scattering of itinerant electrons with thermally excited phonons and magnons. [2] This process initiates with coherent scattering between a magnon ($\hbar\omega_q$) and an itinerant electron ($\epsilon_{\vec{k},\sigma}$) resulting in momentum ($\vec{k}$) and spin (σ) transfer to the scattered electron ($\epsilon_{q+\vec{k},\sigma'}$). This event is followed by incoherent scattering of the itinerant electrons with thermally excited phonons and magnons, resulting in magnetic relaxation [117]. This scattering event may be defined by characteristic spin-flip time $\tau_{sf} = \tau_m/(\Delta g)^2$ which is proportional to the momentum relaxation time (τ_m) and inversely proportional to the squared deviation of the g-factor (g) from $\Delta =$ g-2, as a result of spin-orbit coupling. The Gilbert damping constant ($G = \gamma M\alpha$) is therefore proportional to $1/\tau_{sf}$ and thus scales with the resistivity [117] (only at low temperatures). This is valid if the change in energy ($\Delta\epsilon$) involved in the scattering event is sufficient to allow interband transitions ($\Delta\epsilon \ll \hbar/\tau_m$). In cases where the latter is not verified ($q \ll k$), the Gilbert damping is linearly proportional to the conductivity ($G \simeq (\Delta g)^2\tau_m$).

Less dominant contributions to the intrinsic relaxation may appear due to Eddy currents and direct magnon-phonon scattering [118]. Moreover, if one considers

[2] In brief, the definition of itinerant electrons is associated with electrons which belong to overlapping s-p orbitals, which is the case for metals such as permalloy.

the existence of non-magnetic metallic layers adjacent to the precessing magnetic film, two additional contributions to the damping are expected due to: 1) the spin-flip mechanism at the interfaces due to electron-magnon interactions [119]. This observation does not necessarily require the current to propagate in the non-magnetic layer [118] and leads to an increase in the damping of the magnetic layer; and 2) spin pumping may also occur when a ferromagnetic material is at resonance, as the precessing spins dissipate energy by emitting spin currents which then transfer to the non-magnetic metallic layer [117, 120]. This effect may be seen as the inverse of current induced magnetisation dynamics, where currents in non-magnetic metallic layer induce precession in ferromagnetic films. A more detailed description of these mechanisms can be found in Refs. [112, 117, 121].

In real magnetic systems, it has been shown that inhomogeneities and defects cause additional broadening of the linewidths as well as a zero-frequency linewidth. Intrinsic relaxation mechanisms are not sufficient to explain the resonance linewidth and therefore, extrinsic relaxation mechanisms must be considered.

Defects and periodic modifications in the magnetic texture may result in spin-spin interactions whereby an uniform mode (k= 0) scatters to non-uniform spin wave modes ($k \neq 0$) [122]. This process is also designated as two-magnon scattering. A description of the two-magnon scattering mechanism can be found in Ref. [123] for the case of ultra-thin films magnetised in-plane. This mechanism leads to changes in the linearity with frequency of the linewidths as well as shifts in resonance frequency. Consider that the uniform mode (k= 0) is excited. In the presence dipolar coupling between spins, short wavelength spin waves with ($k \neq 0$) may emerge as degenerate modes relative to the uniform mode. The inhomogeneities enable the transfer of energy from the uniform mode to the degenerate modes. Subsequent to the excitation of the degenerate spin wave modes, intrinsic relaxation mechanisms take part in the dissipation of the energy to the lattice. Two-magnon scattering should only be seen as a means to redistribute the energy between the several modes which leads to the de-phasing of the transversal magnetisation component of the uniform mode [117, 124].

Ferromagnetic resonance is widely used to measure resonance linewidths as a function of either the resonance frequency or the resonance field [118, 125–128]. The

linewidths can therefore be expressed as

$$\Delta H(\omega) = 1.16\frac{\omega}{\gamma}\alpha + \Delta H(0) \tag{2.14a}$$

$$\Delta\omega(H) = \frac{\partial\omega}{\partial H}\Delta H, \tag{2.14b}$$

where the first term α accounts for the Gilbert-like damping contributions and $\Delta H(0)$ accounts for the extrinsic broadening. Obtaining the values for the linewidth yields information regarding the quality of the structure and the symmetry of the defects [129–132]. The primary interest in this work is to study the resonance peak position so the analysis of the linewidth was not carried out.

Chapter 3

Overview of the techniques

3.1 Introduction

Having discussed the physical principles of ferromagnetic resonance in chapter 2, it is now relevant to explain how ferromagnetic resonance can be measured using a vector network analyser (VNA-FMR) system.

All FMR results presented in this dissertation were obtained using a VNA-FMR system developed at the University of Glasgow. The microwave excitation was performed using mainly two waveguides in two distinct configurations: a two-port VNA-FMR assembled with coplanar waveguide which was used to obtain the results in chapter 5 and in Sec. 6.4. Details on the technique can be found in Sec. 3.2; a single and a two-port VNA-FMR using a loop shaped microstrip which was designed and assembled with the purpose of performing FMR experiments inside transmission electron microscopes during imaging of the magnetic structure. The FMR results of chapter 4 were obtained with the single-port setup and the FMR results shown in Sec. 6.2 were obtained with the two-port system. Details on the technique and a discussion on the performance of the waveguide in terms of the wavevector excitation in the loop shaped microstrip region are presented in Sec. 3.3.

The Lorentz techniques used to study: 1) the magnetostatic properties of magnetic nanostructures and 2) the interactions between the electron and microwave fields are discussed in Sec. 3.4. The general concepts of Fresnel imaging, low angle diffraction mode and differential phase contrast are also discussed.

Electron beam lithography, combined with reactive ion etching was used to

fabricate the antidot structures discussed in chapters 5 and Sec. 6.4. Micromagnetic simulations were used to assist the interpretation of the dynamic response of the magnetic systems studied in chapters 4, 5 and 6. Microwave simulations using CST microwave studio were carried out to design the waveguides for the in-situ FMR experiments. The details on these techniques can be found in appendix Secs. A, B and C, respectively.

3.2 VNA-FMR

Consider an electrical circuit constituted by a source/analyser of microwaves and a coplanar (CPW) waveguide. These elements are connected by coaxial (RF) cables to form a 50 Ω impedance matched circuit. When performing FMR experiments, the sample is placed on top of the waveguide, so that the microwave fields associated with the high frequency current (h_{mw}) drive the precession of the magnetisation. The coplanar waveguide is positioned between the poles of an electromagnet so that FMR experiments can be performed as a function of static applied field (H). The static magnetic field is induced by a current in the coils, which is supplied by a bipolar power source. A Hall probe is used to measure the field strength in the region of the sample. All equipment is controlled using a home-built Labview program, developed in the context of the research work presented in this thesis. A schematic of the FMR setup is shown in Fig. 3.1. Some elementary concepts of microwave theory applied to the calculation of the characteristic impedance in a lumped-circuit model are now introduced.

3.2.1 Transmission line and S-Parameters

The lumped-circuit equivalent to a transmission line may be represented, as in Fig.3.2, by a series resistance (R) and inductance (L) as well as shunt capacitance (C) and conductance (G). From Kirchoff's voltage law one obtains a set of differential equations (limit of $dx \to 0$) relative to the time variation of the voltage, $V(t)$, and

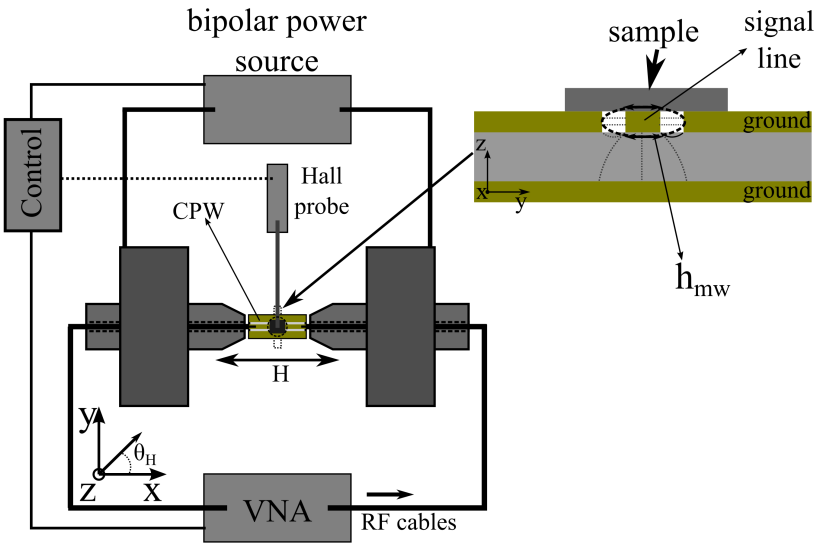

Figure 3.1: Microwave signal is generated in the VNA and propagates through the RF cables to the coplanar waveguide to drive the precession in the ferromagnetic sample. Static external field, H, generated as current circulates in a set of Helmholtz coils. The current is supplied by a bipolar power source and the whole setup is controlled using Labview.

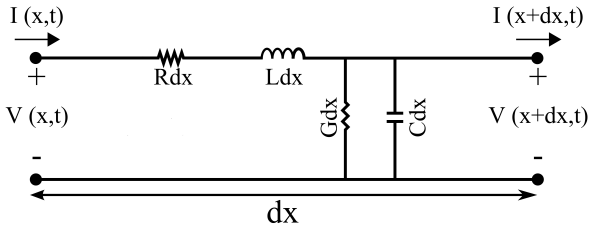

Figure 3.2: Equivalent lumped-circuit model of a transmission line. Voltage(v) and current(i) in a section dx of the transmission with resistance (R), inductance (L), conductance (G) and capacitance (C) [133].

the current, $I(t)$, also known as Telegrapher's equations [133]

$$\frac{\partial V(x,t)}{\partial x} = -RI(x,t) - L\frac{\partial I(x,t)}{\partial t} \tag{3.1a}$$

$$\frac{\partial I(x,t)}{\partial x} = -GV(x,t) - C\frac{\partial V(x,t)}{\partial t} \tag{3.1b}$$

where the values for R, L, C and G may be determined from the magnetic permeability μ, effective permittivity ϵ and the geometry of the transmission line. Defining the voltage $V(r,t)$ and the current $I(r,t)$ as sinusoidal waves in the steady-state condition, it comes that

$$\tilde{V}(x) = \Re\left\{V(x)e^{j\omega t}\right\} \tag{3.2a}$$

$$\tilde{I}(x) = \Re\left\{I(x)e^{j\omega t}\right\} \tag{3.2b}$$

Given Eq. 3.2, a simplified version of Eq. 3.1a and b can be obtained as follows

$$\frac{dV(x)}{dx} = -(R + j\omega L)I(x) \tag{3.3}$$

$$\frac{dI(x)}{dx} = -(G + j\omega C)V(x) \tag{3.4}$$

which can be rearranged to result in

$$\frac{d^2V(x)}{dx^2} = -\gamma^2 V(x) \tag{3.5}$$

$$\frac{d^2I(x)}{dx^2} = -\gamma^2 I(x) \tag{3.6}$$

where γ is a propagation constant defined by

$$\gamma = \sqrt{(R + j\omega L)(G + j\omega C)} \tag{3.7}$$

Solutions to Eq. 3.2.1 are propagating voltage and current waves along $\pm kx$ defined as

$$V(x) = V_0^+ e^{-\gamma x} + V_0^- e^{\gamma x} \tag{3.8}$$

$$I(x) = I_0^+ e^{-\gamma x} + I_0^- e^{\gamma x} \tag{3.9}$$

where the term $\mp\, \gamma x$ corresponds to the propagation direction along $\pm x$. $V_0^{\pm}$ and $I_0^{\pm}$ are the amplitude of the travelling voltage and current waves, respectively. By combining the Eq. 3.2.1 with the Eq. 3.2a an expression for the line impedance Z is obtained as

$$Z = \frac{V(x)}{I(x)} = \sqrt{\frac{R + j\omega L}{G + j\omega C}} \tag{3.10}$$

In the low loss limit, $\omega L \gg R$ and $\omega C \gg G$, the line impedance may be approximated by

$$Z = \sqrt{\frac{L}{C}} \tag{3.11}$$

To enable efficient transmission, impedance matched circuits are normally set to the standard Z_0= 50 Ω. The linearity of Z is not valid as $\omega \to 0$ since the resistance is no longer negligible.

In transmission lines where the electro-magnetic (EM) wave modes are not pure transverse modes and defining the corresponding voltage and current characteristics is not trivial. In practice, the transverse components of the EM waves are dominant so the modes are assumed quasi-transverse. To simplify the characterisation of

transmission lines, a concept of incident and reflected standing power waves is adopted [134]. The incident (a_i) and transmitted (b_i) power waves are defined relative to the voltage and current applied to a known section of the circuit, known as port i with impedance Z_i.

$$a_i = \frac{V_i + Z_i I_i}{2\sqrt{|Z_i|}} \tag{3.12a}$$

$$b_i = \frac{V_i - Z_i^* I_i}{2\sqrt{|Z_i|}} \tag{3.12b}$$

For the case where two ports, 1 and 2, are considered, these wave quantities are expressed in terms of the input wave, the transmitted and reflected power at each port. The most common representation is a matrix of four complex scattering parameters.

$$\begin{pmatrix} b_1 \\ b_2 \end{pmatrix} = \begin{pmatrix} S_{11} & S_{12} \\ S_{21} & S_{22} \end{pmatrix} \begin{pmatrix} a_1 \\ a_2 \end{pmatrix} \tag{3.13}$$

Experimentally, the scattering parameters can be obtained directly from a vector network analyser (VNA) with accurate measurement of both magnitude and phase. Figure 3.3 illustrates the basic operating principles of the VNA. An oscillating wave is generated in the VNA and launched into the circuit through port 1. Ignoring reflection and losses in the RF cables, when the signal reaches the device under test (DUT), because of the difference in impedance at the port Z_0 to the impedance of an unknown device Z_D, part of the signal will be transmitted forward to port 2 and part will be reflected back to port 1. The result, comparing the power wave quantities (Eq. 3.13), yields the parameters S_{11} and S_{21}. Reciprocity in the DUT is verified if S_{21}= S_{12} and the symmetry in the DUT is satisfied if S_{11}= S_{22}.

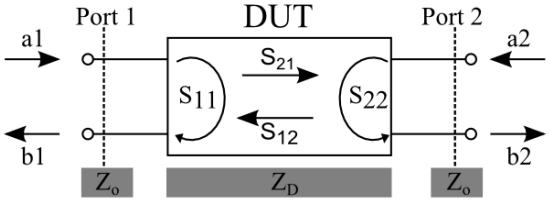

Figure 3.3: The scattering parameters correspond to the power wave ratios. The incident waves are labelled as a1 and a2, and the reflected waves are labelled as b_1 and b_2.

Figure 3.4 shows the scattering parameters as a function of frequency for an unloaded coplanar waveguide, measured in a Rohde & Schwarz ZVA40 (R&S). The

degree of reciprocity of the circuit can be determined by comparing S_{21} to S_{12} and S_{11} to S_{22}. Note that in some frequency regions ($\sim$ 10 GHz) the signals are not reciprocal, but in general the forward transmission coefficients are equivalent. Uncertainties in the measurement of S_{11} and S_{22} are related to low signal amplitude being reflected, since the signal is mostly transmitted, as well as non-reciprocities in the circuit.

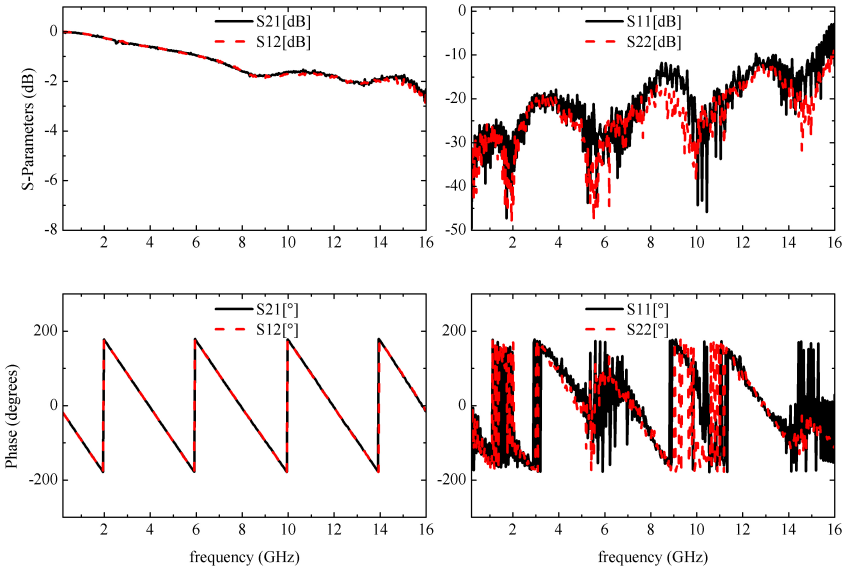

Figure 3.4: Magnitude and phase of the S-Parameters S_{21}, S_{12}, S_{11}, S_{22} as a function of frequency. Traces obtained from the unloaded CPW used in the VNA-FMR measurements while using standard flexible RF coaxial cables. Average trace noise in the frequency range shown is 5 mdB. Normalised trace noise is of the order of 0.12 mdB, which is a useful reference when performing FMR measurements since the data is normalised with a given reference spectra.

It is important to perform a full port calibration of the electrical system for the purpose of correcting all phase and amplitude variations due to the cabling and connectors. In practise, this error correction is applied so that the reference phase plane moves from the VNA ports to the connecting ports of the coplanar waveguide. A full port calibration involves the use of standards open, short, match and through connectors, which in our case were supplied by the manufacturers R&S. To further improve the error correction, one could perform error correction up to the sample level by using a probe station system combined with coplanar on-board calibration standards that would moved the phase correction beyond the connector port.

For the calibration to be accurate, the VNA settings must be set prior to the

correction. The output power, P_{out}, the integration bandwidth, Δf, the frequency window and the number of points are essential for the calibration to be implemented correctly. Table 3.1 contains all the input parameters applied prior to the full port calibration.

Output power P_{out}	frequency range	N points	Δf	averaging
5 dB (1.7 mW)	1-16 GHz	500	1 KHz	5

Table 3.1: Settings used in the VNA calibration. Linear output power calculated assuming that P_{out}[dBm]= 10 $ln\frac{P_{out}}{P_{REF}}$, where P_{REF}= 1 mW. The power level sits well within the linear response of the VNA, the frequency of interest for the ferromagnetic materials is coincident to 1-16 GHz and the detection bandwidth/averaging factor where chosen to achieve optimal trace noise (0.12 mdB) while achieving a good measurement time (20 seconds per frequency sweep).

As a general rule one must choose P_{out} to be within the linear response of the signal detection. The schematic diagram of Fig. 3.5 illustrates the power range over which the detection system has non-linear sensitivity due to compression and noise [135].

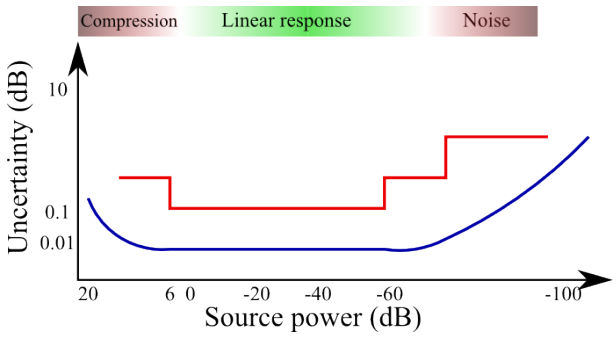

Figure 3.5: Characteristic power detection response of the VNA. High power values at source will cause compression in the signal, adding uncertainty to the power detection. Normally this is seen through spikes at low frequencies, as in this region typically more power returns to the VNA.

3.2.2 Detection of the precessing magnetisation

In FMR experiments, the DUT consists of the uncalibrated section of the circuit: the coplanar waveguide and the ferromagnetic sample. For the measurements

performed, the coplanar waveguide was comprised of a signal line sitting between two ground planes which are placed symmetrically one on each side. The ground-signal-ground configuration is such that the oscillating electromagnetic fields are exposed to air at the top surface of the waveguide. When placed on top of the CPW, the ferromagnetic sample is exposed to the travelling oscillating magnetic fields, $h_{mw}(\omega)$, as illustrated in Fig. 3.6.

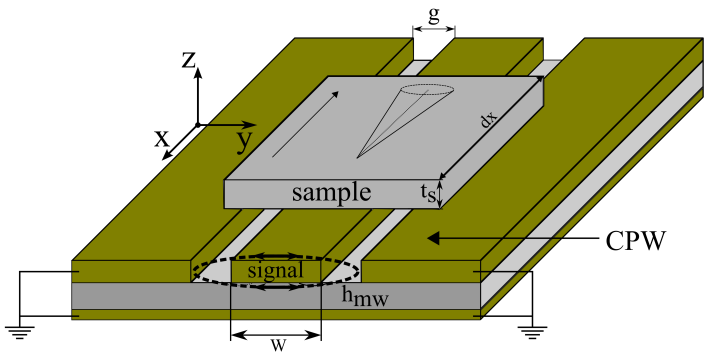

Figure 3.6: Illustration of the coplanar waveguide and the sample. Even though this circuit is referred as CPW, its configuration is a co-planar circuit with an additional ground plane at the opposite side of the substrate. The two ground planes are shorted near the edges of the ground planes which are levelled with the signal plane.

The grounded coplanar waveguide used in the experiments has the following dimensions: signal line is 2.54 mm long, the width is w= 355 μm, the gap between signal line and ground is g= 128 μm, thickness of the substrate is 200 μm (ROGERS RO4003C [136]). Considering that the thickness of the conducting layer is much smaller than the width [137], w, the strength of the dynamic magnetic field on top of the signal line can be approximated to $\mu_0 h_{mw} \sim I/(2w)$= 0.14 mT, where the current is obtained from I= $(P_{out}/50\Omega)^{1/2}$. This value is an overestimate as the power attenuation in the electric system and the air gap between the sample and the conductors are neglected. The air gap is essential to prevent shorting the signal and ground lines. The excitation field is therefore expected to be well below the limit for non-linear excitations [138]. When a ferromagnetic film is placed on top of the waveguide, the precessing magnetisation component will cause a variation in the magnetic flux, ϕ, which for an infinitesimal section of the sample dx, can be expressed as

$$\mathrm{d}\phi \simeq \mu_0 m_y(t) t_s dx, \tag{3.14}$$

where $m_y(t)$=$m_y e^{i\omega t}$ is the magnetic component parallel to the driving field and t_s is the film thickness. Following Faraday's law of induction, an equivalent voltage can be determined (electromotive force) [139] as

$$\Delta V = -\frac{d\phi}{dt} = -\mu_0 \frac{dm_y(t)}{dt} t_s \Delta x = -\mu_0 j\omega m_y t_s \Delta x \tag{3.15}$$

Assuming that m_y= $\chi_{yy} h$[1] (see Sec. 2.1.1) and $h(t)$= $I(t)/2w$ it follows that

$$\frac{dV}{dx} = -\mu_0 j\omega \chi_{yy} \frac{t_s}{2w} I(t). \tag{3.16}$$

Equation 3.16 is equivalent, in form, to Telegraph Eq. 3.1 and although it represents the change in inductance due to the magnetic sample, it may not represent the total impedance change as the circuit itself is also affected by external fields. The term

$$\Delta L = \mu_0 \chi_{yy} \frac{t_s}{2w} \tag{3.17}$$

may be interpreted as variation in the inductance of the microwave circuit due to the ferromagnetic sample. Clearly the variation in inductance of the DUT will be linearly proportional to the dynamic susceptibility of the sample. Since $\chi = \chi^{'} + \chi^{''}$ the impedance may also be seen as having both real and imaginary parts. The change in the signal, as the sample undergoes resonance, is measured in the VNA through the relative variation of the transmission and reflection coefficients, S_{21} and S_{11}, as a result of the variation in the impedance due to the magnetic sample. More complex methods to the modelling of equivalent circuit relative to the ferromagnetic sample and waveguide can be found in Ref. [140, 141].

3.2.3 FMR measurements and data acquisition

In order to access a wide range of ferromagnetic states, a Kepco BOP (100-10MG) bipolar source supplies current to a set of coils to generate a DC magnetic field, H. This external field is applied perpendicular to dynamic excitation field $h_{mw}(\omega)$ as illustrated in Fig. 3.1. The maximum field magnitude achievable in the setup is 200 mT, which is limited by the maximum voltage that the power source can supply (100 V), the resistance of the copper coils ($\sim$ 40 Ω) and the distance between the pole pieces ($\sim$4 cm).

[1] If the out-of-plane field at the gap between the ground and the signal line is considered, one must also include the component χ_{zy}.

In FMR experiments, a sample with a typical size of 2 mm×2 mm × 20 nm, contributes only to a small variation in the impedance of the system ($\sim$ %1) so in order to obtain the resonance trace it is necessary to normalise the data with a reference signal. This will allow for measurements in which the signal to noise ratio is approximately 1 mdB. Moreover, the commercially available RF connectors contain elements such as Nickel, which will also affect the experimental data. In order to reduce the experimental artefacts, a reference measurement is obtained, S_{21}^0, at high applied fields, well above the range of the FMR in the experiment. These spectra are used to correct the experimental data over the entire field range. Figure 3.7 shows the magnitude of S_{21}/S_{21}^0 as a function of the applied field and microwave frequency for an unloaded waveguide. As can be seen on both the surface plot (left) and the line traces (right), even though the signal attenuation is largely reduced by performing S_{21}/S_{21}^0, a variation in the signal is still observed, especially at frequencies between 1 GHz and 6 GHz, due to residual signal from the connectors.

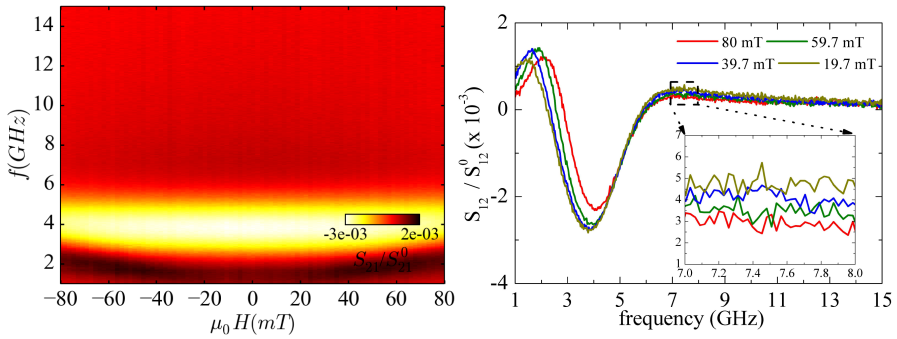

Figure 3.7: Left: Colour plot showing the magnitude of S_{21}/S_{21}^0 as a function of frequency (f) and field for an unloaded coplanar waveguide, normalized with reference spectra S_{21}^0 taken at $\mu_0 H$= 150 mT (trace noise of 0.12 mdB). Right: Traces corresponding to $\mu_0 H$= [80,60,40,20] mT and normalized with reference spectra taken at $\mu_0 H$ = 150 mT. The change in signal does not follow any kittel-like dependence and may therefore be considered an experimental artefact due to the connectors or RF cables.

Time fluctuations were also addressed in the data correction procedure. As demonstrated in Fig. 3.8, there is a time dependence associated with the measurement of the scattering parameters. Sources of variations include VNA instability, stress in the coplanar waveguide due to the positioning of the sample and mechanical vibrations on the platform that holds the experimental apparatus. To minimize these effects, a dynamic signal acquisition procedure was implemented, whereby the

reference signal S_{21}^{0} was reacquired for each applied field during the experiment.

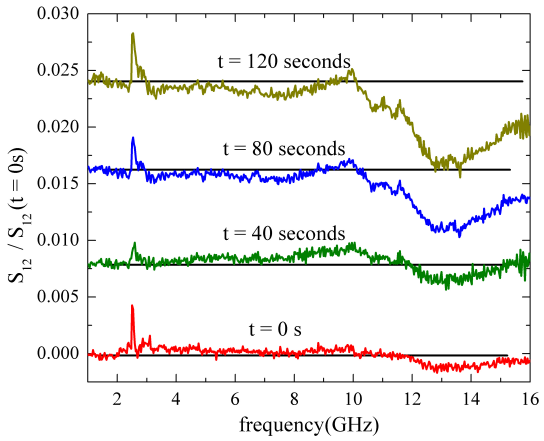

Figure 3.8: Time dependence of S_{21}/S_{21} at a time t= 0, 40, 80, 120 s. The noise levels comply with the specifications provided by the manufacturer (10^{-4}dB at room temperature), except for the case of the sharp noise peak at 2.58 GHz.

A final correction procedure can be implemented (if necessary) to further reduce the influence of the magnetic components and the variation in impedance due to the shape and dielectric properties of the sample, on which the FMR measurement is repeated using only a substrate with approximately the same dimensions as the sample under study. This spectra is defined as S_{21}^{0S}. Ultimately, the sample can be flipped upside down to have the substrate in direct contact with the waveguide. This option should be discarded in case the measurements show any hints of resonance, meaning that the microwave fields reaches the ferromagnetic layer. This improvement in the signal is demonstrated by comparison of Fig.3.9a and b.

3.2.4 FMR Analysis

Figure 3.9 shows the normalised transmission parameter S_{21} as a function of frequency and field of a FeMn(20nm)/NiFe(15nm) sample with an external field applied perpendicular to the exchange bias direction. The spectra of Fig. 3.9a were recorded with the dynamic background while in the spectra of Fig. 3.9b the data was normalised with the substrate signal (S_{21}/S_{21}^{0S}). A clear improvement in the flatness of the resonance spectra is obtained by the full correction procedure. From here on, the fully corrected spectra will be referred as S_{21}.

To determine magnetic parameters from the FMR spectra, a fitting procedure

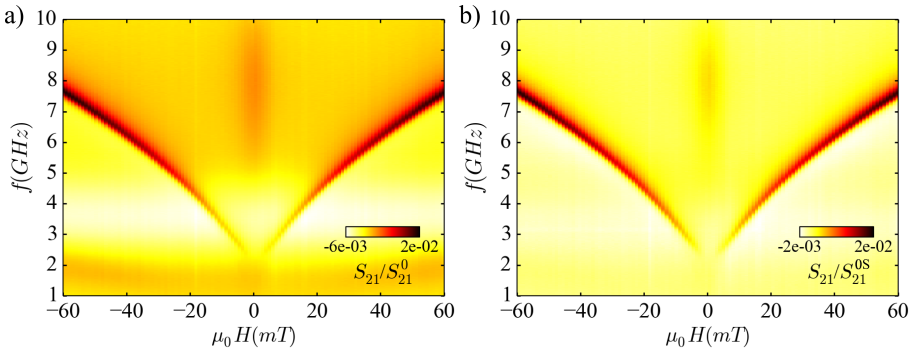

Figure 3.9: a) Magnitude of the transmission parameter S_{21} as function of the frequency and field of Ta(5nm)/FeMn(20nm)/NiFe(15nm)/Ta(5nm)/Si substrate. Direction of the applied field is perpendicular to the exchange bias direction. b) Experimental data corrected with the signal from the substrate.

was employed. This is demonstrated using the FeMn(20nm)/NiFe(15nm) data of Fig. 3.9 in Fig. 3.10.

To investigate the resonance linewidths and the susceptibility a complex analysis would have to be made. In particular, the magnitude and phase of all S-parameters would have to be accounted for in order to correct for phase mismatches due to positioning of the sample on the waveguide. References [128, 142–144] provide methods that yield accurate measurements of the dynamic susceptibility. The primary interest here of fitting the experimental data is to extract the resonance peak position so the information extracted from fitting the magnitude of the forward scattering parameter S_{21} is sufficient.

In order to find the resonance position and the resonance linewidths the first order derivative of the experimental data, $\mathrm{d}S_{21}/\mathrm{d}f$, is applied to reduce the background variations. The derivative of the Lorentz function, $\mathrm{d}L/\mathrm{d}f$, is employed in the fitting process. Figure 3.10 shows an example of $\mathrm{d}S_{21}/\mathrm{d}f$ (a), the spectra relative to the fitted function $\mathrm{d}L/\mathrm{d}f$ (b) and the residuals (c). The higher amplitudes in the residual plot are coincident with the local maxima and minima of $\mathrm{d}L/\mathrm{d}f$, indicating that the resonance is asymmetric.

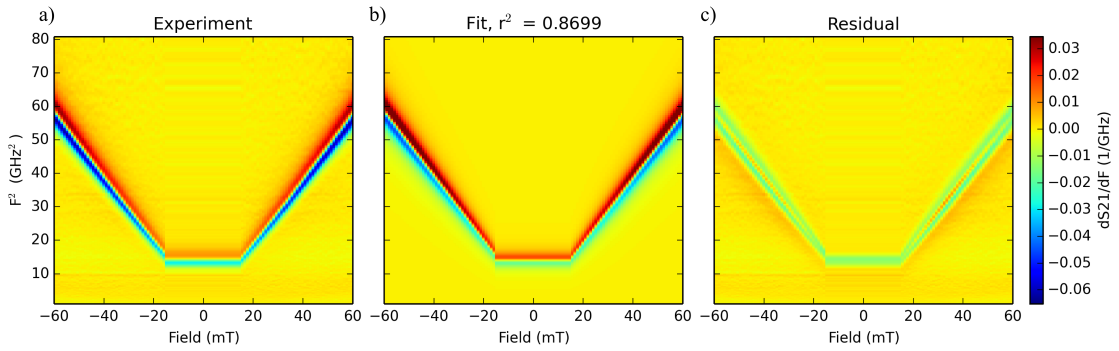

Figure 3.10: a) Derivative of the experimental data shown in Fig. 3.9b, $\mathrm{d}S_{21}/\mathrm{d}f$. b) Fitted derivative of the Lorentzian function. c) Residual plot. Field region between H = [-15,15] mT was not fitted as it corresponds to the unsaturated region and appears here as a flat region.

3.3 In-situ FMR rod

In this section a description of the TEM in-situ FMR apparatus is provided. Two configurations were developed: a single port VNA-FMR designed for operation in a FEI Tecnai T20 and a two port system designed to operate in a JEOL ARM-200F. To maximise the efficiency of the microwave excitation and detection near the optical axis of the TEM, loop shaped microstrip waveguides [145, 146] were designed and fabricated. At an early stage of the project, the microstrip was intended for operation at fixed frequency (resonator). However, the tests carried out in the TEM demonstrated that the impedance of the resonator was very sensitive to the tilt in the TEM sample holder so it was decided to use the microstrip as a broadband waveguide. The reason for having single and two port configuration was the space available in the specimen holders to accommodate the RF cables and the microstrip waveguides. To allow for transmission experiments in the TEM, a cylindrical section of the microstrip substrate was etched, as illustrated in Fig. 3.11.

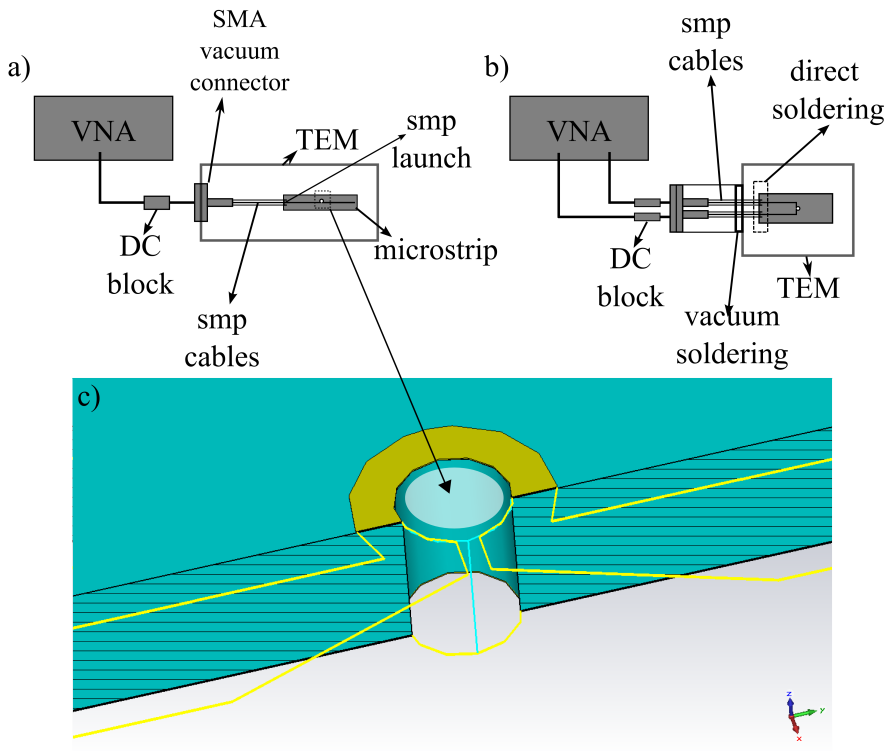

Figure 3.11: Schematic of the two in-situ apparatus for: a) single port measurements and b) two port measurements; c) Illustration of the loop shaped microstrip fabricated for the in-situ experiments. The regions labelled as TEM correspond to the section of the setup that is inserted in the TEM.

3.3.1 Single-port setup

Figure 3.11a shows a schematic of the single port configuration. The microwaves are generated in the VNA which is connected to the TEM specimen holder via an SMA vacuum tight connector. The vacuum connector and the microstrip are connected using a coaxial cable which is 0.8 mm in diameter and 180 mm in length. The cable launches the microwave signal to the microstrip via a mini-SMP board launch connector.

Within the TEM, the holder stage is held at 1 V above ground to allow detection in case the holder collides with the objective lenses which surround it. An inner-outer DC block was used to decouple the ground of the TEM and the VNA to prevent the holder being pushed to ground (0 V) resulting in a pole touch alarm, which would prevent the stage movement[2].

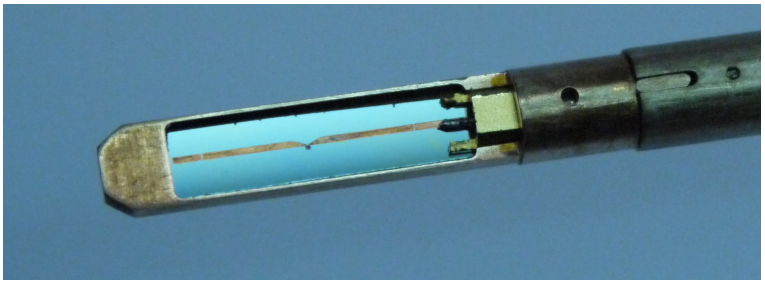

Figure 3.12: Microstrip loaded onto the TEM sample holder. The TEM sample holder encloses the microstrip and the surrounding metal (brass) acts as the ground plane. The specimen is then loaded onto the substrate in a flip-chip configuration. A careful alignment is required, in order to ensure that the electron transparent window of the specimen is coincident with the hole in the waveguide substrate.

Figure 3.12 shows the microstrip device assembled onto the TEM substrate holder. The metal surrounding the microstrip acts as the ground for the microwave circuit. The substrate size meets the TEM specimen carrier geometry and height limits within the confinement of the pole pieces inside the TEM. The dimensions of the waveguide will be presented along with microwave simulations performed using CST Microwave Studio. The details of the simulation tool can be found in Sec. C. The results of the simulations and the characterisation of the device via VNA are now discussed.

[2]Inner-outer DC blocks have a DC capacitor on both signal and ground lines.

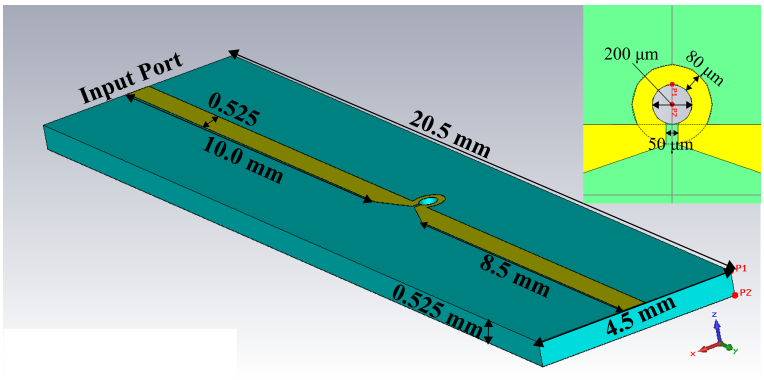

Figure 3.13: Geometry of the loop shaped microstrip and the dimensions implemented. Following the specifications of the substrate used in the experiments the resistivity of the substrate was set to 2.500 Ω.cm.

Figure 3.13 shows the design implemented. The Si substrate is 4.5 mm wide, 20.5 mm long and 0.525 mm thick. The width of the loop shaped signal line is 80 μm and the diameter of the hole in the inner part of the loop is 200 μm. The microstrip feed line is 0.5 mm wide and 10 mm long on the input port side. The other side of the microstrip is left as open, as the setup will operate in single port configuration. The port impedance as a function of frequency is shown in Fig. 3.14, which shows that $Z_0 \sim 50\ \Omega$ over the whole frequency range.

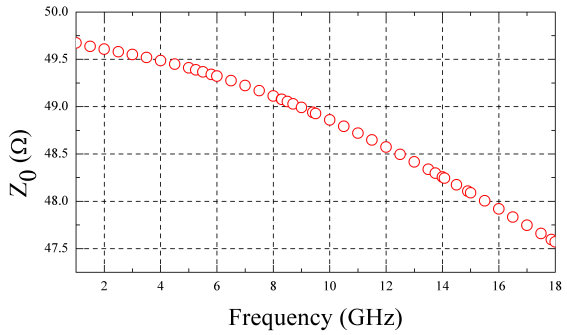

Figure 3.14: Port impedance obtained from CST microwave studio.

Figure 3.15 shows the reflection coefficient S_{22} of the circuit measured using the VNA, compared to the reflection coefficient obtained from the simulations. The VNA trace was obtained after performing a single-port open, short, load calibration, which moved the reference plane to the microstrip connector and allowed the response of the microstrip itself to be measured. Both experimental data and simulation agree in terms of the shape of the oscillation in the S_{22} parameter up 10 GHz. Above this frequency, the results are rather different. The calibration failed to accurately

account for all the RF connectors involved in the circuit, as well as the soldering of the microstrip port, which is likely to be the cause for some of the reflection peaks observed in the spectrum. The arrows in the plot identify some of the sharp peaks separated by Δf_1= 2.1 GHz and Δf_2= 1.2 GHz, which can be associated with structural reflections inherent to the waveguide. The oscillations observed in the VNA

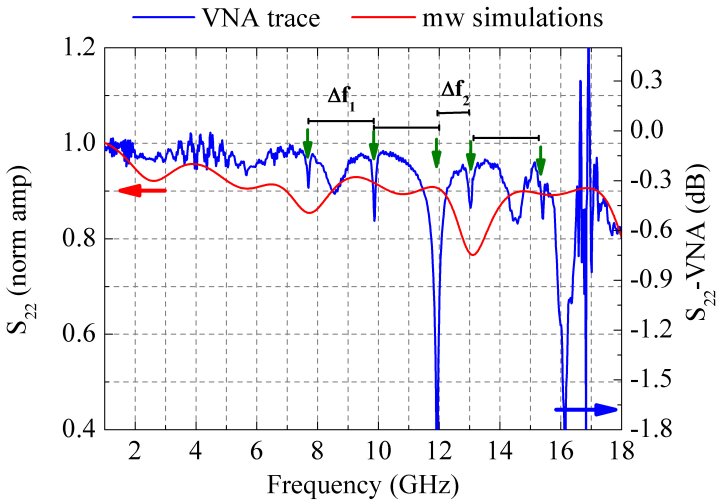

Figure 3.15: Comparison between the magnitude of the reflection coefficient S_{22} as a function of the frequency from the microwave simulations and VNA measurements. The trace noise in the VNA data is 40 mdB.

spectrum S_{22} are in part related to the SMA vacuum connector, which causes periodic oscillations resulting from an impedance mismatch (even though a calibration was applied). The ripple observed throughout the whole frequency range is caused by an additional mismatch between the reference impedance of the calibration standard and the actual impedance of the coaxial cables and connectors. Moreover, the calibration was performed outside the TEM environment, so further alterations to the ground position cannot be accounted for whithout custom waveguide standards.

To test the performance of the vacuum through connector, a VNA measurement was performed in transmission. These spectra were then compared to those of a standard SMA-to-SMA through connector, which is known to have 50 Ω impedance. In Fig. 3.16 a comparison is made between the magnitude of the forward scattering parameter S_{21} and S_{12} relative the vacuum through connector and a the standard connector. As can be noted, there are much higher losses in the transmitted signal with increase in frequency for the case where a vacuum connector is used. This will

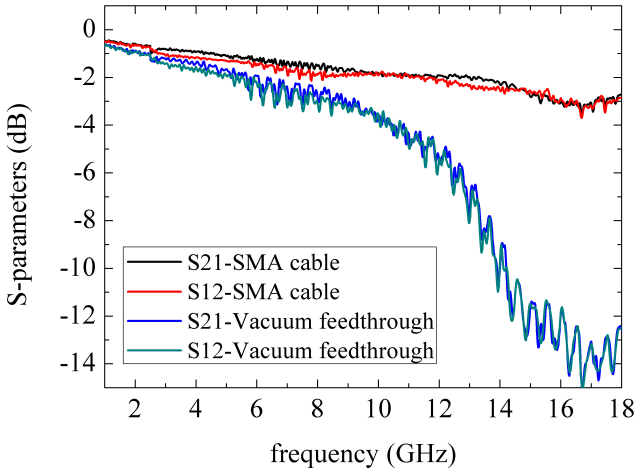

Figure 3.16: Comparative measurement of the magnitude of the transmission S-Parameters between the normal SMA (female-female) connector and the vacuum feed-through used in the T20 experiments. Ripple like oscillations on the measurement of the vacuum feedthrough have a periodicity of ∼500 MHz, which can be associated with the length of the test cables.

have a direct effect on the power that reaches the microstrip waveguide, as well on the power detected by the VNA while performing the calibration. This leads to a large phase mismatch and poor error correction. This is likely to be the source of the high amplitude peaks of S_{22} at frequencies around 17 GHz.

The FMR experiments discussed in chapter 4 were performed using this apparatus with a large sample placed on the loop shaped region. The electromagnetic field distribution produced in the loop shaped region is complex and determines the spin wave modes that may be excited in the magnetic material. This will be discussed in Sec. 3.3.3.

3.3.2 Two-port setup

As shown in Fig. 3.11b, the equipment used in the 2 port apparatus is essentially the same as for the single port, except that two RF cables are fed up to the microstrip port, enabling FMR measurements in transmission. As a consequence of having two RF cables, it was not possible to accommodate the mini-smp board launch connectors, so the signal lines of the coaxial cables were soldered directly onto the microstrip board. The TEM holder enclosing the microstrip served as the ground plane. In this

apparatus, the vacuum feed-through connectors were not used. Instead the solid copper of the outer conductor of the coaxial cable was soldered to the vacuum seal of the TEM rod, after verifying that this would not result in vacuum leakage. A photograph of the end piece of the TEM rod is shown in Fig. 3.17. For the initial set of experiments, the sample was fixed onto the substrate. The microstrip itself has the same properties as for the single port configuration, but the signal line contains 90° bends on each side of the loop shaped region, to allow insertion of two ports from the same edge of the substrate. The FMR experiments performed with this configuration are presented in chapter 6.

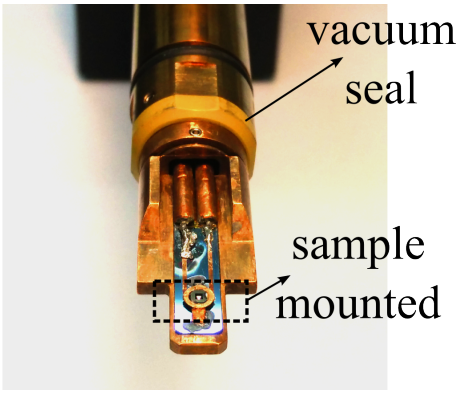

Figure 3.17: Two port system designed to operate in a JEOL ARM-200F rod. A sample is mounted and glued onto the loop shaped region of the signal line. In this configuration, rigid RF cables were used.

The microwave response of the 2-port system is shown in Fig. 3.18. Note the reciprocity of the circuit, given that $S_{21} \approx S_{12}$ and $S_{11} \approx S_{22}$, for most of the frequency range. However, there is frequency region which is not suitable for broadband FMR experiments. In particular, the frequency region between 3-4.2 GHz, where the transmission is rather diminished, while the reflection coefficients are large.

3.3.3 Excitation spectra of spin waves

Given the loop shape of the signal line, it is anticipated that the microwave fields driving the resonance in the magnetic material will be highly non-uniform. Figure 3.19 shows the electric field distribution from a cross-section of the loop shaped region. The distribution of the electric and magnetic fields, around the loop shaped region will be discussed in order to understand their effect on ferromagnetic resonance

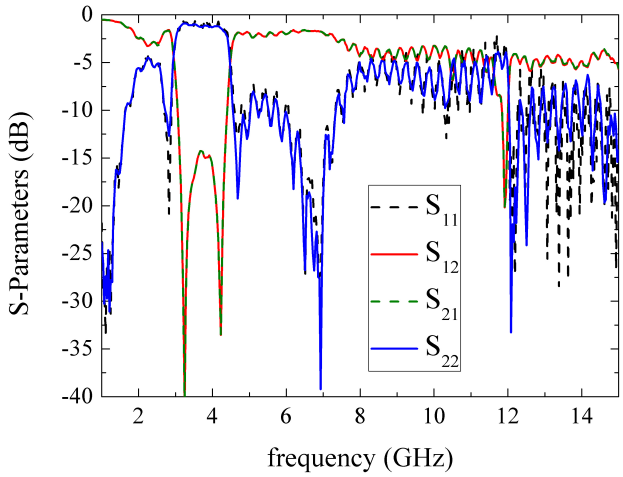

Figure 3.18: Magnitude of the scattering parameters relative to the u-bend loop shaped microstrip. The trace noise of the transmission parameter is 25 mdB. It was not possible to perform a VNA calibration so the measurement of the phase is misleading (not shown).

experiments.

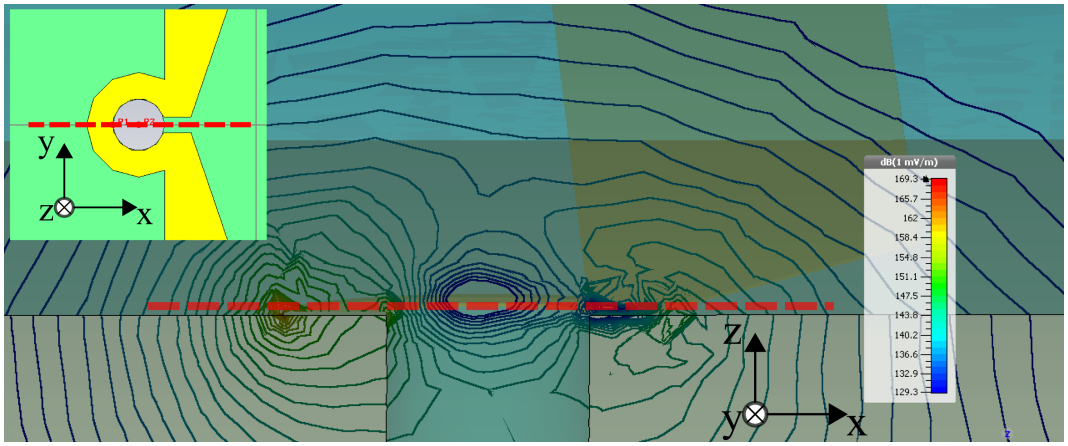

Figure 3.19: Distribution of the electric field (f= 4 GHz) in a cross-section along the xz plane of the loop shaped region (red dashed line in inset), obtained from CST microwave studio. The contour lines represent the magnitude of the electric field at the sectional plane relative to the centre of the loop shaped region. The dashed red line indicates the position of the field section with respect to the loop shaped microstrip, shown on the inset schematic. Shaded regions of the microstrip correspond to the conductive line (at a perspective) and the substrate.

Following the electric field distribution, one can determine the magnetic field components from $\vec{H}= 1/Z_{eff}(\vec{n} \times \vec{E})$, where $\vec{n}$ corresponds to the wave vector propagation direction and Z_{eff} the effective impedance [133]. The region just above

the signal line (red dashed line in Fig. 3.19) corresponds to the position where the sample would sit, in order to perform the FMR experiments. The magnetic field components along the directions x, y and z are plotted separately so that different excitation directions can be distinguished. From the real space components of the excitation field, one can determine the excitation spectrum by performing a Fourier transform of the field components. Figure 3.20 shows both field distribution and excitation spectra relative to h_x, h_y and h_z, obtained from the loop section indicated in Fig. 3.19 by the red dashed line.

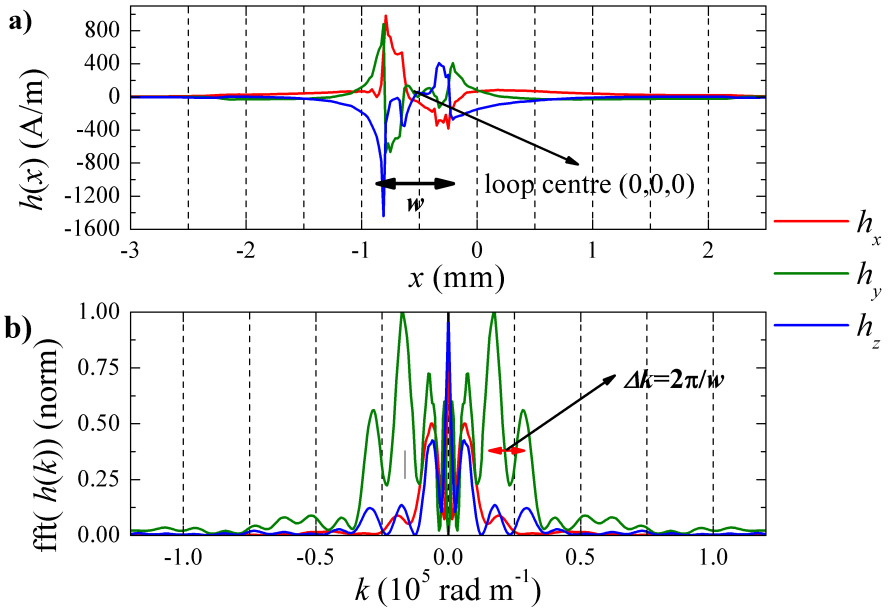

Figure 3.20: Distribution of the electric field at a frequency $f = 4$ GHz in a section of the loop shaped region and excitation spectrum. The directions x and y correspond to the in-plane direction and z corresponds to the out-of-plane direction.

Assuming that in the FMR setup the static applied field is set along the direction x of the waveguide, the non-zero dynamic field components driving the precession will be h_y and h_z. The wavevector excitation spectra for both h_y and h_z have different amplitude but the peaks of both field components correspond to the same wavenumbers. The excitation spectra can be defined as a rapidly oscillating component with periodicity of $\Delta k \sim 10^4$ radm^{-1}. The term Δk is associated with an effective width w of the signal line [138], which can be estimated from $w = 2\pi/\Delta k = 560$ μm. The value of w value is coincident with the region over which the magnetic field is highly non-uniform as shown in Fig. 3.20a. In Refs. [138, 147], the spin wave excitation

spectra is characterised in terms of the dynamic fields in the microstrip and coplanar waveguides, respectively. In particular, the effect of the dynamic excitation spectra on broadening of the linewidths in the FMR spectra are discussed. Considering the loop shaped microstrip, unlike in a straight microstrip or coplanar structure, the wave vector excitation is not exclusively along a fixed axis. Instead, the excitation will have components along x, y and z. Due to the finite bandwidth and the excitation of multiple wavevector directions, relative to the applied field, shifts in the resonance frequency and linewidth broadening can be expected [138]. Following Ref. [138], a more accurate expression for the resonance equation would have to account for the angle θ between the wavevector direction and the applied field, and is approximated by:

$$\omega(k,\theta)) = \omega_0^2 - \frac{1}{2}\gamma^2\mu_0^2 M_{eff}(H_0 - [H_0 + M_{eff}]\sin^2\theta)kd_f, \tag{3.18}$$

where $\omega_0^2 \simeq \gamma^2\mu_0^2 H_0 M_{eff}$ in the limit of $M_{eff} \gg H_0$, the term k corresponds to the wave number and d_f is the thickness of the film. This approximation is only valid for $kd_f \ll 1$, as the surface and magnostatic spin waves are degenerate. This implies that spin wave excitation is also related to the dimensions of the loop structure itself. The resonance shift and the linewidth broadening due to non-uniform (or multiple) excitation wave vectors can be expressed as in Eq. 3.19a and Eq. 3.19b, respectively [138].

$$\delta\omega_0(k_{max},\theta) = \frac{1}{2}[\omega_s(k_{max},\theta) - \omega_0] \tag{3.19a}$$

$$\Delta\omega_0(k_{max},\theta) = \Delta\omega_{int}\sqrt{1 + \left(\frac{\omega_s(k_{max},\theta) - \omega_0}{\Delta\omega_{int}}\right)^2} \tag{3.19b}$$

where $\Delta\omega_{int}$ corresponds to the intrinsic linewidth broadening, which accounts for all the Gilbert-like damping terms discussed in Sec. 2.3.

Given the considerations above, if FMR measurements are carried out using a sample large enough to cover the entire microwave structure, the non-uniform excitation can cause a linewidth broadening and enhanced spin wave excitation due to the broad wave number excitation bandwidth.

Another aspect worth noting is the fact that in the single port setup, the measurements were carried out in reflection mode. It is reported in literature that

measurements in reflection, with appropriate phase correction, yield accurate measurements of the resonance characteristics, for the case of linear excitations of the uniform (k= 0) mode using a coplanar waveguide [148]. However, according to Ref. [149] the detection of non-uniform modes may differ from reflection and transmission experiments.

3.4 Lorentz microscopy

Imaging methods where the contrast is a result of electrons being deflected due to the Lorentz force are described in this section and generally pertain to magnetic information. These methods are accessible in the environment of a transmission electron microscope (TEM) and belong to the research field of Lorentz microscopy. The implications of propagating electrons in electric and magnetic fields, from both classical and quantum mechanical perspectives will be discussed in chapter 7.

The main reasons for using Lorentz TEM are the high spatial resolution (1-20 nm) and that by switching to conventional TEM (CTEM) one can also obtain structural and compositional information.

There is a key difference between using the microscope for CTEM and for Lorentz microscopy. In CTEM the specimen is immersed in a strong, out-of-plane, magnetic field (1-3 T) created by the objective lenses, which dramatically affects the magnetic properties of the sample. A necessary condition for Lorentz microscopy is that the objective lenses are de-excited to levels where the out-of-plane magnetic field is of the order of 0.2-0.3 T, allowing for the magnetic moment of the specimen to lie in plane. When this condition is satisfied, it is possible to study the hysteresis behaviour of the specimen by tilting it with respect to the applied field created by the objective lenses. Alternatively, specimen holder rods can be modified to generate in-plane fields [150, 151].

In the context of this thesis, the techniques used for magnetic imaging were Fresnel, low angle diffraction (LAD) and Lorentz differential phase contrast (DPC). These are described next.

3.4.1 Fresnel

In Fresnel imaging, the contrast arises due to constructive or destructive interference between electron waves transmitted near the boundaries of the magnetic domains. Consider a specimen with 3 magnetic domains, separated by domain walls, as shown in Fig. 3.21. The magnetic contrast is achieved by moving the object plane away from the specimen level, i.e. defocusing the image by Δ_F. This is done to enhance the contrast from constructive and destructive interference of the electron waves experiencing the induction fields, near the boundaries of each of the domains. From a classical perspective, the image is formed by regions where deflection from two domains will converge and regions where deflections will diverge. This method provides only qualitative information on the position of the domain walls and the relative orientation of the domains due to fact that the intensity images have a non-linear dependence on the defocus. Quantitative Fresnel imaging can be obtained using the transport of intensity equation (TIE) formulation. Following TIE, the projected magnetic induction can be determined from reconstruction of the phase image [152, 153]. This requires the use of under-focused ($+\Delta_F$), in-focus and over-focused ($-\Delta_F$) images.

3.4.2 Low angle diffraction

Low angle diffraction [154] (LAD) is an alternative to direct imaging of the magnetic domains. In this method, the reciprocal space is imaged and the magnetic contrast arises in the form of small deflections from the central diffraction spot. In the context of electron scattering from nano-structured materials, this technique is known as small angle electron scattering (SAES) [155].

Typically, the deflection due to the Lorentz force in a magnetic specimen ($\sim$ 1 T induction field) is of the order of 10^{-6} radians, whereas the diffraction patterns with origin in the crystalline structure have typical angles of the order of 10^{-3} radians, since the periodicity in crystal is of the order of angstroms. In order to detect such small deflections, the diffraction pattern around the centre spot must be magnified in order to be imaged. In LAD, this is achieved by using a long camera length, in the order of 100-3000 metres [154, 155][3]. One should be reminded that in conventional

[3]The camera length, corresponds to the magnification in diffraction mode and can be tuned by

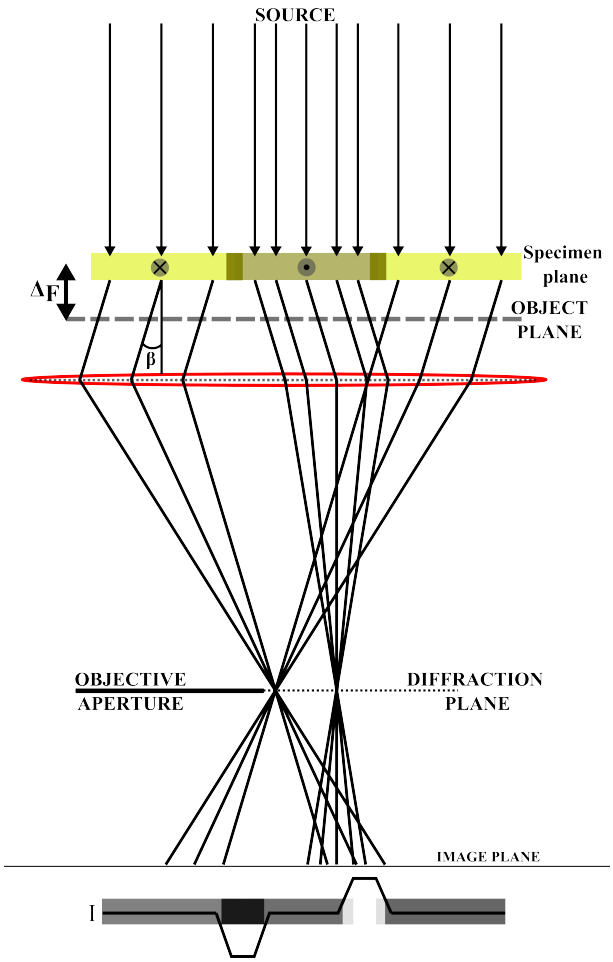

Figure 3.21: Simplified optics diagram of TEM Fresnel imaging. Specimen comprised of three magnetic domains. The phase change due to the magnetic induction of each domain will generate an image which results from the electron waves interfering constructively (on each domain) and destructively, near the boundary of the domain walls. Schematic is not to scale.

diffraction experiments of crystalline structures, the camera length is of the order of a few metres only. The long camera length enables an increase in the magnification of the diffraction pattern. Moreover, one must ensure that parallel illumination is obtained from the condition of Fraunhofer diffraction to be applied, i.e. for the diffraction pattern to be formed in the back focal plane of the imaging lens.

The diffraction images are calibrated using a known structure at a given camera length. Figure 3.22 shows the real space and diffraction space images of a gold cross grating with a periodicity, d, of 463 nm and whose diffraction pattern was obtained using a camera length of 720 metres. The diffraction angle per unit pixel can be determined from $\beta = \lambda/(2d \times n_p) = 0.04$ radp^{-1}, where $\lambda = 2.5$ pm corresponds to the wavelength of the electrons and n_p corresponds to the separation in pixels between two adjacent spots.

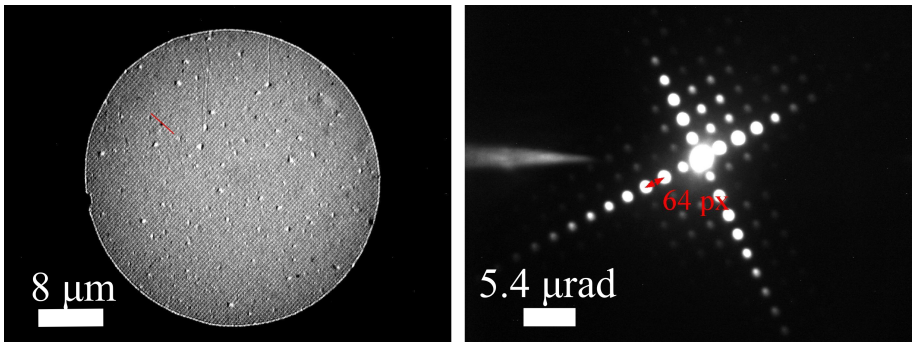

Figure 3.22: Low magnification image (left) and Bragg diffraction pattern (right) of a gold cross grating with 2160 lines per mm, which results in a grating line period of 463 nm. The LAD pattern allows to obtain the Bragg scattering angle per unit pixel. The separation, in number of pixels, between two consecutive diffraction spots is 64 (red arrow). Considering the camera length used (720 m), a value of 0.04 μradians of deflection per unit pixel was obtained.

Often LAD is combined with Fresnel imaging so that real and reciprocal space images can be obtained iteratively. Figure 3.23 shows an example of how Fresnel imaging and LAD can be combined to image domain structure and to extract quantitative information. The images correspond to a Fresnel image and the LAD pattern resulting from an antidot lattice (ADL) with a hole diameter of approximately 200 nm and a pitch of 690 nm, with the field (H) applied along the diagonal of the ADL. The Fresnel contrast appears as vertical and horizontal dark/white domain

changing the current in the image forming lenses.

walls. The closely spaced spots, labelled as ADL, correspond to the diffraction from the structured material. In addition to the Bragg diffraction due to the nano-structured film, four broad spots, encircled in red, are obtained as a result of the Lorentz deflection due to magnetic induction. These spots are rotated by 45◦ relative to each other as the magnetic moment is aligned along both axes of the ADL. Knowing the film thickness, t= 40nm, and the deflection angle, β , the magnetic induction can be obtained as $B_d = \beta h/(\lambda et)$= 0.45 T, where e represents the electron charge.

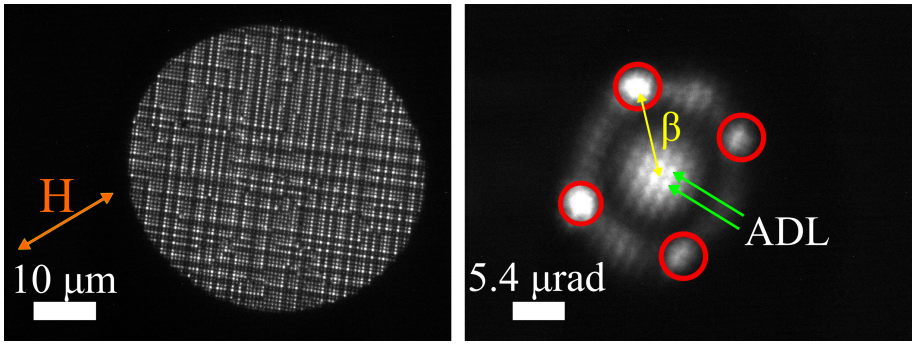

Figure 3.23: Fresnel and LAD pattern of Ni_80Fe_20 (t= 40 nm) ADL fabricated by focused ion beam. Image acquired at remanence, while performing a field sweep which started from saturation, with the applied field along the diagonal of the ADL. Note the that the LAD image shows some effects of astigmatism (spots are slightly deformed). The Fresnel image is highly defocused so the ADL geometry is not as obvious.

An obvious drawback of LAD is that this imaging method illuminates large areas, so extracting local information can be challenging.

An alternative method to LAD is Foucault imaging [156]. The objective aperture is inserted at the level of the back focal plane (diffraction plane) with the purpose of partially blocking the diffraction pattern. This results in a selective reconstruction of the contrast originated in a single domain, when changing to Fresnel mode. When operating the TEM in low magnification ($< 1850\times$) the selected area aperture swaps function with the objective aperture due to de-excitation of the objective lenses and the projection system.

3.4.3 Differential phase contrast

Differential phase contrast (DPC) is the most complete of the magnetic imaging techniques. It renders high resolution and quantitative information on a nanometre scale. This method requires a sophisticated detection system implemented on a scanning TEM (STEM). Unlike LAD, this technique makes use of a focused beam probe which scans over the specimen generating a deflection cone at each step of the raster movement, with the resolution limit being the probe size. Recently, a resolution of 1 nm has been achieved with an aberration corrected STEM [46]. The measurement of the deflected cone is performed using a segmented quadrant detector. Assuming that the undeflected beam is equally distributed between all segments of the detector, when a region with magnetic induction is probed, the deflection cone will shift in accordance to the Lorentz force experienced locally. This is illustrated in Fig. 3.24, where α is defined as the convergence angle of the electron probe as it reaches the specimen and β the deflection angle experienced as a result of the Lorentz force.

In operation, the segmented detector acquires four images simultaneously, each one corresponding to a quadrant of the detector. Subtracting the components opposite to each other allows mapping the deflection along the two orthogonal directions so a complete map of the magnetic induction can be achieved. So far, it was only mentioned that contrast is due to magnetic induction. However, contrast in DPC imaging also arises due to variations in the electric potential due to the crystal lattice, grain boundaries, defects and due to a variation in thickness at the edges of nano-structures. These features emerge in the images as the high spatial frequency components [4]. At the other end, the low spatial frequency components emerge due to the slow phase varying objects such as the magnetic induction distribution and the stray fields of a specimen. As the whole spatial frequency range appears in the same image, often the high spatial frequency components undermine the sensitivity to the magnetic signal. To overcome some of these issues, each quadrant of the detector was split into [157] an inner and an outer (annular) detectors. The inner quadrants contain information on the structure (high spatial frequencies) and the outer detectors

[4] maximum spatial frequency is given by the α/λ, where α is the probe forming cone angle and λ is the wavelength of the electrons

contain information on the magnetic induction (low spatial frequencies). Nowadays, and in particular for the equipment used, the detector consists on 8 components (4 outer and 4 inner), labelled from 0 to 3 in Fig. 3.24.

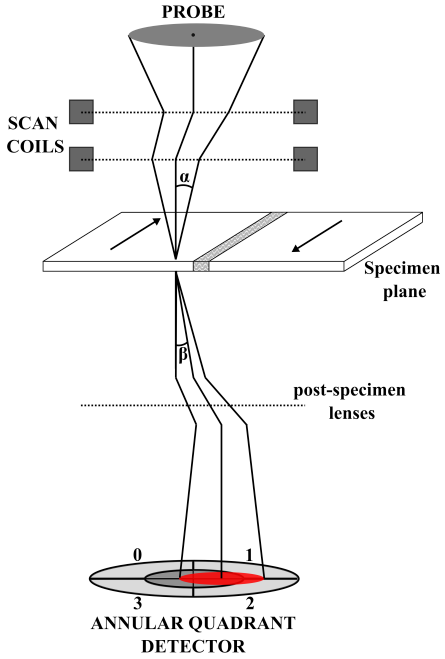

Figure 3.24: Schematic of the equivalent electron optics in DPC Lorentz microscopy. In an aberration free system, the resolution is limited by the diffraction limit which is given by $1.22\lambda/\alpha$, where α is the probe convergence angle and λ is the electron wavelength (2.5 pm at 200 kV). Annular quadrant detector comprises four inner and four annular (outer) detectors. The inner detectors contain information regarding the high spatial frequency components whereas the annular detectors are more sensitive to the low spatial frequency components, as the magnetic induction for instance.

Figure 3.25 shows an example of the DPC image components obtained while studying an ADL. The four outer annular components were subtracted to form the data shown in Fig. 3.25a and b, which correspond to the diametrically opposed quadrants, 0-2 and 1-3, respectively. These images correspond to orthogonal components of the magnetic induction. A colour map can be produced, as demonstrated in Fig. 3.25c, by computing the arctangent resulting from the ration of the 0-2 and 1-3 images. The sum of all components corresponds to a bright field image, shown in Fig. 3.25d, where the grain contrast of the films can be observed. The strong contrast at the edges of the holes is associated with the electrostatic phase variations as a result of the change in thickness and the presence of the edges. One would expect to map

the stray fields at the hole regions. However, given the rather sloped edges of the holes the electrostatic phase contrast appears to swamp the stray field variation.

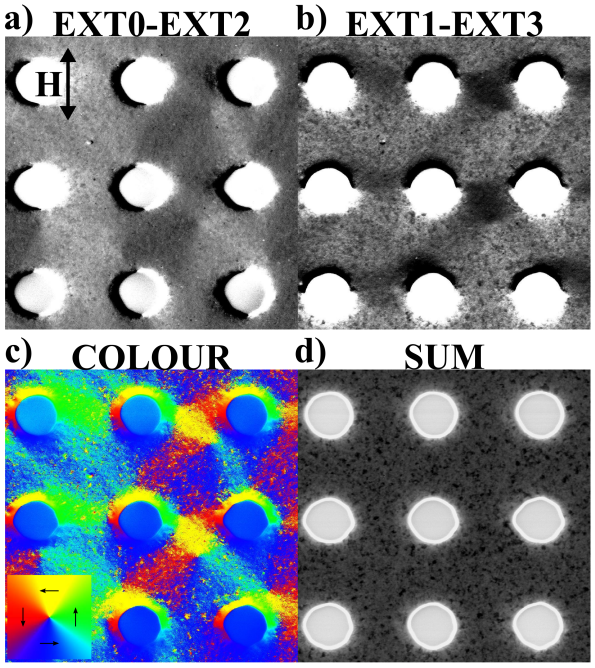

Figure 3.25: Example of image operations in DPC which allow to obtain magnetic contrast. a)-b) correspond to the subtracted components 0-2 and 1-3 of the external (outer) annular detectors, respectively. c) Colour image, generated by computing $\arctan(\mathrm{EXT0}-\mathrm{EXT2}, \mathrm{EXT1}-\mathrm{EXT3})$, represents the direction of the magnetic induction (colour code as inset). d) Sum image demonstrates the formation of a bright field image, from which the grain contrast can be observed, as well as the clear change in contrast near the edges of the holes.

From the example shown in Fig. 3.25 it is possible to draw a number of advantages of this imaging method. The fact that the electron beam is focused (as opposed to the Fresnel mode), one can recover the structural properties of the specimen, while still being able to image the magnetic induction with unprecedented resolution.

Chapter 4

Unbalanced magnetic pole distribution on exchange biased antidot templates

A single port VNA-FMR with a loop shaped microstrip was used to study the magnetodynamic response of NiO/NiFe bilayers with antidot structuring. A large frequency asymmetry with respect to the applied magnetic field is found across a broad field range whose underlying cause is linked to the distribution of surface magnetic poles at the antidot surfaces. This distribution is found to be particularly sensitive to the effects of exchange bias, and robust in regards to the quality of the antidot geometry. The template based antidot geometry studied here offers advantages for practical device construction. The results demonstrate that the template approach is suitable for broadband absorption and filtering applications, allowing tunable anisotropies via interface engineering. This chapter has been adapted from a manuscript published recently and can be found in Ref. [158].

4.1 Introduction

Periodic arrangements of non-magnetic holes (antidots) embedded in a continuous film are of great interest for high frequency applications due to the versatility with which microwave properties can be tailored. One can, for example, confine and direct the propagation of spin waves [87, 102, 159, 160] for applications such as spin wave

logic and interferometry [9, 161]. Antidots have proven to be extremely effective in terms of modulating local effective anisotropies and coercivities by altering hole diameter and periodicity [84, 162–167]. In this chapter, it is demonstrated that anisotropies in template based antidots can be modified to allow an asymmetric broadband absorption, whose frequency range is dependent on the direction of an applied field.

Unidirectional anisotropy can be introduced into a ferromagnet through exchange coupling with an antiferromagnet. This effect, called exchange bias, is often described by an effective field which causes a shift in the hysteresis loop of the ferromagnetic film, as well an increase in the coercivity [18, 20]. The induced anisotropy in exchange biased antidots has been studied as a function of lattice geometry [14, 34, 41, 42, 168] and the interplay between internal fields [32, 40, 169]. Patterning allows tailoring of the magnitude and direction of the exchange bias field [43, 170]. Some interesting applications are within reach, by making use of multi-state remanent processes occuring in structures with combined positive and negative exchange bias fields [4].

Most important for the present work, the effective exchange bias field can modify ferromagnetic resonance response[171]. Ferromagnetic resonance frequencies can be shifted upwards or downwards, depending on the strength and polarity of the exchange bias field. In this chapter, it is shown that the existence of a unidirectional bias induced asymmetric microwave response with respect to an external applied field, which is linked to an unbalanced distribution of the demagnetisation fields around the holes of the antidot structure.

A scanning electron microscopy (SEM) image of an antidot lattice (ADL) comprising a bilayer of NiO and NiFe deposited on a template is shown Fig. 4.1a. The existing holes create a non-uniform distribution of demagnetisation fields (H_d) arising from local deformations in the spin configurations, as illustrated in the inset of Fig. 4.1a.

The details on the structure of the antidot template and the VNA-FMR experiments are presented and discussed in section 4.2. The NiO/NiFe bilayer exhibits a room temperature exchange bias field of -1.5 mT, as shown by the lateral field displacement of the hysteresis loop in Fig. 4.2a. What is particularly interesting is that the ferromagnetic resonance profile is highly asymmetric around zero applied

field. Even for the small exchange bias observed here, the resonance frequency is different for a positive field, $+H_0$ (18 mT), and a negative field, $-H_0$. This is seen in Fig. 4.2c, for ferromagnetic resonance spectra acquired with the applied field along a direction parallel to the lattice edge. In section 4.3 micromagnetic results are presented in order to show that the asymmetry in the dynamics spectra provides a quantitative measure of the extent to which the pole distribution at the holes is pinned by the exchange bias.

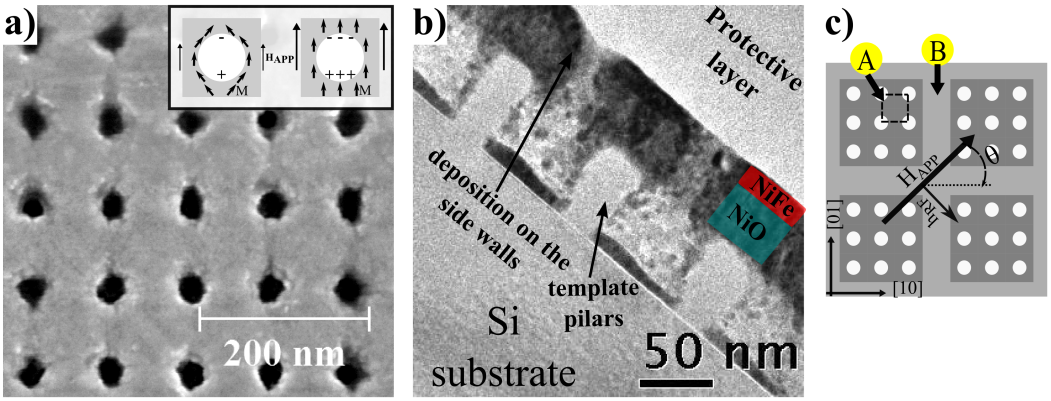

Figure 4.1: a) Scanning electron microscopy image of the NiO/NiFe ADL under investigation: NiO(36nm)/NiFe(12nm) pitch: $\sim$ 100 nm, holes: 45/50 nm b) Bright field transmission electron microscopy image of the cross-section. Note that some magnetic material appears also at the bottom of the holes and on the side walls of the Si template. c) Schematic of the silicon template and respective angle nomenclature: θ corresponds to the angle between H_{app} and lattice edges; direction [10] collinear with θ= 0° and direction [01] collinear with θ= 90°. The ADL template consists of arrays hole etched on a silicon substrate. Following the schematic, this sample consists of 600 × 600 μm^2 arrays (region A) spaced by non-etched regions (region B) which are 100 μm in width. The sample was fabricated and characterized via TEM by Prof. Ko-Wei Lin and Ms. Shan Su from National Chung Hsing University, Taiwan.

4.2 Experimental data and discussion

The NiO/NiFe bilayer was deposited onto a silicon ADL template substrate at room temperature and zero field using a dual ion-beam deposition system [172]. The substrate consisted of a silicon template in which the holes, with elliptical shape (45/50 nm), are periodically spaced by 100 nm. In this deposition setup, a Kaufman

ion source was used to focus an argon ion beam onto a $Ni_{80}Fe_{20}$ (at.%) and Ni targets, while an End-Hall ion source was used to bombard the ADL template during the deposition of the bottom NiO layer. A fixed voltage of 140 V at the End-Hall ion source ensured a constant ion-beam bombardment energy. During deposition, the Ar/O_2 ratio in the End-Hall source was kept at 16% to ensure the formation of NiO.

Figure 4.1b shows a bright field transmission electron microscopy image of the antidot cross-section, cut by focused ion beam. Note that the NiFe/NiO films were sputtered uniformly onto the ADL silicon template so one should expect a finite layer of the deposited materials at the bottom of the holes as well as at the side walls of the template. The thickness of the NiFe film in the bottom of the holes is negligible possibly due to masking of the template pillars. However, one must account for the material deposited on the curved edges of the side walls as this will add roughness to the edges of the antidots. Nevertheless this sample is, to a good approximation, an ADL from which one should expect a ferromagnetic resonance broadened by edge roughness. Also, as illustrated in Fig. 4.1c, the sample consists of 600 μm large arrays of holes spaced by 100 μm wide regions of continuous film. These antidot arrays and the continuous film regions are labelled as A and B, respectively. The magnetometry data shown in Fig. 4.2a were obtained with a Quantum Design SQUID MPMS XL-5 from 5 K to 350 K within a field range of ± 2 T after initially field cooling the sample in a 2 T field from 400 K. The hysteresis loop acquired at 300 K exhibits a small exchange bias field and a rather uniform reversal process. The inset loop, acquired at 10 K, shows a stepped magnetisation curve which is attributed to reversals of the antidot region and continuous film region at different applied fields. As expected, in the low temperature regime, both coercivity and exchange bias field are enhanced.

For the VNA-FMR measurements shown here, a loop shaped microstrip operating in a single-port configuration was used. The details of the experimental apparatus can be found in section 3.3. Each measurement began well above the saturation field, at H_{REF}= 150 mT, where a reference spectra is acquired for background correction purposes. Then, starting at a maximum applied field H_{app}= 60 mT, the VNA signal is swept five times and averaged; the static field is linearly reduced once the frequency sweep is completed. This procedure is repeated over the range H_{app}=

±60 mT. Example results are shown in Fig. 4.2b (±80 mT field range),c and d.

The ferromagnetic resonance data shown in Fig. 4.2b corresponds to a single layer of NiFe antidots, which shows no asymmetric behaviour as the exchange bias field is zero. One should note the difference in effective anisotropy, H_k^{eff}, by comparing frequencies at θ= 0° (top) to those at θ= 90° (bottom), as the resonance frequency $f_R(\theta = 0°)$= 2.3 GHz is lower than $f_R(\theta = 90°)$= 3.1 GHz, respectively, for $\mu_0 H \sim$ 40 mT. This change in effective anisotropy is attributed to a 5% deviation from square of the lattice as can be seen from the Fig. 4.1a.

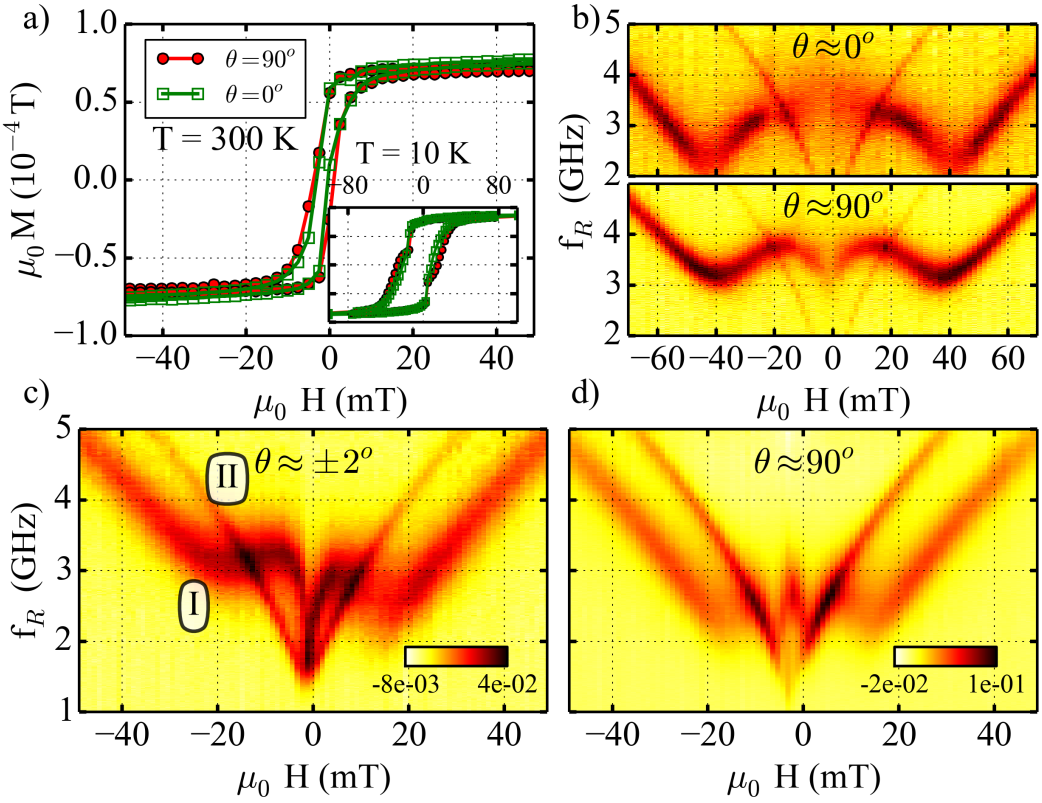

Figure 4.2: The hysteresis loops in a) correspond to the NiO(36nm)/NiFe(12nm) antidot sample at the temperatures 300 K and 10 K (inset). b) The spectra (normalised magnitude of S_{11}) correspond to the ferromagnetic resonance spectra of NiFe (18nm) antidots acquired with $\mu_0 H$ (H_{APP}) applied along θ= 0° (top) and 90° (bottom). This sample does not exhibit the asymmetric response as the system is not exchange biased. Ferromagnetic resonance spectra of the NiO/NiFe antidots taken with the applied field at: c) θ= ±2° off the lattice direction [10] and d) θ = 90°, collinear with the direction [01]. Trace noise in the FMR data is 0.25 mdB and the lowest signal to noise ratio is 1 mdB. The magnetometry data was provided by Prof. J. van Lierop and Dr. R. Desautels from the University of Manitoba, Canada.

Figures 4.2c and d correspond to frequency versus $\mu_0 H$ traces of the NiO/NiFe sample measured relative to the main axes of the ADL, with $\theta = \pm 2°$ and $\theta = 90°$. In Fig. 4.2c, a clear asymmetry is visible, with a frequency difference of approximately 0.5 GHz between $f_R(\mu_0 H = 18mT)$ and $f_R(\mu_0 H = -18mT)$.

The ADL and the frame generate distinct ferromagnetic resonance spectra, denoted as resonance mode I and mode II in Fig. 4.2c, thereby providing a useful comparison. It is shown later that these modes can be associated with the regions A and B, respectively, in Fig. 4.1c. Both resonance modes I and II are centered at $\mu_0 H =$ -1.5 mT, which is attributed to the exchange bias field. Given the distribution of the internal fields within the antidots, the resulting magnetic properties are primarily seen as an effective four-fold anisotropy in which the hard axes are along the edges [10] and [01], and the easy axes along the diagonal [11] of the unit cell. This is consistent with results discussed in Ref. [14] and [168]. In ferromagnetic resonance, the magnetic hard axis is obtained for a direction along which the resonance frequency reaches a local minimum of $f_R^{min} = 2.5$ GHz (softening) when the applied field $\mu_0 H = \pm 18$ mT $\sim H_k^{eff}$. Mode II results from the continuous film (B) region which surrounds the antidot arrays and shows no angular dependence. By comparing the spectra of Fig. 4.2c and d, a marked decrease in the frequency asymmetry from $\theta = \pm 2°$ to $\theta =$ 90° is noted. From observing the angular variation of the ferromagnetic resonance as a function of applied field angle, note that the amplitude of the asymmetry drops to zero when $\theta = 0°$ and $\theta = 90°$. This behaviour results from competition between the fourfold anisotropy and the exchange bias field. At $\theta = 0°$ and 90°, the fourfold anisotropy field is much larger than the exchange bias field and therefore the asymmetry is less pronounced. A large asymmetry is obtained only when the applied field is off the high symmetry directions by a few degrees, with respect to the ADL. The angular variation of the antidot modes in general is discussed in chapter 5.

4.3 Micromagnetic simulations

Micromagnetic simulations were carried out in order to understand the dipolar effects on the ferromagnetic resonance. Details on the simulation tool (Mumax) can be found in appendix section B [173]. The simulated geometry corresponded

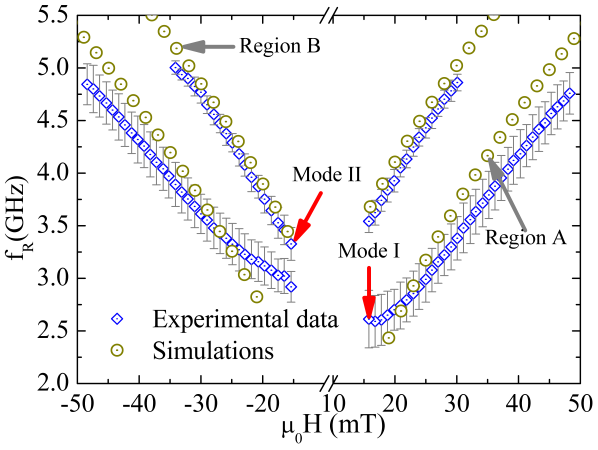

Figure 4.3: Simulation results overlaid with FMR data obtained experimentally. The simulated spectra relative to region I and region II were obtained by calculating the dynamics spectra from the antidot region (A) and the continuous film region (B) as shown in Fig. 4.1c.

to a 9x9 array of 35 nm circular holes spaced by 65 nm, and a continuous film region, both with identical parameters (mesh = 3.125 nm, M_S= 820 × 10^3 A/m, A_{EX}= 13 × 10^{-12} J/m, γ= 0.02). The applied field and the initial magnetic state are at an angle of 2° from the lattice direction [10] in order to avoid artifacts at high symmetry directions [102]. The dynamics spectra were obtained by performing a Fourier transform of the time (t) dependent magnetisation, after applying a pulse in the form of $A_0 \sin(t - t_0)/(t - t_0)$, where A_0= 1 mT and t_0= 3 ns, in the out-of plane direction. A pinning field of -3 mT along the direction [11] of the ADL was added to account for the exchange bias. The resulting spectra are shown in Fig. 4.3, where the simulation results are overlaid with experimental data. In the simulations, the resonance modes I and II were acquired from the magnetisation dynamics of the antidots, labelled as region A, and the continuous film, labelled as region B.

The spectra from region A resembles the asymmetric mode labelled as mode I in the experiments. At positive $\mu_0 H$ the resonance frequency, f_R^{min}, at around the H_k^{eff} is shifted downwards whereas at $-H_k^{eff}$ the f_R^{min} is shifted upwards. To interpret this observation consider the effect of exchange bias in the local distribution of the poles around the holes defining the antidot geometry. The demagnetisation fields are influenced by the unidirectional field acting on the magnetisation and leads to asymmetries in the ferromagnetic resonance spectra in the positive and negative

directions. The spectra obtained by sampling in region B resembles mode II from the experimental data.

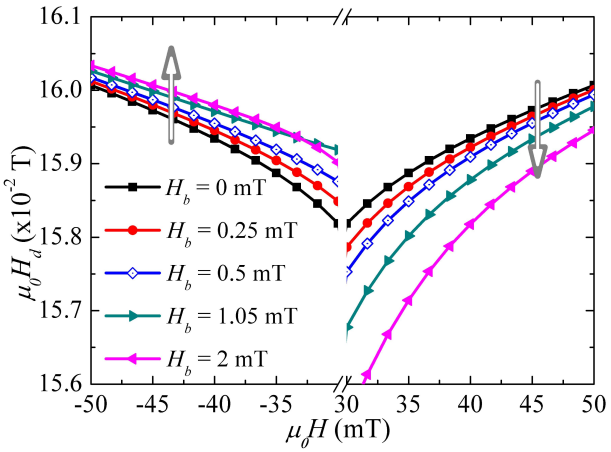

Figure 4.4: Amplitude of the demagnetisation field as function of $\mu_0 H$ for different amplitudes of H_b. The demagnetisation fields where calculated by averaging over the holes set in the Mumax geometry. This field quantity measures the strength of the poles around the edges of the holes. Note the break in the $\mu_0 H$ axis. The unsaturated region ($\leq H_k^{eff}$) is discarded as it requires a different model of interpretation, hence the break in the field axis.

The variation of the demagnetisation fields, $|H_d|$, calculated by averaging inside the holes, as function of the applied field is shown in Fig. 4.4. Each curve corresponds to a sightly increased pinning (bias) field. For the case where the pinning field is zero, a symmetric response is obtained. When the pinning field is non-zero, note that at positive $+\mu_0 H$ the H_d decreases as the amplitude of the pinning increases. However, for $-\mu_0 H$ the H_d increases as the pinning field increases. This asymmetry in the variation of H_d shows the effect of the exchange bias field on the ADL. The strength of the fields in the holes is proportional to the surface pole distribution. This indicates that the bias is affecting the ferromagnetic resonance primarily through the pole distribution.

4.4 Conclusions

The asymmetric magnetodynamic response depends on the distribution of surface magnetic poles created at the inner surfaces of the antidots. From the analysis of the demagnetisation field predicted to arise from the surface pole distribution, it

is clear that exchange bias can lead to significant changes in the pole distribution through modifications of the magnetic order near the antidots. Most importantly, the asymmetry can be created in antidots produced using a template method, which may allow a practical method for device integration. Because the asymmetry is driven by the exchange bias, an estimate of the operating range in terms of temperature, would be given by the ordering temperature of the antiferromagnetic material (below 500 K for NiO). In the low temperature regime, the exchange bias is enhanced so one can expect an increase in the asymmetry. However, from the device perspective it may not be realistic to consider temperatures below 280 K.

The large linewidths do not allow resolution of the finer structure, i.e. multiple resonance modes. This is discussed in the next chapter, for a different ADL. Nevertheless, the resonance modes obtained in this system indicate a strong dependence on the orientation of the applied field relative to both the exchange bias and the ADL. As discussed in section 3.3.3, the excitation field in the loop shaped microstrip is highly non-uniform, which is likely to result in broadening of the resonance linewidths.

Chapter 5

Competing anisotropies in exchange biased 2-D nano-structured systems

The magnetodynamic properties of an exchange biased $Fe_{50}Mn_{50}/Ni_{80}Fe_{20}$ system with a specific type of antidot structuring are investigated in this chapter. The ferromagnetic layer (NiFe) is modulated in thickness and in the presence of an exchange bias. The ferromagnetic resonance (FMR) spectra are complex, exhibiting predominantly an antidot anisotropic behaviour. Using FMR, it is found that the anisotropy has an 8-fold and 4-fold component. Brillouin light scattering measurements (BLS) show magnonic band gap as expected in periodic structures such as the one reported here. To understand these observations, the precessional modes obtained experimentally are correlated with localised mode profiles obtained from micromagnetic simulations. Due to the effect of exchange bias, the magnetodynamic response of this system is asymmetric with respect to an applied field. The large asymmetries observed, are obtained along directions off the main axes. This hybrid structure is a good candidate for applications such as selective/directional microwave filtering and prospective multi-state magnetic logic, given the degree to which one can tailor the ground state.

5.1 Introduction

An interesting aspect of patterned films is that they induce a non-uniform magnetisation reversal process, which can be advantageous for the development of multi-state memory devices [4, 84, 102]. A stepped magnetisation reversal, necessary for such applications can be achieved by patterning a bi-component structure, typically comprised of antidot structuring with the holes filled with a different magnetic material [105, 108, 110, 174], or by adding positive/negative exchange bias on a single ferromagnetic layer system [4, 43]. Exchange bias can also be seen as a way to modify the dynamic response of the magnetic system, as a result of the competing unidirectional and anisotropic field distribution [40]. In particular, an asymmetric microwave response, with respect to the applied field, has been demonstrated to have origin in the unbalanced pole distribution at the edges of the holes in the antidot lattice (ADL), as demonstrated in Chapter 4.

In this chapter, the magnetodynamic properties of an antiferromagnet - ferromagnet (AF/FM) system with antidot structuring on the AF, but incomplete etching of the holes in the FM layer, are studied using a range of spin wave detection techniques. This type of structuring results in a periodic modulation of the FM layer thickness, and exchange bias between the holes, as illustrated in Fig. 5.1a. In a way, the sample can be seen as a bi-component magnonic crystal, whereby introducing the antidot structuring a complex magnetodynamic response is obtained. Importantly, the structure still behaves as magnonic crystal with characteristic spin wave band gaps. Having a continuous film adjacent to the ADL allows the spin wave modes to have a complex dependence on the applied field angle, as spin waves are allowed to propagate in all directions [108].

Applied field angle dependent FMR results show an 8-fold symmetry for the lowest resonance modes and a dominant 4-fold symmetry for the highest resonances. Also, the variation of the exchange bias field with applied field direction, exhibits an interesting dependence. It is widely known that that exchange bias in continuous films possesses a unidirectional symmetry with regards to an external field [18, 20]. However, in the case of the ADL here studied, the effect of exchange bias field on the ferromagnetic resonance properties varies greatly with the symmetry of the structuring.

Micromagnetic modelling was performed in order to obtain the angular dependence and the mode profile of the resonance modes. A comparative analysis was made on how the partially etched holes can affect microwave properties of the magnetic structure by varying the film thickness in the region of the holes, t_h= 0, 5, 10, 20 nm, with respect to the 20 nm thick layer of antidots.

The chapter is structured as follows: The details on the film growth, patterning and structural analysis are presented in Sec. 5.2, where magnetometry data relative to the patterned and unpatterned films is also included. The magnetodynamic properties of the patterned and unpatterned films are discussed in Sec. 5.3. This section is divided in three parts: Sec. 5.3.1 FMR studies on the mode structure; Sec. 5.3.2 spin wave dispersion obtained via BLS studies; Sec. 5.3.3 the angular dependence of the resonance modes is presented and analysed. Micromagnetic simulations carried out to interpret the anisotropy in the antidots is presented in Sec. 5.4. This section is divided in two parts. The result of varying the thickness of the patterned layer is shown in Sec. 5.4.1 and the origin of the resonance modes is presented in Sec. 5.4.2. The asymmetric variation of the resonances, with respect to the applied field direction is discussed in Sec. 5.5.

5.2 Film growth and patterning

A Si substrate was sputtered with an 8 nm thick layer of Ta. Layers of $Fe_{20}Ni_{80}$ and $Fe_{50}Mn_{50}$ were deposited on a sequential sputtering system (Shamrock SFI) at a base pressure of 10^{-8} mbar, in the presence of an in-plane magnetic field of 9 mT. The bi-layer was capped with 8 nm Ta layer to prevent oxidization. Following deposition, the sample was annealed at 498 K in a 0.2 T magnetic field (3°C/minute ramp, 120 minutes at maximum temperature) in order to set the exchange bias direction.

To initiate the patterning process, a 120 nm layer of silicon nitride (SiN) was deposited on the top of tantalum (Ta), as a hard mask. The sample was subsequently patterned using electron beam lithography combined with reactive ion etching. A 200 nm thick layer of ZEP520 resist was exposed on a Vistec VB6 UHR EWF e-beam writer and developed in O-Xylene. The pattern was then transferred to the hard

mask via a reactive ion etching process (RIE) involving CHF_3/O_2, on a 80+RIE etching tool. At a final stage, the NiFe/FeMn/Ta was etched on a ET340 RIE tool, using CH_4/H_2 with resulting etching rates of 3 nm/min. Further details on the patterning process can be found in Sec. A. The ADL covers an area of $1.5 \times 1.5\text{mm}^2$. The unit cell size is 420 nm, with 280 nm diameter holes. A representative Scanning Electron Microscopy (SEM) image of the structure is shown in Fig. 5.1.

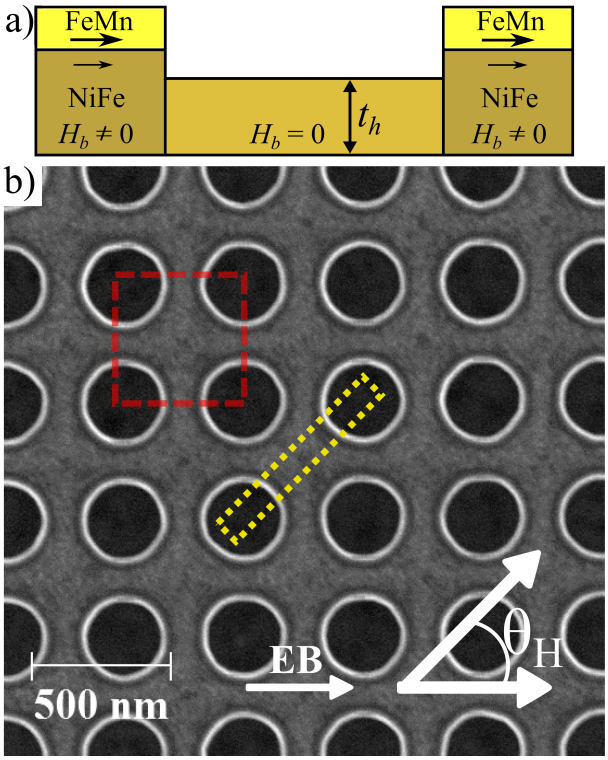

Figure 5.1: a) Illustration of the cross-section of the partially etched ADL. b) Scanning electron microscopy images of the ADL fabricated: NiFe(20nm)FeMn(10nm) pitch: 420 nm holes: 280nm. The change in contrast in the magnetic material is result of the SiN which remained on the surface after the reactive ion etching. Red dashed square illustrates the ADL unit cell. Yellow dashed rectangle illustrates the orientation of the cross-section discussed in Fig. 5.2.

Cross-sectional transmission electron microscopy and electron energy loss spectroscopy (EELS) were performed in order to determine the thickness and elemental composition of each layer. The preparation of the cross-section using FIB involved the following steps: 1) deposition of a protective (platinum) layer on the surface of the sample. The area deposited is typically a 10×4 μm^2 rectangle; 2) a series of FIB milling steps are performed on each side of the rectangle, and at a tilt angle with respect to the film normal, so that the end result is wedge shaped cross-section;

3) the wedge shaped element is attached to a micro-manipulator and an under-cut is done in order to detach the cross-section from the remaining bulk substrate; 4) further milling on the side-walls of the cross-section is carried out in order to thin the specimen below a 100 nm, which is the typical limit for electron beam transparency in the TEM. 5) finally, the sample is attached to a specimen holder and tested in the TEM.

Figure 5.2 shows a cross-section of the antidot structuring which was cut along the diagonal of the ADL. The two regions labelled as I and II refer to the Ta/NiFe and the Ta/NiFe/FeMn/Ta, respectively. The elemental maps of each of the regions are shown in Fig. 5.2 I and II. From analysing the region I, it was detected the presence of silicon (Si), tantalum (Ta), nickel (Ni), iron (Fe), carbon (C), oxygen (O), platinum (Pt) and titanium (Ti), from the substrate to the top. It has not been possible to identify the origin of the Ti, but it is believed that its origin is related to contaminations during the etching process since this element only appears in regions etched during the reactive ion etching process. The presence of Carbon and Oxygen are the result of etching and to the fact that this surface, rich in Ni and Fe was not capped in any way, promoting the formation of oxides at the interface as well as a carbon layer. In the region II, one is able to identify the elements Si, Ta, Ni, Fe, Mn, Ta, N. Based on the elemental composition shown in Fig. 5.2c-d relative to the several elements across the sample, the thickness is estimated for the case of the Ta, NiFe and FeMn layer. This was done by measuring the width at half height of the elemental distribution.

Magneto-optic Kerr effect (MOKE) magnetometry was employed to obtain the hysteretic behaviour of the continuous films and patterned sample. MOKE hysteresis loops are shown in Fig. 5.3 for both the (a) continuous film and (b) ADL. The setup was operated in the longitudinal configuration, with a laser spot size of 500 μm in diameter. For the continuous film, the hysteresis was obtained while the magnetic field was applied parallel (θ_H= 0°) and perpendicular (θ_H= 90°) with respect to the exchange bias direction and lattice edge. The results show a clear easy axis direction with a exchange bias field, H_b, of ∼5 mT. In the case of the ADL, the hysteresis was measured with the applied field along the lattice edges. For both θ_H= 0° and θ_H= 90° the exchange bias field is ± 1.5 mT. In a patterned film, the low field

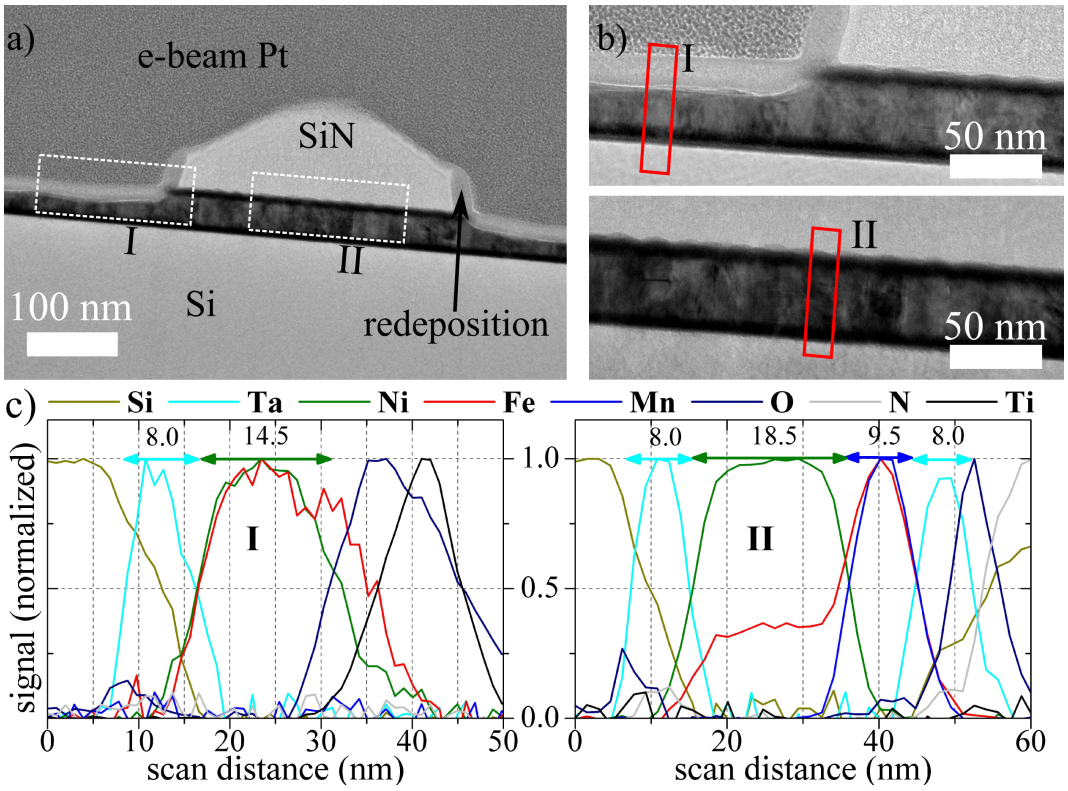

Figure 5.2: a)- b) Bright field TEM images of the ADL cross-section and EELS data relative to the region I and region II.c)- d) Normalised elemental profiles of regions I and II. Dashed yellow rectangle of Fig. 5.1 illustrates the orientation of the cross-section examined here and cut using FIB. Re-deposition of material occurred during the etching process. Platinum (e-beam Pt) deposited as a protective layer for the FIB preparation of the cross-section. The thickness of each layer can be seen in the line plots and is expressed in nanometres.

magnetisation processes are dominated by the ADL anisotropy so that the effect of exchange bias is not as trivial as a lateral shift in the hysteresis loop, as it is typically observed in a continuous exchange biased film. The fact that both directions exhibit a net exchange bias field, may be an indication of possible misalignment between the exchange bias field direction and the axis of the ADL. This aspect will be discussed when looking at the ferromagnetic resonance results.

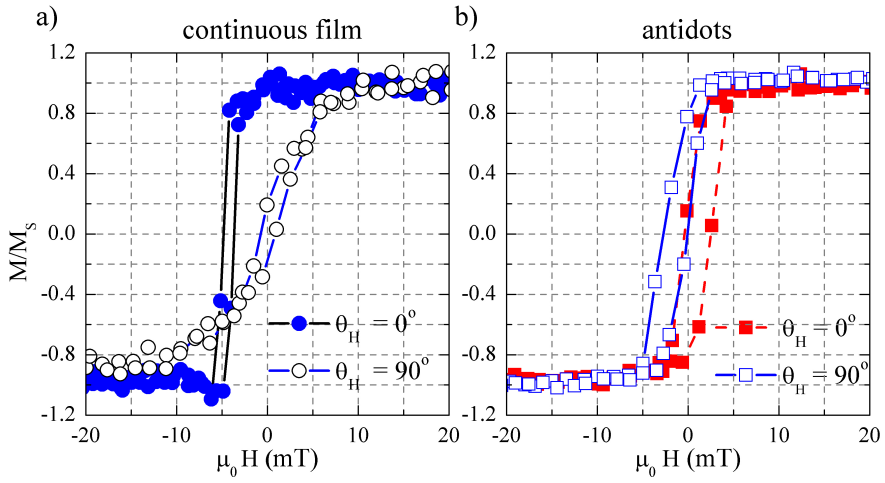

Figure 5.3: Hysteresis loops obtained from MOKE: a) continuous exchange bias film where the external field, $\mu_0 H$ was applied parallel, θ_H= 0°, and perpendicular, θ_H= 90°, to the exchange bias direction. Along θ_H= 0°, a lateral displacement of the hysteresis loop is obtained as a result of exchange bias. The hysteresis obtained for θ_H= 90° does not exhibit lateral displacement, which is consistent with the unidirectional nature of exchange bias. b) ADL where the external field was applied along the edges of the lattice. Note that for both θ_H= 0° and θ_H= 90° a lateral shift is observed, which suggests that patterning has affected exchange bias distribution. The MOKE data was provided by Prof. Gianluca Gubbiotti from the University of Perugia, Italy.

5.3 Mode structure

Broadband ferromagnetic resonance spectroscopy was performed using a vector network analyser, VNA-FMR. The sample was placed on top of a coplanar waveguide with the system operating in a 2-port configuration. Details of the VNA-FMR technique are discussed in Sec. 3.2. Each measurement was initiated well above the saturation field, at H_{REF}= 150 mT, where a reference spectrum was acquired for background correction purposes. Then, starting at a maximum applied field H_{app}=

65 mT, the VNA signal was swept, in frequency, five times and averaged to improve the signal to noise ratio; the static external field H_{app} was linearly reduced once the frequency sweep was completed. This procedure was repeated in the applied field range of H_{app}= |65mT|, with a field step of 1.2 mT. The experimental error associated with the measurement of the applied field with an Hall probe is 0.1 mT. As a final outcome, the relative variation of the scattering parameter S_{21}, as a function of frequency and field, is obtained.

Brillouin light scattering (BLS) is an optical technique which relies upon the inelastic scattering of light from spin wave excitations in magnetic systems, enabling the study of wave vector resolved spin wave dispersion [175]. The principle consists of the interaction of photons with a certain energy and momentum $(\hbar\omega_I, \hbar\vec{q}_I)$ with magnons $(\hbar\omega, \hbar\vec{q})$. The terms ω and $\vec{q}$ correspond to the frequency and wavenumber of the incident photons and magnons. The annihilation or creation of optically excited magnons can be retrieved by measuring the energy and momentum transfer of the scattered photons $\hbar\omega_S(\vec{q}_S) = \hbar(\omega_I(\vec{q}_I) \pm \omega(\vec{q}))$. In materials with modulated magnetic properties, the spin wave dispersion relation exhibits prohibited and allowed frequency bands, similarly to the case of electron scattering due to an atomic lattice or the diffraction of photons in the case of a photonic crystals.

BLS experiments were performed in the backscattering configuration using a Sandercock 3+3-type tandem Fabry-Perot interferometer in the Damon-Eshbach (DE) scattering configuration ($\vec{k} \perp \vec{H}$). A description of the DE spin wave modes was done in Sec. 2.2. The wavelength of the incident light is λ= 532 nm. Due to the photon-magnon conservation law of momentum in the scattering process, the in-plane component of the excitation wave vector (k) varies with the incidence angle of light (θ) according to $k = \frac{4\pi}{\lambda}\sin\theta_H$ where λ is the light wavelength. A static external field of 50 mT was applied in the direction parallel to the lattice edge and collinear with the exchange bias direction, coincident with $\theta_H = 0^\circ$ (see Fig. 5.1).

5.3.1 Field dependent magnetodynamics using VNA-FMR and BLS

To ensure that the magnetic properties of the films have not been affected by the temperature changes throughout the fabrication process, a comparison was made

between the ferromagnetic resonance data relative to the continuous film as-deposited (AD) and after the patterning process (AP). The results are shown in the Fig. 5.4a and 5.4b, respectively. The spectra in Fig. 5.4b were measured for a sample of continuous film which was subject to the same lithography process (resist bake, etc) as the ADL, except that it was not etched as it was protected by the hard mask. For each sample, an FMR spectra was measured along the parallel (left) and perpendicular (right) to the exchange bias direction. This data was fitted with the Kittel equation, in order to determine the exchange bias field, H_b, anisotropy, H_k, and the effective magnetisation, M_{eff}. A summary of the fitting parameters is shown in the table 5.1. As can be noted, the magnetic properties are similar for both AD and AP samples. The amplitude and direction of the exchange bias field remained unchanged. The anisotropy field amplitude, H_k, obtained from the fitting is small on both AD and AP films so the uniaxial anisotropy term can be assumed negligible.

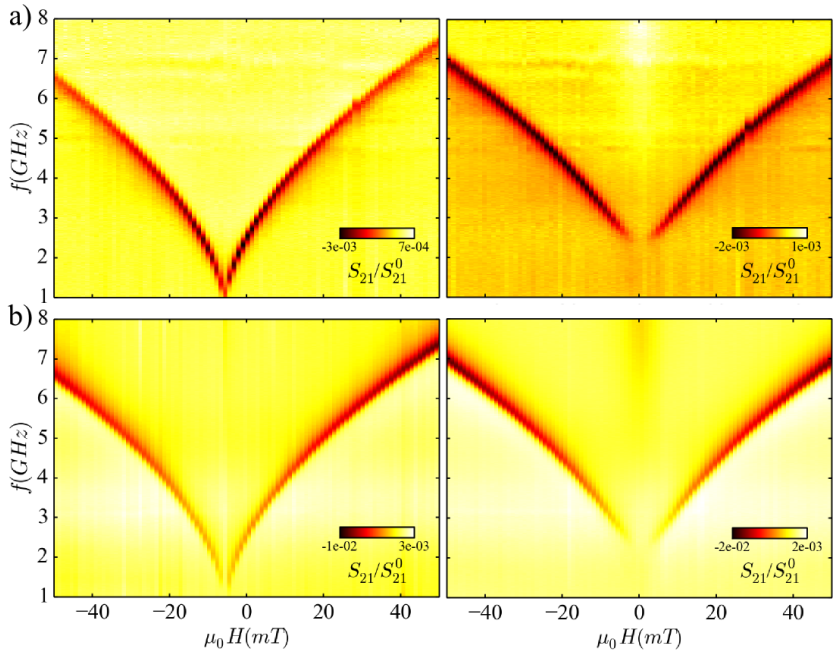

Figure 5.4: Resonance frequency versus field maps (magnitude of S_{21}) from the continuous films at the as-deposited (a) and post-patterning (b) stages. The applied field varies from the directions parallel (left) and perpendicular (right) to the exchange bias direction. The spectra in b) were measured from a sample of continuous film which was subject to the same lithography process as the ADL, except that it was not etched. Note that the FMR data on right-hand side still exhibits an exchange bias field indicating that the $\mu_0 H \perp H_b$ condition was not fully satisfied. The thin film deposition was performed by Dr. Sinead O'Reilly from Queen's University, Belfast, UK.

Sample	H_b (mT)	H_k (mT)	M_{eff} (T)
AD	5.0	1.0	1.16
AP	5.2	1.1	1.21

Table 5.1: Fitting parameters for the continuous films at the as-deposited (AD) and post-processing (AP) stages. One notes that the anisotropy field is negligible in the continuous films. Fitting errors for H_b, H_k, and M_{eff} are 0.2, 0.1 and 5 mT, respectively.

The ferromagnetic resonance spectra shown in Fig. 5.5 were obtained from the ADL, where the magnetic field is applied (approximately) parallel to the lattice edge (θ_H= 0^{c}irc) and the exchange bias direction. The full spectra contains 4 resonances and all are centered at around $\mu_0 H \sim 0$ mT. The modes are labelled as I, cf, II and III, from lower to higher frequencies. The mode 'cf' is labelled differently since its origin is related to the continuous film underneath the ADL (recall Fig. 5.1a and Fig.5.2a), due to incomplete etching of the holes. The modes I, II and III are intrinsically related to the patterned layer.

Features worth noting are the field regions at which softening of modes I and II occur. These are indicated with arrows numbered as 1 and 2, respectively. For the case where the applied field is aligned with the edges of the lattice, the magnetisation reversal undergoes a hard-axis like behaviour (see Fig. 2.3), i.e. at a certain stage of the reversal, the external field cancels the effective anisotropy. Consequently the resonance frequency drops to a minimum value, as result of the vanishing (or canted) torque along the applied field direction. When the applied field is lower than the anisotropy field, the torque is restored and the resonance frequency increases. The field region numbered as 3 highlights the overlap between the resonance mode I and the 'cf' mode. The region numbered as 4 highlights the difference in the resonance frequency of the modes 'cf' and II, as $\mu_0 H \leq 40$ mT.

One should also note the effect of exchange bias in the FMR response. This appears as a lateral displacement of the spectra and a noticeable asymmetry in resonance frequency between positive and negative applied fields. The asymmetric behaviour is result of unidirectional nature of the exchange bias field, which at positive applied fields will shift the resonance frequency downwards, whereas for negative fields the resonances are shifted upwards, raising an asymmetry noted in

the figure as Δf_R. For the case of mode I, an asymmetry of 1 GHz is obtained when evaluating the difference, in resonance frequency between, $\mu_0 H$= 20 mT and $\mu_0 H$= -20 mT. The same behaviour is observed for the resonance mode II, where the asymmetry is 0.4 GHz for $|\mu_0 H|$= 20 mT. The asymmetry is expected to be larger when $\mu_0 H \simeq H_k$, given that the exchange bias field becomes the only ordering parameter of the magnetisation.

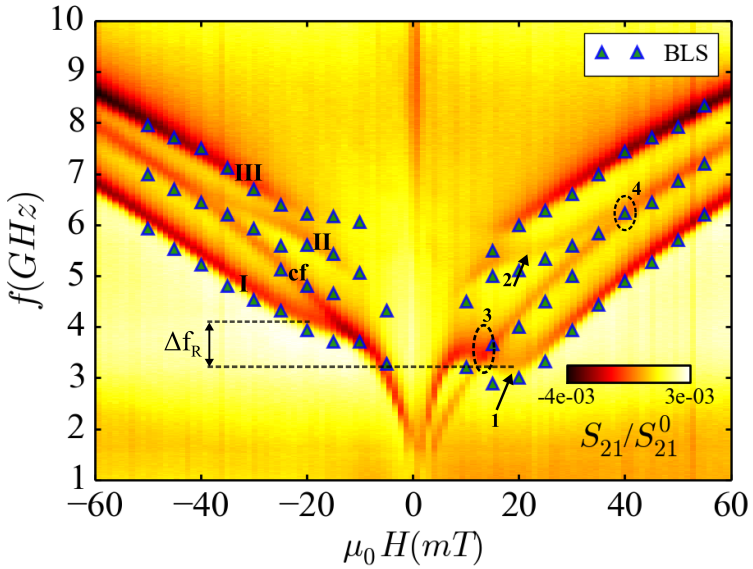

Figure 5.5: The colour plot shows the normalised magnitude of S_{21}, which represents the ferromagnetic resonance data relative to the ADL. The scatter plot shows the BLS data at $\theta_H \sim 0°$. From lower resonance frequency to higher resonance frequency four modes are labelled in the figure as I, cf, II and III. The field/frequency regions numbered from 1 to 4 highlight the softening of the modes I and II (1 and 2, respectively) and the intersection of mode 'cf' with the the modes I and II (3 and 4, respectively). The term Δf_R represents the asymmetry in frequency between the resonance at $\mu_0 H$= 20 mT and $\mu_0 H$= 20 mT.

Field dependent BLS measurements are also shown in Fig. 5.5. Note the good agreement with the FMR data. The small deviations between the FMR and BLS data can have origin in a possible misalignment of the sample relative to θ= 0° or an uncertainty associated with the measurement of the frequency shifts in the BLS experiments. The wavevector dispersion studied using BLS is discussed in the following section.

5.3.2 Spin wave dispersion using BLS

Figure 5.6 shows the wavevector dispersion relation of the ADL and the continuous film. The largest wave number measured was $k_{max} = 2.6(\pi/a)$, with a being the hole spacing (420 nm), which, in the reciprocal space corresponds to a wave vector just above the second Brillouin zone (BZ). At normal incidence (k= 0) the modes agree well with the resonance peaks obtained from the FMR experiments. Similarly to the FMR results, at k= 0 the resonance mode relative to the continuous film, cf, overlaps with mode II from the ADL.

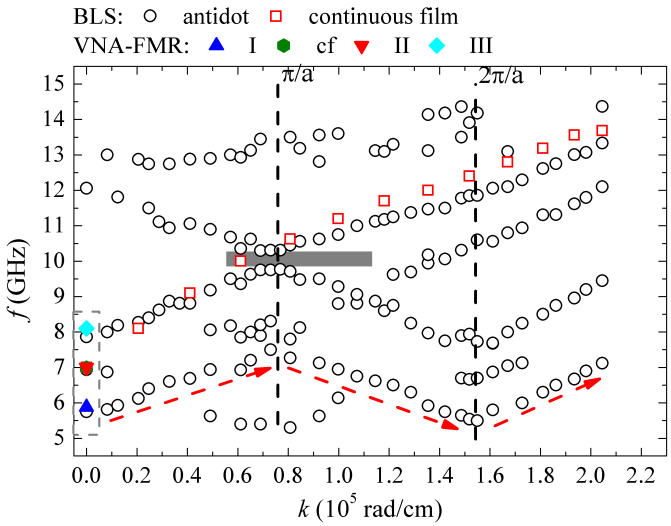

Figure 5.6: Brillouin Light scattering measurements at $\mu_0 H$= 50 mT and θ_H= 0^{c}irc. For the wave number k= 0 the BLS matches the FMR data f= 5.7 GHz, 6.97 GHz, 7.83 GHz, 12.01 GHz. Wave vector of the excitation is perpendicular to the applied field direction (DE modes). The shaded region highlights the frequency bandgap obtained, which is result of repulse spin wave interactions due to Bragg scattering. The dashed arrows highlights the periodicity of the ADL. The BLS data was obtained by Prof. Gianluca Gubbiotti from the University of Perugia, Italy.

Note the existence of a forbidden bandgap (BG) of 0.6 GHz at k= 0.77×10^5 radcm^{-1} (π/a), located at the boundary of the 1st BZ. The emergence of a BG is evidence of repulsive interactions due to Bragg scattering of spin wave modes. Experimental evidence for Bragg scattering of spin waves was first demonstrated in Ref. [54] for the case of simple 2-D nano-structures. In Ref. [52] the spin wave dispersion for a type of bi-component ADL demonstrated the emergence of a BG. The results here presented show that the formation of BG is also possible in the

current geometry. The periodicity of the lattice is reflected in the BLS data, as can be seen by following the frequency variation of the modes highlighted by the red dashed arrows.

The spin wave dispersion of the ADL was simulated using Mumax. The structure was comprised of 24 unit cells (420 nm $\times$ 420 nm) along the wavevector propagation direction and 1 unit cell along the applied field direction. The long propagation distance is necessary to obtain well resolved spectra in the Fourier domain as Δk is inversely proportional to the propagation length. Boundary conditions were applied along the direction of the applied field so that the finite length of the ADL along the field direction does not affect the results. The symmetry of the excitation corresponds to the DE configuration used in the BLS experiments. The sample was discretised along the out of plane direction, using Δz= 5 nm as cell size, to account for the variations in thickness at the hole sites, t_h. The magnetic system was excited with a temporally and spatially modulated field pulse. The time and space profile was defined as $\sin(\omega_{cut}t)/\omega_{cut}t$ and $\sin(k_{cut}x)/k_{cut}x$, respectively. As expected the calculated spin wave dispersion reflected the periodicity of the lattice. The results are not shown here since only a general agreement between the simulations and the BLS data was obtained. In order to enhance the results, several aspects must be considered: 1) the discretisation unit along the out-of-plane direction, should be of the order of $\Delta z \sim 2$ nm, so that magnetostatic and exchange interactions can be accounted appropriately. Computationally, this is hard to achieve given the overall size of the simulated structure; 2) the excitation pulse requires further optimization, in order to ensure that the wavevectors in the range of interest are evenly excited; and finally 3) data processing must be done in such a way that averaging over the film thickness is considered.

5.3.3 Angular dependence of FMR and magnetic anisotropies

In-plane angular dependent FMR measurements were performed in order to evaluate the anisotropic behaviour of the resonance modes. In the angles between θ_H= $[0°, 190°]$ the FMR spectra was acquired every 10°, except when around the directions $[0°, 45°, 90°]$ where the step was reduced to 5°. Representative spectra are

shown in Fig. 5.7. On all spectra shown, the dashed lines represent the fit to each resonance mode using a Kittel-like equation shown in Eq. 5.1b and plotted here only as a guide for the angular dependence. The softening of the different modes can be noted, as well as the dependence with external field direction relative to the ADL. Mode softening is observed when the magnitude of the applied magnetic field, along a certain direction, is sufficient to balance the internal fields of the magnetic material. When this condition is reached, the net magnetic moment parallel to the applied field direction is largely reduced, and the torque vanishes. The internal fields account for the anisotropy field due to the patterning, H_k, and the effect of the exchange bias field, H_b.

The data relative to θ_H= 10° shown in Fig. 5.7 is used to demonstrate the existence of two softening regions in field. At $\mu_0 H$= -17 mT the decrease in resonance frequency of mode I is associated with the balance between the external field and the effective anisotropy which is result of the competing shape anisotropy and exchange bias. The difference in behaviour for $\mu_0 H = \pm 17$ mT is associated with exchange bias which for positive fields, counts as a positive contribution to the anisotropy, and for negative fields, counts as a negative contribution. At $\mu_0 H \sim 0$ mT the magnetisation undergoes the reversal process, which is understood as mode softening followed by complete reversal of the magnetisation via rotation of domains. Similar behaviour is observed when the applied field is set along, for example, θ_H= 20° and 30°. In these spectra, the resonance frequency of mode I is higher, when compared to θ_H= 0°, and the directions $\theta_H = 20° - 30°$ is associated with an easy-axis behaviour as opposed to the directions θ_H= 0°, 45°, 90° where a hard-axis behaviour is observed.

In Fig. 5.7, at angles corresponding to θ_H= 45° and θ_H= 50° two sets of symbols were added (square and circular) to highlight two frequency modes which appear in the angular range of $\theta_H = [30° - 60°, 120° - 160°]$, within the frequency and field range marked with the dashed grey boxes. To aid the discussion, these two modes are shown in more detail in Fig. 5.8. The two low amplitude modes appearing in the frequency region between 7-10 GHz show an interesting behaviour: On each spectrum, blue and green dashed lines were added so that the resonance modes are more easily followed. Note that the mode marked with the blue line is moving upwards, whereas the mode marked with the green line is moving downwards with

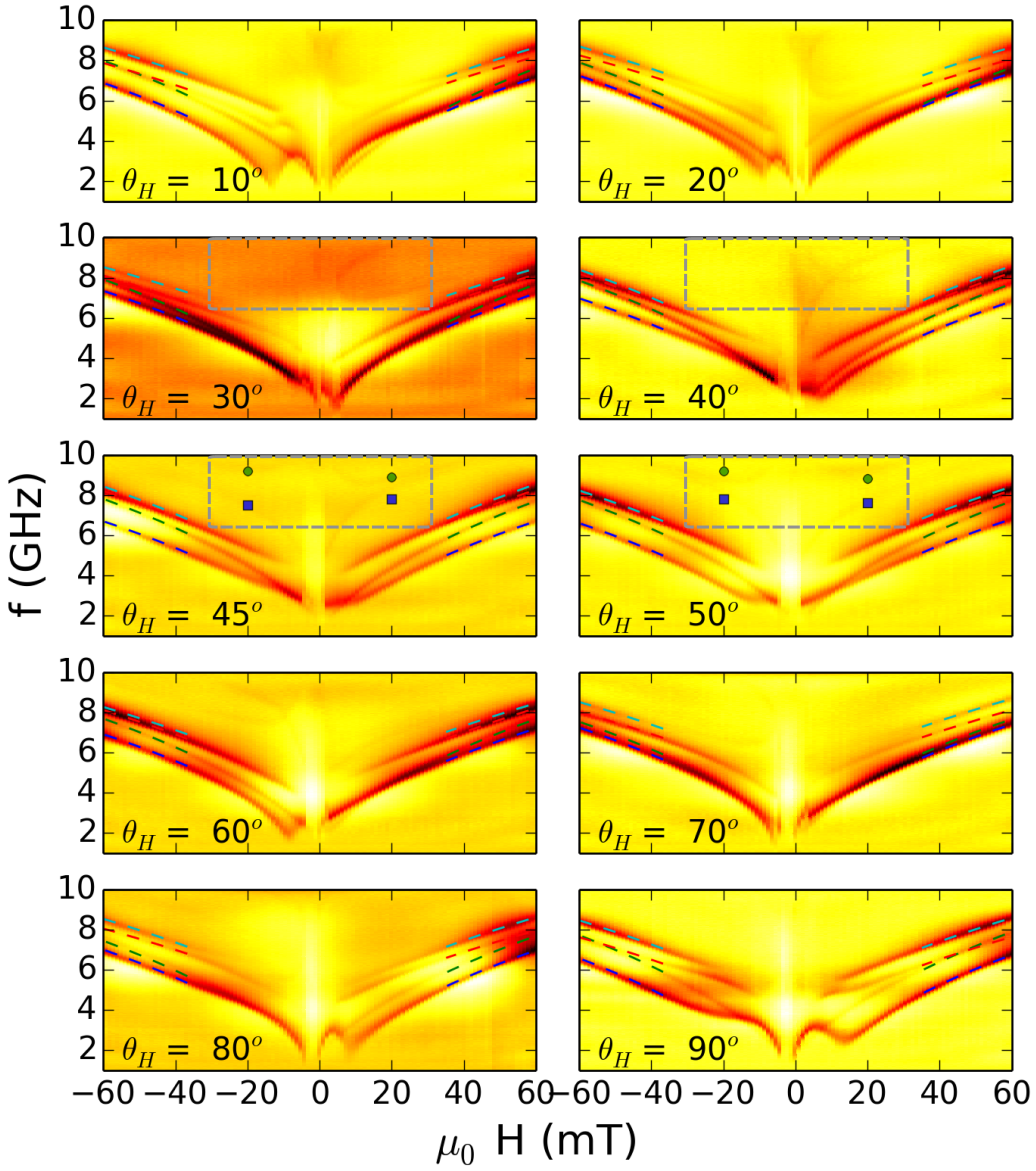

Figure 5.7: Normalised magnitude of S_{21} representing the ferromagnetic resonance data at different applied field angles, θ_H. Each resonance mode was fitted with a Kittel like equation and the fitting results are shown by the different dashed lines. One can observe the softening of some resonance modes, in particular the modes at lower frequencies. The gray dashed rectangle highlights high frequency modes which appear only at certain angles. These modes have low signal to noise and are also labelled with square and circular symbols in the spectra relative to θ_H= [30° − 50°].

increasing the applied field angle. The ascending movement of the mode marked with a blue line may be seen as the continuation of the mode III. Instead of considering that mode III remains in the same frequency range as mode II, as suggested in Fig. 5.7, our interpretation is that mode III undergoes an increase in resonance frequency,

whose movement is given by the blue line. The green line moving downwards in resonance frequency, as a function of the applied field angle, may be related to the high frequency mode observed in the BLS spectra (Fig. 5.6). At θ_H= 0° this mode is expected to exist at high frequencies, which in principle could coincide with the mode at 12.01 GHz observed in the BLS measurements. The fact that these two modes change rapidly with θ_H suggests great sensitivity to the anisotropy of the patterned structure. The limited sensitivity of the FMR apparatus constrained the observations at high frequency. Nevertheless, additional modes are identified, which appear to shift significantly in resonance frequency with varying θ_H.

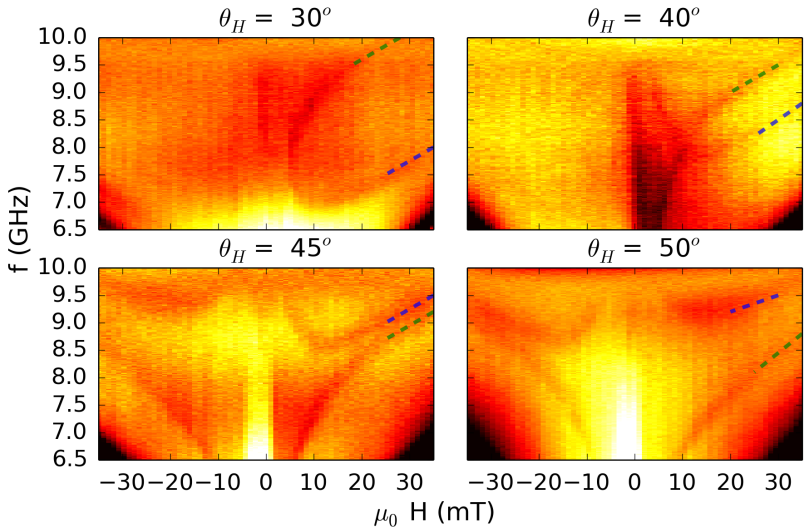

Figure 5.8: Resonance modes with low amplitude in the high frequency regions. These correspond to sections of the spectra in Fig. 5.7 but with improved contrast.

A detailed description of the anisotropies of different resonance modes is shown in Fig. 5.9, which was constructed by performing a multi-peak fit over the field range of $|\mu_0 H| > 35$ mT, thus considering only the saturated states. The fittings were performed on the derivative of the signal so a derivative of the Lorentzian function was used to fit each resonance line, with an average R^2 of 0.88± 0.04. At each angle, the data was fitted with four resonance lines, as illustrated in Fig. 5.7 by the four dashed lines, allowing the assessment of the anisotropy field, the exchange bias field and the effective magnetisation, following a general Kittel formula, Eq. 5.1a, discussed in Sec. 2.1. The fact that $\mu_0 M \gg \mid H + H_b \mid + H_k$ leads to the

approximation shown in Eq.5.1b.

$$f^2 = \gamma^2(\mid H + H_b \mid + H_k)(\mid H + H_b \mid + H_k + \mu_0 M) \tag{5.1a}$$

$$f^2(\theta) \approx \gamma^2(\mid H + H_b \mid + H_k)(\mu_0 M) \tag{5.1b}$$

The anisotropy field as function of angle, $H_k(\theta_H)$, obtained from fitting the data with

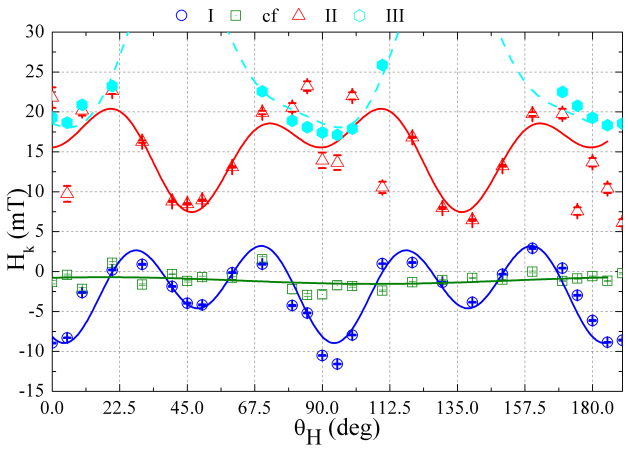

Figure 5.9: Angular variation of the anisotropy fields obtained by fitting the experimental data to Eq. 5.1b. The continuous lines represent a fit to the proposed model for the anisotropy, shown in Eq. 5.2a. The dashed line is in agreement with the description of mode III, which suggests that between $\theta_H = 22.5° - 67.5°$ the resonance frequency of this mode goes above the measurement window. The variation in anisotropy follows the vertical displacement of the resonance of each mode.

Eq. 5.1b, is plotted in Fig. 5.9. The results suggest the presence of an apparent 8-fold anisotropy, combined with a four-fold symmetry term. The solid lines represent a fit to the Eq.5.2a, which accounts for an offset constant, H_k^0, a 8- and 4-fold anisotropy constants, which are labelled as $H_k^{'}$ and $H_k^{''}$, respectively[1].

$$H_k(\theta_H) = H_k^0 + H_k^{'} cos^2(2(\theta_H + \theta_0)) + H_k^{''} cos^2(4(\theta_H + \theta_0)) \tag{5.2a}$$

$$H_b(\theta_H) = H_b^0 + H_b^1 cos(\theta_H + \theta_0) \tag{5.2b}$$

Figure 5.10 shows the angular variation of the exchange bias field (H_b), for all the modes. The continuous lines represent a fit to Eq. 5.2. It is important to

[1]Uniaxial field component was not considered given the results obtained for the thin film configuration discussed in section 5.3.1

note that the angular dependence of the mode 'cf' is in agreement with the angular variation of a continuous exchange biased film [32], as will be demonstrated later using micromagnetic simulations (Fig.5.11 for t_h= 20 nm). The behaviour of mode I illustrates an interesting property of this magnetic system. The combined anisotropies give rise to a non-uniform variation of the exchange bias field, with regards to the applied field direction, which could possibly enable the use of such systems as enhanced tunable microwave filtering devices. This aspect will be discussed later in Sec. 5.4.2. The angular variation of the modes II and III is rather complicated to follow, given the strong dependence on the anisotropy and mode behaviour itself. It is therefore a challenging task to extrapolate information regarding the exchange bias.

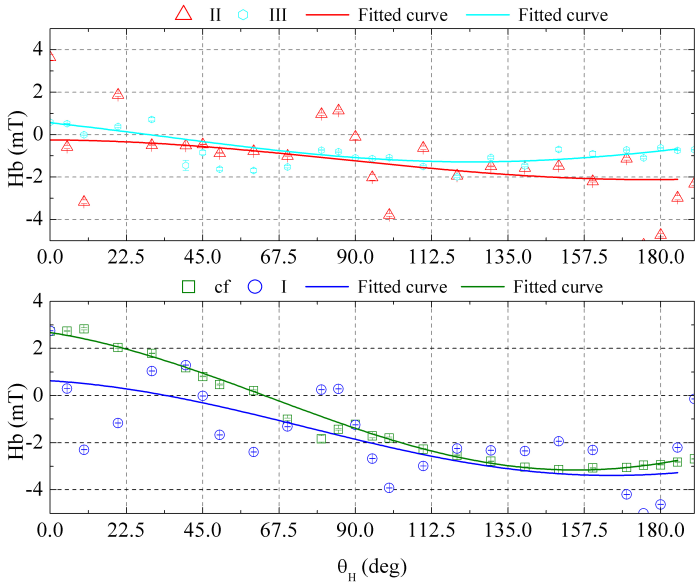

Figure 5.10: Angular variation of the exchange bias field of mode the resonance modes obtained by fitting the experimental data to 5.1b. The variation of exchange bias field follows the lateral displacement of the resonance spectra.

Table 5.2 gathers the fitting terms for the values of $H_k(\theta_H)$ and $H_b(\theta_H)$ described in Eqs. 5.2a and b. A fitting parameter, θ_0, was added to account for: a) misalignment between the exchange bias axis and the edges of the ADL and b) experimental error in measuring the rotation angle. A small offset angle can be observed in Fig. 5.9 and 5.10 as a lateral displacement of the local minima/maxima with respect to the main directions, θ_H= 0°, 90°.

In previous reports of antidot systems, the diagonal of the lattice is assumed to be

Mode	H_b^0 (mT)	H_b^1 (mT)	H_k^0 (mT)	H_k' (mT)	H_k'' (mT)	M_{eff} (T)
I	-1.6 ±0.5	1.8 ±0.4	-8.9 ±0.6	-4.5 ±1.0	8.6 ±1.1	1.1
cf	0.05 ±0.02	3.5 ±0.1	-1.7 ±0.4	-1.0 ±0.7	–	1.3
II	-1.7 ±0.6	2.4 ±0.6	7.4 ±1.3	-7.2 ±1.3	-7.6 ±1.6	1.1
III	-0.1 ±0.08	1.17 ±0.25	13.6 ±3.2	22.1 ±5.1	5.6 ±1.2	1.2

Table 5.2: Fitting parameters for the anisotropy, exchange bias field and effective magnetisation of the ADL obtained for each of the resonance modes analysed. The fitting errors are of the same order in all resonances. Fitting error obtained for M_{eff} is $\pm 10^{-3}$ T.

the easy axis. However, in this sample it is observed that this direction corresponds to a hard-axis like behaviour. Given the previous reports and based on the cross-sectional analysis, it is understood that the difference in anisotropic behaviour can be attributed to modifications in the nearest and next-nearest neighbouring holes, as a result of having partially etched NiFe/FeMn ADL. Moreover, in addition to the partial etch of the holes, the material remaining in the holes is not exchange biased, as the FeMn has been removed from its surface. The periodic modulation of the exchange bias, the etching depth and the possibility of contamination in the holes, could have also affected the microwave properties of the system. The NiFe present in the holes represents approximately 30% of the total volume of the unit cell. With this is mind, a comparative study was performed with Mumax, covering four different layer configurations.

5.4 Partial patterning and mode analysis

5.4.1 Partial patterning

To understand the origin of the unusual anisotropic behaviour, micromagnetic simulations were performed using Mumax. In this study, the magnetic properties, the hole size and the periodicity of the holes were kept constant, whilst varying the thickness of the magnetic material in the holes, t_h. Details on the simulation tool and the data processing are discussed in appendix Sec. B. The FMR spectra as function of the applied field angle (θ_H) as well as the mode profiles were obtained

from the simulations. The spatial profiles of the resonance modes were obtained at a fixed magnetic field magnitude of 50 mT and a fixed exchange bias field with magnitude of 5 mT, set at θ_b= 11.25° in respect to the lattice edge. All spectra were obtained by performing a Fourier analysis of the time dependent out-of-plane component of the magnetisation, $m_z(t)$, after applying a spatially uniform pulse in the form of $A_0 \sin(t-t_0)/(2\pi t)$, where A_0= 1 mT and t_0= 3 ns. To obtain the spatial distribution of the precession modes at fixed applied field, a time domain Fourier analysis of the magnetisation component $m_z(x, y, t)$ was performed. Functions in the form of $\sin(t)/t$ are preferred as in the Fourier domain, these possess an uniform and well defined excitation bandwidth.

The angular variation of the resonance modes is summarized in the Fig. 5.11 for: a) A fully etched antidot geometry; b) a partially etched antidot geometry where the thickness of the magnetic layer in the hole is t_h= 5 nm, ; c) where t_h= 10 nm and d) where t_h= 20 nm, resembling a continuous film. To comply with the variation of the exchange bias field, the pinning field (H_b) was only applied in the antidot regions. In Fig.5.11a, the high frequency resonance modes appear labelled as HF (10.8 - 14 GHz), the intermediate frequencies as IF (5.0 - 10.5 GHz) and the lowest frequency modes as LF (1.5 - 4.8 GHz). At this stage, the intention is to describe the general behaviour of the resonance modes, so that a decision can be made on which configuration best represents the experimental data.

When comparing the results of the Fig. 5.11 a,b, c and d, it is observed that the modes in the HF band become weaker with an increase in t_h. The frequency range of the IF modes becomes narrower while the IF mode amplitude becomes dominant with increasing t_h. More importantly, a change in symmetry of the angular variation is observed, with increasing t_h. For $t_h = 0$ nm the resonance frequencies in the IF range reach a maximum at θ_H= 45°, whereas for t_h= 10 nm, this angle corresponds to a local minimum. The frequencies of the modes LF move upwards as t_h increases, moving towards the IF range. For the limiting case of t_h= 20 nm all resonances should collapse to a single mode in the IF range, resembling the FMR response of a continuous exchange biased film, as observed in the Fig. 5.10 for the mode 'cf'. Interestingly, the modulation of the exchange bias field itself (without the thickness modulation) did not produce any effect on the response of the system.

In terms of anisotropy, the HF modes appear to have a 4-fold symmetry shifted by 45 degrees with respect to the 4-fold symmetry observed in the IF range. This is important to note as a similar trend is observed in the experimental data.

The most relevant feature of the simulations is the variation in the anisotropy of the intermediate resonance modes. In the antidot configuration, t_h= 0 nm, a clear 4-fold symmetry is obtained, however, when looking at the angular dependence for t_h= 5 nm (black dashed line) and t_h= 10 nm, a certain transition between 4-fold and 8-fold is observed, i.e. the flattening of the frequency response around θ= 45°. The observation of this transition in the simulations is consistent with that of the experimental data, where an 8-fold symmetry is observed for mode I (Fig. 5.9). One notes that when t_h= 10 nm the symmetry of the IF modes exhibits a 4-fold dependence (following the dashed lines). Alternatively, one may consider that in the case of t_h= 10 nm, the LF mode appears to exhibit an 8-fold symmetry. The LF mode is associated with the precession amplitude located at the edges of the ADL. Experimentally, this mode may be hard to detect since interface roughness smears the FMR signal.

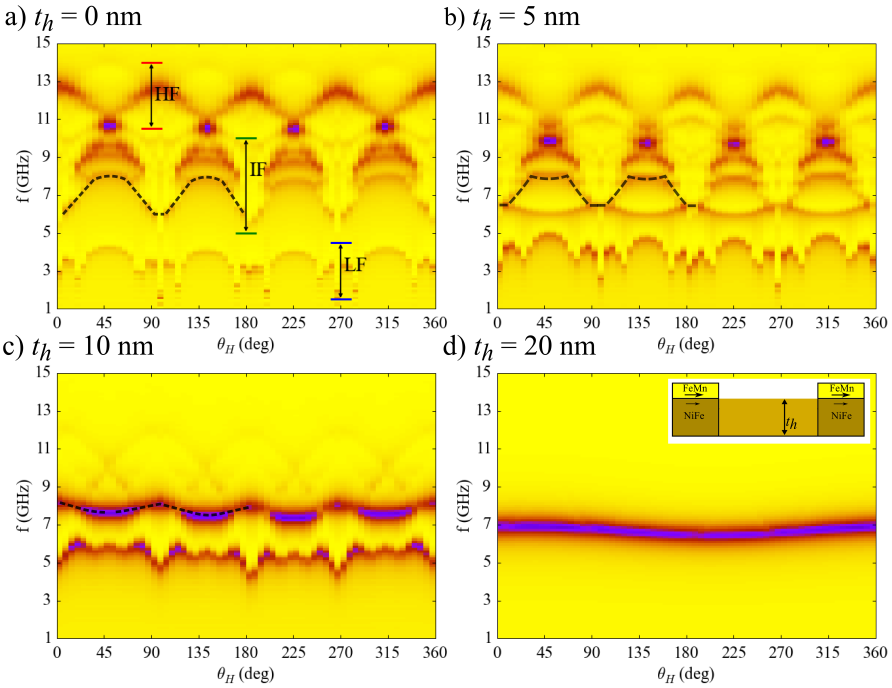

Figure 5.11: Angular variation of the calculated FMR spectra for t_h= 0, 5, 10, 20 nm. The high, intermediate and low frequency regions are labelled as HF, IF and LF, respectively. Note the black dashed line for t_h= 0, 5 and 10 nm. The angular variation suggests a change in the symmetry to an 8-fold like dependence of the IF modes when t_h= 5 nm. Despite the fact that the LF mode for t_h= 10 nm exhibits an 8-fold dependence it is unlikely that this mode was experimentally detected given that the Mumax simulations revealed that the LF mode is an edge mode. Magnetic parameters used in the Mumax simulations: M_S= 1 T, A_{ex}= 1.3e^{-}12 J/m and α= 0.02.

5.4.2 Origin of the dynamic modes

In general, the precessional modes in the ADL result from a localisation of the precessional amplitudes due to the highly non-uniform demagnetisation fields which are ultimately related to the pole distribution around the edges of the holes [54, 87].

Figure 5.12 shows the angular dependent FMR spectra (a) and the spatial distribution of the resonance modes obtained at θ_H= 0°, 22.5° and 45°, which are labelled with red, green and blue dashed lines. Each of the line profiles contains a number of resonance peaks, which are associated with the corresponding mode profiles shown in Fig. 5.12b, c and d. The precession amplitudes are colour coded in the images.

The spectra corresponding to θ_H= 0°, 22.5° and 45° contain 8, 8 and 6 modes, respectively. The eigenmodes are indexed in ascending order from 0 to 7, and the corresponding frequency is noted in the respective mode profile. The resonance modes can be characterized by the amplitude distribution, number of nodes and orientation relative to the applied field. Throughout the discussion, the modes are labelled based on the applied field angle and mode number, following the nomenclature: θ_H-[mode number].

The modes 0°-[0,1], 22.5°-0 and 45°-0 occur at low frequencies and are highly dependent on the shape of the holes. This can be observed as the largest amplitude variation is localised at the hole edges, within the unit cell of the antidot geometry. These are commonly designated as edge or localised modes [102]. As can be noted from the amplitude distribution, the localised modes extend from one hole edge to the nearest neighbour (NN) or next nearest neighbour (NNN), which suggests that within the unit cell, the localised modes are coupled via dipolar and exchange interactions. These modes are mainly confined to the antidot region, i.e. outside the holes, and it is observed that the largest precession amplitude occurs either at the hole edges or at the inter-hole spacing. With varying θ_H, the density of poles rotates around the edges of the holes and therefore the localisation of the modes varies. The fact that $\theta_H \neq \theta_b$ induces a canting of the magnetisation with respect to the external field direction ($\theta_M \neq \theta_H$) and raises an asymmetric distribution of the poles. This is in part the reason why the amplitude profiles extend up to the NN and NNN, even at θ_H= 0°.

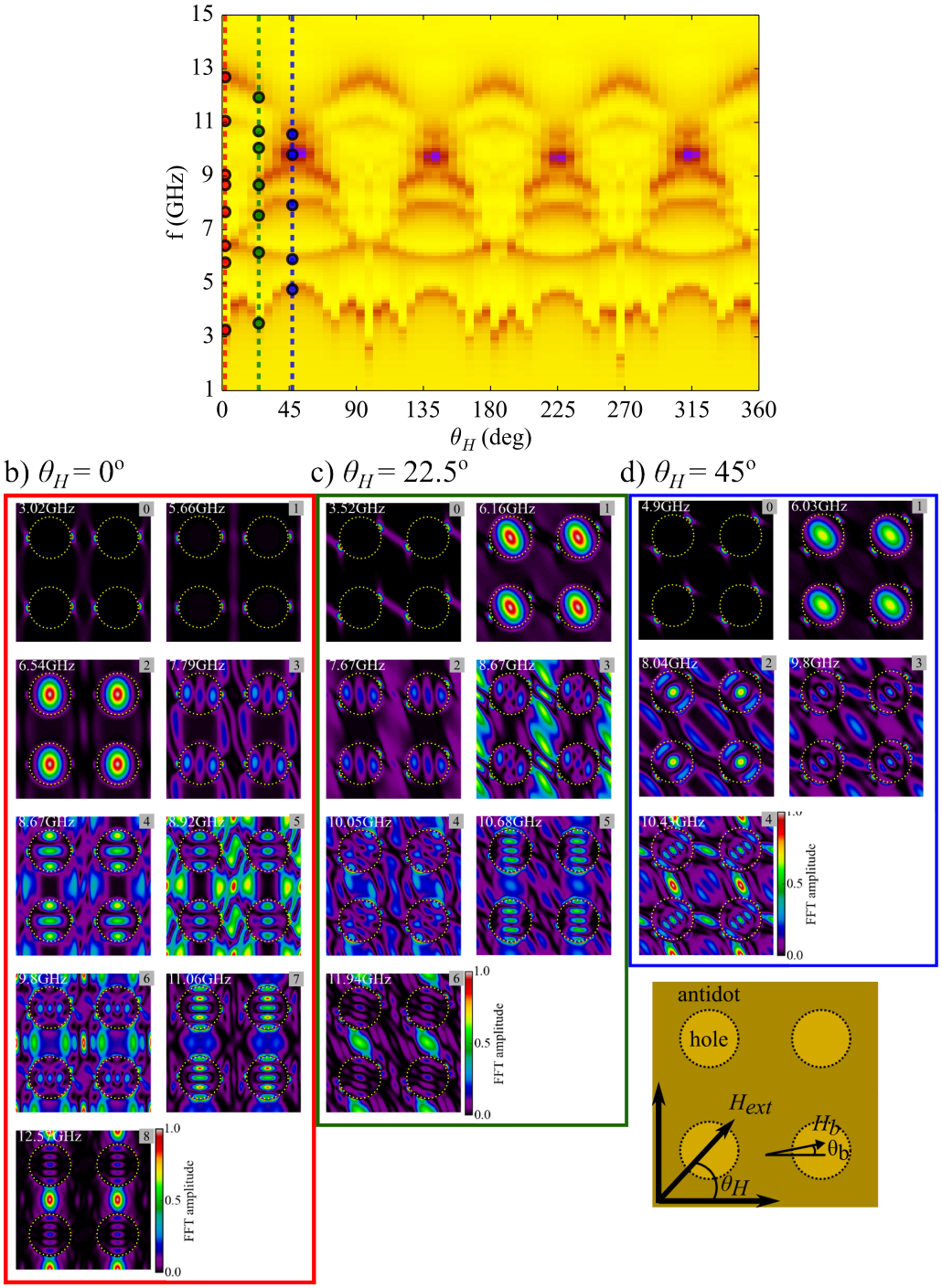

Figure 5.12: a) Simulated angular variation of the resonance modes of the ADL for t_h= 5 nm. b), c) and d) Precession amplitudes at θ_H= 0°, 22.5°, 45°, respectively. The exchange bias field direction was kept fixed, at θ_b= 11.25°. The inset illustrates the simulated geometry which appears subdivided in antidot and hole regions. Boundary conditions were employed in Mumax to ensure that the finite size of the system did not affect the results.

The modes $0° - 2$, $22.5° - 1$ and $45° - 1$ are predominantly localised in the region inside the holes, as seen from the relative large amplitude of these modes, compared to the antidot region. Still, there is some degree of coupling to the antidot region, as the profile also extends beyond the holes. Such modes are only observed in hybrid structures, whereby modes in the hole region merge with modes in the antidot structure. The hybrid behaviour is more pronounced in 0°-3, 22.5°-2, 45°-3, where the precession amplitude appears more evenly distributed across the whole structure. The modes contain three amplitude nodes in the hole region and two predominant nodes in the antidot region. Because of the applied field angle, the mode 0°-3 extends to NN whereas the modes 22.5°-2, 45°-3 extend further to the NNN.

The modes $0° - 4$ and $0° - 5$ have a similar amplitude distribution, with the main difference being the localisation of the amplitude maximum. In the mode $0° - 4$ the maximum is located in the holes, whereas in the mode $0° - 5$, the amplitude maximum is located in the antidot region. There is also a slight difference in the shape of the amplitude nodes, which is likely to contribute to the offset in resonance frequency, from 8.67 GHz to 8.92 GHz, between both modes.

By comparing the mode $0° - 3$ to the modes $0° - [4, 5]$, a change in symmetry of the amplitude distribution in hole regions is observed. In mode $0° - 3$ the amplitude profile is elongated vertically, and thus perpendicular to the applied field direction, while the elongation in the profile of the modes $0° - [4, 5]$ is parallel to the applied field. Interestingly, the amplitude profile of mode $0° - 6$ returns to the perpendicular orientation, relative to the external field. The elongation of the modes $0° - [7, 8]$ is once again parallel to the applied field, with the only noticeable difference being the increase in number of nodes. In the antidot region, the modes are dominated by the NN and NNN interactions, where no significant changes to the symmetry of the amplitude profiles are observed.

Despite the complexity of the spectra we note that in general the mode profiles at $\theta_H = 0°$ evolve to those observed for θ_H= 22.5° and 45°, given that the symmetry mode rotates with external field. A direct comparison between the modes observed at θ_H= 0°, 22.5° and 45° can hardly be established, especially at high frequencies where the modes are constituted by many nodes and a complex amplitude distribution. Some modes, for example the modes 0, 1 and 2 keep their profile even if the field

rotates. On the other hand, the modes $22.5° - 2, 3$ and $45° - 3$ do not seem to have a unique counterpart at 0°. In fact, it appears as if the modes $0° - 4, 5, 6$ merge to form $22.5° - 3, 4$ which in turn evolve to mode $45° - 3$. Similarly, the modes $0° - 7, 8$ evolve to $22.5° - 5, 6$, which then merges to $45° - 4$.

5.5 Asymmetry

In section II, the anisotropic and biased magnetodynamic response of the ADL was discussed. It was noted that $H_b(\theta_H)$ is not trivial in the sense that it does not follow the $\cos(\theta_H)$ behaviour of Eq. 5.2b, which is normally obtained in a continuous exchange biased film. This can be seen by comparing $H_b(\theta_H)$ in Fig. 5.10 with the corresponding fitted lines. All resonance modes exhibit an oscillatory behaviour different to $cos(\theta_H)$, with exception of mode 'cf' where the fitted function agrees well with the data. In mode I the oscillation of $H_b(\theta_H)$ is more pronounced, with the largest exchange bias field amplitude obtained at $\theta_H = -10°, 10°, 80°\text{and}100°$, where $\Delta Hb \approx \pm$ 2 mT (Fig. 5.10). The direction relative to $\theta_H = -10°\text{and}10°$ were considered in particular as they produced the largest exchange bias field shifts. In general, for $H_{ext} > 0$, the exchange bias field acts as positive contribution to the resonances, while for $H_{ext} < 0$, it acts as a negative contribution to the resonance frequency. Moreover, as the exchange bias field is in competition with the 8-fold anisotropy, the result is that the exchange bias field will have positive polarity for $\theta_H = 10°$ and negative polarity at $\theta_H = -10°$. At $\theta_H = 0°$, the effect of the exchange bias field is not observable, mainly because the spin configuration is dominated by the anisotropy of the lattice. By combining the anisotropy of the ADL and the exchange bias one adds a degree of tuning to the resonance frequencies, whereby positive and negative frequency shifts are obtained by small variation in the applied field angle.

Figure 5.13 shows the asymmetry (Δf_R) in resonance frequency between $\mu_0 H_{ext}$ = 20 mT and $\mu_0 H_{ext}$ = -20 mT, as function of θ_H, as illustrated in Fig. 5.5. The applied field section $\mu_0 H = |20|$ mT represents a good approximation to the anisotropy field associated with ADL, given that the softening of the mode I occurs in this field range ($H_k \sim \mu_0 H$). The magnetic configuration at this applied field will

be highly non-linear at certain angles due to the proximity to the hard-axis of the ADL, for example at $\theta_H = \pm 10°$. The asymmetric response is primarily caused by the presence of the exchange bias which, at positive fields shifts resonances upwards, and at negative fields shifts the resonances downwards. The dependence observed in Fig. 5.13 indicates that even though the asymmetry is due to bias, its angular variation is result of the competing anisotropies given the 8-fold oscillation in the asymmetry. The change in polarity for $\theta_H = -10°$ and $\theta_H = 10°$ can be understood from the perspective of the spin configuration and the offset angle between the exchange bias field direction and the ADL edges. As illustrated in the inset of Fig. 5.13, at $\theta_H = 10°$, the y component of the exchange bias field (Hb_y) is projected along the axis of the ADL as a positive field contribution. When $\theta_H = -10°$, the exchange bias field is projected as a negative field, possibly due to the reversibility of the exchange bias field direction. This field component is particularly relevant in the vicinity of the hard direction, due to the softening of the magnetisation. The micromagnetic simulations do not exhibit this change in polarity, as can be understood by comparing the spectra at $\theta_H = 10°$ and $\theta_H = 350°$, suggesting that by simply defining the exchange bias field as a uniform pinning field may be an incomplete approach to the problem of exchange bias in patterned structures, as local deformation of spin texture of the antiferromagnet may occur.

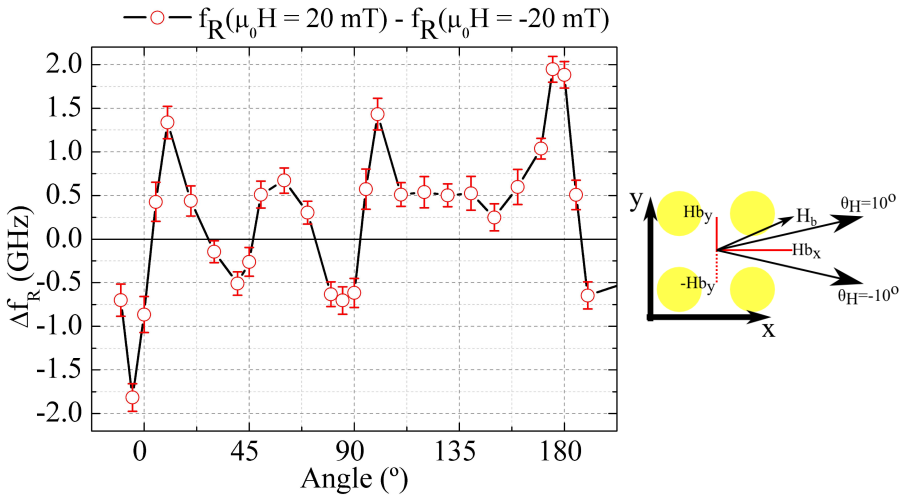

Figure 5.13: Angular variation of the frequency asymmetry of mode I, Δf_R, measured as the difference in resonance frequency between $\mu_0 H = 20$ mT and $\mu_0 H = -20$ mT. The oscillatory behaviour of Δf_R follows the trend of $H_b(\theta_H)$ shown in Fig 5.10.

The asymmetry appears to have different behaviour in the angle range $\theta_H =$

[112.5° : 135°], possibly due to non-uniformities in the switching process of the magnetisation, caused by pinning sites.

5.6 Conclusions

Magnetodynamic studies on the exchange biased bi-component structure, i.e. an ADL adjacent to a continuous layer, has revealed a number of magnetostatic spin wave modes with origin in the enhanced dipole field distribution at the hole interfaces. The VNA-FMR studies have demonstrated that the ADL structuring combined with exchange bias results in further modifications to the microwave response. The presence of exchange bias allows to engineer the microwave properties, in particular to enable an asymmetric response of the multiple resonance modes with regards to the applied field and lattice direction. An 8-fold and 4-fold anisotropy components were obtained from the angular dependence of the resonance modes, which is attributed to the nearest and next-nearest neighbour interactions. The change in unidirectional behaviour of the exchange bias is likely to result from modifications in the reversal process due to patterning.

Micromagnetic simulations revealed a change in symmetry on the resonance modes, due to changes in the thickness of the film in the hole regions. The modelling carried out with Mumax lead to an understanding of the degree to which the magnetic properties have been affected by the etching of the holes. Further optimization would be required in order to obtain a quantitative match between the experimental data and the simulation results. Despite the fact that the TEM cross-sectional analysis shows that the remaining NiFe layer in the holes was 14.5 nm in thickness, the comparison between the FMR data and the simulated spectra indicates that realistically, only 5 to 10 nm of NiFe contributes to the ferromagnetic layer. Modification of the magnetic properties at the hole sites, due to contaminations, may have also affected the anisotropy properties of the ADL.

The field dependent BLS results are in good agreement with the VNA-FMR data. Furthermore, the BLS results reflect the periodicity of the ADL, as well as the emergence of a frequency band gap at the wave number corresponding to the 1st Brillouin zone.

Chapter 6

3-D nanostructures: Lorentz DPC and VNA-FMR studies on bi-layered antidots

The previous chapters demonstrated the effect of demagnetisation fields in single exchange biased layers of antidots. This chapter is dedicated to the study of a highly configurable three dimensional magnetic structures, in which two films, one exchange biased and one unbiased, are stacked upon one another and patterned with an antidot geometry. The exchange bias on the bottom film allows for pinning of its magnetisation while the free layer reverses, allowing for parallel and anti-parallel configurations. The magneto-static properties of the stacked structure are studied via high resolution differential phase contrast Lorentz transmission electron microscopy, to understand how the transition from parallel to anti-parallel occurs, with focus on the interlayer dipolar effects. Interestingly, it was also observed that the stacked structure allows for the emergence of stable magnetic vortices, whilst a single layer does not exhibit this feature. These experiments were carried out using the TEM in-situ two port VNA-FMR rod, described in Sec. 3.3.2, so it was possible to obtain an immediate assessment of the microwave properties of the whole sample. In this case, it was useful to confirm the anti-parallel configuration, as the net FMR response is much reduced.

The magnetodynamic properties of a bi-layer structure, equivalent to the one studied with Lorentz microscopy, is investigated using VNA-FMR, in order to study

the effect of the cancelling demagnetisation fields in the microwave response of the system. The distribution of the magnetic poles on both layers is asymmetric due to the presence of exchange bias on one layer. Therefore, it is expected that inter-layer coupling will cause an effect on the net microwave response of the system.

6.1 Introduction

The mechanisms which govern the magnetisation reversal in an antidot lattice (ADL) are highly dependent on the hole diameter (d) and the lattice periodicity (s) as these have a direct influence on the distribution of the demagnetisation fields [84, 162]. In the limiting case of isolated elements ($d \geq s$) the reversal occurs through fast switching and formation of magnetic vortices and in the extreme case of an unperturbed film with largely spaced holes ($d < s$) the magnetisation reversal undergoes long range domain wall motion and rotation [17, 176, 177]. At an intermediate range ($d \sim s$) both vortex formation and domain wall reversal are expected [45, 167]. The choice of the ratio d/s helps establishing the type of applications to target. For $d > s$, the ADL behaves as a group of isolated elements, which in case of reduced dimensions, is suitable for data storage applications. In cases where $d < s$, the applications lean towards spin wave dynamics [178].

Following previous studies using Lorentz TEM and magnetic force microscopy [44, 159], the in-plane magnetisation reversal undergoes three main stages: 1- formation of long chains of domains, collinear with the applied field direction relative to the ADL; 2- depending on the applied field direction, long range domains may be observed along the direction perpendicular to the applied field direction; and 3- the formation of short range domains which evolve to hole-to-hole super domain walls (SDW). These can be distinguished as high energy or low energy.

When considering a magnetic system with several layers, one may expect that interlayer exchange and dipolar coupling plays a role in modifying the switching mechanisms and the microwave properties [179–182]. Exchange coupling effects are highly dependent on the spacing between layers, the type of non-magnetic spacer and the exchange coupling effect of each layer individually. Exploring the effects of exchange interaction is beyond the scope of this work, as exchange coupling effects

are assumed to be weak in a system where the internal fields are dominated by dipole field distribution.

The interest in studying a multilayered antidot structure resides in the fact that the dipole fields, for example, at a free and a pinned layer, will add another degree of freedom when it comes to the modification of the spin wave properties of the system. This heterostructure allows for the existence of at least the parallel (P) and anti-parallel (AP) configurations, where the demagnetisation fields on each layer will add up or partially cancel each other out. This multi-state switching process can be achieved by stacking an exchange biased layer upon a non-biased layer, resembling a spin valve configuration. Eventually this can also be achieved with two exchange biased layers, each with different bias magnitudes. The exchange bias will contribute to an increase in the internal energy of one of the layers, allowing for it to switch at higher fields and therefore promote the anti-parallel alignment [20, 32].

The concept of field cancellation in the double-layer configuration is illustrated in Fig. 6.1.

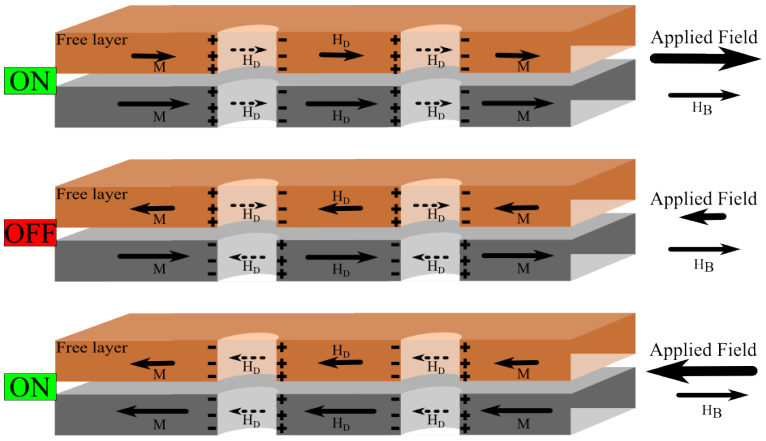

Figure 6.1: Schematic illustrative of the demagnetisation field configuration in a bi-layered system. Here, one layer is free and the other layer is exchange biased.

For positive applied fields, with the same polarity as the exchange bias, it can be seen that the demagnetisation fields on both layers have the same polarity. By applying a negative field, which is only sufficient to reverse the free layer, the anti-parallel configuration is achieved and the demagnetisation fields must partially cancel. When the external field is further decreased, the magnetic moment of both layers realigns and the parallel state is restored. This results in a highly

configurable three dimensional magnetic structure. If in the parallel configuration one expects to obtain a complex ferromagnetic resonance mode structure, the anti-parallel configuration allows only for a reduced number of resonance modes. This gives rise to the potential to produce a microwave ON/OFF switch. This chapter is structured as follows. Section 6.2 provides details on the samples used in the TEM in-situ Lorentz experiments. Magnetometry and FMR results from unpatterned films are presented and discussed. The magnetisation reversal of the multi-layered system is described in Sec. 6.3. The details of the fabrication and FMR measurements on a large array of a double exchange biased system are given in Sec. 6.4.

6.2 Fabrication, patterning and magnetic properties

Two samples were studied by Lorentz DPC: A single exchange biased layer IrMn/CoFe (S1), and a double layer system IrMn/CoFe/Cu/CoFe (S2). Both samples were deposited on top of buffer layers, Ta/Ru, and capped with Ta. The layer configuration and thickness are illustrated in Fig. 6.2a. A sputtering system (Hitus) was used for the deposition, and followed by field and temperature annealing in order to set the bias direction [183, 184]. These thin continuous films were deposited and characterised via VSM by Dr. Gonzalo V. Fernandez from the University of York, UK.

Focused ion beam milling (FEI Nova 200) was used to fabricate the antidot structures. This method requires the use of a software mask that defines the regions were the ion beam is either blank or milling the surface of the sample [185]. The mask (bitmap file) resolution was chosen to match the ion beam raster step (15.5 nm). The antidot array covered an area equivalent to the field of view (FoV) of the ion beam (85.3 μm). At the edges of the large array a trench was milled to physically separate the antidot region from the surrounding continuous film.

Figure 6.2b shows a bright field TEM image of the antidots. The unit cell size is 550×560 nm^2 and the average hole size 280×320 nm. The elliptical shape as well as the kink in the curvature of the holes is a result of the mismatch between the resolution of the mask and the different FoV for the horizontal and vertical axis, in

the FIB. A regular grain structure is observed across the film, except near the edges, where the enhanced grain structure is obtained as a result of the milling process, i.e. Ga^+ implantation [186, 187].

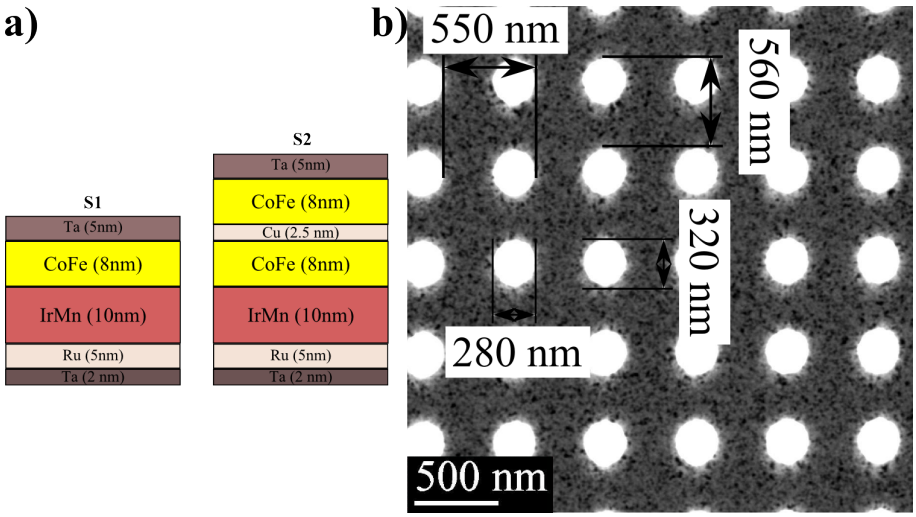

Figure 6.2: a) Illustration of the multi-layers S1 and S2 used in the Lorentz TEM experiments. b) Bright Field TEM image of S2 obtained from the sum of all DPC components (see Sec. 3.4.3).

Figure 6.3a shows the hysteresis loops, obtained via VSM, relative to the samples S1 and S2 while unpatterned. The applied field was set along the exchange bias direction. In S1, the magnitude of the exchange bias field is H_b^{S1}= 16.7 mT and in S2 H_b^{S2}= 13.8 mT for the pinned layer. Note that in S2 the parallel state corresponds to the saturation region $M/M_s \sim \pm 1$ and the anti-parallel state corresponds to the field region where $M/M_s \sim 0$. The slope in the magnetisation in the antiparallel region indicates the varying alignment of the magnetisation of both layers. These two states are illustrated in the Fig. 6.1 as the ON and OFF states, respectively.

Figures 6.3b,c and d show the derivative of the normalized magnitude signal of the forward scattering parameter (S_{12}) as function of frequency and applied field. The variation in the colour contrast follows the resonance behaviour of the magnetic system. The FMR spectra shown in Fig. 6.3b, d were obtained via VNA-FMR using a coplanar waveguide (Sec. 3.2.4) while the spectra shown in Fig. 6.3c was obtained using the TEM in-situ VNA-FMR setup (Sec.3.3.2). The spectra of Fig. 6.3b corresponds to the single exchange biased layer, S1, where the applied field was set along the bias direction. The lateral displacement of the spectra corresponds mainly to the exchange bias amplitude H_b^{S1}. This agrees qualitatively with the value

measured in the VSM data.

Figures 6.3c, d show the FMR data from sample S2. Due to exchange coupling at the interface between the IrMn and the CoFe one expects the resonances of the exchange biased layers to have broader linewidths and lower resonance amplitudes, while the linewidths of the free layer are noticeably narrower and with higher amplitude. This explains why the resonance of the pinned layer is hard to observe in the spectra of S2. The free layer switches uniformly at $\mu_0 H \sim$ -4 mT and then a jump in the resonance frequency is noted when the pinned layer switches, at $\mu_0 H \sim$ -16 mT. This variation in the resonance frequency indicates that the AP state is being driven to some extent by interlayer coupling between both pinned and free layer [25]. The anti-parallel state is confirmed by the change in contrast of the microwave signal (vertical band) in the field region $\mu_0 H =$ [-16,-4] mT, which is expected due to variations in the magnetoresistance [182, 188].

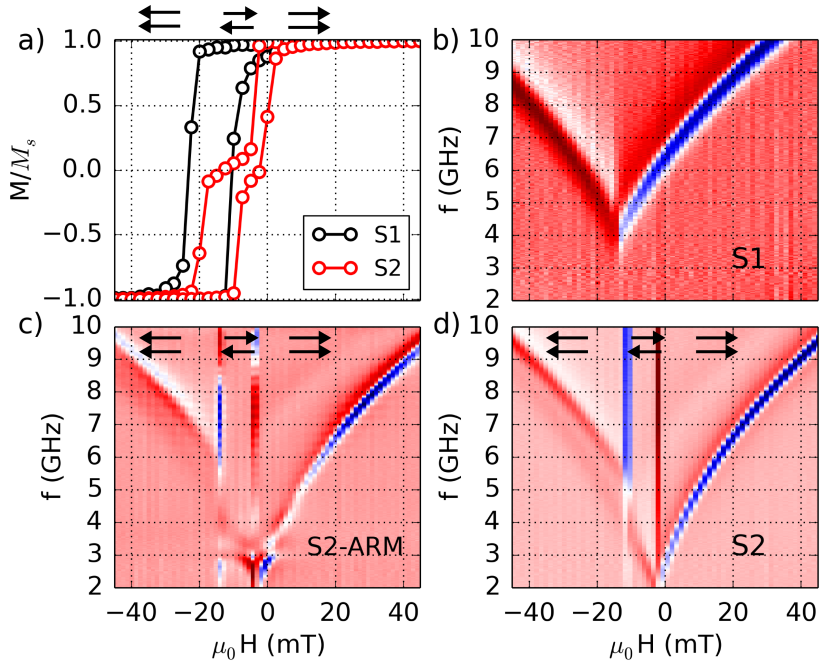

Figure 6.3: a) VSM data of S1 and S2 in continuous film configuration; b) Derivative of the magnitude of S_{21} as a function of the frequency and external field, representing the derivative of the resonance spectra of: b) the single FM layer; c) the double FM sample acquired with the in-situ FMR setup (after normalisation, the trace noise and signal to noise ration are 0.2 mdB and 2 mdB, respectively); and d)the double FM sample acquired with the conventional VNA-FMR setup.

It was not possible to obtain either the FMR response or the hysteresis behaviour of the ADL alone due to the small area patterned. From the literature, a general approach was taken to estimate the change in coercivity with the structuring, where the coercive field increases with the spacing [42]. Regarding the FMR signal, from the results presented in Chapter 5, the resonance frequency is not too different to that of the continuous film, but evidently more resonance modes are expected. Micromagnetic simulations were carried out to estimate the coercivity enhancement with patterning, as well as the FMR response. These are only an estimate as the reversal of the patterned film will be largely modified by the presence of defects will act as nucleation sites. These were not reproduced in the micromagnetic simulations.

6.3 Lorentz DPC studies of S2

The Lorentz DPC data were obtained from a JEOL Atomic Resolution Microscope JEM-ARM200, operating at 200 kV. Details of the measurement technique can be found in Sec. 3.4.3. A tilt series was performed on both S1 and S2 samples in order to obtain magnetic induction maps as the systems underwent reversal. The sample S1 follows essentially the same reversal as that of S2, with the exception that the S1 does not exhibit the magnetic vortices or the cancellation effects since it is a single layer. For that reason the Lorentz DPC studies on sample S1 are presented in Appendix D.2.

Figure 6.4 contains all DPC images acquired during the tilt series from sample S2. The colour code was implemented after balancing all image components adequately [157]. The high amplitude signal (contrast) near the holes is primarily caused by the electrostatic phase contributions due to the local variations in thickness [189].

The reversal process will be described with respect to the behaviour of the vertical (i)- horizontal (ii) wire channels and the hole column (iii)- rows (iv), as labelled in Fig. 6.4-5° (Fig. 6.4-tilt angle).

The first DPC image was acquired at a tilt angle of 5° (after coming from 15°), which is equivalent to an in-plane field of 17.4 mT. A zig-zag pattern is observed in the vertical wire channels, with the symmetry being parallel to the direction of the applied field (↓).

At 3° tilt the horizontal components yellow (←) and blue (→) become more dominant, indicating domain rotation towards horizontal direction. Long range domains pointing left-to-right (LR) and right-to-left (RL) are observed along the horizontal wire channels (ii). As a consequence of the domain rotation in the wire channels, strong vertically pinned regions prevail in the hole rows, given by the red contrast (↓). Locally, this enables the formation of 90° domain walls. The formation of long range zig-zag domains can be described as the first clear stage of the domain propagation in the antidots.

At a tilt angle of 1°, the corresponding in-plane field is 3.5 mT. The horizontally aligned RL and LR domains prevail, but also note the emergence of green (↑) contrast in certain hole columns, indicating an upward magnetisation direction. The long range domains have evolved to short range domains and are now confined to the hole-to-hole distances. An example is highlighted by the box labelled as v.

Interestingly, at 0° tilt (in-plane field of 0 mT), and for the first time in the field reversal, three magnetic induction components meet at the edges of the holes, forming a 'c' shaped magnetic configuration, as highlighted by the circles. It is also noticeable that the strongly pinned regions in red (↓) are no longer confined to the hole rows, and now extend to the neighbouring cells.

At $-1°$ tilt the magnetic textures which were previously marked with the circles have evolved to vortex states and these are now located at the center of the unit cell. At each vortex site, the nearest vortices have opposite sense of rotation. In the 6 $\times$ 6 hole array here shown at least 12 vortices are observed so this appears to be a stable configuration.

When the applied field is decreased, down to -7.0 mT ($-2°$ tilt), the majority of the vortices move towards the edges of the holes, forming a 'c' magnetic configuration. The existing vortices have shifted towards the hole edges and are likely to subsequently vanish. At this stage of the reversal a change in the directionality of the domains is noted. The domains are still confined to the hole-to-hole range, but the strongest colours are green (↑) and red (↓), along the vertical wire chains. While for the 0° tilt image the domains in red (↓) were located in the hole rows, they now appear in the hole columns, whereas the green (↑) domains are located in the hole rows.

The conclusive evidence for the anti-parallel configuration between the two

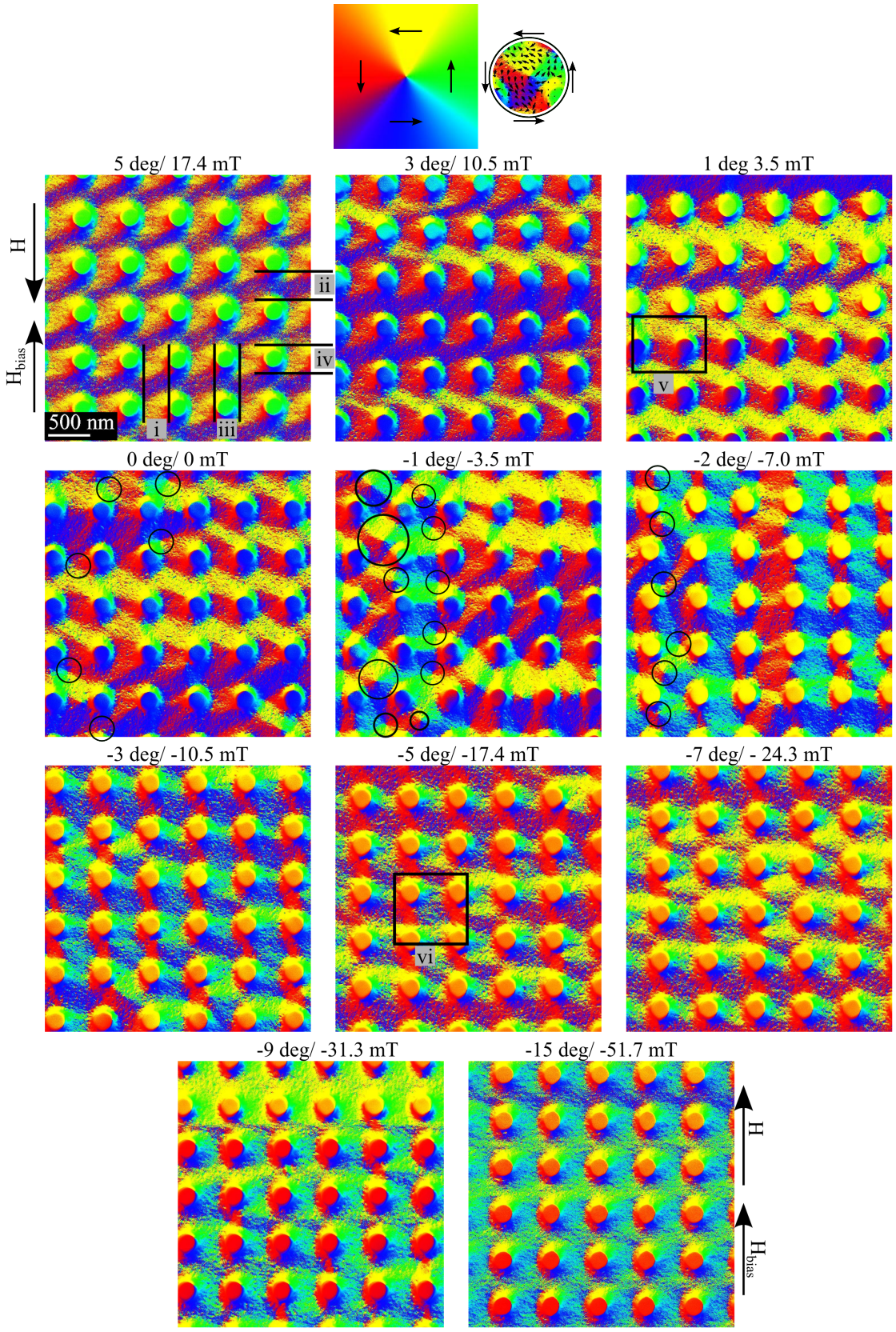

Figure 6.4: Colour coded DPC data as a function of applied field angle (tilt). The images correspond to the induction field maps obtained using DPC. The contrast in the holes is greatly enhanced due to the electrostatic phase contrast due to the sloped variation of the layer thickness across the edges of the holes. Effectively, one should assume that the magnetic contrast is being generated by the material away from the hole edges of the ADL. Contrast due to physical structure can also be observed in the form of the high spatial frequency components observed here as the granular features. This effect is minimised as

ferromagnetic layers is observed from $-3°$ to $-7°$ tilt angles. The anti-parallel configuration should in principle produce very low contrast as a result of the net zero moment. In the DPC images the zero net moment regions appear as a superposition of the 4 colours and an enhanced grain contrast, which is the case for the regions between four holes, as highlighted in region vi. The parallel and anti-parallel regions are more noticeable in the figures relative to $-5°$ and $-7°$ tilt angles. The field region at which the cancellation region occurs is consistent with the step in magnetization reversal, expected for the bi-layered antidot structure. However, the cancellation of the magnetic induction is only partial since there are still regions where the magnetic induction of both layers is parallel, i.e. regions which are either strong red ($\downarrow$) or strong green ($\uparrow$). These are located in the hole rows and in the hole columns, respectively.

At $-9°$ tilt, the parallel configuration appears to be restored, given the dominance of the green ($\uparrow$) coloured contrast with the same zig-zag configuration also observed for high positive tilt angles. The final figure corresponds to a tilt angle of $-15°$. This magnetic state and the magnetic state observed at $5°$ clearly possess the same symmetry, except with opposite direction in terms of the magnetic moment.

The most relevant features of the magnetisation reversal are summarized in Fig. 6.5. The orientation of the arrows, represent the direction of the induction field, obtained from a magnetic vortex state (see supplemental D.4). The absolute length of the arrows should be neglected, as it is scaling with the amplitudes obtained near the edges of the holes. A unit cell was taken from each magnetic state of Fig. 6.4 and the illustrations represent the local magnetic configuration on the corresponding unit cell. The most important features are: a) zig-zag domains; b) the break up into short range domains in the range of the unit cell; c) emergence of the vortex texture from the ‘c‘ configuration, at the hole edges; d) the vortices move to the center of the unit cell; e) the vortices move towards the edges of the holes, form a ‘c‘ state and annihilate; f)-g) ferromagnetic layers reach the anti-parallel state and h) near saturation.

The anti-parallel state was noted due to the strong reduction of the contrast at the centre of the unit cell, shown in Fig. 6.4, relative to $-5°$ tilt and in Fig. 6.5g-h. This was also confirmed in the magnetic induction magnitude maps, where a very

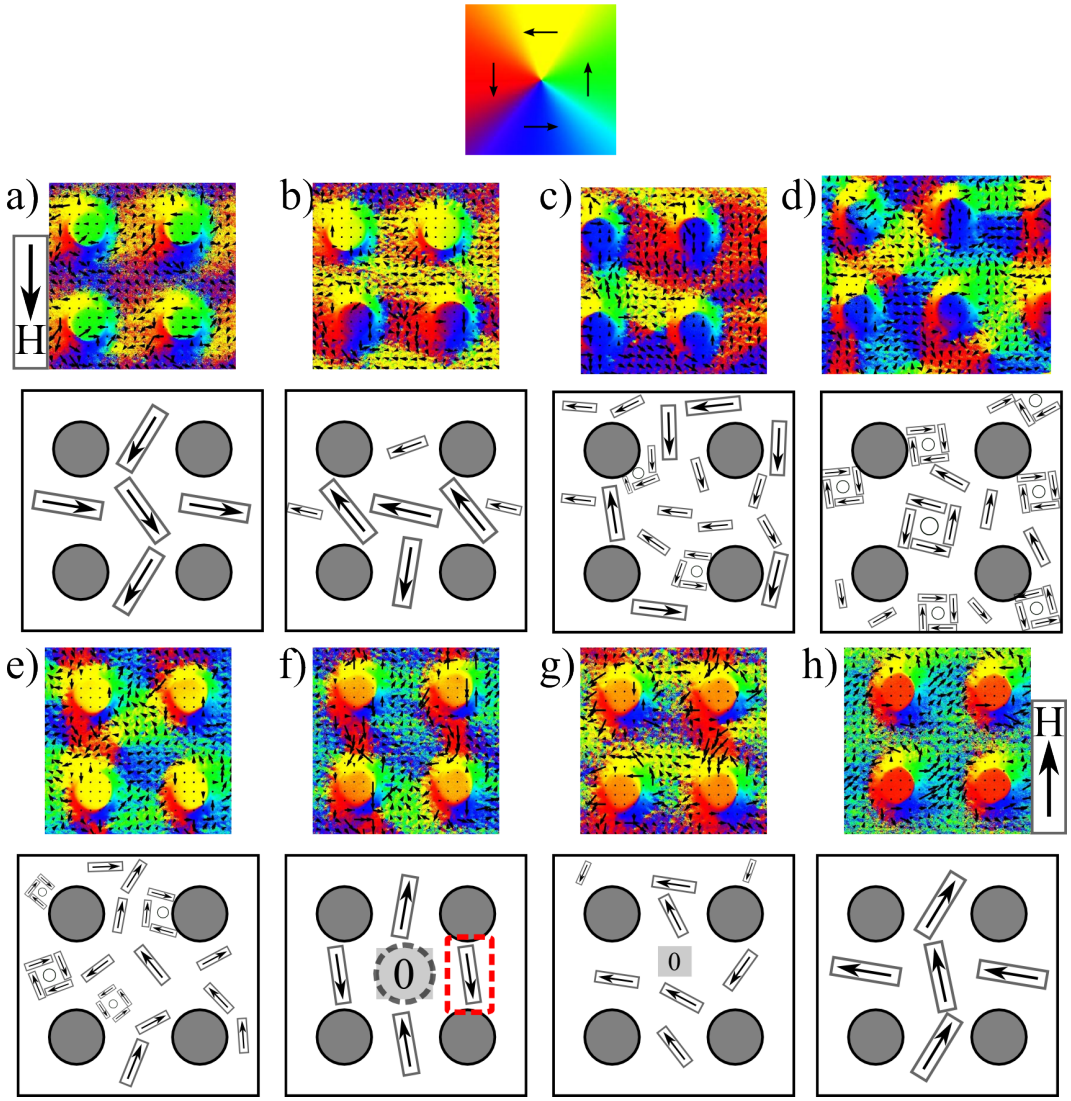

Figure 6.5: Summary of the most relevant stages of the magnetisation reversal. The images presented here were obtained from those shown in Fig. 6.4.

strong variation in the contrast is observed, between the hole columns and the regions at the centre of 4 holes. A low value in the induction magnitude was obtained due to the anti-parallel configuration, as opposed to the regions with parallel alignment where the magnetic induction magnitude is much higher. The magnitude maps are shown in appendix Sec. D.3.

Micromagnetic simulations were performed to identify the most relevant features of the reversal process of the double layer of antidots. The presence of thickness variations, hole defects and grain structure were not accounted for, so one must expect that some critical features, such as magnetic vortices, may not appear in the simulated data. Figure 6.6 shows the hysteresis loop relative to the structure, comprised of a free and a pinned antidot layer, separated by a 5 nm gap. The magnetisation component parallel to the applied field, was recorded in the applied field range of [20,-20] mT. This field range covers all the important features of the reversal process studied using Lorentz DPC. A pinning field of 10 mT was set on one layer which enabled the multi-step reversal shown in the hysteresis. The field regions labelled from I to VIII represent the most relevant stages of the reversal. In particular, the starting magnetic state (I), the magnetic states pre- and post-switching of the first layer (II-IV:V), the cancellation region (VI) and the switching of the second layer (VII:VIII).

The magnetic configuration relative to the stages labelled from I-VIII are shown in Fig. 6.7. Both color and arrow codes represent the magnitude and direction of the magnetisation across the unit cell of the ADL. The images in the first two columns correspond to the magnetisation of the pinned and free layer respectively. The third column shows the magnetisation which results from the sum of both layers. The sum image should in principle correspond to the magnetic state observed in the Lorentz DPC experiments. At stage I it is noted that the dispersion of the magnetisation of both layers is different due to the presence of the pinning field. The sum image shows that in the vertical hole columns, the magnetisation is canted towards the horizontal axis, similarly to the 5° image shown in Fig. 6.4. It is also noted that both horizontal and vertical wire channels have a zig-zag configuration. In the reversal stages shown in the II and III, the magnetisation of the free layer rotates towards the horizontal axis, which in terms of the Lorentz DPC data, would correspond to

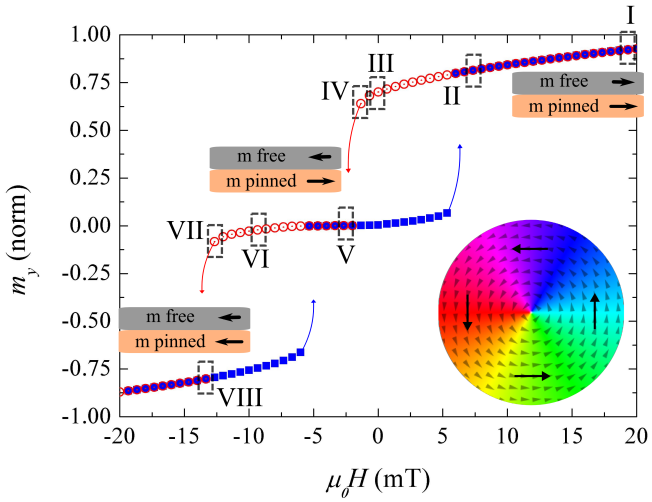

Figure 6.6: Hysteresis obtained from mumax simulations on a system equivalent to S2. Simulation parameters: $M_S = 1.7$ T, $A_{ex} = 3.5\text{e}^{-12}$ J/m, $\alpha = 0.02$. The holes have elliptical shape 280×320 nm^2 and the periodicity of the lattice is 550 × 560 nm and discretisation units are c_x= c_y= 3.5 nm, c_z= 5 nm. Arrow code and colour code represent the direction f the magnetic moment. Colour wheel illustrates the direction of the magnetisation vector discussed in Fig. 6.7.

the stage where long range domains start to break into short range domains (1° tilt).

The pre-switching stage IV should in principle contain some magnetic vortices. However, this is not observed possibly due to the absence of defects, which would promote the nucleation of the vortex states.

Stage V shows that magnetisation of the free layer has reversed so the sum image shows very low contrast, due to the AP configuration across the entire structure. This complete cancellation of the magnetisation is mainly due to two aspects: 1) the magnetisation of both layers is independent so no exchange coupling is considered; 2) the absence of defects does not promote the nucleation of any type of domains, so the switching of the magnetisation is rather abrupt. The interlayer coupling and the nucleation of domains at the holes columns and rows are the primary reasons for not observing the full AP state in the experimental data.

Interestingly, the stages VI and VII show that, as the pinned layer initiates reversal, the contrast in the sum image reappears as a result of the dispersion of the magnetisation on both layers. The contrast in the sum image appears primarily in the hole columns, which is consistent with the experimental observations in Fig. 6.4,

relative to $-5°$ tilt.

In VIII the magnetisation of both layers has reversed and the zig-zag configurations are restored.

On all stages of the magnetisation, it is noted that the hole edges appear with low contrast. This can be associated with permanent interlayer cancellation effects due to strong divergence of the magnetic charges at the edges of the holes.

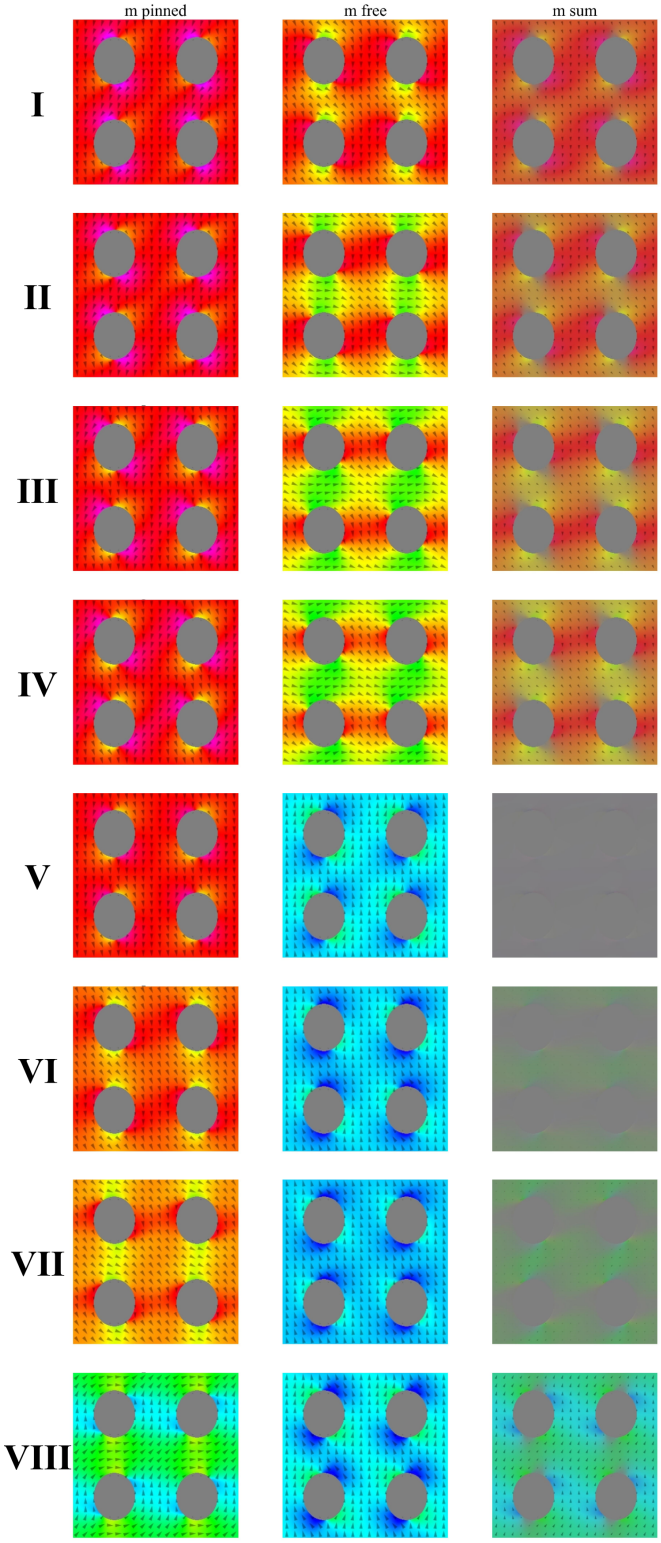

Figure 6.7: Summary of the magnetisation profiles of the stages I-VIII, highlighted in the hysteresis loop of Fig. 6.6. The column on the left contains the magnetisation profile of the pinned layer, the column at the centre shows the magnetisation profiles of the free layer and the column on the right shows the magnetisation profiles of the sum of both layers. The induction field profiles are equivalent to the magnetisation profiles shown here.

6.4 Ferromagnetic resonance of antidot bi-layers

The effects of inter-layer coupling on a bi-layered exchange biased antidot array are investigated in this section. The sample consisted of a double exchange biased system of Ta/[NiFe/FeMn]×2/Ta. Both deposition and patterning were executed in the same way as for the single exchange biased layers studied in chapter 5. This system differs to the one studied in the previous section as the FMR data of the large ADL of S2 exhibited very weak FMR signal, so it was necessary to use an alternative sample which produced a measurable FMR spectra, while maintaining similar magnetic properties. Figure 6.8 shows SEM images acquired at normal incidence (left) and at 45° (right). The hole spacing is 420 nm and the estimated hole diameter is 280 nm. On the SEM image acquired at 45° incidence, a ring pattern at the wall of the holes is observed indicating the presence of several layers. This image also suggests the presence of a step in the morphology of the holes.

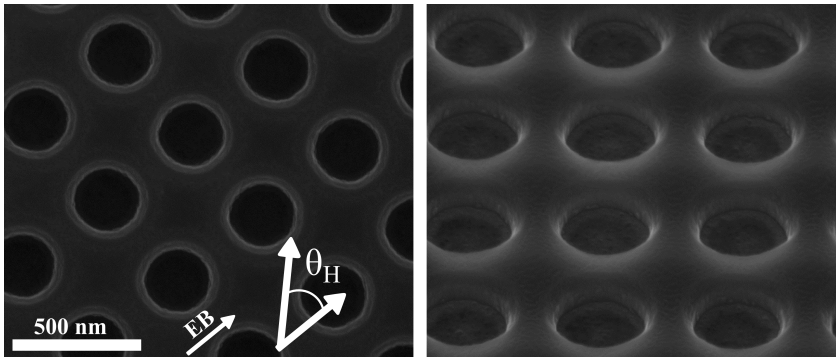

Figure 6.8: SEM images of the bi-layered ADL sample, comprised of the layers NiFe/FeMn/NiFe/FeMn. Top view SEM image on the left and 45° SEM view on the right. This sample was patterned as an alternative to S2 presented in the previous section. Nonetheless, it possesses the similar overall magnetic properties, i.e. stepped reversal process with an anti-parallel magnetic state. Note the ring pattern on the image obtained at 45°.

Figure 6.9 shows the cross sectional TEM analysis performed to accurately evaluate the layer distribution and the morphology of the etched holes.

As can be noted in this image, the shape of the holes is not uniform across the multi-layer. The hole diameter at the top layers is $\emptyset_1$= 280 nm while at the bottom layers is $\emptyset_2$= 230 nm. The difference in hole diameter is attributed mainly to an over etch of the top layers due to the low etch rates of the Ta. At the beginning of the

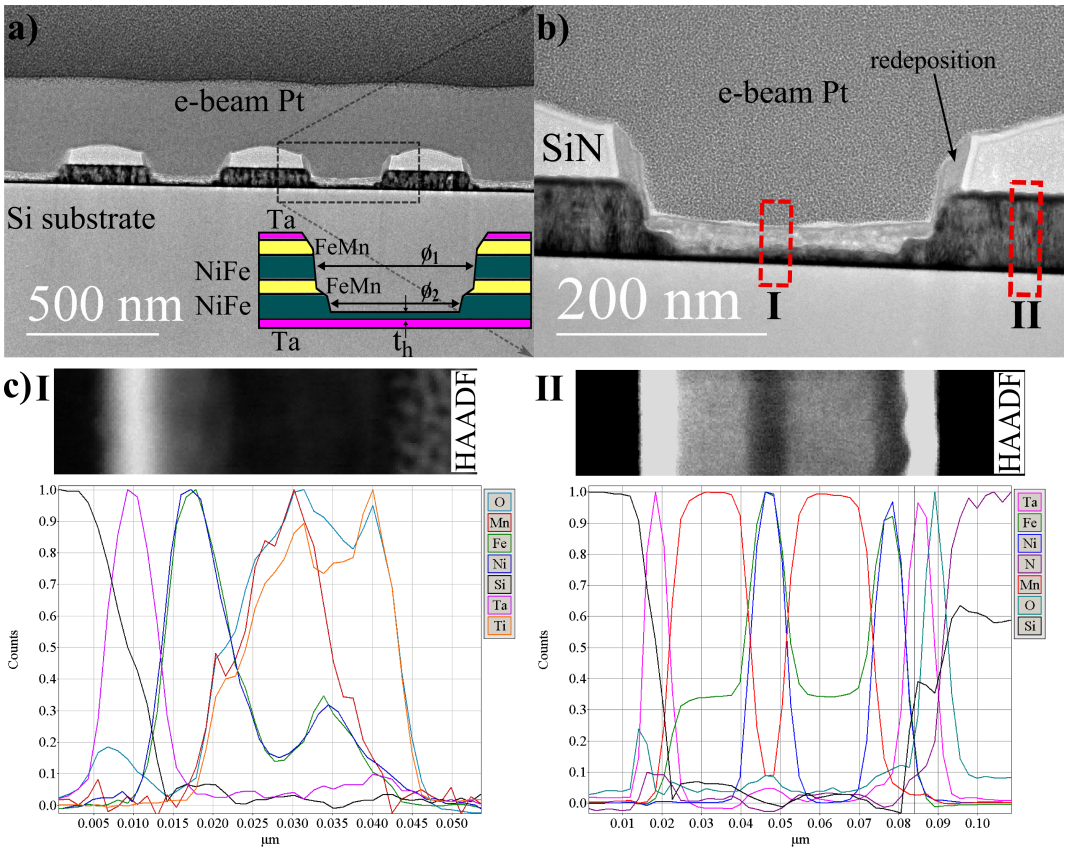

Figure 6.9: a) and b) Bright field TEM data from the cross section of the ADL comprised of FeMn/NiFe/FeMn/NiFe layers. The inset schematic in a) illustrates the diameter and layer configuration. Note the stepped morphology of the hole regions, showing an incomplete etching of the holes. c)Elemental profile of regions I and II obtained with EELS. At the top of the elemental plots, a high-angle annular-dark field (HAADF) image was added to better understand the elemental distribution across each section. Data acquired from regions I and II, highlighted in b).

etching process, the etch of the Ta was very slow so the side walls of the hard mask widened. It should be noted that reactive ion etching is isotropic so all interfaces are chemically etched. This resulted in the holes being wider at the top, which then became narrower due to the accumulation of re-deposited material on the side walls. The step observed in the profile of the hole is coincident with the thickness of the bottom NiFe layer. This feature appeared due to a difference in etch rates of FeMn to NiFe. Elemental mapping on the hole region, shown in Fig. 6.9c-I, revealed the existence of titanium (Ti) which may have a caused slowing of the etching process. Note the presence of tantalum (Ta) which was used as the buffer layer for the sample growth and a NiFe layer with thickness t_h remaining at the bottom of the holes. The

presence of oxygen (O) and given its overlap with the spatial distribution of iron (Fe), manganese (Mn) and titanium (Ti), may suggest the formation of oxide compounds. Table 6.1 summarizes the thickness of the layers obtained from the elemental maps by measuring the half width at half maximum of the normalized amplitudes.

Probed elements	Ta	NiFe	FeMn	NiFe	FeMn	Ta
Region I ± 0.5 nm	8.0	6.0	–	–	–	–
Region II ± 0.5 nm	8.0	20.0	10.0	20.0	10.0	8.0

Table 6.1: Thickness, in nm, of the layers obtained from the elemental distribution of survey sections I and II shown in Fig. 6.9.

Figure 6.10 shows the derivative plot of the FMR data relative to the continuous film as deposited. The spectra exhibits two well defined resonance traces due to the presence of two layers with different exchange biased fields. Given the layer configuration (inset), the top NiFe layer contains two interfaces in contact with the FeMn, i.e. two exchange biased interfaces, whereas the bottom NiFe layer contains only one exchange biased interface. The exchange bias field scales with the number of interfaces, therefore the bias field in the top layer is $2\times$ H_b, with $H_b \sim 7$ mT. This explains why each NiFe layer reverses at different applied field magnitudes.

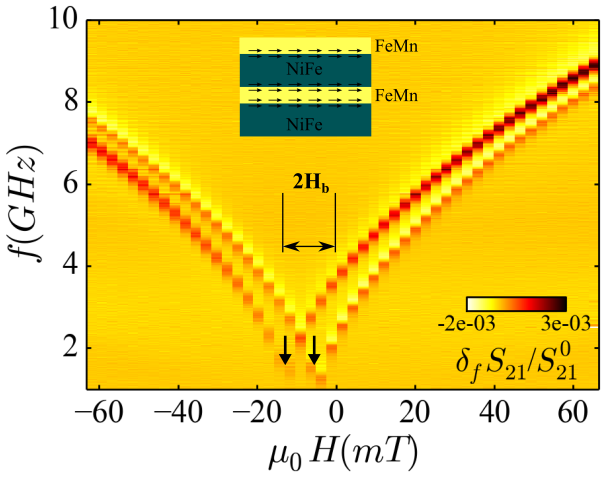

Figure 6.10: Derivative of the normalised magnitude of S_{21} plotted as function of frequency and external magnetic field. Data from the continuous film as deposited. Inset illustrates the layer configuration.

Note that in the applied field region, where $2H_b > \mu_0 H > H_b$, the magnetisation of

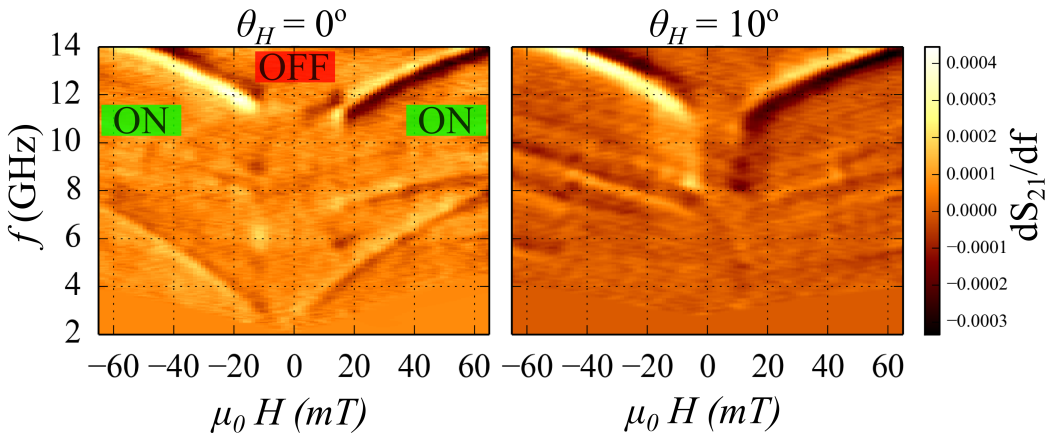

Figure 6.11: Derivative plot of the forward transmission parameter S_{21} as function of frequency and external magnetic field. FMR data relative to the ADL and the external magnetic was applied along θ_H= 0° and θ_H= 10° with regards to the ADL and exchange bias (see Fig. 6.8).

both layers is expected to be in the anti-parallel configuration as described earlier in Sec. 6.1.

FMR results from the ADL are shown in Fig. 6.11, where the external applied field was set to θ_H= 0° and at θ_H= 10° with respect to the ADL edge (6.8. These spectra can be described by two distinct regions within the field range here shown. The microwave response at both high positive and negative fields consists of a superposition of the resonance modes from each of the ferromagnetic layers. These regions are labelled as the ON state. The center field region, where the magnetisation of the bottom FM layer is anti-parallel with respect to the top layer, causing an abrupt variation in the number of resonance modes and in the amplitude of the FMR signal over a field range of approximately 20 mT. This field region is labelled as an OFF state.

In the light of the conclusions from the Sec. 6.3, one should expect that within the anti-parallel configuration, not all resonance modes vanish, given the fact that the reversal of the magnetisation is non-uniform across the ADL. While certain regions have reversed, others may still be strongly pinned and thus still capable of creating coherent spin precession. It is therefore expected that some modes will exist even in the anti-parallel state. In the FMR data, the lowest resonance mode is visible over the whole field range, except in the proximity to $\mu_0 H$= 0 mT.

From an overall qualitative perspective, the microwave response of the system

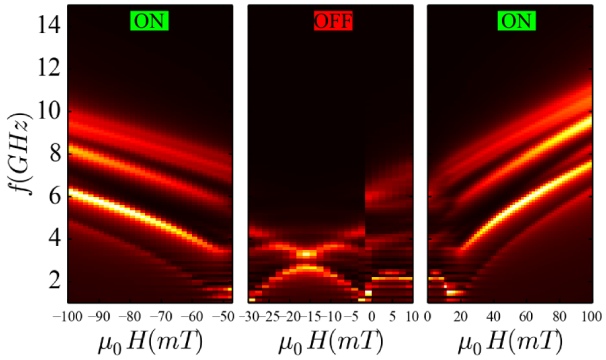

Figure 6.12: Micromagnetic simulation results of a double exchange biased layer system. The layer configuration resembles the one studied in this section. The spectra appear subdivided in three regions: ON at large positive and large negative fields and OFF in the low field region. The OFF state corresponds to the anti-parallel (AP) state between both ferromagnetic layers and consequently the net microwave response is much narrower in frequency, over the field region corresponding to the AP state. The thickness of both ferromagnetic layers is kept the same (20 nm) and the separation between them is 5 nm. The top layer was pinned by an exchange bias field of 15 mT and the bottom layer was pinned by an exchange bias field of 7.5 mT. Magnetic parameters used in the Mumax simulations: M_S= 1 T, A_{ex}= 1.3e^{-}12 J/m and α= 0.02.

follows the magnetostatic description obtained from the Lorentz DPC studies. While previous work in multi-layered structures have shown that in the AP configuration, the resonance modes are independent of the applied field, as long as the cancellation state prevails [111, 190]. This was not observed in the FMR experiments of the ADL presented here, as the cancellation effects of the magnetisation are only partial. This observation may have also been affected by the low signal-to-noise ratio achieved in the measurements. For a quantitative evaluation of the resonance modes on the bi-layered structure, it would be necessary to obtain FMR results with improved signal-to-noise ratio.

To further explore this concept, micromagnetic simulations were performed using Mumax, to determine the frequency response of a system with an equivalent layer configuration. The procedure to obtain these results was similar to the one implemented in Chapter 5. A description of the simulation method can also be found in Sec. B. Figure 6.12 shows the simulated dynamics spectra, which was conveniently divided in three field regions, relative the two parallel (ON) and the anti-parallel (OFF) state.

As observed in the experiments, in the field region relative to the anti-parallel (OFF) configuration, the dynamic response of the system is much narrowed, which is in broad agreement with the experimental findings.

6.5 Conclusions

In this chapter, the concept of a multi-layered ADL was explored. The use of both Lorentz DPC and FMR enabled the determination of the magneto-static and dynamic behaviour of the 3-D structure upon magnetisation reversal. It was observed that microwave properties can be further engineered with the introduction of multi-stage magnetisation reversal, whereby the dipole field distribution around the hole edges of each layer promotes a net cancellation (or suppression) of the microwave response.

From the Lorentz DPC results, it can be concluded that the cancellation effects are not entirely uniform across the ADL, as the reversal itself undergoes a complex process. Nevertheless, at a well defined field range, the partial cancellation of the net induction field was observed. While in the anti-parallel configuration, the net induction field is nearly zero at the center regions (between holes) of the antidot unit cell. However, in the regions between two adjacent holes (hole columns), the net induction field is enhanced. This observation suggests that field cancellation regions (OFF) are a combination of anti-parallel and parallel magnetic configurations, as the net moment varies within the unit cell. This interpretation was validated by the FMR studies, where it was observed that not all resonance modes vanish in the anti-parallel configuration, as the pinned regions may still produce coherent spin precession.

Interestingly, this layer configuration allowed the emergence of magnetic vortex textures with a well defined behaviour. The vortices emerge when 3 three magnetic components meet at the edges of the holes forming a ‘c‘ state, which later shifts towards the center of the unit cell. The discontinuity at the hole edges, as well as the most certainly sloped profile of the hole walls (due to the ion beam milling) may be the reason as to why such states nucleate [186]. Nevertheless, the vortices appeared to be quite reproducible across the ADL that was imaged. Often, vortex

states in isolated elements are subject to investigation due to the emergence of strong out-of-plane stray fields at the vortex core regions [191–193], which can be used to influence the magnetic properties of adjacent layers due to exchange or dipolar coupling. This study demonstrates the feasibility of vortex state formation in antidots. Therefore, it may be suggested that such structures can be studied from the perspective of interactions between spin waves and magnetic vortices. In which case, one may think first of the effect of the potential wells [194] associated with the magnetostatic spin wave modes and then the effect of magnetic vortices on the propagation of spin waves. To fully understand the mechanism promoting this magnetic state, further experiments are required, where one would investigate the formation of magnetic vortices in unbiased films, patterned with FIB but also with e-beam lithography, for comparison. Large array patterning, suited for TEM substrates, would also allow to obtain TEM in-situ VNA-FMR data from the ADL.

Chapter 7

TEM in-situ dynamic experiments: the mapping of electromagnetic fields

Lorentz microscopy was used to probe the in-plane distribution of electromagnetic fields in the gigahertz operating frequency of a loop shaped microstrip operating in a single port in-situ FMR rod. This work paves the way towards TEM in-situ ferromagnetic resonance spectroscopy, combined with the high spatial resolution inherent to the TEM. Prior to TEM in-situ FMR experiments on a magnetic material, an understanding of the interactions between the microwave field distribution and the electron beam is required. The electron beam propagating along the optic axis of the electron column is affected by the amplitude and phase distribution of the microwave fields. As the microwave frequencies are varied, the electron beam acquires different intensity profiles, which are associated with the field amplitude and phase experienced by the electron as is propagates through the field regions. Microwave simulations allowed the calculation of the EM field values in the region of interest, which was then used to reproduce the TEM results, under the considerations of the Aharonov-Bohm effect for magnetic and electric fields. This apparatus can be used for high resolution probing of electromagnetic fields.

7.1 Introduction

Electron microscopy has been employed to map static electric and magnetic fields via off-axis electron holography. Several examples of static electric and magnetic field mapping in nano-structures can be found in the literature in Refs. [195–198]. What is presented here differs in a way in that it allows the observation of time averaged radio frequency oscillations of electromagnetic fields. From the example structure presented here, it was possible to correlate the experimental observations with the dominant polarisation state of the in-plane fields obtained from the microwave simulations.

Mapping of electromagnetic fields has also been explored via scanning electron microscopy. This technique is widely known as electron beam testing and has enabled the characterisation of the EM fields in monolithic microwave integrated circuits (MMIC) [199]. The experiments consist in measuring the energy distribution of secondary electrons which experience the effects of not only the metallic interface, but also the field surrounding the conductors. Several problems have been identified, such as broadening of the energy spectra, as the microwave fields have a large propagation range. Improvements in the energy filtering techniques enabled a whole new range of experiments to be performed such as the study of excited plasmons.

Outside the field of electron microscopy, the characterisation of microwave devices has been addressed with a broad range of techniques, which can be described as passive or active techniques, depending on the degree of interaction between the probe and the device itself. Passive measurements normally involve the characterisation of the microwave device based on the characteristic impedance via, for example, the vector network analyser. This capability was demonstrated in Sec. 3.2. Such methods yield information averaged over an entire structure. Attempts were made to retrieve local impedances and local field distribution by scanning a microwave antenna over the device under test and measure the local variation of the impedance condition, however in general this approach is intrusive and does not provide details on a micrometer scale. There exist a range of other experimental techniques which allow spatially resolved mapping of microwave fields and dielectric properties. In particular, the electro-optic near-field scanning probes (EONM) and near-field microwave microscopy (NSMM). In EONM, a laser beam is guided through an electro-optic crystal while scanning above the surface of a planar device [200]. The resolution of this method

depends directly on the spot size of the beam and ultimately the relative movement of the stage. In NSMM, a tapered microwave resonator creates a strongly confined field distribution on a tip, which is then scanned in proximity to the surface of another microwave device or a thin dielectric film [201]. As it performs the scan, the relative shifts of the resonance frequency allow the retrieval of the amplitude and phase maps, with the resolution being limited by the tip apex. State-of-the-art set-ups allow the field mapping with sub micrometer resolution. The general drawback of such techniques is that they are, to some extent, intrusive, in a way that the presence of the sensing elements, affects the field distribution. Significant improvements of these methods have been obtained by a thorough understanding of the near field distribution of the tip, and tip-sample coupling.

Another interesting technique makes use of ultra cold atoms, in the μK temperature regime. A cloud of ultra cold atoms is released on top of a microwave device, whilst an applied DC field creates the quantization axis for hyperfine transitions due to the Zeeman effect. The energy shifts of the split energy levels are obtained by sweeping the microwave frequency, thereby fulfilling the resonance condition. This experiment yields the equipotential lines across the structure. The low temperature requirement makes this technique viable for the characterisation of superconducting quantum devices [197] (MMIC's for example).

Having briefly outlined the techniques applied to EM field mapping, there is a general need for room temperature, high spatial resolution and non-invasive methods to retrieve the near-field distribution of microwave circuits. With this in mind, a method to obtain radio frequency electromagnetic field distribution is proposed, which consists in using a transmission electron microscope, operating in low angle diffraction mode (LAD). The effects of microwave fields on propagating electrons are discussed next.

7.2 Theoretical considerations

At the core of the electron interaction with EM fields lies the Aharonov-Bohm effect (field gauges). A beam of coherent electrons propagating along the optical axis z of an electron microscope can be interpreted as a monochromatic plane wave

$\Psi = Ae^{ik_z.\vec{z}}$ with complex amplitude $A = A_0(r,z)e^{i\phi(r,z)}$. The effects of propagation of the electron beam in a region with non-zero electric and magnetic potentials can be expressed as a phase gradient $\nabla\vec{\phi}(r,z)$, which is given by [202]:

$$\nabla\phi(x,y) = C_U\nabla(t\vec{V}(r)) - \frac{e}{\hbar}[\hat{n}_z \times t\vec{B}(r)] \tag{7.1}$$

where the constant C_U is given by $C_U = \left(\frac{2\pi}{\lambda}\right)\left(\frac{U+U_0}{U(U+2U_0)}\right)$. The term λ corresponds to the electron wavelength and the terms U and U_0 correspond to the kinetic energy and rest mass energy of the electrons, respectively. The term t corresponds to the distance over which the magnetic field is non-zero, $B \neq 0$ and $\hat{n}_z$ the unit vector parallel to the propagation direction of the electrons. The first term on the right accounts for the gradient of the potential $\vec{V}(r)$ and the second term accounts for the induction field components perpendicular to propagation direction.

The intensity distribution of an image obtained with LAD corresponds to a magnified view of the pattern formed in the back focal plane of the image forming lens [203]. In this plane, the electron wave is given by the Fourier transform $\mathcal{F}[A_0e^{i\nabla\phi.\vec{z}}]$ of the wave transmitted through the region with non-zero EM fields. Thus the intensity pattern imaged in LAD corresponds to the magnitude of $|\mathcal{A}_0e^{i\nabla\phi.\vec{z}}|^2$.

Figure 7.1 illustrates the formation of a diffraction pattern resulting from an 'ideal' specimen with two magnetic domains, whose magnetic moment is in opposite direction, and separated by a domain wall (neglected). The LAD pattern was obtained following the implications of Eq. 7.1 described above.

In cases where the magnetic induction can be considered uniform across the film thickness and the gradient of the potential may be neglected, the diffraction pattern can be described as two intensity spots deflected by an angle β. The deflection angle, β, is directly proportional to the thickness, t, of the region with non-zero magnetic induction, B_0, as expressed in Eq. 7.2.

$$\beta = \frac{e\lambda B_0 t}{h} \tag{7.2}$$

Figure 7.1 presents an intermediate step, showing the behaviour of the phase variation. Often the field gradients are not uniform and thus generate complex deflection patterns which require an understanding beyond the classical approach taken in Eq. 7.2. In this case, one must consider Eq. 7.1.

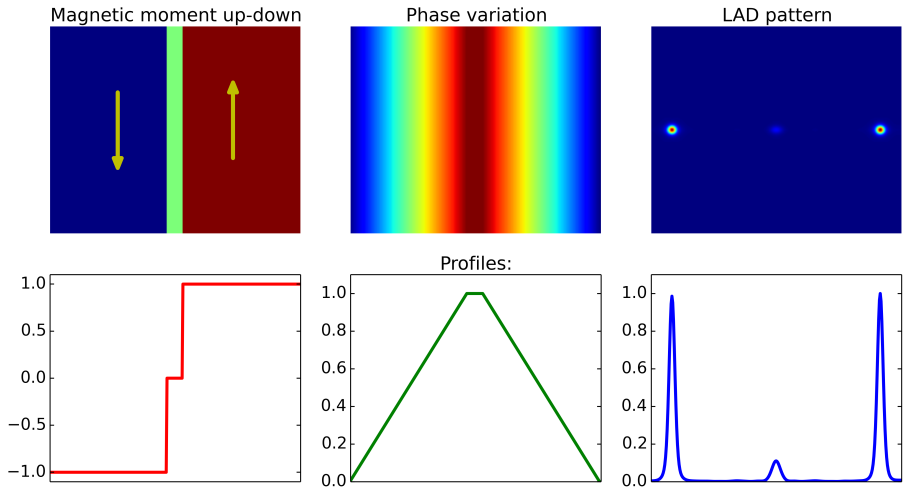

Figure 7.1: Illustration of the effect of two magnetic domains on the electron beam. Two magnetic domains opposed to each other (left) induce a phase shift (center) on the travelling electron beam. When the image is acquired in the back focal plane of the image forming lens, the pattern observed resembles the image shown on the right, which is known as LAD pattern. Horizontal axis corresponds to the horizontal spatial profile of the magnetic state shown. From a classical perspective, the electron beam experiences a Lorentz deflection proportional to the layer thickness and magnetic induction, as expressed in Eq. 7.2. The separation between the two spots on the image on the right correspond to 2 × the deflection angle, β. Small amplitude signal at the centre of the LAD pattern corresponds to the undeflected beam which crossed the domain wall where the net induction field is assumed negligible.

Having discussed an example of static field distribution, it is now relevant to discuss the nature of dynamic EM fields, in the microwave frequency range. EM fields in the microwave range are time and space varying waves whose electric field component can be expressed as [133]:

$$\vec{E} = \Re\{\vec{E}_0(x, y, z)e^{i\omega t - \vec{k}.\vec{r}}\}, \tag{7.3}$$

where E_0 is the wave amplitude, ω is an angular frequency and k represents the propagation vector. Following Maxwell's equation, $\nabla \times \vec{E} = -i\omega\mu_0\vec{H}$, the magnetic field component can be obtained as $\vec{H} = \hat{n}_z \times \vec{E}/Z_0$, where Z_0 corresponds to the impedance and $\hat{n}_z$ represents a unit vector parallel to the propagation direction. For simplicity, assume that the wave vector, $\vec{k}$, propagates along $\hat{z}$ (only $\vec{k}.\hat{z} \neq 0$) and that $\vec{E}$ and $\vec{H}$ are transverse wave modes so the field components are along $\hat{x}$ and $\hat{y}$. If only the time varying components of Eq. 7.3 are considered (fixed z= 0), the

electric field can be written as

$$\vec{E} = \hat{x}E_0^x \cos(\omega t) + \hat{y}E_0^y \sin(\omega t). \tag{7.4}$$

Note that at a fixed position $z = 0$, the electric field direction rotates with ωt following what is defined as a polarisation state. The relative amplitude of the E_0^x and E_0^y as well as the phase, given by

$$\phi = tan^{-1} \frac{E_0^y \sin(\omega t)}{E_0^x \cos(\omega t),} \tag{7.5}$$

will define the polarisation of the electric field. EM waves can be described as linearly polarized if either E_0^x or E_0^y components are zero or $\phi = \pi/4$ radians. The waves will have circular polarisation if $E_0^x = E_0^y$ and $\phi = \pi/2$ radians. Elliptical polarisation will be obtained for $E_0^x \neq E_0^y$. The case described above consists in evaluating a single polarisation state, which is suitable if a single transverse EM wave has a well defined propagation direction. In a microstrip with non-linear features, such as loops or bends, the polarisation state will not be as trivial since propagating waves cannot be approximated to transverse EM modes. Their propagation direction cannot be trivially determined since the propagating modes in the loop shaped region of the microstrip are hybrid transverse electric (TE) and transverse magnetic TM) modes.

7.3 Experimental results

In this work, the deflections originating from the EM distribution in a loop shaped microstrip were investigated using low angle diffraction (LAD). Figure 7.2a shows the geometry of the structure. The microstrip was designed to fit on a TEM specimen holder, as shown in Fig. 7.2b. In the interior region of the loop, the Si substrate was etched so that the electron beam could propagate freely along the optical axis of the TEM column (Fig. 7.2c). Due to the complexity of the EM wave modes, the field distribution in the loop shaped region was not determined analytically but instead, microwave simulations were used to obtain a numerical solution. [1]

A vector network analyser (VNA) was used as a source of microwave signal as well as the analyser for the reflection parameter S_{22}. The VNA output RF power was

[1] In the quasi-static approximation, as discussed in Sec. 3.3, quasi-TEM modes were assumed along the microstrip, except in the loop shaped region, where this approximation is incomplete.

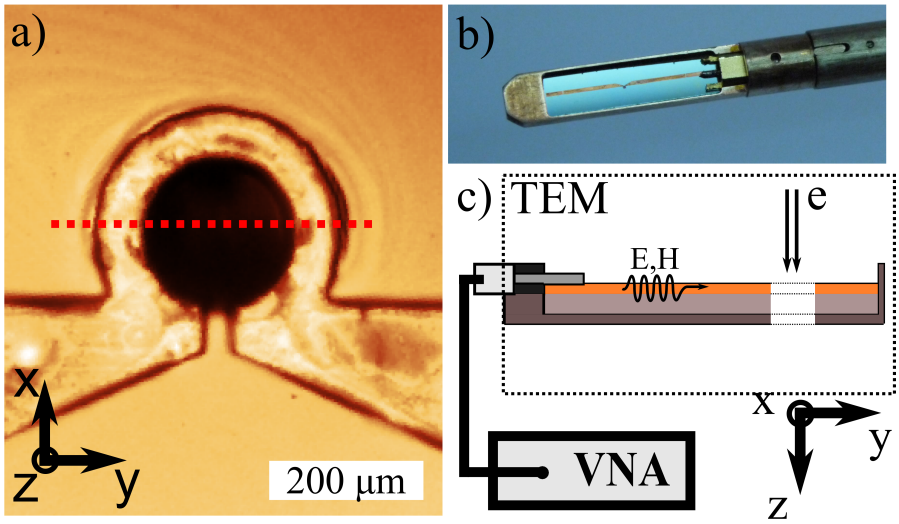

Figure 7.2: Microwave device used in the experiments. a) Optical image of the loop shaped region of the waveguide (3 μm thick copper metal layer) fabricated on top of an Si (undoped) substrate. In the center of the loop hole, the Si has been etched to allow the transmission of the electrons. b) TEM specimen holder is set as the ground for the waveguide. c) Schematic of the setup.

set to 15 dBm (31 mW). The description of the apparatus can be found in Sec. 3.3. The loop shaped microstrip used in this experiment was fabricated via optical lithography, on a Si substrate. The width of the loop shaped signal line is 80 μm, the hole diameter is 0.2 mm and the microstrip feed line is 0.5 mm wide. The Si substrate was 4.5 mm wide, 20.0 mm long and 0.525 mm thick, to meet the specimen holder geometry and height limits within the confinement of the pole pieces, inside the TEM. Using a microwave simulation tool (CST, see appendix Sec. C), the effective dielectric constant $\epsilon_{eff} = 8.65$ (averaged over the frequency range) as well as the input port impedance $Z_0 = \sim 50\ \Omega$ were determined.

The in-situ experiments were performed on a FEI Tecnai T20 TEM with an accelerating voltage of 200 kV using Lab_6 filament source of electrons. The acceleration voltage defines the wavelength (energy) of the electrons, which in this case corresponds to 2.5 pm. The filament source plays a relevant role in defining the coherence of the electron beam and therefore its suitability for this type of experiments (LAD) where parallel illumination is assumed. The camera length in LAD used was 410 m. A condenser aperture with 30 μm diameter was added and the spot size was increased to number 7 to spread the illumination, which resulted in a beam diameter

of approximately 100 μm. For the camera acquisition, the electron counts at the peak position were set to 3000 electrons, to avoid over exposure. Further details on the LAD technique can de found in Sec. 3.4.

Prior to the frequency sweep, the LAD pattern of the undeflected beam (L_0), without any excitation field (RF power off), was recorded. This data was used as a reference for the analysis (details in Appendix E) of the experimental data. Also, by measuring the half width at half maximum of the beam profile the beam divergence could be estimated. Following the description of the LAD technique in Sec. 3.4 a reference image of a gold cross grating was acquired, in order to determine the Bragg diffraction angle of a known periodic structure and thus determine the angular resolution in the camera length used. The reference image provided a net diffraction angle as the distance (in pixels or radians) from the centre spot to the first order of the diffraction pattern. Then, by dividing the net deflection angle by the number of pixels it was determined that the deflection angle per unit pixel was 0.04 μradians.

Figures 7.3- 7.5 show a number of LAD patterns acquired while sweeping the frequency of the microwave source from 1 GHz to 18 GHz. As the frequency is varied the electron beam is deflected. In addition to this, the pattern appears to rotate continuously with the increase in frequency. Over the entire frequency sweep, the electron beam acquires elongated, elliptical and circular shapes. Note, the elongated beam profiles at f= 8.48 GHz and f= 14.77 GHz, elliptical shapes at f= 5.42 GHz and f= 12.22 GHz and circular shapes obtained at f= 5.59 GHz. At f = 16.64 GHz the beam appears undeflected due to low field amplitude. Later it will be discussed how this is related to high signal losses in the circuit.

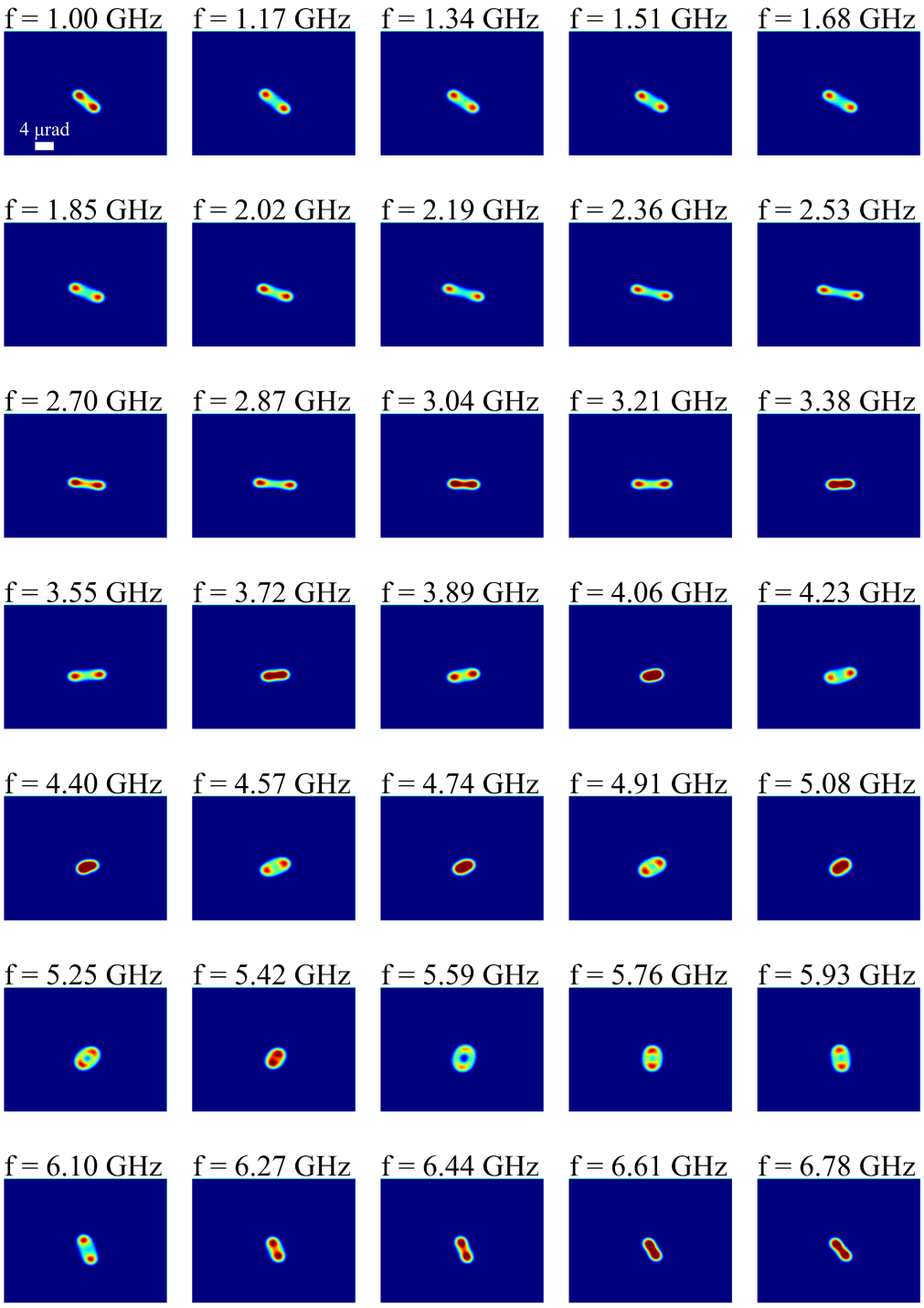

Figure 7.3: LAD pattern of the electron beam transmitted through the hole in the loop shaped waveguide at f= [1-6.78] GHz.

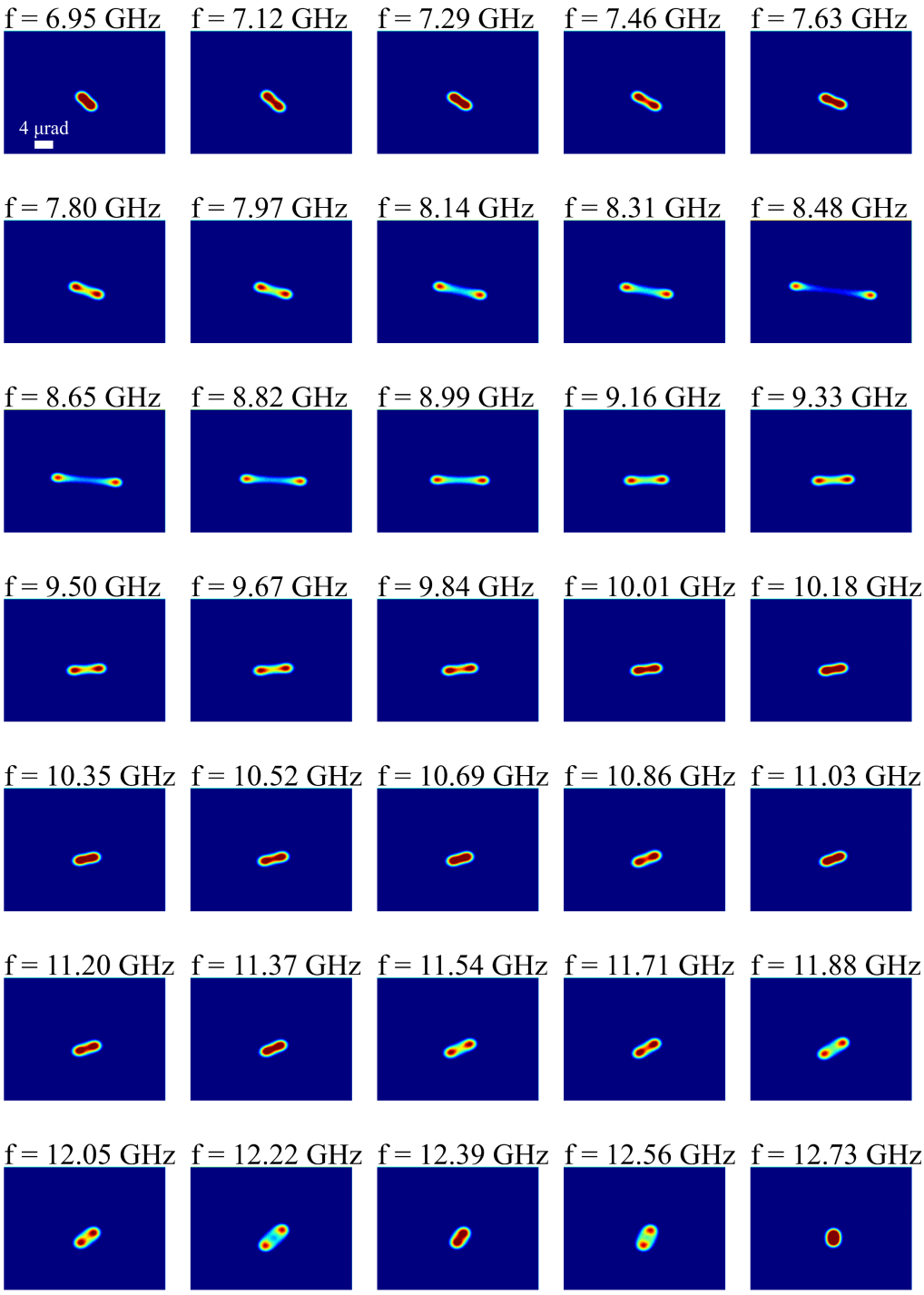

Figure 7.4: LAD pattern of the electron beam transmitted through the hole in the loop shaped waveguide at f= [6.95-12.73] GHz.

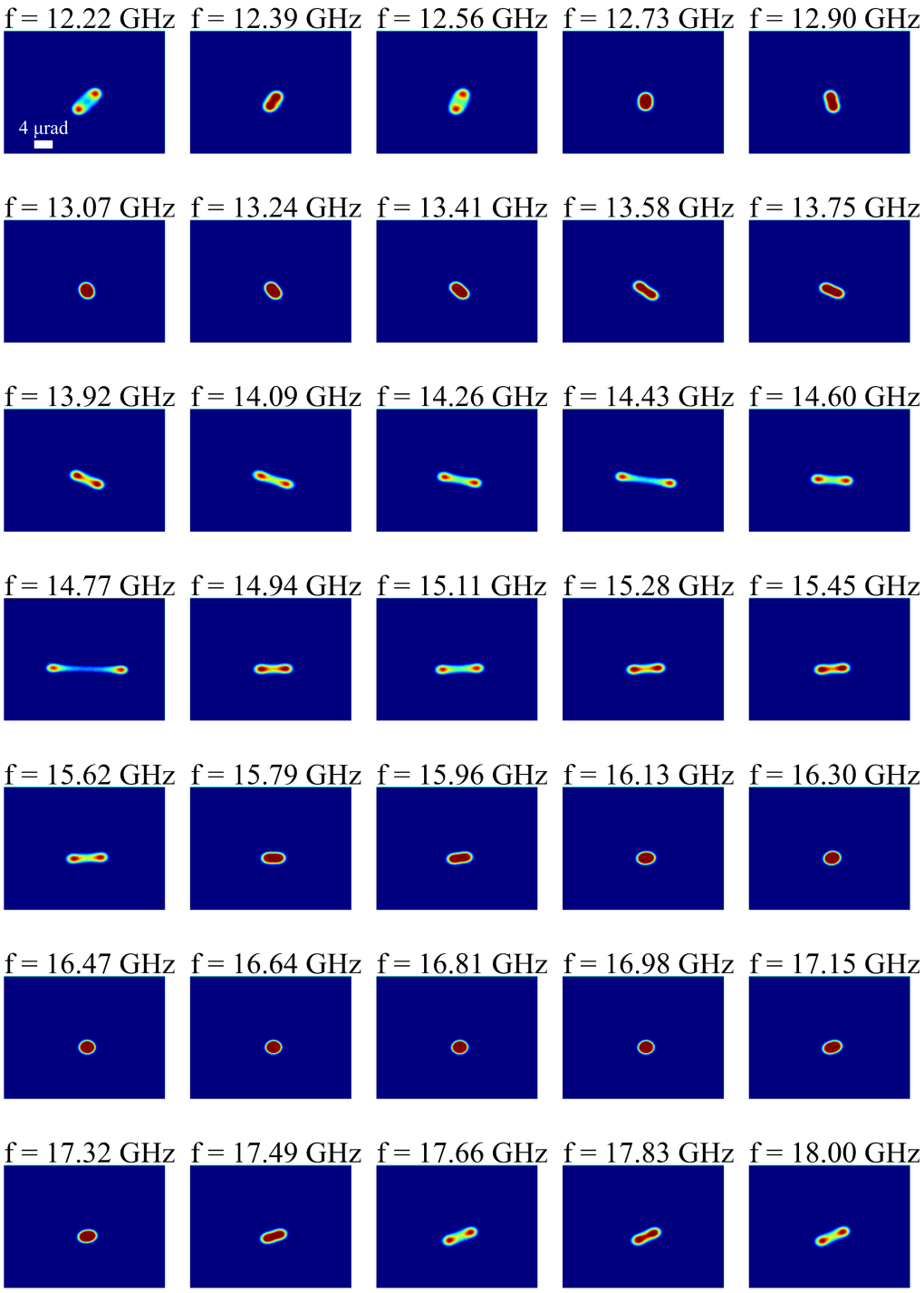

Figure 7.5: LAD pattern of the electron beam transmitted through the hole in the loop shaped waveguide at f= [12.22-18] GHz.

Considering the discussion in the Sec. 7.2 regarding the Aharonov-Bohm effect and the existence of EM polarisation states, the different LAD patterns can be seen as a result of the in-plane components of the polarisation states of the dynamic EM fields which are inherent to the loop shaped region. An analogy may be established with the LAD pattern obtained in Fig. 7.1, with the key difference that instead of two peaks, deflected by β, one observes a time averaged EM magnitude forming a deflection pattern. This pattern encodes the in-plane polarisation of the EM field.

Figure 7.6a illustrates the procedure to analyse the experimental data. In the LAD pattern shown here, the position of the intensity maxima was measured in terms of the deflection along v_x and v_y, and the rotation angle, ϕ. In principle, the components v_x and v_y correspond to the orthogonal EM field components in the plane of the loop shaped microstrip. These are measured here in terms of the deflection angle. The peak position, the ellipticity of the beam shape and the rotation angle, ϕ, relative to the vertical axis were obtained from the images by using a shape detection routine, implemented in Python. An example of the processing steps is shown in appendix Sec. E.2.

Figure 7.6b shows the amplitude of the beam deflection in terms of the two orthogonal directions v_x and v_y in the LAD pattern and the rotation angle ϕ (inset) of the LAD pattern as a function of the microwave frequency.

To understand the experimental observations, the electric and magnetic field distributions were calculated using CST® microwave studio.

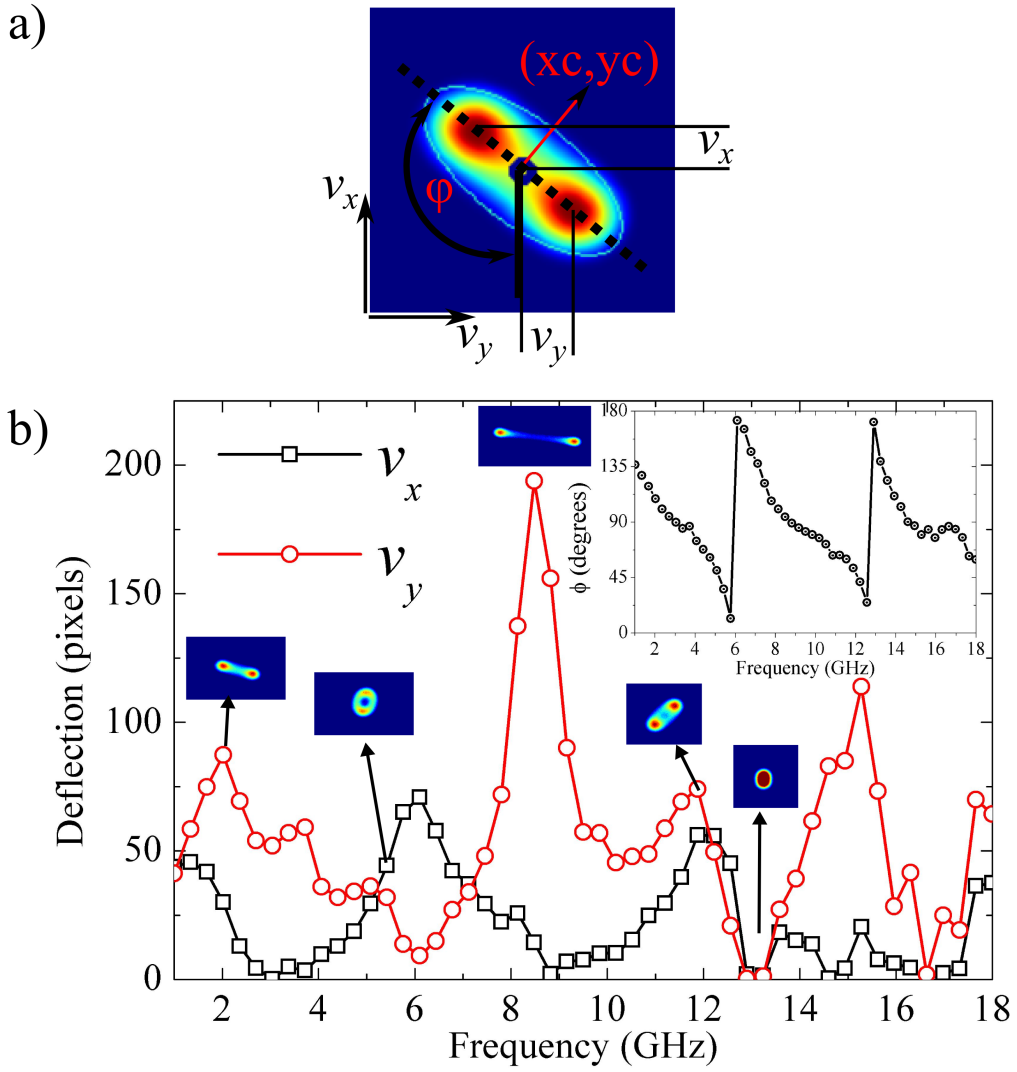

Figure 7.6: a) Illustration of the measured quantities v_x, v_y and ϕ. b) Deflection amplitudes projected along the v_x and v_y axis as function of frequency. The inset shows the extracted rotation of the beam patterns. The inset images shown represent the experimental data obtained while performing the frequency sweep.

7.4 Microwave simulations

The response in frequency and the port impedance was calculated with CST® microwave studio. The simulated structure was comprised of a rectangular shaped $4.5 \times 20.5 \times 0.525$ mm substrate with a 0.525 mm wide signal line with input port impedance Z_0= 50 Ω. In the loop region, the width of the signal line was reduced to 0.080 mm, in order to obtain enhanced field strength in the hole region. Further details on the simulated structure can be found in Sec. 3.3. The background walls were set 4 mm away from the sides of the substrate and 8 mm away from the top of the waveguide. The boundary conditions at the walls of the background were set to open and electric. The calculated microwave response was identical in both situations indicating that the reflections from the conducting walls at the boundaries are negligible. Further details on the simulation tool can be found in appendix Sec. C.

From the microwave simulations, the EM field components were obtained, within a distance of 8 mm above and 1 mm below the signal line. The extracted volume is representative of the near-field distribution as the distance from the antenna is smaller than the characteristic wavelength of the microwaves $D<\lambda$. The appendix Sec. E shows several images corresponding to the field distribution as a function of distance from the waveguide. At an height of 8 mm the field has decreased by a factor of 100 relative to the field magnitude at the microstrip surface and at a distance of 1 mm below the waveguide, the EM fields are largely suppressed mainly due to the presence of the ground plane at a distance of 0.525 mm below the signal line. The EM fields were probed over a frequency range from 1 to 18 GHz ($\lambda \sim$ 30-1 cm). The volume information is illustrated in Fig. 7.7a by equally spaced nodes, where the $\vec{E}/\vec{H}$ vectors are calculated.

The form of the extracted $\vec{E}$ and $\vec{H}$ fields is represented in Eq. 7.6 as a function of the coordinates (x,y,z).

$$\begin{bmatrix} E^x(x,y,z) \\ E^y(x,y,z) \\ E^z(x,y,z) \end{bmatrix} = \begin{bmatrix} E_0^x \\ E_0^y \\ E_0^z \end{bmatrix} + exp \begin{bmatrix} \phi_0^{ex} \\ i\phi_0^{ey} + i\omega t \\ \phi_0^{ez} \end{bmatrix} \tag{7.6}$$

At each value of ωt, the cuboid corresponding to each field component represented

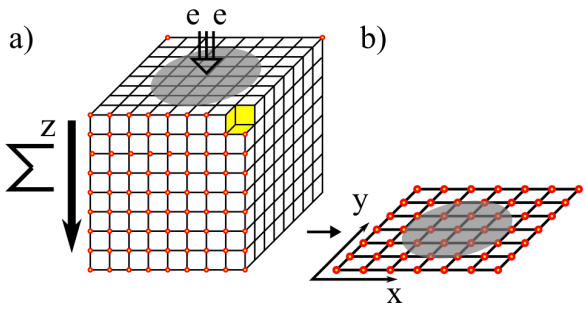

Figure 7.7: The cuboid (a) represents the volume of information extracted from CST, which is then reduced to a single plane (b) by performing a sum along the direction of propagation of the electron beam.

in Eq. 7.6 is reduced to a single plane by performing a sum of the field values along the z direction, as shown in Fig. 7.7a-b. This approximation takes into account the fact that the time required for the electrons to cross the field region ($\sim$ 25 ps) is smaller than the characteristic time of the oscillating fields (55 ps).

The sum of the $\vec{E}$ and $\vec{H}$ field components over the entire height range at a frequency f= 8.7 GHz is shown in Fig.7.8. The dashed circles correspond to the inner diameter of the loop shaped microstrip. Note the dominance of the y component of the E field.

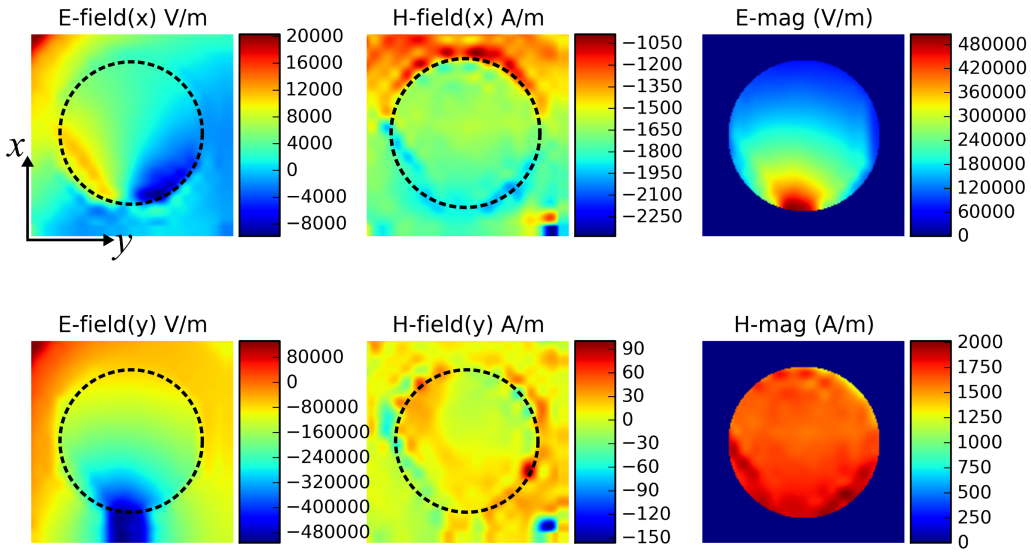

Figure 7.8: Field distribution at f= 8.7 GHz and processing steps for ωt= 0 (top). From left to right: in-plane field components and its magnitude multiplied by a top hat coincident with the hole diameter, to mask regions opaque to the electron beam. Asymmetry in the distribution of the E-field emerges due to the gap in the omega shape of the microstrip (See Fig. 7.2a).

Following the Aharonov-Bohm effect discussed in Sec. 7.2, the phase variation corresponding to each direction can be calculated. From Eq. 7.1, the phase terms ϕ_x, ϕ_y and ϕ_z, experienced by the travelling electrons, given by the gradient of the electric potential, $\vec{V}$ ($\vec{E}$= -$\nabla\vec{V}$), and by the transverse component of the magnetic field, can be expressed as

$$\phi_x(x,y) = C_U \sum_{zmin}^{zmax} E^x(x,y) - \frac{e}{\hbar} \sum_{zmin}^{zmax} H^y(x,y) \tag{7.7a}$$

$$\phi_y(x,y) = C_U \sum_{zmin}^{zmax} E^y(x,y) - \frac{e}{\hbar} \sum_{zmin}^{zmax} H^x(x,y) \tag{7.7b}$$

$$\phi_z(x,y) = C_U \sum_{zmin}^{zmax} E^z(x,y)dz \tag{7.7c}$$

$$\phi(x,y) = \phi_x(x,y) + \phi_y(x,y) + \phi_z(x,y) \tag{7.7d}$$

The constants are defined in Sec. 7.2. In the case of ϕ_z, only $E^z(x,y)$ is considered since the z component of the magnetic field does not affect the electron beam ($\vec{n}_z \times \vec{H}_z$= 0).

Equations 7.7 are valid at a static phase. The time dependence is encoded in ωt and can be implemented by applying Eq. 7.7 N times, in the range of ωt= [0,2π]. Effectively, this process will generate N phase patterns, each corresponding to a time step in the oscillation of the EM field, at a fixed frequency.

At each of the N steps of ωt, the Fourier transform ($\mathcal{F}$) of the wave-function is determined, which describes the electron beam crossing the field region in the hole. To account only for the hole region, the phase distribution is multiplied by top-hat function, $\Pi(x,y)$, in order to match the region illuminated by the electron beam (circular aperture). Ultimately, the illuminated region is coincident with the inner diameter of the loop. This leads to an expression for the wave-function of the form:

$$\psi(\omega t) = \mathcal{F}[\Pi(x,y) \times e^{i\phi_x(x,y)+i\phi_y(x,y)}] \tag{7.8a}$$

$$I(\psi) = \sum_{\omega\Delta t=0}^{2\pi} \mid \psi \mid^2 \tag{7.8b}$$

The LAD pattern corresponds to the intensity of ψ, as shown in Eq. 7.8b, since the intensity profile is imaged at the back focal plane of the image forming lens.

Figure 7.9 shows the phase terms $\phi_x(x,y)$, $\phi_y(x,y)$, the resulting $\phi(x,y)$ and the corresponding intensity profiles obtained from Eqs. 7.8, using the EM field

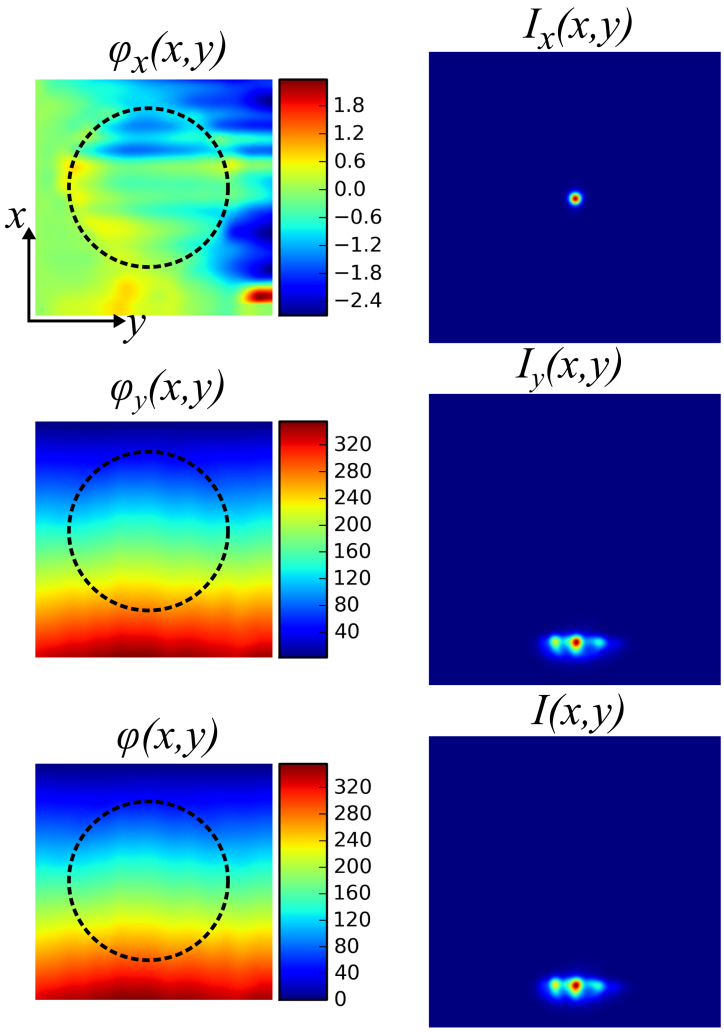

Figure 7.9: Resulting phase, in radians, from the individual and combined EM field components along x and y, corresponding to f= 8.7 GHz at ωt= 0. Corresponding intensity patterns. Encircled region in the phase images correspond to the top-hat function $\Pi(x, y)$ (circular aperture), as shown in Eq. 7.8b.

distribution relative to f= 8.7 GHz. In the example shown here, the term $\phi_x(x, y)$ does note appear to modify the diffraction spot, while the term $\phi_y(x, y)$ dominates the phase variation, seen by the strong displacement with respect to the centre of the intensity plot. As a consequence, it is noted that the total intensity pattern is similar to the intensity pattern using only ϕ_y ($I(\phi) \sim I(\phi_y)$).

Figure 7.10 shows the intensity profile resulting from the phase modifications experienced by the beam, while only the out-of-plane component of the electric field is considered, as expressed in Eq. 7.7c. The out-of-plane component of the electric field has a negligible effect on the phase of the electron beam so the diffraction

pattern resembles one of a circular aperture, imposed by the function $\Pi(x, y)$.

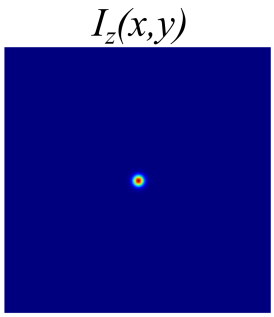

Figure 7.10: Contribution of the out-of-plane E-field component on the phase of the electron beam. The scaling factors are the same as for the in-plane components. Magnetic field components were not considered since this field direction is collinear with the electron beam propagation direction.

The time averaged intensity image is obtained by performing a sum of all N intensity profiles. In the following section, the time averaged LAD obtained from the simulations will be compared with the experimental observations.

7.5 Discussion

As discussed in earlier sections, the intensity patterns obtained in the LAD experiments correspond to the deflections caused by the EM field strength in the region of the loop shaped microstrip. To further investigate this possibility, the calculated LAD patterns, are compared to the experimental data. The calculated intensity profiles were obtained at each ωt= [0,2π] in N steps and then a sum was performed over all the intensity profiles, to result in the time averaged intensity distribution. A comparison between the experimental data and the patterns generated from the numerical calculations is shown in Fig. 7.11.

Note the agreement in terms of the deflection magnitude and polarisation state, at f= 2.5, 5.79 and 8.7 GHz. However, in the remaining patterns, the agreement is almost non-existent, both in terms of the deflection magnitude and polarisation. In general, the mismatch between the experiments and the simulations increases with frequency. This is possibly due to the fact that in the experiments, the microwave power decreases with increase in frequency due to losses in the connectors and cables. As a consequence, there is low EM field strength available to deflect the electron

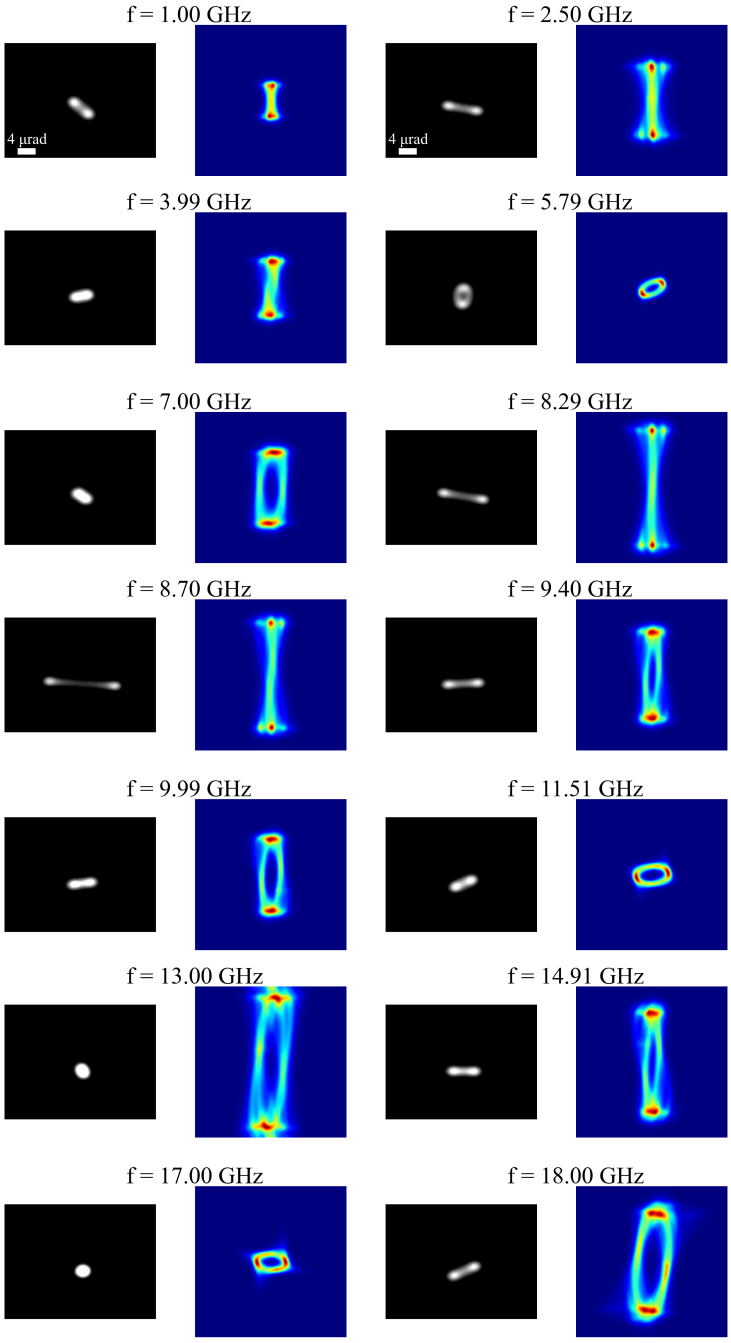

Figure 7.11: Images in black and white (1st and 3rd columns) correspond to the experimental LAD data while the colour images (2nd and 4th columns) correspond to the calculated patterns.

beam. On the other hand, the calculated patterns are a result of uniform input power across the frequency range here investigated. Across the whole frequency range, the calculated patterns are predominantly linearly polarized along one direction as for example at f= 8.29 GHz and 8.70 GHz. However, note also the circular and elliptical polarisations at f= 5.79 GHz and f= 11.51 GHz.

Figure 7.12a allows a comparison between the net beam deflection ($\sqrt{v_x^2 + v_y^2}$) obtained in the experiments and the power delivered to the circuit ($1 - S_{22}$), obtained from the microwave simulations. Note that for $f < 10$ GHz, the variation of the deflection is similar to that of the power delivered to the microstrip. However, for $f > 10$ GHz the agreement is lost due to an increase in the signal attenuation at higher frequencies. In Fig. 7.12b the reflection coefficient, S_{22}, measured with the VNA, is compared with the net beam deflection.

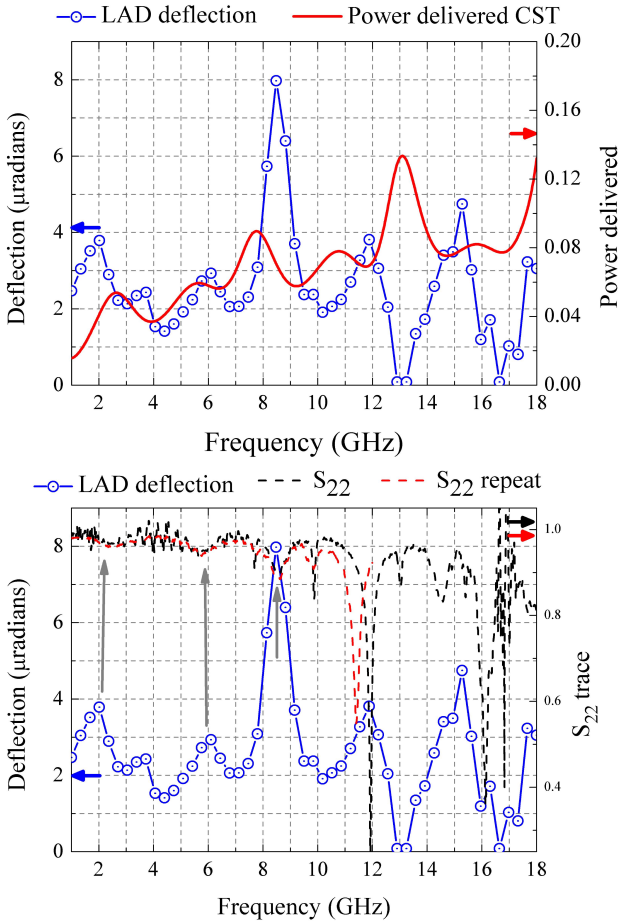

Figure 7.12: Comparison between the power delivered (1-S_{22}), the LAD deflection angles and S_{22} parameter measured with the VNA.

Again, it is noted that the oscillation in the LAD patterns appears to correlate with the oscillation of the S_{22} parameter measured in the VNA. The minima of S_{22} at $f = 2.5$, 6, 8.8 GHZ, signed with the gray arrows, are coincident with the (local) large deflections in the LAD pattern. The signal measured in the VNA exhibits a ripple-like, oscillatory, behaviour (short wavelength), which can be caused by signal losses in the coaxial cables due to impedance mismatch.

To understand and interpret the differences between the LAD data and the VNA spectra, consider the schematic of a simple transmission line, shown in Fig. 7.13, which can be seen as an equivalent circuit to that of the microstrip used in the experiments. i.e. a transmission line terminated by an high load impedance, Z_L ($Z_L \gg Z_0$), since one side of the microstrip has an open-port termination. The propagation constant, γ, of the travelling voltage, $V(x) = V_o^+ e^{-\gamma x}$, and current, $I(x)$=$I_0^+ e^{-\gamma x}$, waves is assumed complex as the transmission line has losses due to finite conductivity and dielectric losses, γ= α +$j\beta$. The attenuation constant (α) and propagation constant (β) are defined by the resistance (R), inductance (L), capacitance (C) and conductance (G) of the circuit. In the low-loss limit, these can be written as α= $R\sqrt{C/L}$ and β= $\omega\sqrt{LC}$. In a more accurate approach, the inductance of the loop shaped microstrip would have to be included in the total impedance of the circuit.

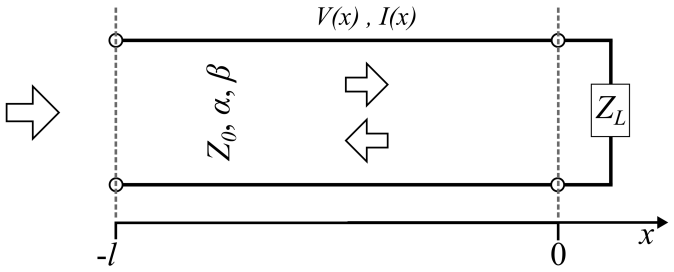

Figure 7.13: Illustration of the circuit equivalent to the microstrip used in the VNA and LAD experiments. Inward and outward arrows illustrate the input and reflected waves.

The voltage and current waves propagating in the circuit are given by [133]:

$$V(x) = V_o^+(e^{-\gamma x} + \Gamma e^{\gamma x}) \quad and \tag{7.9a}$$

$$I(x) = \frac{V_o^+}{Z_0}(e^{-\gamma x} + \Gamma e^{\gamma x}), \tag{7.9b}$$

where Γ= $\dfrac{Z_L - Z_0}{Z_L + Z_0}$, is the reflection coefficient at x= 0 and V_o^+ the input voltage amplitude. Note that the circuit is operating in open-port, which implies that the load impedance Z_L can be considered large when compared to the input port impedance, Z_0. As consequence of $Z_L \gg Z_0$, there is nearly total reflection of the propagating voltage and current, since $\Gamma \to 1$. This enables the emergence of standing waves in the length of the circuit. Due to losses in the circuit and impedance mismatch, the power loss must be accounted for. The total power loss (P_{loss}) can be obtained

from the difference between the incident and reflected waves [133]. This is what one observes on both VNA and LAD patterns. In the VNA spectra, one measures the signal which is proportional to $1 - P_{loss}$, while the deflection in the LAD experiments appears as a function of the P_{loss}, directly. The major difference is that the VNA spectra shows the loss from the whole circuit, while the LAD shows the losses of the signal, existing only in the section of the loop cavity.

The possibility of measuring the EM field strength as a function of position in the loop shaped microstrip is discussed next.

By moving the stage of the microstrip with respect to the electron beam it was possible to partially block the illumination. Figure 7.14 shows the deflections v_x and v_y measured in five different regions of the loop shaped region (inset). Note that the deflection amplitude is similar on all positions probed. The beam diameter was too large (100 μm) to detect local variations in the EM fields, as shown by the fact that the probed regions all display a similar behaviour with frequency.

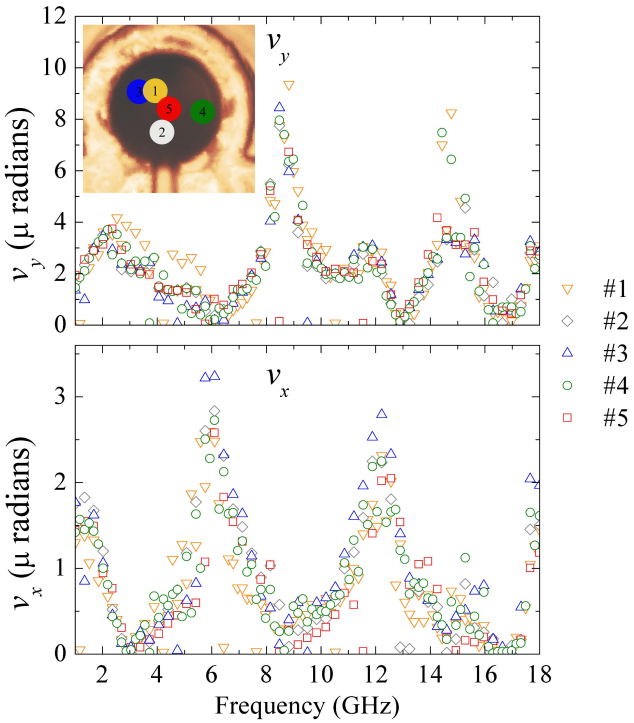

Figure 7.14: Deflections v_x and v_y measured in five different regions of the loop shaped region. This was obtained by shifting the waveguide with respect to the electron beam.

Figure 7.15 shows the phase measured in the VNA and the rotation angle, ϕ, of the LAD patterns, both as a function of frequency. The phase measured with the

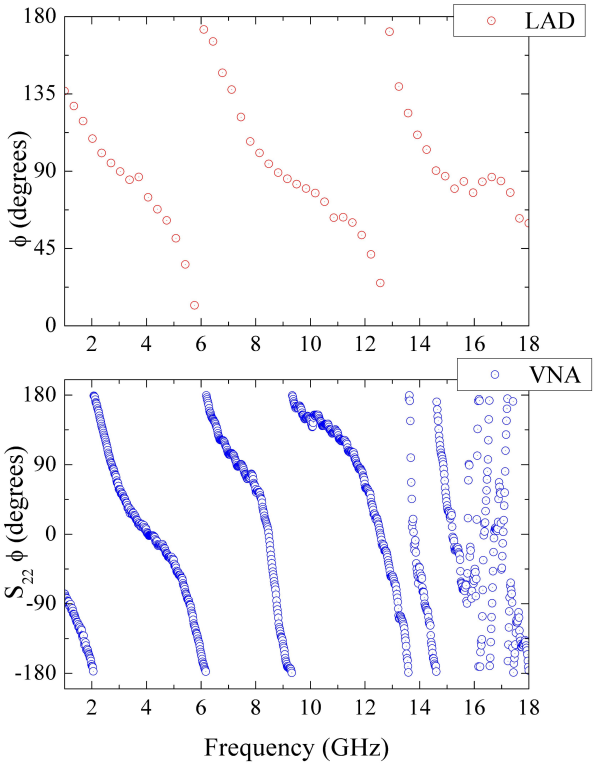

Figure 7.15: Rotation of the pattern as a function of the frequency (LAD), and of the phase variation obtained from measuring S_{22} in the VNA. At each frequency, the expected phase difference between the VNA and the LAD data is proportional to the difference in propagation distances l and l', relative to open-port.

VNA regards the variations of the travelling waves from the input port at x= -l to x= 0 and the return path (consider Fig. 7.13), so the total phase can be written as $\Delta\phi$= 2$l\gamma$. The rotation observed in the LAD data represents the phase variation over the distance, l', between the loop shaped region and the load impedance (open-port) termination, resulting in a phase variation $\Delta\phi$= 2$l'\gamma$. However, the phase difference may vary given that in this circuit, the open-port termination is not the only source of reflections, as the impedance varies also due to the loop shape region itself.

The reflection coefficient S_{22} obtained from the VNA, provides the overall response of the microstrip, whereas the electron beam deflection is a direct measure of the fields in the confined regions of the structure.

7.6 Conclusions

In this chapter it was demonstrated that LAD can be used to map the in-plane EM field distribution in the gigahertz frequency range. This technique provides a unique way to study the dielectric properties of thin films or optimized planar structures (or sections), in addition to the combined high resolution structural and elemental analysis inherent to CTEM or STEM. From the viewpoint of characterising magnetic structured materials, this technique allows for in-situ microwave field driven perturbations to be observed. Thus, an understanding of the direct effects of the microwave fields on the electron beam is crucial.

While the LAD patterns are a measure of the dominant polarisation state of the EM field in the region of the loop shaped microstrip, the effects of the magnetic and the electric field are indistinguishable since the phase alterations to the electron beam depend on both. However, from the analysis of the simulation results it was noted that the deflections are largely dominated by the electric field.

The calculations of the LAD patterns, using the EM field distribution obtained from the microwave simulations, were carried out following the considerations of the Aharonov-Bohm effect. To fully represent the electron beam trajectory across the TEM column, further considerations must be taken, to account for the aberration imposed by the magnetic lens system.

The position dependent mapping of the deflection was not successful due to the dimensions of the area illuminated by the electron beam when compared to the diameter of the loop shaped microstrip. To overcome such limitation, one may consider the use of a focused electron beam, in a scanning TEM, operating in the Lorentz DPC mode.

Chapter 8

Conclusions and outlook

Research in nanostructured magnetic materials has attracted great attention due to the potential use of enhanced spin wave properties in material science and technology. In particular, antidot lattice structures (ADL), were proposed for microwave filtering [5–8] and magnetic logic devices [3, 4]. These are interesting not just from the magnonics perspective, but also from the view point of making ADL more applicable, towards the use in sensors for functionalised magnetic nano-particles [204]. Periodic modulation of materials, combined with the highly non-uniform demagnetisation fields, which are a result of the distribution of magnetic poles around the hole edges, offers the possibility to control the static properties, via the manipulation of the reversal processes, coercivity and local anisotropies. On the other hand, it has been demonstrated that with structuring, spin waves can become highly sensitive to local internal fields. To further modify the static and spin wave properties, one can make use of external magnetic fields, exchange bias, or multilayer structuring. In the latter, dipolar inter-layer coupling between adjacent ferromagnetic layers can affect the net pole distribution of one another, which in turn affects the spin wave response.

The driving forces of this research field were the recent advances is the fabrication [205] and characterisation [6, 79]. At the fabrication level, patterning with nanometer resolution allows unprecedented control over the anisotropic properties and has enabled access to spin wave interactions on the length scale of dipole-dipole, magnetostatic, interactions and further down to the length scale of exchange interactions.

On the characterisation level, the study of spin waves with origin in dipole interactions is widely studied using VNA-FMR, which has demonstrated great sensitivity in the detection of localised spin wave precession modes in ADL. With this technique, the microwave excitation field induced by a current travelling in a conductive signal line, acts as the driving field for the spin waves. In order to promote the direct coupling between the excitation wavevectors and the spin waves, it is necessary to scale the conductive signal line so that its characteristic width matches the wavelength of the spin waves under study. However, this is not often accessible in terms of fabrication of both waveguide and sample. Similarly, excitation of exchange spin waves is even more difficult due to challenges in fabricating nanometer scale conductors which are capable of effectively coupling energy to this type of spin wave. A modified VNA-FMR apparatus, whereby the excitation source and the detection probe are independent from each other, allows the excitation and detection of high frequency spin waves. This technique is referred to as all-electrical spin-wave spectroscopy (AESWS) and enables the study of the spin wave dispersion with respect to both applied field and spin wave propagation direction [107, 113, 206]. Other inductive techniques are available such as pulse inductive microwave magnetometer, which uses pulsed microwave excitation, combined with time and space resolved Kerr microscopy [79]. A powerful technique is Brillouin light scattering (BLS). BLS is an optical technique which relies upon the inelastic scattering of light via spin wave excitations in magnetic systems, enabling the study of wave vector resolved spin wave dispersion [175, 207].

The focus of this thesis was the effect of the demagnetisation fields on the magneto-static and spin wave properties of exchange biased ADL, in single and multi-layer configurations. The soft magnetostatic spin waves modes were studied using VNA-FMR, as a function of the applied field magnitude and direction relative to the ADL symmetry. This study allowed the characterisation of the magnetic system in terms of effective anisotropy and to demonstrate that exchange bias raises an asymmetric (static and dynamic) response with respect to the direction of the applied field. The FMR results show an 8-fold dependence with the applied field direction relative to the lattice, which can be attributed to the next-nearest neighbour (NNN) interactions. The contribution from the NNN may be enhanced in this particular

case due to the existence of the continuous layer, adjacent to the ADL. The spin wave properties of ADL systems were studied, following the Damon-Eshback configuration ($\vec{k} \perp \vec{M}$), using BLS. When possible, these studies were supported by micromagnetic simulations. In particular, it was possible to demonstrate the effect of exchange bias on the distribution of the magnetic poles at the hole sites of the ADL. Moreover, the modelling of the resonance behaviour of an ADL, allowed the determination of the effect of the continuous film thickness at the hole sites. The change in thickness of the continuous layer affected the anisotropic properties of the system, especially when the layer thickness is comparable to the exchange length (5.7 nm).

While the VNA-FMR setup used here cannot measure spin wave dispersion due to inappropriate excitation bandwidth of the waveguide, BLS is a more adequate technique as it enables access to a wide band of excitation wavevectors, in the range of interest. The spin wave dispersion, measured using BLS, exhibited the periodicity of the lattice ($\sim$ 420 nm) and the emergence of a forbidden frequency gap of 0.7 GHz, at the edge of the first Brillouin zone. The form of the dispersion is a direct consequence of structuring, as the periodic potential inherent to the ADL scatters the spin waves, while the frequency band gap is a direct consequence of scattering of two spin wave modes. The attempt to recreate the spin wave dispersion of the ADL discussed in chapter 5, using micromagnetic simulations, encountered an obstacle in the computational power required. To fully replicate this sample, the approximation of a single layer film is inadequate, given the structural properties examined using cross-sectional TEM. This obstacle is generally encountered when studying 3-D magnonic structures [79, 116]. Further optimization of the simulation parameters is required. A comparison to the analytical methods, employing plane-wave theory [53], may be necessary to overcome this challenge. This may be of interest due to the possibility of exploring the spin wave dispersion properties of bi-component magnonic crystals [107, 108]. Bi-component structures open new channels for spin wave propagation, by overcoming the confinement of the ADL symmetry.

Multilayer structuring has been demonstrated to modify the overall static and dynamic properties, via interlayer dipole field interactions. The static spin configuration around the holes of the ADL was investigated using high resolution Lorentz DPC TEM, which, from an overall perspective, revealed the domain behaviour

inherent to an ADL, which consists of domain formation, on the length scale of several holes, and subsequent breakup into smaller domains, confined to the second nearest neighbours. The pinning at nearest neighbour sites has been observed, which suggests that the demagnetisation fields are rather strong. Thereby a control of the magnetic state can be achieved. This study can be taken further by exploiting the presence of exchange bias, modulated in space, to obtain multi-stage reversal [4]. From the static standpoint, it was also observed that magnetic vortices emerge at the hole edges. These features are often studied in structures, such as isolated circular elements, as the ground state curls the magnetisation, forming magnetic vortices. This observation opens the possibility of studying the effect of complex magnetic textures on spin wave localisation and propagation [208, 209], since the formation and control of domain walls can be achieved in ADL, which also have well defined propagation channels for spin waves.

In the context of this thesis, three methods were used to obtain ADL structures. In particular, ADL were fabricated using (1) template assisted deposition, (2) electron beam lithography and (3) focused ion beams (FIB). Each technique presents its own advantages and disadvantages, depending on the intended application. For instance, the use in microwave applications, such as tuning of broadband microwave response, template assisted is suitable as the cost of fabricating large scale samples is lower when compared to other methods. A natural disadvantage is the degree to which one can finely tune narrow band microwave responses, as these structures often have a degree of interface roughness. For this purpose, electron beam lithography appears to the suitable candidate, as this technique allows to achieve lateral resolution at the nanometer scale. FIB is recommended only for small area patterning since it is a slow and costly process. In terms of resolution, this technique can achieve resolutions on the scale of several tens of nanometers. However, the magnetic properties of these structures may be highly modified by ion implantation [186]. Ensuring the sample quality in terms of structure and contamination can be a considerable challenge. Electron beam lithography allows high resolution patterning. However if the choice of the etching method is inappropriate, the final outcome is not a well controlled structure. In particular, the reactive ion etching method used to fabricate two of the ADL reported in this thesis has not demonstrated the efficiency intended.

Structural analysis and elemental mapping allowed the assessment of the quality of the nanostructures. In method (2) it was noted that the difference in etching conditions between NiFe, Ta, and FeMn dictate the final profile of the antidots. This can be seen in the double exchange biased layer, where a clear step was obtained in the cross-section of the antidot. A more adequate way to proceed would be through the use of Argon etching, instead of the RIE method employing CH_4H_2. FIB may be seen as a time effective way of obtaining small patterned areas. Although the effects of ion bombardment have not been thoroughly discussed. It has been demonstrated that ion implantation at the edges of holes induces alterations in the grain structure, which was indeed observed in the sample studied in the Lorentz DPC experiments of chapter 6.

Nowadays, great attention is given to time and space resolved measurement techniques which in would allow high resolution imaging of magnetisation dynamics. The TEM with in-situ microwave excitation developed in the the context of this thesis addresses the high spatial resolution combined with microwave excitation. This method is, to my knowledge, unique and has demonstrated great potential for use in many different magnetic systems. One aspect left out of this work is associated with the temporal resolution for the detection of the magnetisation dynamics. To achieve this under the current circumstances, one has to consider the following paths: 1) sub-nanosecond resolved TEM data acquisition with an ultra-fast camera, which is unlikely to happen in the near future given the current limitations in terms of acquisition rate (MHz regime); or 2) time resolved magneto-optic excitation incorporated in the TEM, with the electron beam being synchronized and pulsed in the sub-nanosecond regime. This is equivalent to an all-optical pump probe method but combined with an electron beam. However, such high-end instrumentation is accessible only to few research groups.

A third alternative emerges in the light of the work presented here. It was demonstrated that EM field polarisation affects the electron beam. This, a priori, would mean that any deflections of the electron beam due to the magnetic specimen would be smeared by the deformations caused by the EM field distribution. However, if one considers a scenario where the EM polarisation is well know/controlled, then any additional deformations to the electron beam would solely be related to the

precession of the magnetisation, in case the magnetic material is driven at resonance. While at resonance, one expects to observe a change in the symmetry of the beam due to the precession cone, which is nonetheless very small in comparison to the standard deflections due to magnetic induction. To enhance the detection, one may make use of a careful correlation between the deflection pattern of the electron beam on and off resonance. This is the only way to achieve a certain degree of quantisation of the precessional motion of the magnetisation. This method may be extended to a DPC Lorentz microscopy instrument, where having a focused probe would minimise the effects of the microwave fields on the beam and would also be more sensitive to the magnetic induction of the sample. Additionally, one may also take advantage of the pixelated DPC acquisition camera, rather than the standard quadrant detector, which has been demonstrated to have enhanced sensitivity.

A breakthrough in the concept of combined static and dynamic experiments is reported in this thesis. The development of the in-situ TEM setup enables a number of experiments. In the short-term, this allows a correlation the dynamic state obtained in the FMR data with the exact spin configuration observed in the microscope. Alternatively, one may consider performing microwave assisted magnetisation reversal [210–212] experiments with the unique capability of simultaneously performing high resolution imaging. An interesting study would consist in exploring networks of nano-elements, whereby the tuning of the internal fields and the use of microwave excitation would allow imaging of modifications in the ground state of the network. Additionally, the study of active/passive microwave planar structures can also be achieved, whereby, the microwave circuit can be coupled to a DC voltage/current supply, so that both dynamic and static properties can be modified and imaged by any of the Lorentz techniques.

From a long-term perspective, the knowledge gained on ADL and the TEM in-situ microwave experiments can in future allow the realisation of experiments in the field of surface plasmon resonance (SPR) in heterostructures. Of great interest, are the coupling between the spin wave modes, excited in a ferromagnetic material and the effect of these in the SPR of nanostructured non-magnetic elements. Both, TEM in-situ microwave excitation and high resolution electron energy low spectroscopy (HREELS) are available. Both can be combined for the excitation of the precession

amplitudes and detection of plasmonic modes.

It is worth discussing the suitability of the microstrip waveguide, here implemented, for ferromagnetic resonance experiments. The design adopted was of an omega loop shaped microstrip resonator, which is normally used for operation at fixed frequency [145, 146]. However, in the experiments here reported, the microstrip was used for broadband frequency FMR measurements on samples with large area (larger than the loop region). This poses two immediate challenges: 1) the omega shape of the microstrip will induce non-uniform field excitation on the sample. The results of chapter 7 lead to the conclusion that the polarisation of the electromagnetic fields varies with frequency due to the geometry of the probed region (loop-shaped) and to the fact that the system is operating in a single port configuration. At each frequency, the polarisation state is affected by the constructive/destructive wave interference between the incoming and reflected waves. In such case, one cannot assume that microwave excitation will occur predominantly in the direction perpendicular to the static magnetisation, as it is generally assumed in spin wave dynamics. It is known that in systems with non-uniform wavevector excitation, linewidth broadening and frequency shifts may occur [138, 147], 2) to minimize the effect of the non-uniform fields, the area of the magnetic sample must be enclosed in the inner diameter of the loop shaped microstrip. In cases where experiments at fixed frequency are performed, the polarisation state of the excitation field may be obtained by performing LAD experiments, similar to those reported in chapter 7. Nonetheless, the loop shaped geometry may be advantageous since that in the region enclosed by the loop, the out-of-plane field components should be capable of driving the resonance of the magnetic material.

As the linearity of the excitation field is relevant in the study of nanostructured systems, it is anticipated that shorted straight microstrip lines or co-planar waveguides are more adequate if one requires linear excitation fields. These aspects will be addressed in future work. In order to ensure sensitivity in the in-situ FMR experiments, the ferromagnetic sample must be deposited directly on top of the signal line. The substrate is then assembled in the VNA-FMR apparatus by replacing the current waveguide configuration by a co-planar launch waveguide which is wire bonded to the substrate containing the specimen. An illustration of this configuration

is shown in Fig. 8.1. In the configuration discussed here, the coplanar structure may also be shorted, by either deposition of a metal or wire-bonding between the signal line and ground) just after the specimen, so that stronger magnetic fields can be obtained in the region of the specimen.

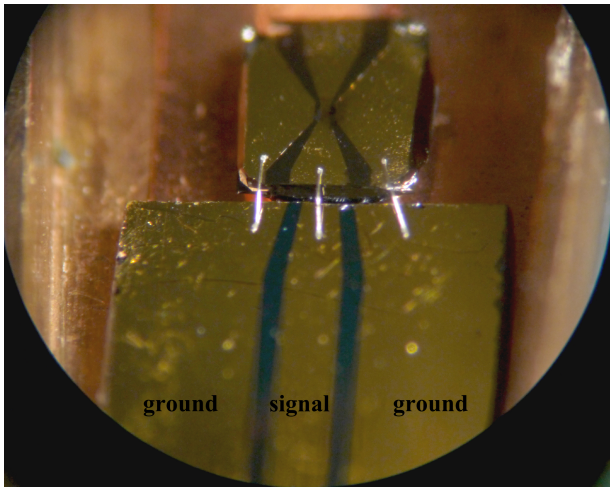

Figure 8.1: Photograph showing a TEM substrate patterned with a coplanar waveguide (and a sample). The specimen substrate is wire bonded to a second coplanar structure, for TEM in-situ microwave excitation experiments.

Bibliography

[1]R. L. Stamps et al., "The 2014 Magnetism Roadmap", Journal of Physics D: Applied Physics **47**, 333001 (2014) 10.1088/0022-3727/47/33/333001.

[2]R. P. Cowburn, A. O. Adeyeye, and J. A. C. Bland, "Magnetic switching and uniaxial anisotropy in lithographically defined anti-dot Permalloy arrays", Journal of Magnetism and Magnetic Materials **173**, 193–201 (1997) 10.1016/S0304-8853(97)00191-1.

[3]M. T. Niemier et al., "Nanomagnet logic: progress toward system-level integration", Journal of Physics: Condensed Matter **23**, 493202 (2011) 10.1088/0953-8984/23/49/493202.

[4]R. Morales, M. Kovylina, I. K. Schuller, A. Labarta, and X. Batlle, "Antiferromagnetic/ferromagnetic nanostructures for multidigit storage units", Applied Physics Letters **104**, 032401 (2014) 10.1063/1.4862317.

[5]M. Krawczyk and D. Grundler, "Review and prospects of magnonic crystals and devices with reprogrammable band structure.", Journal of physics. Condensed matter : an Institute of Physics journal **26**, 123202 (2014) 10.1088/0953-8984/26/12/123202.

[6]V. V. Kruglyak, S. O. Demokritov, and D. Grundler, "Magnonics", Journal of Physics D: Applied Physics **43**, 264001 (2010) 10.1088/0022-3727/43/26/264001.

[7]E. K. Semenova and D. V. Berkov, "Spin wave propagation through an antidot lattice and a concept of a tunable magnonic filter", Journal of Applied Physics **114** (2013) 10.1063/1.4812468.

[8]A. V. Chumak, V. I. Vasyuchka, A. A. Serga, and B. Hillebrands, "Magnon spintronics", Nature Physics **11**, 453–461 (2015) 10.1038/nphys3347.

[9]M. P. Kostylev, A. A. Serga, T. Schneider, B. Leven, and B. Hillebrands, "Spin-wave logical gates", Applied Physics Letters **87**, 153501 (2005) 10.1063/1.2089147.

[10]K. Vogt et al., "Realization of a spin-wave multiplexer", Nature Communications **5**, 1–5 (2014) 10.1038/ncomms4727.

[11]A. V. Chumak, A. A. Serga, and B. Hillebrands, "Magnon transistor for all-magnon data processing", Nature Communications **5**, 4700 (2014) 10.1038/ncomms5700.

[12]L. Torres, L. Lopez-Diaz, and O. Alejos, "Micromagnetic analysis of recording processes in periodic antidot arrays: Interaction between adjacent bits", Journal of Applied Physics **87**, 5645 (2000) 10.1063/1.372476.

[13]U. Welp, V. K. Vlasko-Vlasov, G. W. Crabtree, C. Thompson, V. Metlushko, and B. Ilic, "Magnetic domain formation in perforated permalloy films", Applied Physics Letters **79**, 1315–1317 (2001) 10.1063/1.1396623.

[14]A. O. Adeyeye, S. Goolaup, N. Singh, W. Jun, C. C. Wang, S. Jain, and D. Tripathy, "Reversal mechanisms in ferromagnetic nanostructures", IEEE Transactions on Magnetics **44**, 1935–1940 (2008) 10.1109/TMAG.2008.924539.

[15]N. G. Deshpande, M. S. Seo, X. R. Jin, S. J. Lee, Y. P. Lee, J. Y. Rhee, and K. W. Kim, "Tailoring of magnetic properties of patterned cobalt antidots by simple manipulation of lattice symmetry", Applied Physics Letters **96**, 122503 (2010) 10.1063/1.3368691.

[16]F. J. Castaño, K. Nielsch, C. A. Ross, J. W. A. Robinson, and R. Krishnan, "Anisotropy and magnetotransport in ordered magnetic antidot arrays", Applied Physics Letters **85**, 2872–2874 (2004) 10.1063/1.1800281.

[17]S. Mallick and S. Bedanta, "Size and shape dependence study of magnetization reversal in magnetic antidot lattice arrays", Journal of Magnetism and Magnetic Materials **382**, 158–164 (2015) 10.1016/j.jmmm.2015.01.049.

[18]J. Nogues and I. K. Schuller, "Exchange bias", Journal of Magnetism and Magnetic Materials **192**, 203–232 (1999) 10.1016/S0304-8853(98)00266-2.

[19]A. E. Berkowitz and K. Takano, "Exchange anisotropy– a review", Journal of Magnetism and Magnetic Materials **200**, 552–570 (1999) 10.1016/S0304-8853(99)00453-9.

[20]R. L. Stamps, "Mechanisms for exchange bias", Journal of Physics D: Applied Physics **34**, 444–444 (2001) 10.1088/0022-3727/34/3/501.

[21]W. H. Meiklejohn and C. P. Bean, "New Magnetic Anisotropy", Physical Review Letters **105**, 904–913 (1957) 10.1103/PhysRev.105.904.

[22]B. Heinrich, *Magnetic Heterostructures*, edited by H. Zabel and S. D. Bader, Vol. 227, Springer Tracts in Modern Physics (Springer Berlin Heidelberg, Berlin, Heidelberg, 2008), pp. 185–250, 10.1007/978-3-540-73462-8.

[23]J. C. S. Kools, T. G. S. M. Rijks, A. E. M. De Veirman, and R. Coehoorn, "On the ferromagnetic interlayer coupling in exchange-biased spin-valve multilayers", IEEE Transactions on Magnetics **31**, 3918–3920 (1995) 10.1109/20.489816.

[24]M. F. Gillies, J. N. Chapman, and J. C. S. Kools, "Magnetization reversal mechanisms in NiFe/Cu/NiFe/FeMn spin-valve structures", Journal of Applied Physics **78**, 5554–5562 (1995) 10.1063/1.359676.

[25]D. E. Gonzalez-Chavez, R. Dutra, W. O. Rosa, T. L. Marcondes, A. Mello, and R. L. Sommer, "Interlayer coupling in spin valves studied by broadband ferromagnetic resonance", Physical Review B - Condensed Matter and Materials Physics **88**, 1–7 (2013) 10.1103/PhysRevB.88.104431.

[26]N. N. Phuoc, F. Xu, Y. Ma, and C. K. Ong, "Permalloy-FeMn exchange-biased multilayers grown on flexible substrates for microwave applications", Journal of Magnetism and Magnetic Materials **321**, 2685–2690 (2009) 10.1016/j.jmmm.2009.03.073.

[27]S. Yuan, B. Kang, L. Yu, S. Cao, and X. Zhao, "Increased ferromagnetic resonance linewidth and exchange anisotropy in NiFe/FeMn bilayers", Journal of Applied Physics **105** (2009) 10.1063/1.3086292.

[28]N. N. Phuoc, F. Xu, and C. K. Ong, "Ultrawideband microwave noise filter: Hybrid antiferromagnet/ferromagnet exchange-coupled multilayers", Applied Physics Letters **94**, 092505 (2009) 10.1063/1.3094881.

[29]C. Jiang, D. Xue, and W. Sui, "Broadband microwave absorption in [NiFe/FeMn]n exchange-coupled multilayer films", Thin Solid Films **519**, 2527–2530 (2011) 10.1016/j.tsf.2010.11.030.

[30]K. Liu, S. Baker, M. Tuominen, T. Russell, and I. Schuller, "Tailoring exchange bias with magnetic nanostructures", Physical Review B **63**, 060403 (2001) 10.1103/PhysRevB.63.060403.

[31]R. E. Dunin-Borkowski, M. R. McCartney, B. Kardynal, M. R. Scheinfein, D. J. Smith, and S. S. P. Parkin, "Off-axis electron holography of exchange-biased CoFe/FeMn patterned nanostructures", Journal of Applied Physics **90**, 2899–2902 (2001) 10.1063/1.1390493.

[32]J. Nogues, J. Sort, V. Langlais, V. Skumryev, S. Surinach, J. Munoz, and M. Baro, "Exchange bias in nanostructures", Physics Reports **422**, 65–117 (2005) 10.1016/j.physrep.2005.08.004.

[33]G. Gubbiotti et al., "Magnetostatic interaction in arrays of nanometric permalloy wires: A magneto-optic Kerr effect and a Brillouin light scattering study", Physical Review B - Condensed Matter and Materials Physics **72**, 1–7 (2005) 10.1103/PhysRevB.72.224413.

[34]M. T. Rahman, N. N. Shams, D. S. Wang, and C.-H. Lai, "Enhanced exchange bias in sub-50-nm IrMn/CoFe nanostructure", Applied Physics Letters **94**, 082503 (2009) 10.1063/1.3085965.

[35]J. Eisenmenger, Z. P. Li, W. A. A. Macedo, and I. K. Schuller, "Exchange bias and asymmetric reversal in nanostructured dot arrays", Physical Review Letters **94**, 1–4 (2005) 10.1103/PhysRevLett.94.057203.

[36]J. Sort et al., "Magnetization Reversal in Submicron Disks: Exchange Biased Vortices", Physical Review Letters **95**, 067201 (2005) 10.1103/PhysRevLett.95.067201.

[37]J. Sort et al., "Tailoring the magnetization reversal of elliptical dots using exchange bias (invited)", Journal of Applied Physics **103** (2008) 10.1063/1.2840467.

[38]M. Fraune, U. Rüdiger, G. Güntherodt, S. Cardoso, and P. Freitas, "Size dependence of the exchange bias field in NiO/Ni nanostructures", Applied Physics Letters **77**, 3815 (2000) 10.1063/1.1330752.

[39]S. Chung, A. Hoffmann, and M. Grimsditch, "Interplay between exchange bias and uniaxial anisotropy in a ferromagnetic/antiferromagnetic exchange-coupled system", Physical Review B **71**, 214430 (2005) 10.1103/PhysRevB.71.214430.

[40]W. Zhang, D. N. Weiss, and K. M. Krishnan, "Competing anisotropies and temperature dependence of exchange bias in CoFeIrMn metallic wire arrays fabricated by nanoimprint lithography", Journal of Applied Physics **107**, 09D724 (2010) 10.1063/1.3367959.

[41]D. Tripathy, A. O. Adeyeye, and N. Singh, "Exchange bias in nanoscale antidot arrays", Applied Physics Letters **93**, 022502 (2008) 10.1063/1.2959727.

[42]D. Tripathy and A. O. Adeyeye, "Magnetization reversal in exchange biased antidot arrays", Journal of Applied Physics **105**, 07D703 (2009) 10.1063/1.3056400.

[43]M. Kovylina, M. Erekhinsky, R. Morales, J. E. Villegas, I. K. Schuller, A. Labarta, and X. Batlle, "Tuning exchange bias in Ni/FeF_2 heterostructures using antidot arrays", Applied Physics Letters **95**, 152507 (2009) 10.1063/1.3248306.

[44]L. Heyderman et al., "Magnetization reversal in cobalt antidot arrays", Physical Review B **73**, 214429 (2006) 10.1103/PhysRevB.73.214429.

[45]C. I. L. De Araujo et al., "Magnetic vortex crystal formation in the antidot complement of square artificial spin ice", Applied Physics Letters **104** (2014) 10.1063/1.4867530.

[46]S. McVitie, D. McGrouther, S. McFadzean, D. A. MacLaren, K. O'Shea, and M. Benitez, "Aberration corrected Lorentz scanning transmission electron microscopy", Ultramicroscopy **152**, 57–62 (2015) 10.1016/j.ultramic.2015.01.003.

[47]C. Bayer, M. P. Kostylev, and B. Hillebrands, "Spin-wave eigenmodes of an infinite thin film with periodically modulated exchange bias field", Applied Physics Letters **88**, 112504 (2006) 10.1063/1.2184767.

[48]L. Landau and E. Lifshits, "On the Theory of the Dispersion of Magnetic Permeability in Ferromagnetic Bodies", Phys. Zeitsch. der Sow. **169**, 14–22 (1935).

[49]F. Bloch, "Zur Theorie des Ferromagnetismus", Zeitschrift fur Physik **61**, 206–219 (1930) 10.1007/BF01339661.

[50]C. Kittel, *Introduction to Solid State Physics*, 6th (John Wiley Sons, Inc., New York, 1986).

[51]J. W. Klos, M. Krawczyk, and M. Sokolovskyy, "Bulk and edge modes in two-dimensional magnonic crystal slab", Journal of Applied Physics **109**, 2009–2012 (2011) 10.1063/1.3536534.

[52]S. Tacchi et al., "Forbidden band gaps in the spin-wave spectrum of a two-dimensional bicomponent magnonic crystal", Physical Review Letters **109**, 1–5 (2012) 10.1103/PhysRevLett.109.137202.

[53]M. Krawczyk and H. Puszkarski, "Plane-wave theory of three dimensional magnonic crystals", Physical Review B **77**, 054437 (2008) 10.1103/PhysRevB.77.054437.

[54]R. Zivieri et al., "Bragg diffraction of spin waves from a two-dimensional antidot lattice", Physical Review B **85**, 012403 (2012) 10.1103/PhysRevB.85.012403.

[55]S. Neusser et al., "Magnonic minibands in antidot lattices with large spin-wave propagation velocities", Physical Review B **84**, 094454 (2011) 10.1103/PhysRevB.84.094454.

[56]J. O. Vasseur, L. Dobrzynski, B. Djafari-Rouhani, and H. Puszkarski, "Magnon band structure of periodic composites", Physical Review B **54**, 1043–1049 (1996) 10.1103/PhysRevB.54.1043.

[57]R. Bali, M. Kostylev, D. Tripathy, A. O. Adeyeye, and S. Samarin, "High-symmetry magnonic modes in antidot lattices magnetized perpendicular to the lattice plane", Physical Review B **85**, 104414 (2012) 10.1103/PhysRevB.85.104414.

[58]C. Jarufe and R. E. Arias, "Magnonic and plasmonic band gaps in films with periodically modified surfaces", Physical Review B - Condensed Matter and Materials Physics **85** (2012) 10.1103/PhysRevB.85.205411.

[59]R. A. Gallardo et al., "Splitting of spin-wave modes in thin films with arrays of periodic perturbations: Theory and experiment", New Journal of Physics **16** (2014) 10.1088/1367-2630/16/2/023015.

[60]S. Neusser and D. Grundler, "Magnonics: Spin waves on the nanoscale", Advanced Materials **21**, 2927–2932 (2009) 10.1002/adma.200900809.

[61]B. Lenk, N. Abeling, J. Panke, and M. Munzenberg, "Spin-wave modes and band structure of rectangular CoFeB antidot lattices", Journal of Applied Physics **112**, 1–4 (2012) 10.1063/1.4759142.

[62]R. L. Stamps, "Dynamic Magnetic Properties of Ferroic Films, Multilayers, and Patterned Elements", Advanced Functional Materials **20**, 2380–2394 (2010) 10.1002/adfm.201000310.

[63]J. Griffiths, "Anomalous high-frequency resistance of ferromagnetic metals", Nature **158**, 670–671 (1946) 10.1038/158670a0.

[64]C. Kittel, "On the theory of ferromagnetic resonance absorption", Phys. Rev. **73**, 155–161 (1948) 10.1103/PhysRev.73.155.

[65]P. A. Fleury, S. P. S. Porto, L. E. Cheesman, and H. J. Guggenheim, "Light Scattering by Spin Waves in FeF_2", Physical Review Letters **17**, 84–87 (1966) 10.1103/PhysRevLett.17.84.

[66]C. G. Sykes, J. D. Adam, and J. H. Collins, "Magnetostatic wave propagation in a periodic structure", Applied Physics Letters **29**, 388–391 (1976) 10.1063/1.89098.

[67]J. R. Eshbach and R. W. Damon, "Surface magnetostatic modes and surface spin waves", Phys. Rev. **118**, 1208–1210 (1960) 10.1103/PhysRev.118.1208.

[68]R. Damon and J. Eshbach, "Magnetostatic modes of a ferromagnet slab ", Journal of Physics and Chemistry of Solids, 308–320 (1961) http://dx.doi.org/10.1016/0022-3697(61)90041-5.

[69]R. E. Camley, T. S. Rahman, and D. L. Mills, "Magnetic excitations in layered media: Spin waves and the light-scattering spectrum", Physical Review B **27**, 261–277 (1983) 10.1103/PhysRevB.27.261.

[70]M. Jirsa and V. Kamberský, "Angular dependence of spin-wave resonance in thin films with asymmetrical boundary conditions. analytical treatment", physica status solidi (b) **126**, 547–555 (1984) 10.1002/pssb.2221260214.

[71]B. A. Kalinikos and A. N. Slavin, "Theory of dipole-exchange spin wave spectrum for ferromagnetic films with mixed exchange boundary conditions", Journal of Physics C: Solid State Physics **19**, 7013 (1986).

[72]B. A. Kalinikos, M. P. Kostylev, N. V. Kozhus, and A. N. Slavin, "The dipole-exchange spin wave spectrum for anisotropic ferromagnetic films with mixed exchange boundary conditions", Journal of Physics: Condensed Matter **2**, 9861–9877 (1999) 10.1088/0953-8984/2/49/012.

[73]A. A. Serga, A. V. Chumak, and B. Hillebrands, "YIG magnonics", Journal of Physics D: Applied Physics **43**, 264002 (2010) 10.1088/0022-3727/43/26/264002.

[74]J. Jorzick et al., "Brillouin light scattering from quantized spin waves in micron-size magnetic wires", Physical Review B **60**, 15194–15200 (1999) 10.1103/PhysRevB.60.15194.

[75]M. Bailleul, D. Olligs, C. Fermon, and S. O. Demokritov, "Spin waves propagation and confinement in conducting films at the micrometer scale", Europhysics Letters (EPL) **56**, 741–747 (2001) 10.1209/epl/i2001-00583-2.

[76]C. Chappert, A. Fert, and F. N. Van Dau, "The emergence of spin electronics in data storage", Nature Materials **6**, 813–823 (2007) 10.1038/nmat2024.

[77]A. Hirohata and K. Takanashi, "Future perspectives for spintronic devices", Journal of Physics D: Applied Physics **47**, 193001 (2014) 10.1088/0022-3727/47/19/193001.

[78]S. Urazhdin et al., "Nanomagnonic devices based on the spin-transfer torque", Nature Nanotechnology **9**, 509–513 (2014) 10.1038/nnano.2014.88.

[79]B. Lenk, H. Ulrichs, F. Garbs, and M. Munzenberg, "The building blocks of magnonics", Physics Reports **507**, 107–136 (2011) 10.1016/j.physrep.2011.06.003.

[80]G. Nahrwold, J. M. Scholtyssek, S. Motl-Ziegler, O. Albrecht, U. Merkt, and G. Meier, "Structural, magnetic, and transport properties of Permalloy for spintronic experiments", Journal of Applied Physics **108** (2010) 10.1063/1.3431384.

[81]K. Perzlmaier, G. Woltersdorf, and C. H. Back, "Observation of the propagation and interference of spin waves in ferromagnetic thin films", Physical Review B - Condensed Matter and Materials Physics **77**, 1–5 (2008) 10.1103/PhysRevB.77.054425.

[82]M. Wu, B. A. Kalinikos, P. Krivosik, and C. E. Patton, "Fast pulse-excited spin waves in yttrium iron garnet thin films", Journal of Applied Physics **99**, 013901 (2006) 10.1063/1.2150592.

[83]A. Conca, J. Greser, T. Sebastian, S. Klingler, B. Obry, B. Leven, and B. Hillebrands, "Low spin-wave damping in amorphous $Co_{40}Fe_{40}B_{20}$ thin films", Journal of Applied Physics **113**, 2011–2015 (2013) 10.1063/1.4808462.

[84]C. Yu, M. J. Pechan, and G. J. Mankey, "Dipolar induced, spatially localized resonance in magnetic antidot arrays", Applied Physics Letters **83**, 3948–3950 (2003) 10.1063/1.1625104.

[85]C. Yu, "Lateral standing spin waves in permalloy antidot arrays", Journal of Applied Physics **95**, 6648 (2004) 10.1063/1.1687554.

[86]M. J. Pechan, C. Yu, R. L. Compton, J. P. Park, and P. A. Crowell, "Direct measurement of spatially localized ferromagnetic-resonance modes in an antidot lattice (invited)", Journal of Applied Physics **97** (2005) 10.1063/1.1857412.

[87]S. Neusser, B. Botters, and D. Grundler, "Localization, confinement, and field-controlled propagation of spin waves in $Ni_{80}Fe_{20}$ antidot lattices", Physical Review B **78**, 054406 (2008) 10.1103/PhysRevB.78.054406.

[88]O. N. Martyanov et al., "Ferromagnetic resonance study of thin film antidot arrays: Experiment and micromagnetic simulations", Physical Review B - Condensed Matter and Materials Physics **75**, 3–8 (2007) 10.1103/PhysRevB.75.174429.

[89]M. Yu, L. Malkinski, L. Spinu, W. Zhou, and S. Whittenburg, "Size dependence of static and dynamic magnetic properties in nanoscale square Permalloy antidot arrays", Journal of Applied Physics **101**, 1–4 (2007) 10.1063/1.2709501.

[90]M. Kostylev et al., "Propagating volume and localized spin wave modes on a lattice of circular magnetic antidots", Journal of Applied Physics **103**, 5–8 (2008) 10.1063/1.2831792.

[91]D. H. Y. Tse, S. J. Steinmuller, T. Trypiniotis, D. Anderson, G. A. C. Jones, J. A. C. Bland, and C. H. W. Barnes, "Static and dynamic magnetic properties of $Ni_{80}Fe_{20}$ square antidot", Physical Review B **79**, 054426 (2009) 10.1103/PhysRevB.79.054426.

[92]V. N. Krivoruchko and A. I. Marchenko, "Apparent 6-fold configurational anisotropy and spatial confinement of ferromagnetic resonances in hexagonal magnetic antidot lattices", Journal of Applied Physics **109**, 083912 (2011) 10.1063/1.3552913.

[93]F. Haering et al., "Switching modes in easy and hard axis magnetic reversal in a self-assembled antidot array.", Nanotechnology **24**, 465709 (2013) 10.1088/0957-4484/24/46/465709.

[94]S. Tacchi et al., "Mode conversion from quantized to propagating spin waves in a rhombic antidot lattice supporting spin wave nanochannels", Physical Review B - Condensed Matter and Materials Physics **86**, 1–12 (2012) 10.1103/PhysRevB.86.014417.

[95]A. Barman, "Control of magnonic spectra in cobalt nanohole arrays: the effects of density, symmetry and defects", Journal of Physics D: Applied Physics **43**, 195002 (2010) 10.1088/0022-3727/43/19/195002.

[96]J. W. Klos, M. L. Sokolovskyy, S. Mamica, and M. Krawczyk, "The impact of the lattice symmetry and the inclusion shape on the spectrum of 2D magnonic crystals", Journal of Applied Physics **111** (2012) 10.1063/1.4729559.

[97]R. Mandal, P. Laha, K. Das, S. Saha, S. Barman, A. K. Raychaudhuri, and A. Barman, "Effects of antidot shape on the spin wave spectra of two-dimensional $Ni_{80}Fe_{20}$ antidot lattices", Applied Physics Letters **103**, 2011–2015 (2013) 10.1063/1.4860959.

[98]D. Kumar, P. Sabareesan, W. Wang, H. Fangohr, and A. Barman, "Effect of hole shape on spin-wave band structure in one-dimensional magnonic antidot waveguide", Journal of Applied Physics **114** (2013) 10.1063/1.4813228.

[99]S. A. Nikitov, P. Tailhades, and C. S. Tsai, "Spin waves in periodic magnetic structures—magnonic crystals", Journal of Magnetism and Magnetic Materials **236**, 320–330 (2001) 10.1016/S0304-8853(01)00470-X.

[100]Y. V. Gulyaev et al., "Ferromagnetic films with magnon bandgap periodic structures: Magnon crystals", Journal of Experimental and Theoretical Physics Letters **77**, 567–570 (2003) 10.1134/1.1595698.

[101]Z. K. Wang, V. L. Zhang, H. S. Lim, S. C. Ng, M. H. Kuok, S. Jain, and A. O. Adeyeye, "Nanostructured magnonic crystals with size-tunable bandgaps", ACS Nano **4**, 643–648 (2010) 10.1021/nn901171u.

[102]S. Tacchi et al., "Angular dependence of magnetic normal modes in NiFe antidot lattices with different lattice symmetry", IEEE Transactions on Magnetics **46**, 1440–1443 (2010) 10.1109/TMAG.2009.2039775.

[103]D. Kumar, J. W. Kłos, M. Krawczyk, and A. Barman, "Magnonic band structure, complete bandgap, and collective spin wave excitation in nanoscale two-dimensional magnonic crystals", Journal of Applied Physics **115**, 043917 (2014) 10.1063/1.4862911.

[104]S. Tacchi et al., "Universal dependence of the spin wave band structure on the geometrical characteristics of two-dimensional magnonic crystals", Scientific Reports **5**, 10367 (2015) 10.1038/srep10367.

[105]X. M. Liu, J. Ding, and A. O. Adeyeye, "Magnetization dynamics and reversal mechanism of Fe filled Ni_80Fe_20 antidot nanostructures", Applied Physics Letters **100** (2012) 10.1063/1.4729428.

[106]G. Shimon, A. O. Adeyeye, and C. A. Ross, "Reversal mechanisms of coupled bi-component magnetic nanostructures", Applied Physics Letters **101** (2012) 10.1063/1.4747446.

[107]G. Duerr, M. Madami, S. Neusser, S. Tacchi, G. Gubbiotti, G. Carlotti, and D. Grundler, "Spatial control of spin-wave modes in $Ni_{80}Fe_{20}$ antidot lattices by embedded Co nanodisks", Applied Physics Letters **99**, 202502 (2011) 10.1063/1.3662841.

[108]G. Duerr, S. Tacchi, G. Gubbiotti, and D. Grundler, "Field-controlled rotation of spin-wave nanochannels in bi-component magnonic crystals", Journal of Physics D: Applied Physics **47**, 325001 (2014) 10.1088/0022-3727/47/32/325001.

[109]P. Malago, L. Giovannini, R. Zivieri, P. Gruszecki, and M. Krawczyk, "Spin-wave dynamics in permalloy/cobalt magnonic crystals in the presence of a nonmagnetic spacer", Physical Review B **92**, 064416 (2015) 10.1103/PhysRevB.92.064416.

[110]G. Gubbiotti et al., "Magnetic normal modes of bicomponent permalloy/cobalt structures in the parallel and antiparallel ground state", Physical Review B - Condensed Matter and Materials Physics **90**, 1–9 (2014) 10.1103/PhysRevB.90.024419.

[111]G. Gubbiotti, H. Nguyen, R. Hiramatsu, S. Tacchi, M. Cottam, and T. Ono, "Resonant spin-wave modes in trilayered magnetic nanowires studied in the parallel and antiparallel ground state", Journal of Magnetism and Magnetic Materials **384**, 45–48 (2015) 10.1016/j.jmmm.2015.02.012.

[112]A. G. Gurevich and G. A. Melkov, *Magnetizaion oscillations and waves*, edited by C. Press (1996), pp. 11–30.

[113]S. Neusser et al., "Tunable metamaterial response of a $Ni_{80}Fe_{20}$ antidot lattice for spin waves", Physical Review B **84**, 184411 (2011) 10.1103/PhysRevB.84.184411.

[114]F. Giesen, "Magnetization dynamics of nanostructured ferromagnetic rings and rectangular elements", PhD Thesis (University of Hamburg, 2005).

[115]C. Kittel, "Ferromagnetic resonance", Journal de Physique et le Radium **12**, 291–302 (1951) 10.1051/jphysrad:01951001203029100.

[116]D. Kumar, O. Dmytriiev, S. Ponraj, and A. Barman, "Numerical calculation of spin wave dispersions in magnetic nanostructures", Journal of Physics D: Applied Physics **45**, 015001 (2011) 10.1088/0022-3727/45/1/015001.

[117]B. Heinrich, *Spin relaxation in magnetic metallic layers and multilayers* (Springer - Verlag, Berlin/Heidelberg, 2005), pp. 143–210, 10.1007/3-540-27163-5_5.

[118]B. Heinrich, R. Urban, and G. Woltersdorf, "Magnetic relaxation in metallic films: single and multilayer structures", Journal of Applied Physics **91**, 7523–7525 (2002) 10.1063/1.1447215.

[119]L. Berger, "Effect of interfaces on gilbert damping and ferromagnetic resonance linewidth in magnetic multilayers", Journal of Applied Physics **90**, 4632–4638 (2001) 10.1063/1.1405824.

[120]Y. Tserkovnyak, A. Brataas, and G. E. W. Bauer, "Enhanced Gilbert Damping in Thin Ferromagnetic Films", Physical Review Letters **88**, 117601 (2002) 10.1103/PhysRevLett.88.117601.

[121]Y. Tserkovnyak, A. Brataas, G. E. W. Bauer, and B. I. Halperin, "Nonlocal Magnetization Dynamics in Ferromagnetic Hybrid Nanostructures", Reviews of Modern Physics **77**, 1375–1421 (2005).

[122]E. C. Patton, C. Wilts, and B. F. Humphrey, "Extrinsic contributions to the ferromagnetic resonance response of ultrathin films", Journal of Applied Physics **38**, 1358–1359 (1967).

[123]R. Arias and D. Mills, "Extrinsic contributions to the ferromagnetic resonance response of ultrathin films", Physical Review B **60**, 7395–7409 (1999) 10.1103/PhysRevB.60.7395.

[124]R. D. McMichael and P. Krivosik, "Classical Model of Extrinsic Ferromagnetic Resonance Linewidth in Ultrathin Films", IEEE Transactions on Magnetics **40**, 2–11 (2004) 10.1109/TMAG.2003.821564.

[125]R. Urban, B. Heinrich, G. Woltersdorf, K. Ajdari, K. Myrtle, J. Cochran, and E. Rozenberg, "Nanosecond magnetic relaxation processes in ultrathin metallic films prepared by MBE", Physical Review B **65**, 1–4 (2001) 10.1103/PhysRevB.65.020402.

[126]G. Woltersdorf, B. Heinrich, J. Woltersdorf, and R. Scholz, "Spin dynamics in ultrathin film structures with a network of misfit dislocations", Journal of Applied Physics **95**, 7007–7009 (2004) 10.1063/1.1669219.

[127]B. Kuanr, R. E. Camley, and Z. Celinski, "Narrowing of the frequency-linewidth in structured magnetic strips: Experiment and theory", Applied Physics Letters **87** (2005) 10.1063/1.1968433.

[128]S. S. Kalarickal et al., "Ferromagnetic resonance linewidth in metallic thin films: Comparison of measurement methods", Journal of Applied Physics **99** (2006) 10.1063/1.2197087.

[129]A. Ludwig et al., *Quantum Dot Spintronics: Fundamentals and Applications*, Vol. 246 (2013), pp. 235–268, 10.1007/978-3-642-32042-2.

[130]D. J. Twisselmann and R. D. McMichael, "Intrinsic damping and intentional ferromagnetic resonance broadening in thin permalloy films", Journal of Applied Physics **93**, 6903–6905 (2003) 10.1063/1.1543884.

[131]J. Dubowik, K. Zaleski, H. Glowinski, and I. Gocianska, "Angular dependence of ferromagnetic resonance linewidth in thin films", Physical Review B - Condensed Matter and Materials Physics **84**, 1–5 (2011) 10.1103/PhysRevB.84.184438.

[132]A. Azevedo, A. B. Oliveira, F. M. De Aguiar, and S. M. Rezende, "Extrinsic contributions to spin-wave damping and renormalization in thin Ni80F20 films", Physical Review B - Condensed Matter and Materials Physics **62**, 5331–5333 (2000) 10.1103/PhysRevB.62.5331.

[133]D. Pozar, *Microwave Engineering*, edited by J. Wiley and I. Sons (2005).

[134]K. Kurokawa, "Power Waves and the Scattering Matrix", IEEE Transactions on Microwave Theory and Techniques **13**, 194–202 (1964) 10.1109/TMTT.1965.1125964.

[135]M. Hiebel, *Fundamentals of Vector Network Analysis*, edited by Rohde and Schwarz (2008).

[136]B. Rosas, "The Design Test of Broadband Launches up to 50 GHz on Thin Thick Substrates", 28 (2011).

[137]G. Counil et al., "Inductive measurement of the high frequency permeability of a Permalloy thin film", Journal of Magnetism and Magnetic Materials **272-276**, 290–292 (2004) 10.1016/j.jmmm.2003.12.1243.

[138]G. Counil, J. V. Kim, T. Devolder, C. Chappert, K. Shigeto, and Y. Otani, "Spin wave contributions to the high-frequency magnetic response of thin films obtained with inductive methods", Journal of Applied Physics **95**, 5646–5652 (2004) 10.1063/1.1697641.

[139]D. Pain, M. Ledieu, O. Acher, A. L. Adenot, and F. Duverger, "An improved permeameter for thin film measurements up to 6 GHz", Journal of Applied Physics **85**, 5151 (1999) 10.1063/1.369107.

[140]M. Bailleul, "Shielding of the electromagnetic field of a coplanar waveguide by a metal film: Implications for broadband ferromagnetic resonance measurements", Applied Physics Letters **103** (2013) 10.1063/1.4829367.

[141]Z. Lin and M. Kostylev, "A rigorous two-dimensional model for the stripline ferromagnetic resonance response of metallic ferromagnetic films", Journal of Applied Physics **117**, 053908 (2015) 10.1063/1.4907535.

[142]Y. Ding, T. J. Klemmer, and T. M. Crawford, "A coplanar waveguide permeameter for studying high-frequency properties of soft magnetic materials", Journal of Applied Physics **96**, 2969–2972 (2004) 10.1063/1.1774242.

[143]C. Bilzer, T. Devolder, P. Crozat, C. Chappert, S. Cardoso, and P. P. Freitas, "Vector network analyzer ferromagnetic resonance of thin films on coplanar waveguides: Comparison of different evaluation methods", Journal of Applied Physics **101** (2007) 10.1063/1.2716995.

[144]K. J. Kennewell et al., "Magnetization pinning at a Py/Co interface measured using broadband inductive magnetometry", Journal of Applied Physics **108** (2010) 10.1063/1.3488618.

[145]R. Narkowicz, D. Suter, and R. Stonies, "Planar microresonators for EPR experiments", Journal of Magnetic Resonance **175**, 275–284 (2005) 10.1016/j.jmr.2005.04.014.

[146]R. Narkowicz, D. Suter, and I. Niemeyer, "Scaling of sensitivity and efficiency in planar microresonators for electron spin resonance", Review of Scientific Instruments **79** (2008) 10.1063/1.2964926.

[147]K. J. Kennewell, M. Kostylev, and R. L. Stamps, "Calculation of spin wave mode response induced by a coplanar microwave line", Journal of Applied Physics **101**, 7–10 (2007) 10.1063/1.2710068.

[148]C. Bilzer, T. Devolder, P. Crozat, and C. Chappert, "Open-circuit one-port network analyzer ferromagnetic resonance", IEEE Transactions on Magnetics **44**, 3265–3268 (2008) 10.1109/TMAG.2008.2004379.

[149]M. Kostylev, "Waveguide-based ferromagnetic resonance measurements of metallic ferromagnetic films in transmission and reflection", Journal of Applied Physics **113** (2013) 10.1063/1.4790172.

[150]T. Uhlig, M. Heumann, and J. Zweck, "Development of a specimen holder for in situ generation of pure in-plane magnetic fields in a transmission electron microscope", Ultramicroscopy **94**, 193–196 (2003) 10.1016/S0304-3991(02)00264-4.

[151]G. Yi, W. A. P. Nicholson, C. K. Lim, J. N. Chapman, S. McVitie, and C. D. W. Wilkinson, "A new design of specimen stage for in situ magnetising experiments in the transmission electron microscope", Ultramicroscopy **99**, 65–72 (2004) 10.1016/S0304-3991(03)00148-7.

[152]V. V. Volkov and Y. Zhu, "Lorentz phase microscopy of magnetic materials", Ultramicroscopy **98**, 271–281 (2004) 10.1016/j.ultramic.2003.08.026.

[153]S. McVitie and M. Cushley, "Quantitative Fresnel Lorentz microscopy and the transport of intensity equation", Ultramicroscopy **106**, 423–431 (2006) 10.1016/j.ultramic.2005.12.001.

[154]R. P. Ferrier and R. T. Murray, "Low-angle electron diffraction", Journal of the Royal Microscopical Society **85**, 323–335 (1966).

[155]T. Koyama, K. Takayanagi, Y. Togawa, S. Mori, and K. Harada, "Small angle electron diffraction and deflection", AIP Advances **2**, 7 (2012) 10.1063/1.3701703.

[156]Y. Taniguchi, H. Matsumoto, and K. Harada, "Foucault imaging by using non-dedicated transmission electron microscope", Applied Physics Letters **101**, 1–5 (2012) 10.1063/1.4748124.

[157]J. N. Chapman, I. R. McFadyen, and S. McVitie, "Modified differential phase contrast Lorentz microscopy for improved imaging of magnetic structures", IEEE Transactions on Magnetics **26**, 1506–1511 (1990) 10.1109/20.104427.

[158]F. J. T. Goncalves et al., "Anisotropy engineering using exchange bias on antidot templates", AIP Advances **5**, 067101 (2015) 10.1063/1.4922055.

[159]C.-L. Hu et al., "Field tunable localization of spin waves in antidot arrays", Applied Physics Letters **98**, 262508 (2011) 10.1063/1.3606556.

[160]J. Sklenar, V. S. Bhat, L. E. DeLong, O. Heinonen, and J. B. Ketterson, "Strongly localized magnetization modes in permalloy antidot lattices", Applied Physics Letters **102**, 152412 (2013) 10.1063/1.4802278.

[161]T. Schneider, A. A. Serga, B. Leven, B. Hillebrands, R. L. Stamps, and M. P. Kostylev, "Realization of spin-wave logic gates", Applied Physics Letters **92**, 022505 (2008) 10.1063/1.2834714.

[162]B. Van De Wiele, A. Manzin, A. Vansteenkiste, O. Bottauscio, L. Dupré, and D. De Zutter, "A micromagnetic study of the reversal mechanism in permalloy antidot arrays", Journal of Applied Physics **111** (2012) 10.1063/1.3689846.

[163]J. Ding, D. Tripathy, and A. O. Adeyeye, "Effect of antidot diameter on the dynamic response of nanoscale antidot arrays", Journal of Applied Physics **109**, 07D304, 000 (2011) http://dx.doi.org/10.1063/1.3535425.

[164]J. Ding, D. Tripathy, and A. O. Adeyeye, "Dynamic response of antidot nanostructures with alternating hole diameters", EPL- Europhysics Letters **98**, 16004 (2012) 10.1209/0295-5075/98/16004.

[165]R. Rodriguez-Suarez, J. Palma, E. Burgos, S. Michea, J. Escrig, J. Denardin, and C. Aliaga, "Ferromagnetic resonance investigation in permalloy magnetic antidot arrays on alumina nanoporous membranes", Journal of Magnetism and Magnetic Materials **350**, 88–93 (2014) 10.1016/j.jmmm.2013.09.009.

[166]S. Martens, O. Albrecht, K. Nielsch, and D. Görlitz, "Local modes and two magnon scattering in ordered permalloy antidot arrays", Journal of Applied Physics **105**, 07C113 (2009) 10.1063/1.3076144.

[167]V. Bhat et al., "Broad-band FMR study of ferromagnetic thin films patterned with antidot lattices", Physica C: Superconductivity **479**, 83–87 (2012) 10.1016/j.physc.2012.02.003.

[168]C. C. Wang, A. O. Adeyeye, and N. Singh, "Magnetic antidot nanostructures: effect of lattice geometry", Nanotechnology **17**, 1629–1636 (2006) 10.1088/0957-4484/17/6/015.

[169]J. Mohanty et al., "Magnetization reversal studies of continuous and patterned exchange biased nife/femn thin films", Applied Physics A **109**, 181–187 (2012) 10.1007/s00339-012-7031-2.

[170]A. Hoffmann, M. Grimsditch, J. Pearson, J. Nogues, W. Macedo, and I. Schuller, "Tailoring the exchange bias via shape anisotropy in ferromagnetic/ antiferromagnetic exchange-coupled systems", Physical Review B **67**, 220406 (2003) 10.1103/PhysRevB.67.220406.

[171]R. Stamps, R. Camley, and R. Hicken, "Influence of exchange-coupled anisotropies on spin-wave frequencies in magnetic layered systems: Application to Co/CoO", Physical Review B **54**, 4159–4164 (1996) 10.1103/PhysRevB.54.4159.

[172]K.-W. Lin, M. Mirza, C. Shueh, H.-R. Huang, H.-F. Hsu, and J. V. Lierop, "Tailoring interfacial exchange coupling with low-energy ion beam bombardment: Tuning the interface roughness", Applied Physics Letters **100**, 122409 (2012) 10.1063/1.3697405.

[173]A. Vansteenkiste, J. Leliaert, M. Dvornik, M. Helsen, F. Garcia-Sanchez, and B. Van Waeyenberge, "The design and verification of MuMax3", AIP Advances **4**, 107133 (2014) 10.1063/1.4899186.

[174]J. Ding and A. O. Adeyeye, "Binary ferromagnetic nanostructures: Fabrication, static and dynamic properties", Advanced Functional Materials **23**, 1684–1691 (2013) 10.1002/adfm.201201432.

[175]G. Carlotti and G. Gubbiotti, "Magnetic properties of layered nanostructures studied by means of Brillouin light scattering and the surface magneto-optical Kerr effect", Journal of Physics: Condensed Matter **14**, 8199–8233 (2002) 10.1088/0953-8984/14/35/303.

[176]A. Y. Toporov, R. M. Langford, and A. K. Petford-Long, "Lorentz transmission electron microscopy of focused ion beam patterned magnetic antidot arrays", Applied Physics Letters **77**, 3063 (2000) 10.1063/1.1323737.

[177]C. A. Ross, F. J. Castaño, E. Rodriguez, S. Haratani, B. Vögeli, and H. I. Smith, "Size-dependent switching of multilayer magnetic elements", Journal of Applied Physics **97**, 1–6 (2005) 10.1063/1.1850998.

[178]C. Castan-Guerrero et al., "Magnetic antidot to dot crossover in Co and Py nanopatterned thin films", Physical Review B - Condensed Matter and Materials Physics **89**, 1–10 (2014) 10.1103/PhysRevB.89.144405.

[179]S. S. P. Parkin, R. Bhadra, and K. P. Roche, "Oscillatory magnetic exchange coupling through thin copper layers", Phys. Rev. Lett. **66**, 2152–2155 (1991) 10.1103/PhysRevLett.66.2152.

[180]B. Heinrich and J. Cochran, "Ultrathin metallic magnetic films : magnetic anisotropies and exchange interactions", Advances in Physics **42**, 523–639 (1993) 10.1080/00018739300101524.

[181]D. Altbir, M. Kiwi, R. Ramirez, and I. K. Schuller, "Dipolar interaction and its interplay with interface roughness", Journal of Magnetism and Magnetic Materials **149**, L246–L250 (1995) 10.1016/0304-8853(95)00292-8.

[182]J. S. Yang, J. Lee, and C. R. Chang, "Magnet ostatic coupling in patterned spin valve structures", IEEE Transactions on Magnetics **34**, 2469–2472 (1998) 10.1109/20.717568.

[183]G. Vallejo-Fernandez, N. P. Aley, L. E. Fernandez-Outon, and K. O'Grady, "Control of the setting process in CoFe/IrMn exchange bias systems", Journal of Applied Physics **104** (2008) 10.1063/1.2961316.

[184]M. Vopsaroiu, M. Georgieva, P. J. Grundy, G. V. Fernandez, S. Manzoor, M. J. Thwaites, and K. O'Grady, "Preparation of high moment CoFe films with controlled grain size and coercivity", Journal of Applied Physics **97**, 2003–2006 (2005) 10.1063/1.1855276.

[185]J. Martín, J. Nogués, K. Liu, J. Vicent, and I. K. Schuller, "Ordered magnetic nanostructures: fabrication and properties", Journal of Magnetism and Magnetic Materials **256**, 449–501 (2003) 10.1016/S0304-8853(02)00898-3.

[186]M. A. Basith, S. McVitie, D. McGrouther, J. N. Chapman, and J. M. R. Weaver, "Direct comparison of domain wall behavior in permalloy nanowires patterned by electron beam lithography and focused ion beam milling", Journal of Applied Physics **110** (2011) 10.1063/1.3642966.

[187]D. McGrouther, J. N. Chapman, and F. W. M. Vanhelmont, "Effect of Ga+ ion irradiation on the structural and magnetic properties of CoFe/IrMn exchange biased bilayers", Journal of Applied Physics **95**, 7772–7778 (2004) 10.1063/1.1745120.

[188]R. McMichael, M. Stiles, P. Chen, and W. Egelhoff, "Ferromagnetic resonance studies of NiO-coupled thin films of $Ni_{80}Fe_{20}$", Physical Review B **58**, 8605–8612 (1998) 10.1103/PhysRevB.58.8605.

[189]J. N. Chapman and M. R. Scheinfein, "Transmission electron microscopies of magnetic microstructures", Journal of Magnetism and Magnetic Materials **200**, 729–740 (1999) 10.1016/S0304-8853(99)00317-0.

[190]G. Gubbiotti, H. T. Nguyen, R. Hiramatsu, S. Tacchi, M. Madami, M. G. Cottam, and T. Ono, "Field dependence of the magnetic eigenmode frequencies in layered nanowires with ferromagnetic and antiferromagnetic ground states: experimental and theoretical study", Journal of Physics D: Applied Physics **47**, 365001 (2014) 10.1088/0022-3727/47/36/365001.

[191]D.-s. Han et al., "Wave modes of collective vortex gyration in dipolar-coupled-dot-array magnonic crystals.", Scientific reports **3**, 2262 (2013) 10.1038/srep02262.

[192]S. Wintz et al., "Interlayer-coupled spin vortex pairs and their response to external magnetic fields", Physical Review B - Condensed Matter and Materials Physics **85**, 1–8 (2012) 10.1103/PhysRevB.85.224420.

[193]D. V. Berkov and N. L. Gorn, "Magnetodipolar interlayer interaction effect on the magnetization dynamics of a trilayer square element with the Landau domain structure", Journal of Applied Physics **103** (2008) 10.1063/1.2890397.

[194]X. Dong, Z. Wang, and R. Wang, "Deep sub-nanosecond reversal of vortex cores confined in a spin-wave potential well", Applied Physics Letters **104**, 10–15 (2014) 10.1063/1.4868725.

[195]J. F. Einsle et al., "In situ electron holography of the dynamic magnetic field emanating from a hard-disk drive writer", Nano Research (2014) 10.1007/s12274-014-0610-0.

[196]M. Beleggia and G. Pozzi, "Phase contrast image simulations for electron holography of magnetic and electric fields", Journal of Electron Microscopy **62**, 43–54 (2013) 10.1093/jmicro/dft008.

[197]P. Bohi, M. F. Riedel, T. W. Hansch, and P. Treutlein, "Imaging of microwave fields using ultracold atoms", Applied Physics Letters **97** (2010) 10.1063/1.3470591.

[198]D. Shindo and Y. Murakami, "Electron holography study of electric field variations", Journal of Electron Microscopy **60**, 225–237 (2011) 10.1093/jmicro/dfr017.

[199]J. Fehr and E. Kubalek, "Electron Beam Test System for GHz-Waveform Measurements on Transmission Lines within MMIC", in 22nd european microwave conference, 1992 (1992), pp. 163–168, 10.1109/EUMA.1992.335734.

[200]K. Yang, G. David, S. V. Robertson, J. F. Whitaker, and L. P. B. Katehi, "Electrooptic mapping of near-field distributions in integrated microwave circuits", IEEE Transactions on Microwave Theory and Techniques **46**, 2338–2343 (1998) 10.1109/22.739221.

[201]A. N. Reznik and V. V. Talanov, "Quantitative model for near-field scanning microwave microscopy: Application to metrology of thin film dielectrics", Review of Scientific Instruments **79** (2008) 10.1063/1.3020705.

[202]V. V. Volkov and Y. Zhu, "Phase imaging and nanoscale currents in phase objects imaged with fast electrons", Physical review letters **91**, 043904 (2003) 10.1103/PhysRevLett.91.043904.

[203]J. N. Chapman, "The investigation of magnetic domain structures in thin foils by electron microscopy", Journal of Physics D: Applied Physics **17**, 623–647 (2000) 10.1088/0022-3727/17/4/003.

[204]P. J. Metaxas et al., "Sensing magnetic nanoparticles using nano-confined ferromagnetic resonances in a magnonic crystal", Applied Physics Letters **106**, 232406 (2015) 10.1063/1.4922392.

[205]J. Martín, J. Nogués, K. Liu, J. Vicent, and I. K. Schuller, "Ordered magnetic nanostructures: fabrication and properties", Journal of Magnetism and Magnetic Materials **256**, 449–501 (2003) 10.1016/S0304-8853(02)00898-3.

[206]S. Neusser et al., "Anisotropic Propagation and Damping of Spin Waves in a Nanopatterned Antidot Lattice", Physical Review Letters **105**, 067208 (2010) 10.1103/PhysRevLett.105.067208.

[207]S. O. Demokritov, B. Hillebrands, and A. N. Slavin, "Brillouin light scattering studies of confined spin waves: linear and non-linear confinement", Physics Reports **348**, 441–489 (2001) http://dx.doi.org/10.1016/S0370-1573(00)00116-2.

[208]G. Duerr, R. Huber, and D. Grundler, "Enhanced functionality in magnonics by domain walls and inhomogeneous spin configurations", Journal of Physics: Condensed Matter **24**, 024218 (2011) 10.1088/0953-8984/24/2/024218.

[209]S. Zhang, C. Mu, Q. Zhu, Q. Zheng, X. Liu, J. Wang, and Q. Liu, "Propagating and reflecting of spin wave in permalloy nanostrip with 360° domain wall", Journal of Applied Physics **115**, 013908 (2014) 10.1063/1.4861154.

[210]C. Nistor, K. Sun, Z. Wang, M. Wu, C. Mathieu, and M. Hadley, "Observation of microwave-assisted magnetization reversal in $Fe_6 5Co_3 5$ thin films through ferromagnetic resonance measurements", Applied Physics Letters **95**, 3–5 (2009) 10.1063/1.3175721.

[211]M. Hayashi, Y. K. Takahashi, and S. Mitani, "Microwave assisted resonant domain wall nucleation in permalloy nanowires", Applied Physics Letters **101** (2012) 10.1063/1.4764053.

[212]S. Rao, S. Subhra Mukherjee, M. Elyasi, C. Singh Bhatia, and H. Yang, "Electrical detection of microwave assisted magnetization reversal by spin pumping", Applied Physics Letters **104** (2014) 10.1063/1.4869488.

[213]X. Kong, D. Krasa, H. Zhou, W. Williams, S. McVitie, J. Weaver, and C. Wilkinson, "Very high resolution etching of magnetic nanostructures in organic gases", Microelectronic Engineering **85**, 988–991 (2008) 10.1016/j.mee.2007.12.006.

[214]B. Khamsehpour, "High resolution patterning of thin magnetic films to produce ultrasmall magnetic elements", Journal of Vacuum Science & Technology B: Microelectronics and Nanometer Structures **14**, 3361 (1996) 10.1116/1.588536.

[215]B. Khamsehpour, "Use of laser reflectometry for end-point detection during the etching of magnetic thin films", Journal of Vacuum Science & Technology A: Vacuum, Surfaces, and Films **15**, 2069 (1997) 10.1116/1.580610.

[216]S. E. Hicks, "Reflectance modeling for in situ dry etch monitoring of bulk SiO2 and III–V multilayer structures", Journal of Vacuum Science & Technology B: Microelectronics and Nanometer Structures **12**, 3306 (1994) 10.1116/1.587617.

[217]T. Weiland, "Time Domain Electromagnetic Field Computation With Finite Difference Methods", International Journal of Numerical Modelling Electronic Networks Devices and Fields **9**, 295–319 (1996) 10.1002/(SICI)1099-1204(199607)9:4<295::AID-JNM240>3.0.CO;2-8.

Appendix A

Fabrication of antidots

Details of the fabrication of large arrays of antidots by means of electron-beam lithography combined with reactive ion etching (RIE) are discussed in this section. The aim was to etch holes on continuous exchange bias films comprised of [FeMn/NiFe] multilayers, on which Ta was used as buffer and capping layer. Since the films were already deposited, the only possibility was to follow a top-bottom approach. In the James Watt nano-fabrication centre (JWNC), for technical reasons there was only the option of doing reactive ion etching of these elements on a specific etching tool, the ET340, which allowed only for the use of CH_4/H_2 as a chemical etchant [213, 214]. This etching process required the use of a hard mask as the resist itself was easily damaged in this environment. An illustration of the fabrication steps is shown in Fig. A.1 with the processing steps described below.

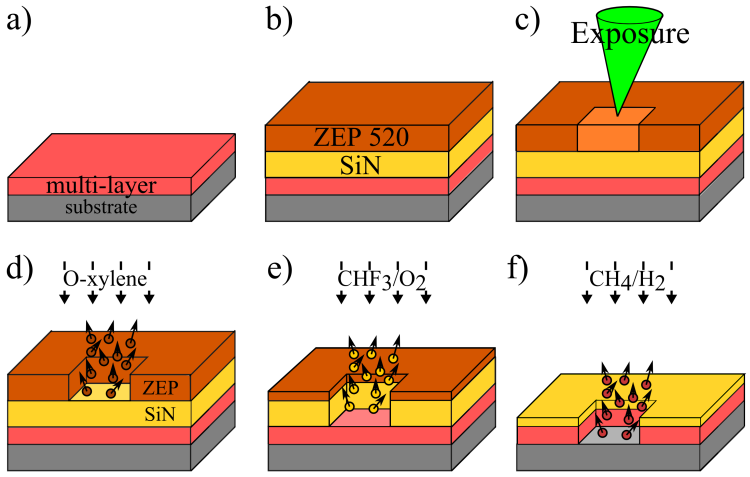

Figure A.1: Illustration of the fabrication steps a to f corresponding to 1,2-3,4,5,6,7, respectively.

1. The samples were cleaned in four consecutive steps involving an ultrasonic bath while immersed in acetone, isopropyl alcohol (IPA), methanol and reverse osmosis (RO) water, for periods of 5 minutes.

2. The hard mask, silicon nitride(SiN), with ∼120 nm in thickness, was deposited on an ICP800 deposition tool.

3. The substrate was spin coated with primer (MCC 80/20) and baked in a oven at 120°C for a period of 15 minutes. Immediately after, the substrate was spin coated with a resist layer of ZEP520, at a rotation speed of 5000 rpm for 1 minute, resulting in a 200 nm thick layer. The substrate was subsequently subject to a final bake for the duration of 1 hour, in an oven at 180°C.

4. In order to proceed with the e-beam lithography, one requires a design file (.gds), which contains the information about the geometry, exposure doses, proximity corrections, e-beam current and step size. These are fundamental to the success of the lithography and often require optimisation. In particular, for the case of large array patterning, where inefficient design implementation can lead to time consuming and therefore expensive lithography. The standard practice within the JWNC is to produce the designs in a CAD software called L-edit. These are then transferred to a software called Layout-Beamer to apply proximity corrections, fracturing and edge corrections. Finally, the job is submitted to the electron beam writer through a software called Belle.

   Prior to the design implementation in L-edit, one must decide which electron beam current to use and the corresponding beam size. The beam size is a necessary reference for L-edit, as the lateral dimensions of the fractured geometry must be equal to the spot size of the electron beam writer, in order to avoid over- or under-exposure. For the fabrication of features with characteristic dimensions of 240 nm in diameter, a beam current of 8 nA is adequate as it results in a 12 nm beam size (specifications of the electron beam writer). With that in mind, the minimum feature size in L-edit must be set to 12 nm. These parameters are set in the tab Menu Properties Grid and adjusting the grid snapping to multiples of 12 nm.

   Initially, a single circular element was created with the desired diameter and

then the circle was fractured into small regular rectangular shapes, as illustrated in Fig. A.2. The single element was then arrayed into a 100x100 μm^2 cell. The design file was exported with .gds format, which is compatible with the next software in the design chain.

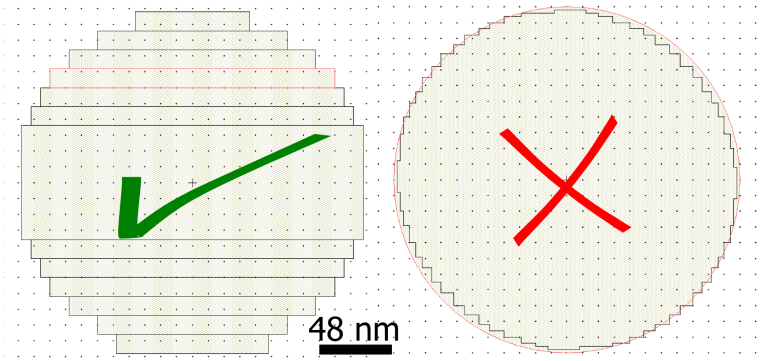

Figure A.2: Illustration of the design cell implemented in L-Edit. In the correct way, one has to consider the smaller feature as the beam size. The incorrect way to implement the unit cell is shown on the right hand side. Here, the smallest edge size is 1 nm. This incorrect procedure leads to slow writing times and over-exposure.

The design file was imported to Layout-Beamer and a calibration file was applied to the geometry to account for proximity corrections related to the backscattering of electrons from the substrate to the resist while writing. Before exporting the design to a .vep file format, the field of view and the beam diameter settings must be updated to 100x100 μm^2 and 12 nm, respectively. The .vep file generated is sent to the server of the electron beam writer. In the final step of the design process the .vep file is opened in the Belle software. Here, the geometry of the substrate, the relative position of the pattern, the beam current and the exposure doses are specified. Based on these parameters, the software estimates the writing time for the whole job. For the case of 4×2 mm^2 array of holes, the estimated writing time was 1.6 hours but the actual writing times was 1.17 hours.

To decide on which exposure dose is more adequate for the substrate and the resist in use, an exposure test is advised. In the dose test, the exposure was ranged between 150-1000 μCcm^{-2} in 12 steps. For that, the 100x100 μm^2 pattern was arrayed in a 3×4 matrix, where each element had a different exposure dose.

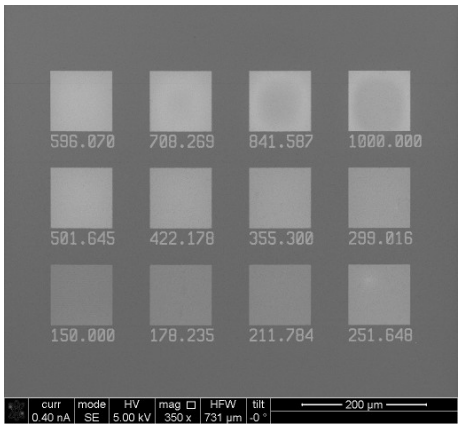

Figure A.3: SEM image of the exposure test. Image acquired after development of the resist.

5. When the beam writing job is finished, one has to develop the resist. When using ZEP520, O-Xylene must be used as a developer. Because this is a positive resist, only the regions exposed with the electron beam will be removed. According to the manufacturer specifications, the development of the resist has to be performed under a controlled temperature of T= 23±0.5°C. The resist must be fully immersed in the solution for 75 seconds and subsequently immersed in IPA for 45 seconds.

   The results of the exposure test are shown in Fig. A.3, after development of the resist. The doses corresponding to 250 and 350 μCcm^{-2} produced good results. An example is shown in Fig. A.4.

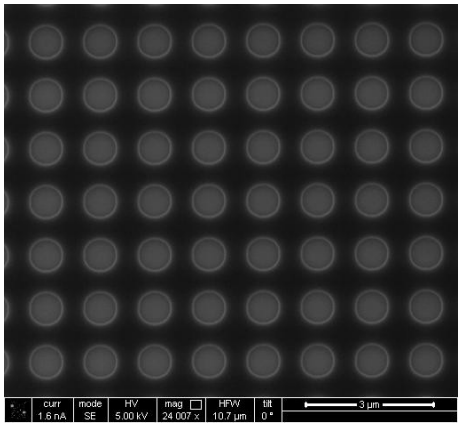

Figure A.4: SEM image of the optimum exposure dose in the case of 450 nm holes spaced by 1.3 μm. Beam current used was 8 nA and exposure dose of 300 μCcm^{-2}

6. At this stage the pattern is transferred from the resist to the SiN by using RIE with CHF_3/O_2, with etch rates of approximately 50 nm/min. Figure A.5 shows

the results of transferring the patterning to the SiN. The top layer corresponds to the remaining ZEP. The SiN layer has been successfully etched, as the depth of the SiN matches the estimated layer thickness. For the success of the mask transfer, it was vital to add a so-called ashing step, prior to the etching of the SiN, in order to remove the thin resist layer from the bottom of the holes. During the etching process, the etch depth was monitored by measuring the reflectance as a function of time obtained from a laser reflectometer [215] focused at an area cleared of resist, on the surface of the substrate. The reflectance will vary as the refractive index is altered with etching. The etch profile of the SiN is shown in Fig. A.5b. An over-etch time was allowed to ensure that the SiN was completely removed from the hole regions.

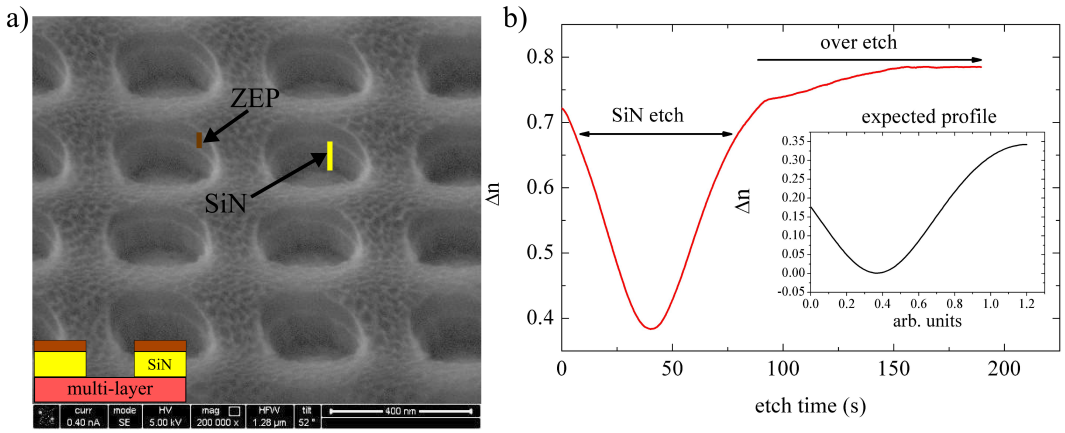

Figure A.5: a) SEM image relative to the etching process of SiN. The top layer corresponds to the remaining resist and the subsequent layer corresponds to the etched SiN. b) etch profile of SiN.

7. The etching of the Ta/NiFe/FeMn/Ta was performed in the ET340 tool by using CH_4/H_2. The expected etch rate was 2-3 nm/min [213]. As the sample is constituted by layers of different metals, the etch rates will differ slightly and therefore we expect the reflectance profiles to exhibit different slopes as the etching progresses. The etching time should be sufficient to allow the reflectance profile to become flat, meaning that the etching process has reached the bottom Si layer. As this process is highly selective, the Si substrate remains un-etched. The etching profiles are shown in Fig. A.6b, with the corresponding derivative and calculated etch profile [216].

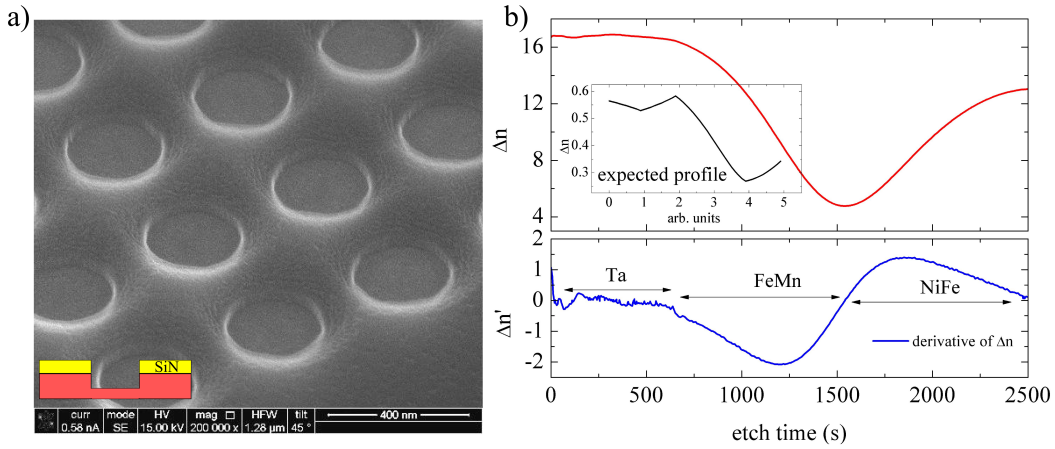

Figure A.6: a) SEM image relative to the etching process of Ta/FeMn/NiFe/Ta. b) Etch profile of the multilayer and its derivative, where three phases can be identified.

This fabrication process was applied to a [FeMn/NiFe]×1 and [FeMn/NiFe]×2. For an accurate evaluation of the etched structure, the use of cross sectional analysis is highly advised. Cross-sectional analyses were carried out on two of the samples. The sample [FeMn/NiFe]×1 is discussed in the chapter 5. The cross- sectional analysis of [FeMn/NiFe]×2 is discussed in the Sec. 6.4.

Appendix B

Micromagnetic simulations

Micromagnetic calculations allow for a numerical simulation of the static and dynamic response of a magnetic system. As shown in Sec. 2.1.2, the equilibrium condition, or ground state, is reached when the total free energy is minimized. This is applicable in the presence of either static or nanosecond time dependent excitations. Micromagnetics solve the torque equation Eq. 2.1, as discussed in Sec. 2.1.

Throughout this dissertation the micromagnetic results were obtained using Mumax3, an open-source GPU backed simulation software [173]. This software calculates the time and space dependent magnetisation dynamics using a finite difference method. Any magnetic element of size $(\mathrm{L_x}, \mathrm{L_y}, \mathrm{L_z})$ is discretised into a number of 3-dimensional cells $(\mathrm{c_x}, \mathrm{c_y}, \mathrm{c_z})$ with orthorhombic shape, forming the simulations box. The key parameters are, the size and number of discretisation cells, the magnetic properties such as anisotropy, exchange constant, saturation magnetisation and damping constant. The shape of the magnetic element and arraying can also be implemented intuitively.

Following Ref. [173], some important details of the simulation tool are now discussed.

- Mumax enables the implementation of periodic boundary conditions (PBC) which allow for the wrap-around of the exchange interaction term at the edges of the simulation box. Performing micromagnetic simulations on large systems can be time consuming and computationally demanding so the PBC are convenient, especially in situations where arraying is possible.

- Mumax has a built-in function called '$relax()$', which determines the lowest

energy state of any initial magnetic configuration. This is done by solving the torque equation until the dynamic component of the magnetisation reaches $10^{-4} - 10^{-7}\gamma$, with γ being the gyromagnetic ratio. This function is applied every time the magnetic state is modified by a static field to ensure that an equilibrium state is reached.

- To ensure accuracy in the numerical evaluation of the exchange energy, the unit cell dimension c_x size must be smaller than the exchange length $l_{ex}=(2A_{ex}/\mu_0 M_s^2)^{1/2}$, where A_{ex} is the exchange constant and M_s is the saturation magnetisation. This is done to ensure that spin-spin exchange interaction is adequately taken into account when solving the dynamic equations.

B.0.1 Spatially uniform excitation

Consider a magnetic system with an in-plane magnetisation collinear with an external static field along the y-axis. Once the ground state is reached, a spatially uniform, time dependent, field pulse is applied along the z-axis. The time profile of the field pulse follows $h(t)=h_0 \sin(\Delta\omega(t-t_0))/\Delta\omega(t-t_0)$, where $\Delta\omega$ is the excitation bandwidth, t_0 corresponds to a time offset and h_0= 0.1 mT is the pulse magnitude, as illustrated in Fig. B.1a. Effectively, with uniform pulse the magnetisation of the entire volume is excited in the same way, i.e. the excitation wavevector is zero (k= 0). Upon excitation with a field pulse, the magnetisation undergoes damped precessional motion as shown in Fig. B.1b. The precession modes can be obtained by applying a time-domain Fourier transform of $m_z(t)$ over the entire simulation time.

In order to obtain the amplitude distribution of the precessional modes, one must perform the time domain FFT at each cell $m(c_x, c_y, c_z, t)$ individually and then build the amplitude maps according to the frequencies of interest. Figure B.2 shows an example of the precessional mode amplitudes for an antidot lattice from which four modes are obtained, which correspond to the four modes (I-IV) in Fig. B.1c. Each mode is localised in a different region of the antidot lattice. In chapter 5 the origin of the magnetostatic resonance modes is discussed in detail, for an equivalent system.

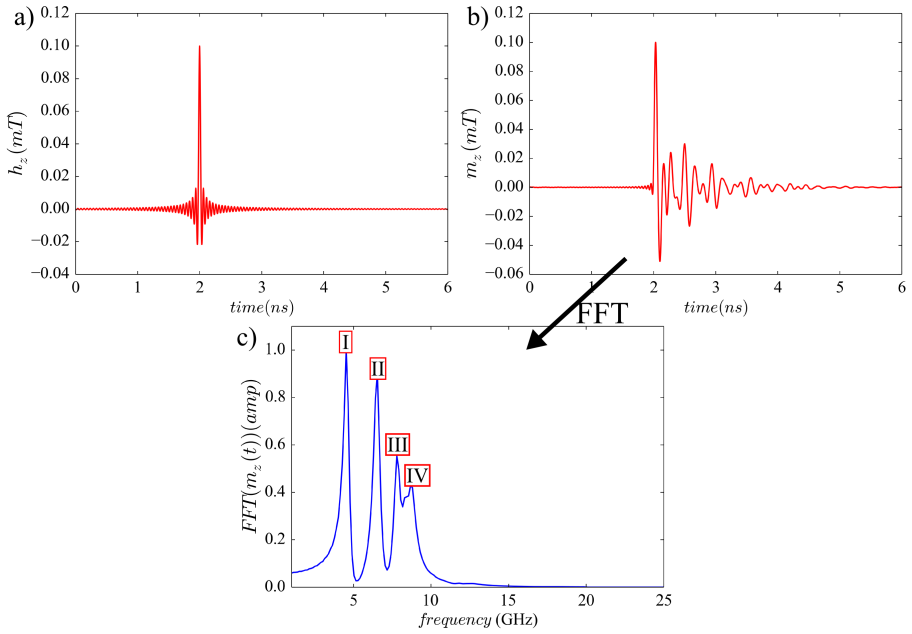

Figure B.1: Illustration of a)the applied field pulse as a function of time; b) the time varying component $m_z(t)$ and; c) time-domain Fourier transform of $m_z(t)$. Results obtained from 2×2 array of holes with 240 nm in diameter, and edge to edge separation of 200 nm (c_x= c_y= 3.4 nm,c_z= 10 nm). Other parameters: M_s= 0.9 T A_{ex}= 13e^{-12} J/m, α= 0.02 and static field H= 0.05 T.

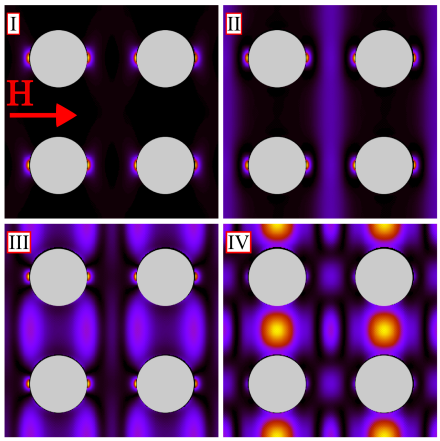

Figure B.2: Illustration of time-domain Fourier transform of $m_z(c_i, c_j, c_j, t)$. Results obtained from 2×2 array of holes with diameter of 240 nm, and edge to edge separation of 200 nm (c_x= c_y= 3.4 nm, c_z= 10 nm). Other parameters: M_S= 0.9 T, A_{ex}= 13e^{-12} J/m, α= 0.02, static field H = 0.05 T.

B.0.2 Spatially non-uniform excitation

In order to study the spin wave dispersion $f(k)$, the uniform excitation must be replaced by a spatially and time varying pulse, as illustrated in Fig. B.3a, allowing for the excitation and propagation of a finite wavelength range of spin waves. The spatial modulation follows $g(x,t) = h(t) \times \sin(\Delta k(x-x_0))/\Delta k(x-x_0)$, where Δk is the wavevector bandwidth and x_0 is a spatial offset. In the configuration of interest, the excitation wave vector is set perpendicular to the applied field direction, to comply with the Damon-Eshbach configuration (see Sec. 2.2). As illustrated in Fig. B.3b, the geometry implemented in the case of the antidots is extended periodically along the direction of the spin wave propagation. To obtain well resolved spin wave dispersion maps, one has to ensure large propagation distances along the direction collinear with k, $\Delta k = \pi/L_x$ [116]. The effect of the pulse on the magnetisation is demonstrated in Fig. B.3c.

The Mumax simulations allowed the analysis of the time dependent components of the magnetisation, $m(t)$, which were subsequently processed according to Eq. B.1.

$$m_z(x,y,z,t) \rightarrow m_z(x,y=n,\overline{z},t) \rightarrow swd(\omega, q^{DE}) = \sum^{y=n} FT^{2D}(m_z(x,t) \qquad \text{(B.1)}$$

The data processing was implemented as follows[1]:

- Run the Mumax3 script and save the spatial distribution of the magnetisation every time step, t_s= 1 ps.
- Import all files to python to build a large array of $m_z(x,y,\overline{z},t=[0-t_{max}])$. If $N_z > 1$ the magnetisation in the out-of-plane direction should be averaged.
- Select the direction of propagation, which in this example is the x-axis, while the magnetic field was applied field along the y-axis.
- Perform a 2-D FFT of $m_z(x,y=n,t=[0-t_{max}])$.
- Iteratively perform a 2-D FFT over the entire y range.
- Sum over all 2D-FFT along the y-axis, as shown in Eq. B.1. Alternatively, one can simply evaluate the spin wave dispersion at the center of the propagation channel.

[1]The data processing was implemented in Python

The results on the spin wave dispersion are presented and discussed in Sec. 5.3.2

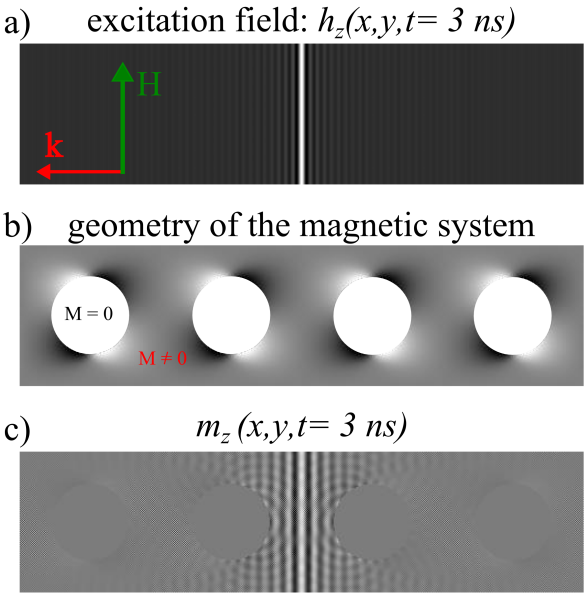

Figure B.3: To obtain the spin wave dispersion numerically, the antidot array must be replicated along the direction of the excitation wave vector. a) Spatially modulated excitation field at t= 3 ns; b) geometry of the sample; c) Response of the magnetisation to the field pulse, $m_z(x, y, z)$ at $t = 3$ ns. The geometry shown is representative of the sample studied in chapter 5.

Appendix C

Microwave simulations using CST

CST Microwave Studio is a 3-Dimensional electromagnetic simulation tool, based on the Finite Integration Technique first proposed by Weiland [217]. It consists of solving the integral form of Maxwell's equations for a discretised object. For the majority of the simulations performed, the Frequency Domain solver was used, which, according to the documentation available, was the most efficient method to obtain the S-parameters over a certain frequency range, as well as the electromagnetic field distribution at given frequencies.

When implementing a simulation, the user must account for the following aspects.

- The dielectric properties of the materials being used in the simulation (dielectric constant and conductivity).
- Evaluate the characteristic port impedance for a given substrate, taking into account its dielectric properties, the thickness of the substrate and the waveguide configuration (co-planar, microstrip, etc). CST contains a Macro function, which allows an immediate calculation of parameters, such as analytical line impedance (Macros>Calculate>Analytical line impedance), which is useful for obtaining the expected value for the port impedance, at a certain frequency.
- Set the appropriate unit system for spatial units, frequency, temperature and time, on tab 'set units'.
- The interface allows the creation of all types of object. These may vary from rectangular, circular and wire shapes and all can be subject to boolean operations. Regardless of the geometry, the objects are discretised in hexahedral

or tetrahedral polygons. The feature size is user defined, within a desired error limit. Tetrahedral meshing was used with an accuracy of 10^{-4} mm.

- CST allows for an adaptive mesh refinement, meaning that edges and more complex parts of the geometry will have smaller calculation grid. An example of the mesh view is shown in Fig. C.1 for one of the simulated geometries. An important aspect to keep in mind is the number of tetrahedrons created after the mesh calculation. This will have an impact on the simulation time. Also, the number of tetrahedrons may vary, depending on whether the convergence criteria for the S-parameter calculation (0.02 was used) is reached within the number of passes (user defined frequency domain solver > adaptive mesh refinement> properties).

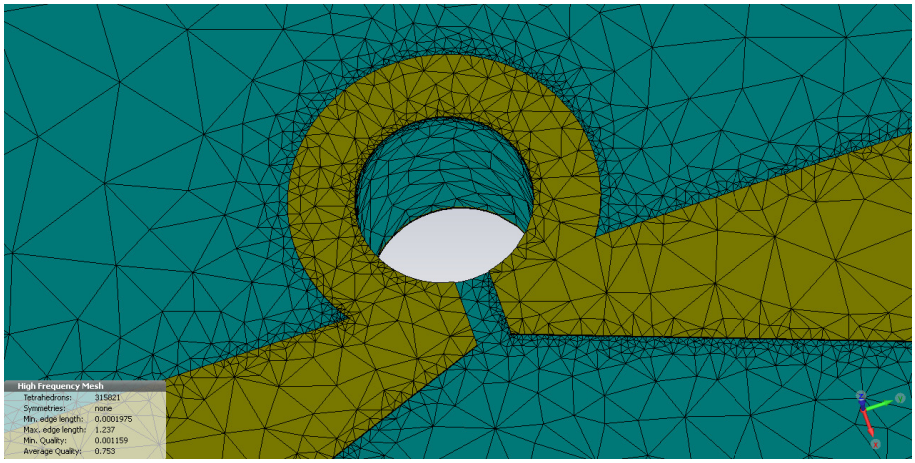

Figure C.1: Adaptive mesh refinement in CST Microwave Studio. For this geometry, the initial mesh calculation results in 351 821 tetrahedrons.

- Before running the solver, one has also to define the frequency range, the waveguide excitation ports, the background material and the boundary conditions.
  - The frequency range must be set within the desired operating limits. A frequency range of [1-18] GHz was used in the simulations.
  - The waveguide ports serve as the input of the excitation signals. An illustration of the waveguide port is shown in Fig. C.2. The time profile of the input wave is shown in Fig. C.3.
  - The background material must be set to allow a gap between the boundaries of the simulation and the bounding limits of the structure. Typically,

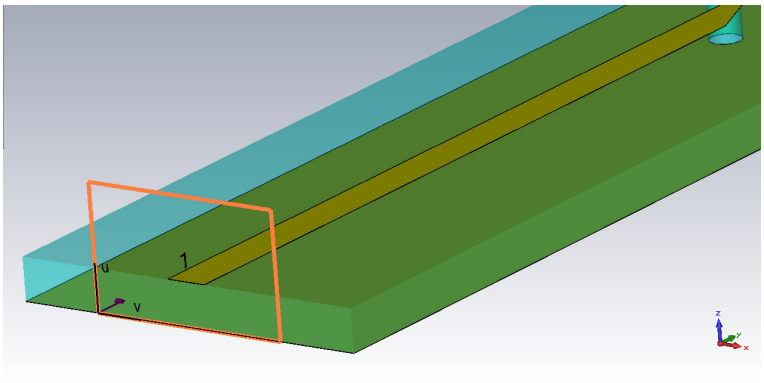

Figure C.2: Illustration of the waveguide port. The rectangle in orange defines the waveguide port dimensions set in CST.

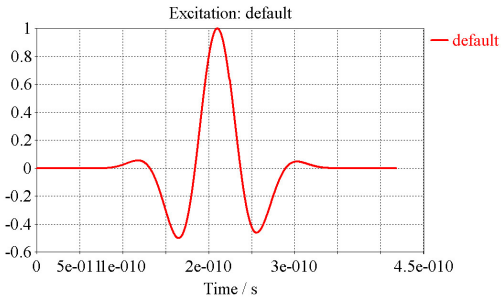

Figure C.3: Standard time profile of the input excitation.

the background material is set to empty space (ϵ_r and μ_r is 1). The face corresponding to the waveguide port must not contain any background material.

- The boundary conditions can be defined as open, electric (tangential e-field= 0), magnetic (tangential h-field= 0), periodic (for arrayed structures) or as conducting walls. The structure was tested with open and electric boundaries. The characteristic impedance and the electromagnetic field distribution in the region of interest was the same for both simulations. As the microstrip contains a ground plane in the bottom of the substrate, the boundary conditions are automatically defined as a ground. Figure C.4 illustrates how the boundary conditions are implemented.

- In order to obtain the electromagnetic field distribution one has to define Field Monitors prior to running the FD Solver. The easiest way to do so is by using a Macro function to set a discrete number of field monitors (Macros> Solver> Monitors and probes> Broadband field monitors). Once the calculations are performed, one is able to evaluate the spatial distribution (2D or 3D) of the

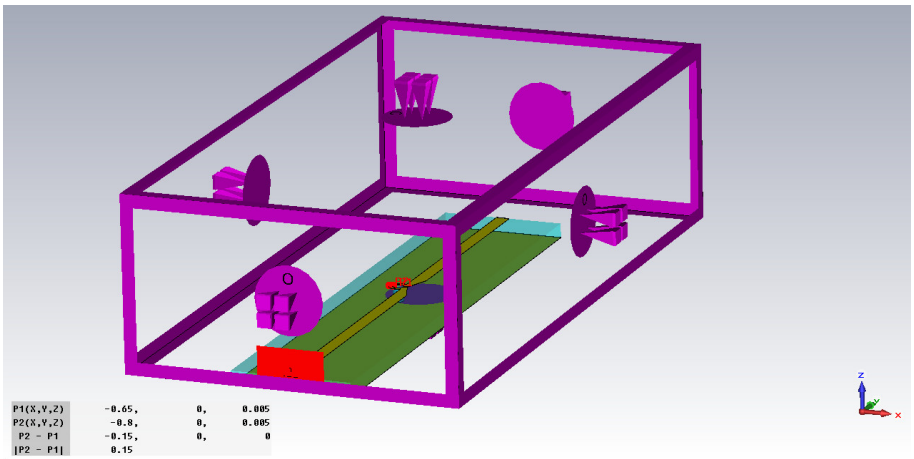

Figure C.4: Walls enclosing the microstrip correspond to the boundary implemented in one of the simulated structures. Note the gap between the simulated structure and the boundary of the simulation.

electromagnetic field by using a post processing template function. The in-plane e-field/h-field components x, y and z both in terms of magnitude and phase were exported for use in assessing the effects of microwave fields in the electron beam of the TEM experiments described in chapter 7.

Appendix D

Appendix- Chapter 5

D.1 Applied field direction in tilt series

Inside the microscope, the rod is tilted around its longest axis which means that the in-plane component of the applied field will be perpendicular to that same direction, as demonstrated in the schematic of Fig.D.1.

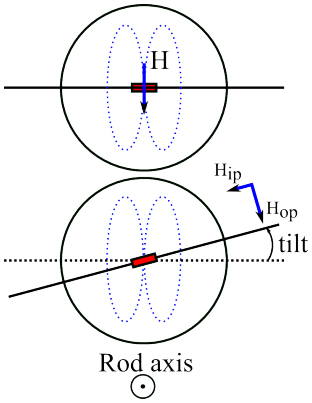

Figure D.1: Schematic of the tilt process inside the microscope. This procedure is applied in order to achieve in-plane magnetic fields, which can be used to tune the magnetic configuration of the specimen.

The periodic features, i.e the holes, can be used as a reference to determine the tilt direction by measuring the relative distortion of the lattice as the sample is tilted. Often this is necessary as the image is virtually rotated by the lens system. The image was rotated in order to align the edges of the hole lattice to the sides of the camera. Figure D.2 shows a series of bright field TEM images, which resulted from performing a sum over all components of the DPC detector. On the right hand

side, the upper and lower plots correspond to the horizontal and vertical profiles, respectively.

By comparing the tilt angles relative to $\pm 3^\circ$ it can concluded that there are no significant distortions in the lattice, so the sample is sitting horizontally in the home-built in-situ FMR (at 0°). The comparison between the images at tilt angles of 0° and 15°, help establishing the tilt and the applied field direction. After tilting, the distortion is more pronounced along the vertical axis, as the number of pixels is reduced from 736 down to 715, which is in agreement with the $\cos(15 \pm 1)$ in-plane projection of the antidot lattice.

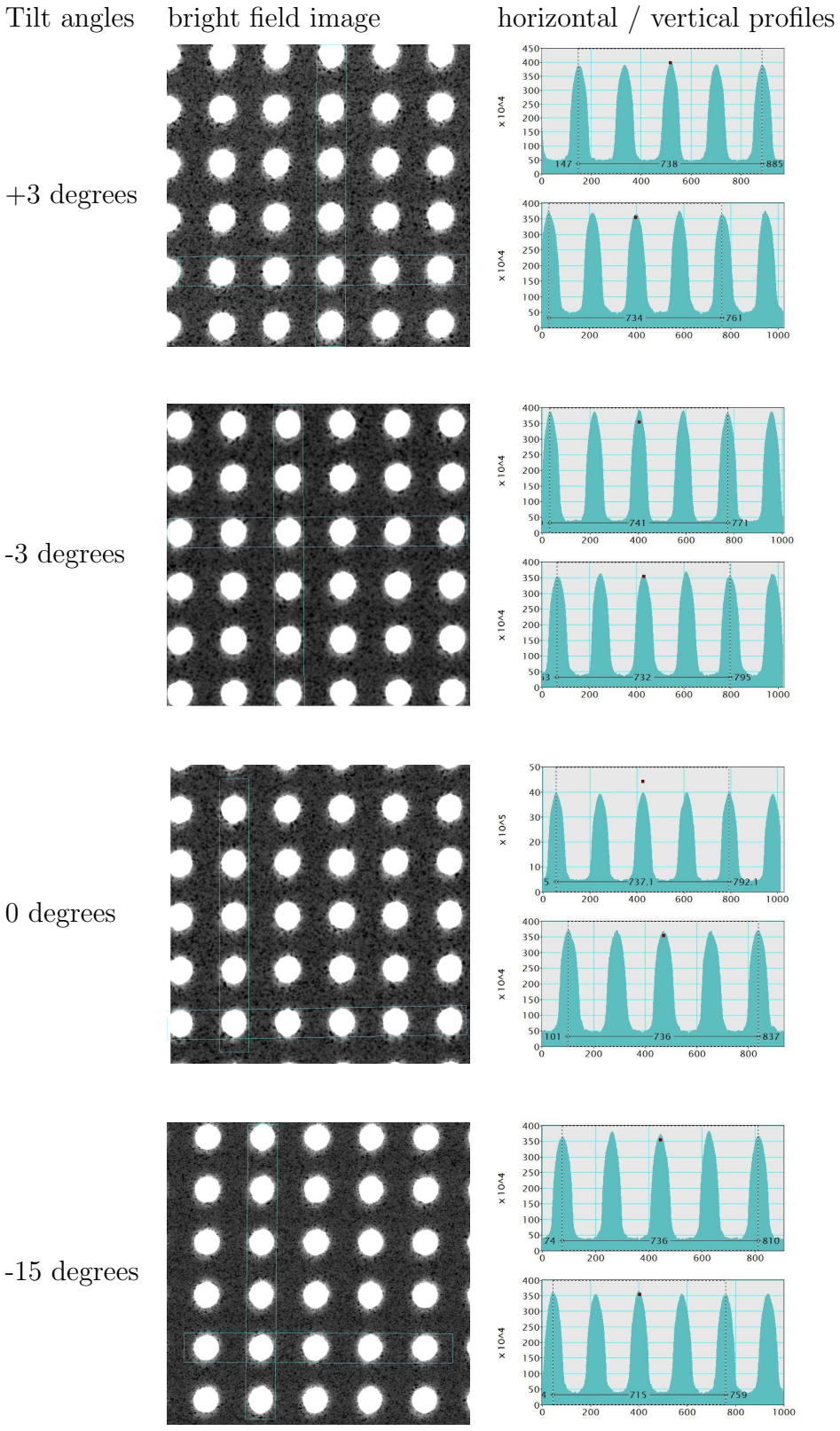

Figure D.2: Sum of all DPC components to form bright field image. Horizontal and vertical profiles added to demonstrate the tilt direction and the flatness of the sample at 0°.

D.2 Single exchange biased layer

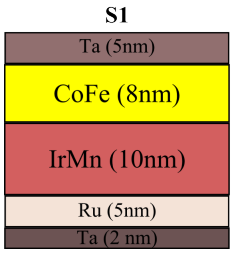

Figure D.3: Schematic of IrMn/CoFe

The field dependent DPC study on the single exchange biased antidot layer (S1) section is shown in Fig. D.4. The images were obtained while performing a field sweep, from positive saturation to negative saturation, which in the TEM corresponds to a change in the out-of-plane tilt angle. Note the misalignment between the applied field and the exchange bias direction. As a reference, the edges of the antidot lattice are parallel to the exchange bias direction as illustrated by the arrows in Fig.D.4-16°.

In brief, the magnetisation goes from saturated (green ↑) at 16°, to near saturation for negative tilt angles, −7°. The magnetisation process between these two saturation angles can be described by the existence of long zig-zag domains along the vertical wire channels (i) at the tilt angles of 10° and 5°.

At 1°, horizontally pinned regions (yellow ←) emerge in the vertical hole channels (iii), indicating that the magnetisation is no longer aligned with the field direction. At 0°, the yellow regions (←) extend through the horizontal wire channels (ii), as illustrated in region v, while in other regions of the antidot lattice, the domains have opposite direction, noted as the blue coloured regions (→), signed as vi. The domain configuration of both yellow and blue regions can be described as horizontal zig-zag patterns.

From −1° to −4° the long range domains break into shorter range domains, confined to the neighbouring holes. Within this tilt range, the domains evolve towards the downwards direction (red ↓). Note that at a tilt angle of −1° vortex states were observed (circled regions). In this sample however, these configurations were not stable enough to be studied in more details, as they vanished even with small variations in the applied field.

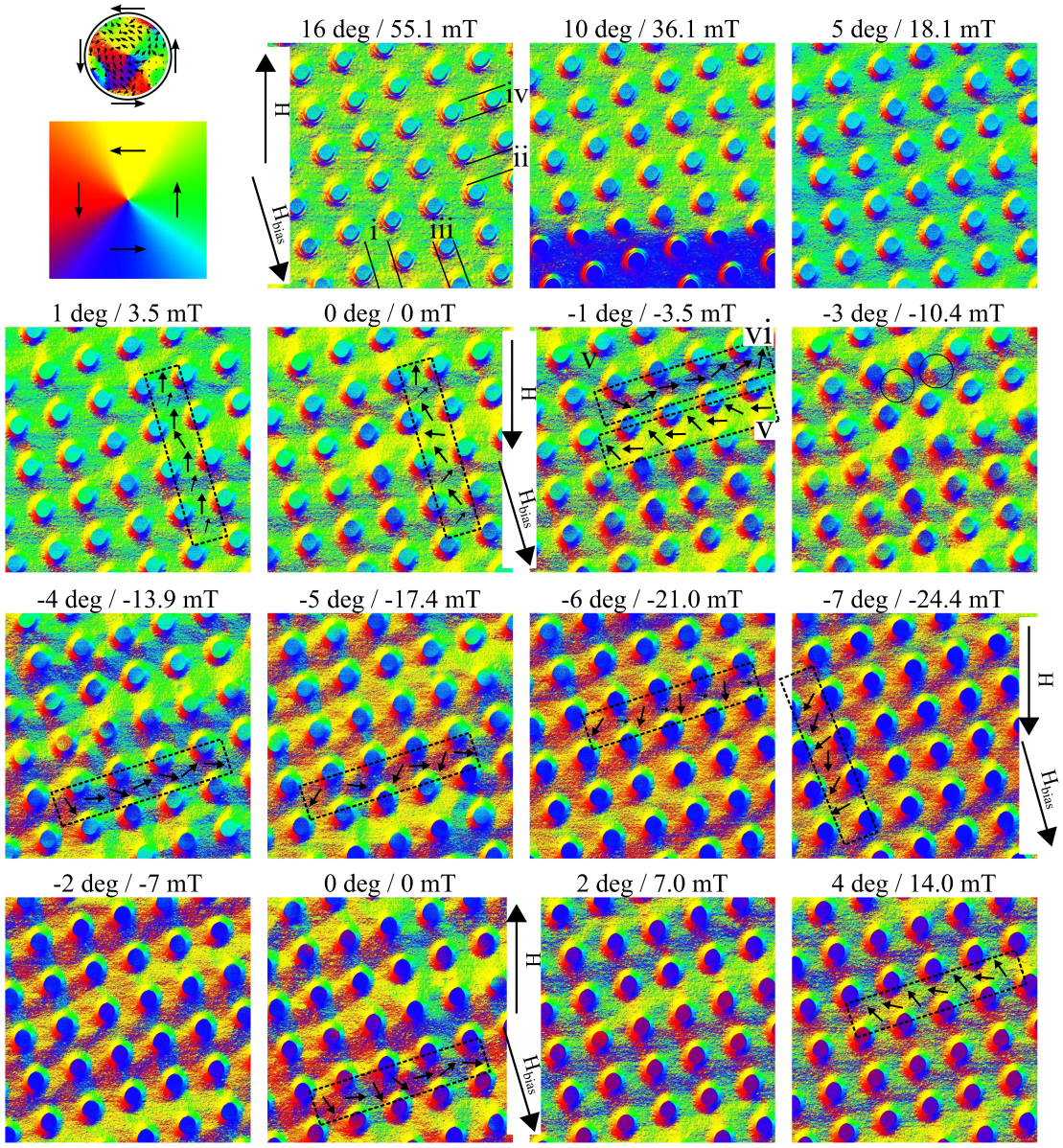

Figure D.4: Tilt series of sample S1, the single exchange biased layer.

From $-4°$ to $-7°$ the domains evolve to long range domains, but now pointing downwards, given by the increasingly strong red ($\downarrow$) contrast.

When the sample is tilted from negative saturation field back to positive tilt angles, it is noted that between $-2°$ and $0°$ long range horizontal domains yellow ($\leftarrow$) and some vertical domains ($\uparrow$) have emerged. This is an indication that large scale reversal has initiated at negative fields. Therefore it can be concluded that a clear exchange bias component is collinear with the applied field direction.

D.3 Cancellation region in S2

In this section it is illustrated how the magnitude of the magnetic induction varies with applied field angle. The gray coded images shown in Fig. D.5 correspond to the magnitude of the magnetic induction (left) $\mathrm{M} = \mathrm{sqrt}(\mathrm{ext02}^2 + \mathrm{ext13}^2)$ and the profiles on the right correspond to vertical and horizontal amplitude profiles (averaged over 30 pixels). The large relative variation of the magnetic induction in the tilt angles between -3° and -7° indicates that the regions with high induction magnitude are strongly pinned while the low contrast regions has little contribution from the induction field, due to partial cancellation on both ferromagnetic layers.

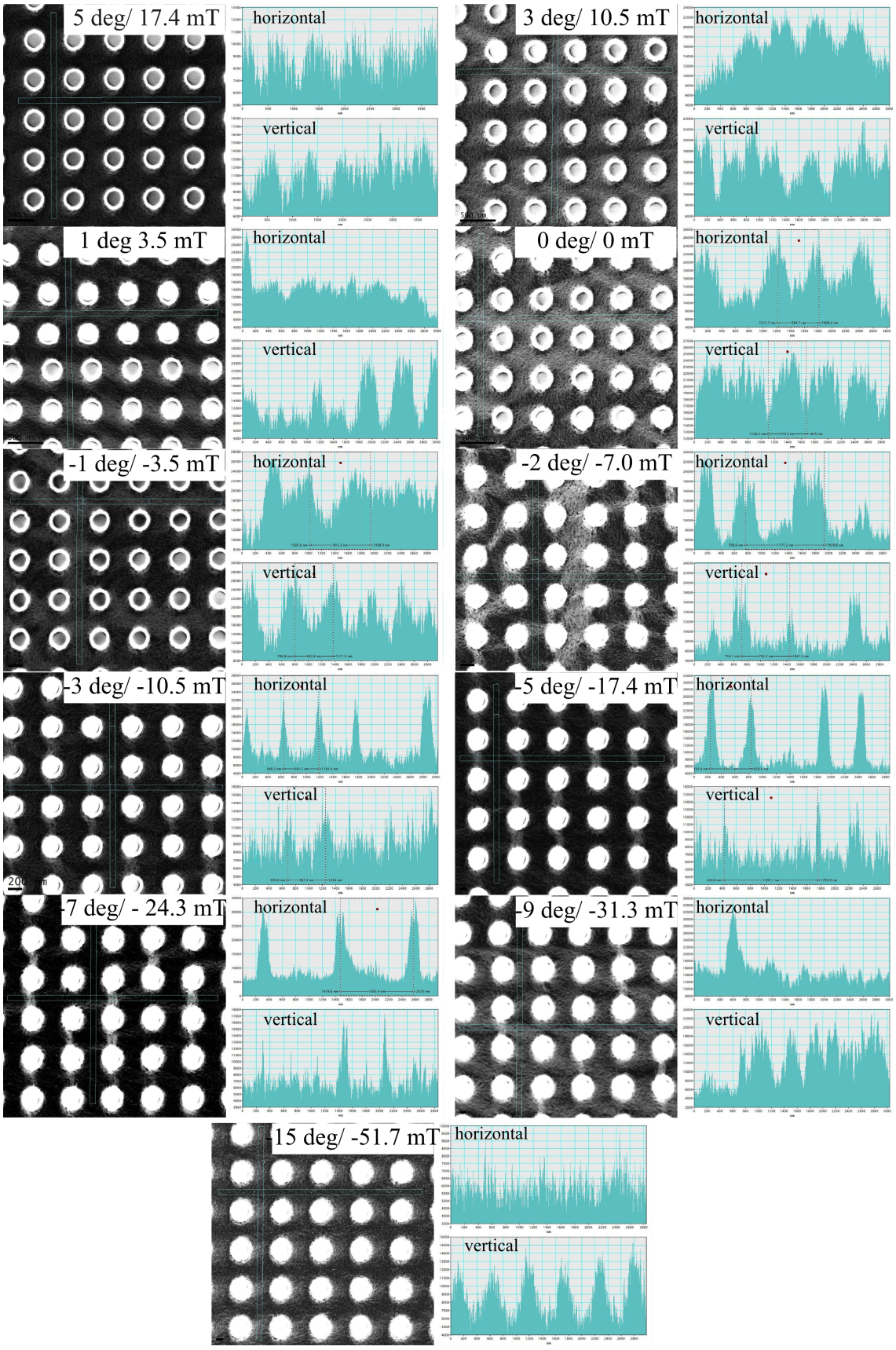

Figure D.5: Magnetic induction as a function of applied field (tilt).

D.4 Balancing the Vortex profile

In this section it is demonstrated how the DPC components can be balanced in order to gain enhanced contrast in the vortex regions. Figure D.6a and b show the components Ext2-Ext0 and Ext3-Ext1, respectively, of the segmented detector. Both components are sensitive to variations in the induction field, given by the black arrows. A vortex region is described as a 360° curl of the magnetisation around a center point. Ideally, this magnetic texture would have equal portions of the magnetic induction around its core, so the counts in the images would be symmetric around it accordingly. For the particular case of the vortices observed in this sample, the balance of the images is not recommended as the sample is constituted by two layers. The vortices are labelled in the DPC images as #1, #2 and #3 and the amplitude profiles shown. The shape of the profiles confirms that the magnetic induction is well balanced between the orthogonal components.

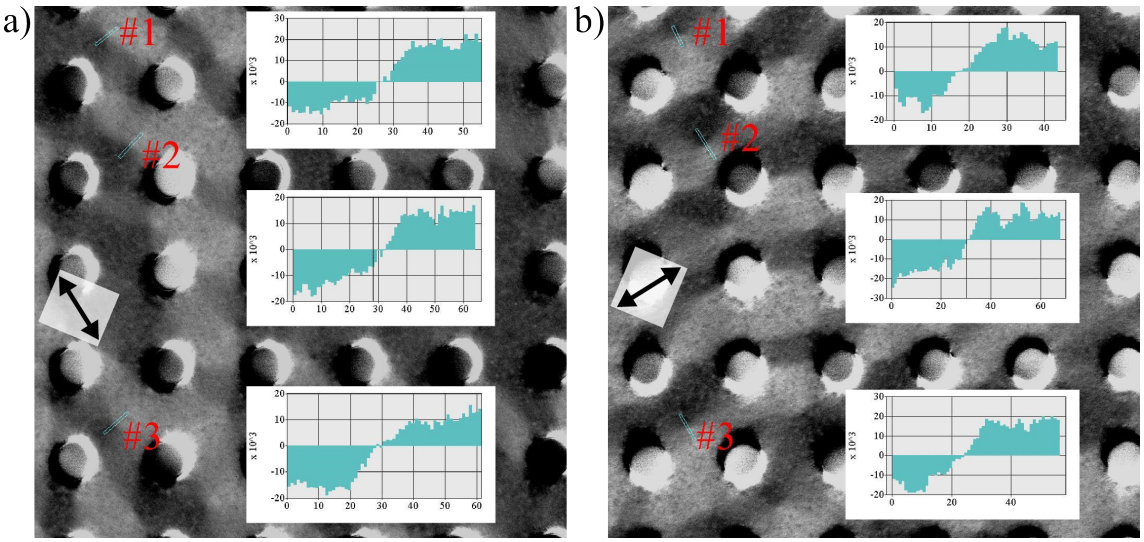

Figure D.6: DPC components a) Ext2-Ext0 and b) Ext3-Ext1. Note the distribution of amplitude in the vortices, given by the inset histograms for 3 distinct vortices. The amplitudes are well distributed around the core of the vortices.

Appendix E

Appendix- Chapter 6

E.1 Processing the experimental data

The experimental data was recorded in video format using Virtual Dub, with a resolution of 720x480 pixels at a rate of 10 frames per second. Prior to the frequency sweep on the VNA, a low angle diffraction (LAD) pattern of the undeflected beam (RF power off) was acquired, L_0. The VNA frequency sweep step time was set to have 4 steps per second. In order to analyse the data, the video was converted to frames, $L(\omega)$, at a conversion rate of 6 frames per second. A deconvolution filter was applied to each frame, i, resulting in $L'(\omega^i)$ frames more suitable for peak detection. The deconvolution procedure follows the expressions in Eq. E.1, which involves Fourier transforms of the frame L_0 and the frames $L(\omega)$.

$$F = \mathcal{F}_{2D}[L(\omega^i)] \tag{E.1a}$$

$$H = \mathcal{F}_{2D}[L_0] \tag{E.1b}$$

$$L^i = I\mathcal{F}\left[\frac{F \times H^*}{H \times H^* + \lambda^2}\right], \tag{E.1c}$$

where the term λ is a correction factor ($\lambda = 5000$).

An example of L_0, $L(\omega)$ and the processed image, $L'(\omega^i)$, is given in Fig E.1a, b and c, respectively.

Figure E.1 illustrates the procedure employed to determine the maxima of the deflected beam. The images labelled with LAD correspond to the experimental data, from which the centre of LAD pattern and the rotation angle was determined. The

images labelled with Dec(LAD) allowed to accurately determine the location of the maxima, relative to the centre of the LAD pattern, which then allowed to calculate the deflection angles. Fit an ellipse to the contours of the LAD image to extract the

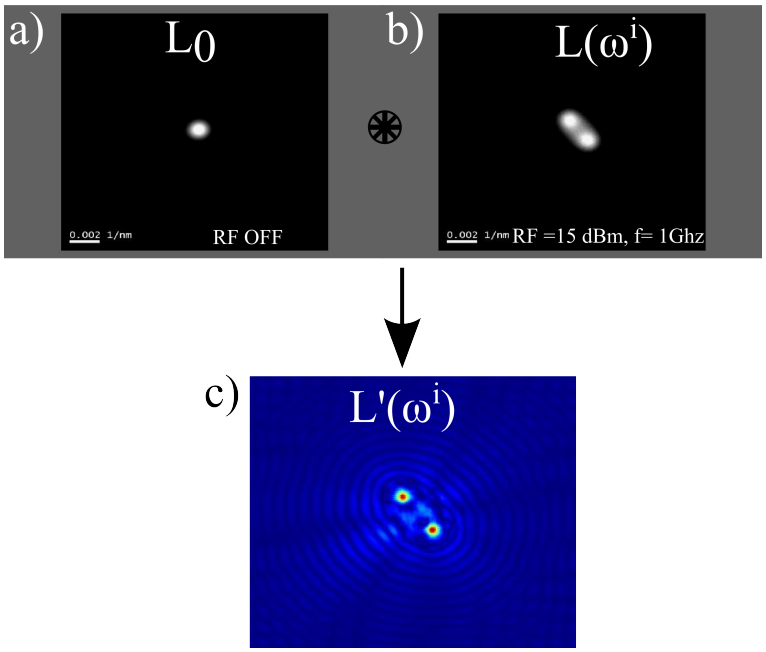

Figure E.1: a) Undeflected beam L_0 (RF off); b) Experimental data, $L(\omega^i)$ at 1 GHz and Rf power set to 15 dBm; c) Processed image $L`(\omega^i)$.

rotation angle and find the maxima from the deconvolved images.

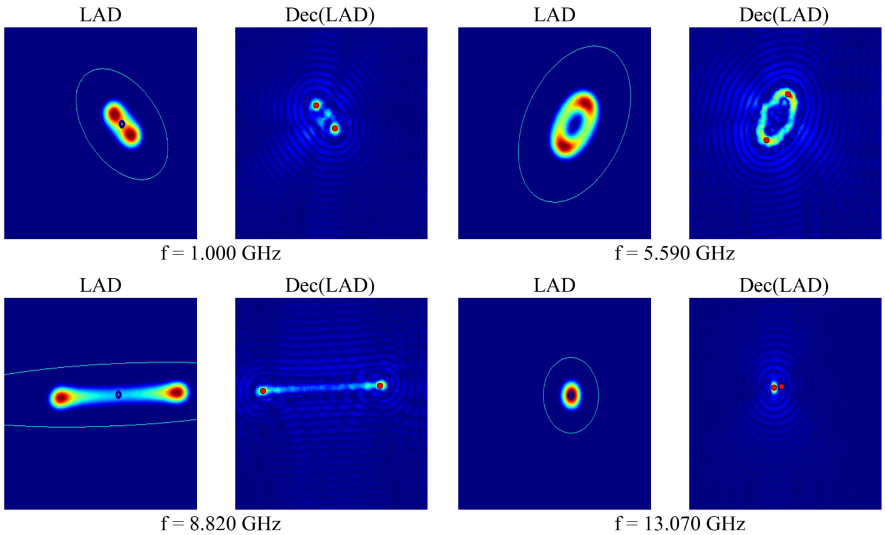

Figure E.2: Examples of the peak and rotation detection

E.2 E/H-field distribution

The 2-dimensional microwave field distribution in the loop shaped region of the microstrip is shown in this section. As can be seen in Figs. E.3-E.8, the amplitude of the field distribution deceases by a factor of a 100 in the distance of 2-3 mm above the signal line.

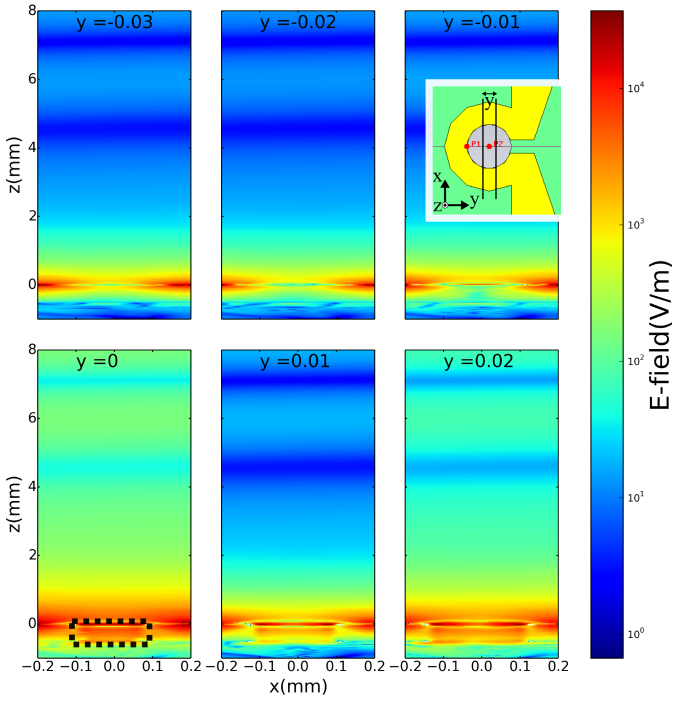

Figure E.3: Distribution of the E-field as a function of lateral position y and vertical distance from the microstrip z at a frequency f=1 GHz.

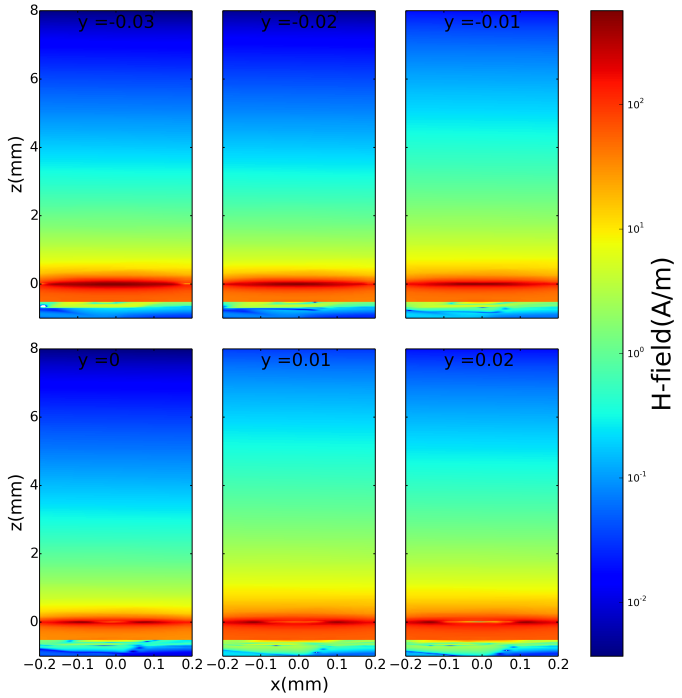

Figure E.4: Distribution of the H-field as a function of lateral position y and vertical distance from the microstrip z at a frequency f=1 GHz.

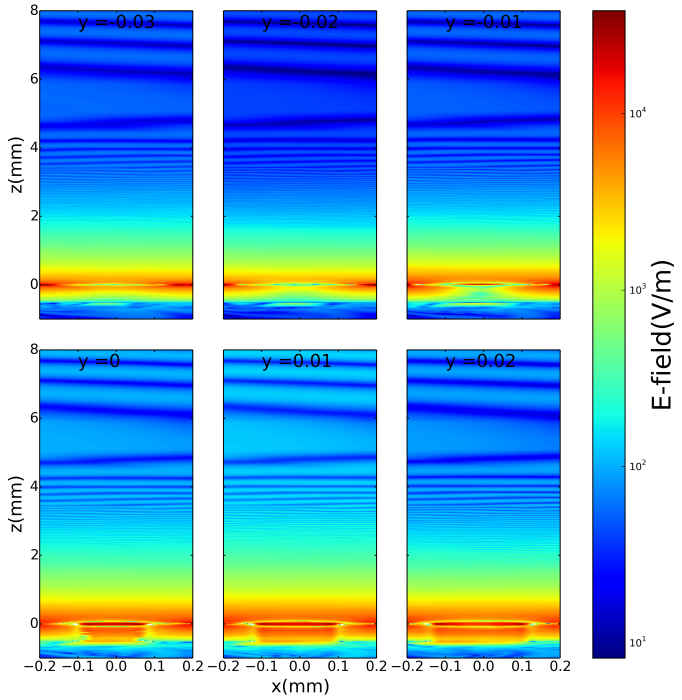

Figure E.5: Distribution of the E-field as a function of lateral position y and vertical distance from the microstrip z at a frequency f=5.8 GHz.

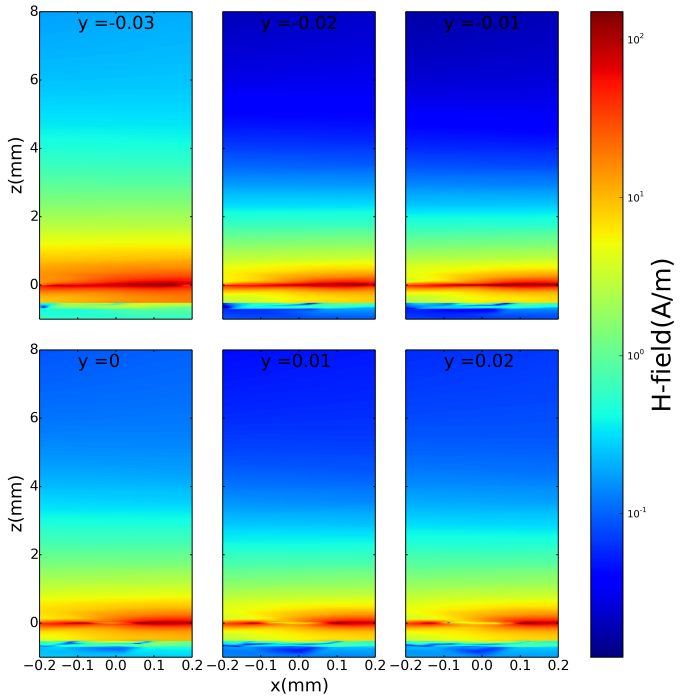

Figure E.6: Distribution of the H-field as a function of lateral position y and vertical distance from the microstrip z at a frequency f=5.8 GHz.

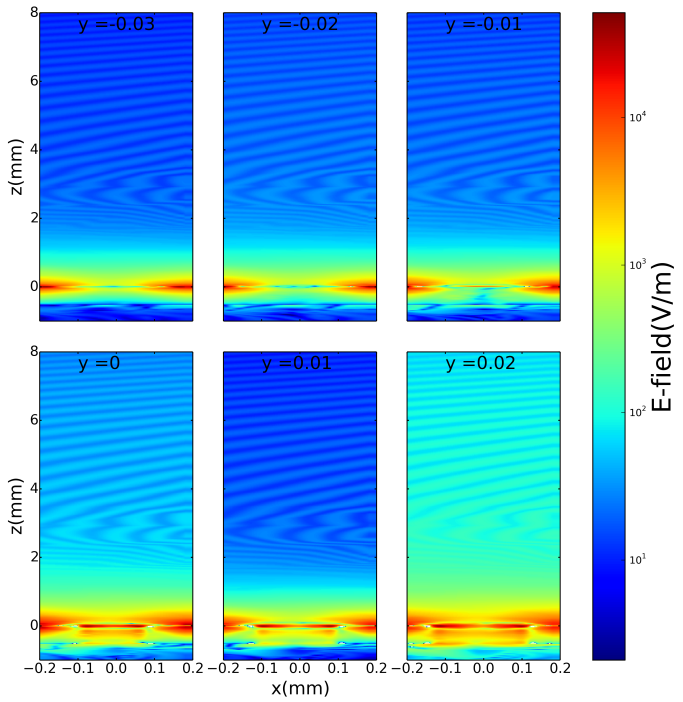

Figure E.7: Distribution of the E-field as a function of lateral position y and vertical distance from the microstrip z at a frequency f=17 GHz.

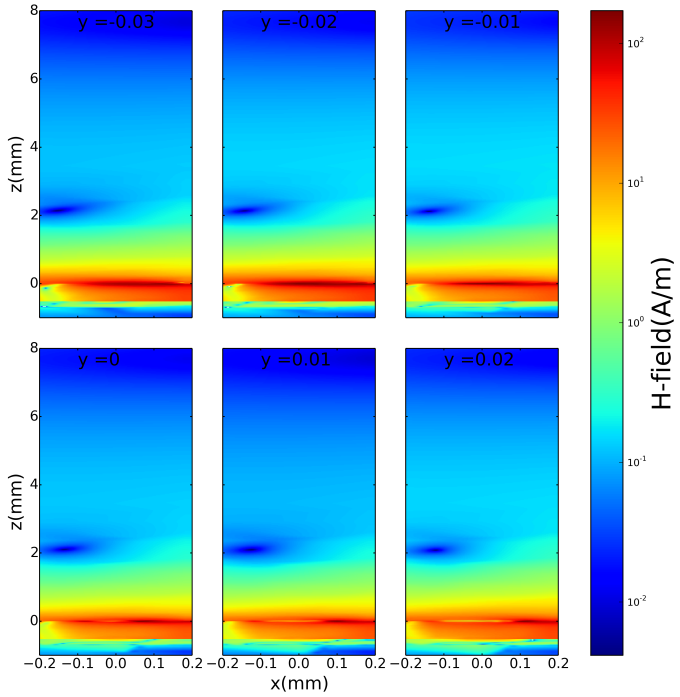

Figure E.8: Distribution of the H-field as a function of lateral position y and vertical distance from the microstrip z at a frequency f=17 GHz.